

TOWARDS MORE OPTIMIZED AND RESILIENT SEISMIC DESIGN OF
BUILDINGS WITH STEEL MOMENT RESISTING FRAMES

TOWARDS MORE OPTIMIZED AND RESILIENT SEISMIC
DESIGN OF BUILDINGS WITH STEEL MOMENT
RESISTING FRAMES

BY

PAUL ROBERT STENEKER, B.Eng.

A THESIS

SUBMITTED TO THE DEPARTMENT OF CIVIL ENGINEERING

AND THE SCHOOL OF GRADUATE STUDIES

OF MCMASTER UNIVERSITY

IN PARTIAL FULFILMENT OF THE REQUIREMENTS

FOR THE DEGREE OF

DOCTOR OF PHILOSOPHY

© Copyright by Paul Robert Steneker, August 2020

All Rights Reserved

Doctor of Philosophy (2020)
(Civil Engineering)

McMaster University
Hamilton, Ontario, Canada

TITLE: TOWARDS MORE OPTIMIZED AND RESILIENT
SEISMIC DESIGN OF BUILDINGS WITH STEEL
MOMENT RESISTING FRAMES

AUTHOR: Paul Robert Steneker
B.Eng. (Civil Engineering),
McMaster University, Hamilton, Canada

SUPERVISOR: Lydell Wiebe

NUMBER OF PAGES: xl, 369

LAY ABSTRACT

Modern buildings can typically withstand earthquakes without collapsing, but extensive repair or replacement of both the structure and its components are often required after a major event. To reduce these costs, improvements to both the structure and its components are continuously being researched. However, these upgrades can compete with one another for limited available funding, and they are not always independent, with structural changes influencing the demands on non-structural components. In an effort to move toward more optimized and resilient seismic design of buildings with steel moment resisting frames, this thesis begins by examining the effects of two newly proposed low-damage connections and investigates the opportunity to apply these low-damage connections at only specific structural locations to provide the desired performance effects more efficiently. In the second half of the thesis, a comparison of this particular upgrade to several other alternatives is accomplished by developing a framework to identify the upgrades having the largest benefit for the smallest cost by including combinations of modifications to both the structure and its components. The framework includes increasing levels of analytical refinement when evaluating upgrade strategies, providing designers with a more streamlined process to design and evaluate seismic resiliency improvement strategies in structures even beyond those used in this thesis.

ABSTRACT

While modern building codes have achieved success in preserving life, current code provisions do not explicitly address damage caused by earthquakes, leading to the prevalence of large economic losses. Examples of this limited scope are the changes made to design provisions for steel moment resisting frames (MRFs) following the 1994 pre-Northridge earthquake, where the pre-qualified connection detailing now prescribed for steel moment resisting frames increases the resistance to collapse but still relies on plastic deformations to dissipate energy, potentially limiting the overall improvement in seismic resiliency when compared to pre-Northridge connections. Since the introduction of these pre-qualified connections, several alternative seismic force resisting systems have been proposed which can reduce the expected economic losses by utilizing innovative energy dissipation methods and self-centering behaviour. However, as the use of these low-damage systems is not prescribed in current codes, their application is limited.

This thesis begins by examining the improvements in global performance obtained by implementing two examples of low-damage and high-performance MRF connections: the sliding hinge joint (SHJ) and self-centering sliding hinge joint (SCSHJ). Since the goal of these connections is to increase the seismic resiliency of MRFs, their impact is evaluated using several metrics including exposure to longer duration or aftershock earthquakes, as well as measuring their impact on different engineering demand parameters (EDPs). Once this impact has been established, an efficient design implementation is explored where these connections are placed only at locations with large ductility demands, allowing detailing

resources to be concentrated at locations where they will provide the largest benefit.

After exploring the global performance measured using engineering demand parameters, the economic and downtime reduction benefits obtained from these low-damage and high-performance connections are compared with alternative upgrade strategies. To help identify the most efficient upgrade strategy, a genetic algorithm is applied to define a methodology for optimizing seismic upgrades, including both structural and non-structural options. The optimization methodology considers the benefits in reductions of economic or downtime losses caused by earthquakes, measured using the performance based earthquake engineering (PBEE) methodology, versus the capital costs required to implement each upgrade. Finally, to aid engineers in selecting upgrades throughout all stages of the design process, this optimization methodology is included as the most advanced stage of a proposed seismic upgrade design framework. In the earlier design stages, the framework relies on a new median shift probability (MSP) method to rapidly summarize the effects of structural upgrades on nonstructural components. While the framework and optimization methodology are demonstrated in this thesis by their application to buildings with steel MRFs, they are easily adaptable to consider multiple objectives, building types, non-structural component populations, and building owners. Overall, this thesis provides insight on both the global performance benefits that can be achieved with the newly developed SHJ and SCSHJ connections, and presents a framework to select and optimize various competing seismic upgrade strategies.

PREFACE

This thesis has been prepared to the requirements of a sandwich thesis format as stipulated by the School of Graduate Studies at McMaster University. In accordance with the requirements of the manuscript-based sandwich thesis format, Chapters 2 through 5 have been either published, submitted to be considered for publication, or are awaiting submission for publication in peer-reviewed journals. The numerical analysis and development of methodologies presented in this thesis was carried out solely by the author and under the primary supervision, guidance, and review of Dr Lydell Wiebe, with assistance from both Dr Andre Filiatrault and Dr Dimitrios Konstantinidis, as noted in the authorship of each manuscript. The manuscripts containing the chapters of this thesis have been co-authored and their status as of August 2020 is as follows:

Chapter 2: Seismic Response Comparison of Steel MRFs with Yielding and Low-Damage Connections

Authors: Paul Stenecker, Lydell Wiebe, and Andre Filiatrault

Under review by the Journal of Constructional Steel Research

Chapter 3: Identifying and Selecting Critical Connections for Seismic Response of Steel Moment Resisting Frames

Authors: Paul Stenecker and Lydell Wiebe

Under review by Engineering Structures

Chapter 4: Integrated Structural-Nonstructural Performance-Based Seismic Design and Retrofit Optimization of Buildings

Authors: Paul Stenecker, Andre Filiatrault, Lydell Wiebe and, Dimitrios Konstantinidis

Published in ASCE Journal of Structural Engineering, May 2020

Full Citation:

Stenecker, P., Filiatrault, A., Wiebe, L., Konstantinidis, D., (2020) "Integrated Structural-Nonstructural Performance-Based Seismic Design and Retrofit Optimization of Buildings." *Journal of Structural Engineering*, 146(8). DOI: 10.1061/(ASCE)ST.1943-541X.0002680

Chapter 5: A Framework for the Rapid Assessment of Seismic Upgrade Viability Using Performance Based Earthquake Engineering

Authors: Paul Stenecker, Lydell Wiebe, Andre Filiatrault, and Dimitrios Konstantinidis

In final stages of preparation for submission to Earthquake Spectra

ACKNOWLEDGMENTS

I would first like to thank the willing participants of this journey, beginning with my supervisor, Dr. Lydell Wiebe, who provided me with an incomparable opportunity to grow as an individual while simultaneously guiding and often participating in my explorations. The quality contained within these next pages is directly attributable to his meticulousness and unyielding desire for perfection. I have no doubt these fortunate years of mentorship will be immensely helpful in all my future endeavors, and I look forward to years of continuing friendship throughout our careers. I would also like to thank Dr. Andre Filiatrault, whose contributions were invaluable to this process in both technical and personal aspects. His guidance, patience, support and friendship throughout the process provided me with countless research breakthroughs, needed personal improvements and many joyful memories. Our time in Pavia will be fondly remembered and hopefully repeated in the future. I would also like to acknowledge the contribution of Dr. Dimitrios Konstantinidis, who provided essential feedback and fresh insights to help positively mature much of the work contained in this Thesis.

Beyond these direct contributors, I would be remiss if I did not acknowledge the many people who have indirectly contributed to this work, often unknowingly or by proxy. My parents, who are excellent examples of such collateral participants, patiently watched as I encountered each obstacle and provided much needed words of support at the most auspicious moments. My friends from Hamilton; Tristan, Kyle, Kevin, Matt, Alex, and Mike, who managed to provide me with much needed positive respite from some of the toughest moments. My colleague and friend, Taylor Steele, who

managed to find a way to be a thoroughly entertaining friend, an endlessly helpful colleague, and an immensely helpful example. I am confident in saying I would not be writing this without his priceless advice all through these years. And lastly, I would like to extend my sincerest recognition and love to Bryanna Noade, who continues to support me wholeheartedly in all of my endeavors with warm compassion and unending patience. Her continued dedication and diligence to all of her own projects provided me with the example I needed to finish this work.

Contents

LAY ABSTRACT	iii
ABSTRACT	iv
PREFACE	vi
ACKNOWLEDGMENTS	viii
NOTATION AND ABBREVIATIONS	xxvii
1 INTRODUCTION	1
1.1 Motivation for Improvements in Seismic Resiliency	1
1.2 Seismic Resiliency of Steel Moment Resisting Frames	5
1.3 Objectives and Organization	15
1.4 References	21
2 SEISMIC RESPONSE COMPARISON OF STEEL MRFS WITH YIELDING AND LOW-DAMAGE CONNECTIONS	28
2.1 Abstract	28
2.2 Introduction	29
2.3 Frame Designs and Modeling Approach	33
2.4 Response Indices	43
2.5 Results and Discussion	50
2.6 Conclusions	62
2.7 Acknowledgments	64
2.8 References	65

3 IDENTIFYING AND SELECTING CRITICAL CONNECTIONS FOR SEISMIC RESPONSE OF STEEL MOMENT RESISTING FRAMES	73
3.1 Abstract	73
3.2 Introduction	74
3.3 Definition of Critical Connections	78
3.4 Application to Archetype Frames	79
3.5 Identification of Critical Connections Using Pushover Analysis	92
3.6 Selection of Critical Connections	96
3.7 Conclusions	107
3.8 Acknowledgments	108
3.9 References	108
4 INTEGRATED STRUCTURAL–NONSTRUCTURAL PERFORMANCE-BASED SEISMIC DESIGN AND RETROFIT OPTIMIZATION OF BUILDINGS	115
4.1 Abstract	115
4.2 Introduction	116
4.3 Review of Optimization Procedures Applicable to PEER-PBEE Framework	118
4.4 Overview of Genetic Algorithm and Implementation in the PEER-PBEE Framework	120
4.5 Retrofit Case Study	127
4.6 Conclusions	151
4.7 Acknowledgments	152
4.8 References	152

5	A FRAMEWORK FOR THE RAPID ASSESSMENT OF SEISMIC UPGRADE VIABILITY USING PERFORMANCE BASED EARTHQUAKE ENGINEERING	160
5.1	Abstract	160
5.2	Introduction	161
5.3	Key Parameters of MSP Method	167
5.4	Deaggregation of Change In Loss From Upgrades	175
5.5	Multiple Framework Levels	182
5.6	Case Study Example	187
5.7	Conclusions	209
5.8	References	211
6	CONCLUSIONS AND RECOMMENDATIONS	218
6.1	Answers to Driving Research Questions	218
6.2	Recommendations for Future Research	224
6.3	Looking Forward	228
6.4	References	230
A	CALIBRATION OF BEAM HINGE MODELS	232
A.1	Modeling of Existing MRF connections	232
A.2	Development of Models for Low-Damage Connections	260
A.3	References	278
B	GROUND MOTION SELECTION	283
B.1	Selection of Ground Motions for Different Hazard Types	283
B.2	Creating Sets of Main-Shock-After-Shock Hazard Scenarios	286

B.3 Conclusion 301
B.4 References 302

C MEDIAN SHIFT PROBABILITY EXCEL

IMPLEMENTATION 358
C.1 User Interface 358
C.2 Hidden Calculation Sheets 365
C.3 References 368

List of Figures

1.1	Isometric view of pre-qualified connections (from top left, clockwise: Reduced Beam Section (RBS), Welded Unreinforced Flange (WUF), Bolted Flange Plate (BFP), Kaiser Bolted Bracket (KBB), Welded Stiffened End Plate (WSEP), Welded Unstiffened End Plate (WUEP) (AISC 2016b)	8
1.2	Isometric View of (a) Pre-Northridge, (b) SHJ, and (c) SCSHJ connections	10
1.3	Scope of upgrades addressed in each chapter	20
2.1	Isometric views of (a) SHJ connection and (b) SCSHJ connection	31
2.2	Layout of (a) 3-story frame, (b) 6-story frame with modeling detail and (c) 12-story frame	34
2.3	Hysteretic model calibration, major model parameters and energy comparison for (a) PRENORTH IMK model (Engelhardt and Sabol 1994), (b) RBS IMK model (Lee et al. 2004), (c) SHJ model (Khoo et al. 2013), and (d) SCSHJ model (Khoo et al. 2013)	38
2.4	Deaggregation of seismic hazard for Seattle site (Lat: 47.6, Long: -122.3) for (a) Peak Ground Acceleration, and 5% damped spectral acceleration at period of (b) 1 second and (c) 2 seconds (Modified from USGS 2014)	46

2.5	Shallow crustal hazard conditional mean spectra for (a) three-story frame, (be) six-story frame and (c) 12-story frame, Subduction hazard conditional mean spectra for (d) three-story frame, (e) six-story frame and (f) 12-story frame, and Hazard curves for (g) three-story frame, (h) six-story frame and (i) 12-story frame	47
2.6	Non-Structural component story loss functions for office archetype for (a) acceleration sensitive and (b) drift sensitive components	50
2.7	Fragility curves for maximum inter-story drifts associated with collapse prevention performance objective for all considered frame types, heights and seismic hazard types	51
2.8	Fragility curves for residual inter-story drifts associated with life safety performance objective for all considered frame types, heights and seismic hazard types	55
2.9	Fragility curves for peak floor accelerations associated with life safety performance objective for all considered frame types, heights and seismic hazard types	58
2.10	Radar plots of median intensities for all response indices of all three frames	59
2.11	Loss Curves for each structure for each hazard	62
3.1	(a) Idealized deformation of six-story MRF, (b) Example of typical deformation of six-story MRF.	77
3.2	Frame layout of (a) 3 story building, (b) 6 story building with modeling detail and (c) 12-story building.	80

3.3	Analytical and experimental moment-rotation behavior for (a) PRENORTH (Choi et al. 2003), (b) RBS (Lee et al. 2004), (c) SCSHJ (Khoo et al. 2013); and (d) SCSHJ model parameters.	84
3.4	Conditional spectra for the first mode period of (a) three-story, (b) six-story and (c) 12-story frames. Ground motion spectra chosen for 1.0 MCE intensity are also shown.	85
3.5	Maximum connection rotations for each ground motion at each floor of each archetype frame.	88
3.6	Probability of exceeding 0.017 rad rotation at each floor for (a) 3 story building, (b) 6 story building, and (c) 12-story building.	90
3.7	Collapse fragility curves for three-story, six-story, and 12-story frame for frames with PRENORTH, RBS, SCSHJ, and both mixed connections configurations.	91
3.8	(a) Triangular and classical modal pushover force vectors; Pushover curves for (b) three-story, (c) six-story, and (d) 12-story archetype frames.	94
3.9	Comparison of pushover beam rotation values to annual frequency of exceedance values	95
3.10	Outline of DDBD Process	98
3.11	Fragility curves for 1st and 2nd isolation floor designs.	103
3.12	Parametric study of large inelastic rotation concentration for (a) 1st isolation floor design and (b) 2nd floor isolation design.	106
4.1	Flow chart for genetic algorithm	121
4.2	Example of population formulation in genetic algorithm	123

4.3	(a) Elevation view and modeling details of seismic force-resisting system of three-story steel office type archetype building, (b) Plan view of archetype building	128
4.4	Conditional spectra for archetype building	129
4.5	(a) Ranking functions for economic target metric, (b) Changes in convergence criteria, (c) Genetic code of optimal solution	138
4.6	(a) Ranking functions for downtime target metric, (b) Genetic code of optimal solution	141
4.7	(a) Ranking functions for casualty reduction targeted metric, (b) Genetic code of optimal solution	142
4.8	Prioritization of structural and nonstructural upgrades for economic, downtime, casualty reduction and combined target metrics for first owner profile	144
4.9	a) Upgrade cost of optimal solution vs internal rate of return, b) Component prioritization for specific rates of return	148
4.10	a) Occupancy time vs upgrade time of optimal solution, b) Component prioritization at specific occupancy time	149
5.1	Levels of assessment of proposed framework to determine upgrade viability and optimization	166
5.2	Input to the construction of a floor hazard curve: (a) Maximum <i>EDP</i> results obtained for different intensity stripes, (b) probability of non-demolition of structure, (c) site hazard curve	170
5.3	Change in frequency of occurrence of damage	174
5.4	Flow Chart for Levels 1 and 2 of MSP method of Assessment of Upgrade Viability	184

5.5	(a) Plan view of archetype building, (b) Elevation view of archetype building with modeling details	189
5.6	(a) Archetype building's site frequency-intensity curve, (b) Conditional mean spectra for multiple stripe analysis	190
5.7	Performance curves for original structure: (a) Structural fragility curves, (b) Roof and floor acceleration hazard curves, and (c) Floor drift hazard curve	191
5.8	EAL values for all four loss categories	200
5.9	Comparison of selected upgrades (for occupancy time = 40 years)	207
5.10	Total optimal upgrade cost obtained from each method	209
A.1	Isometric view of pre-qualified connections (from top left, clockwise: RBS, WUF, BFP, KBB, WSEP,WUEP)	233
A.2	(a) Typical MRF connection component test (Chi & Uang, 2002), (b) Analytical model of MRF connection component test	236
A.3	Influence of major parameters for IMK model	238
A.4	Plot of regression data for pre-capping plastic rotation for RBS connections (ATC, 2010)	239
A.5	Plot of regression data for post-capping plastic rotation for RBS connections (ATC, 2010)	240
A.6	Plot of regression data for cumulative plastic rotation for RBS connections (ATC, 2010)	241
A.7	Plot of regression data for Pre-capping plastic rotation for non-RBS connections (ATC, 2010)	242
A.8	Plot of regression data for post-capping plastic rotation for non-RBS connections (ATC, 2010)	243

A.9	Plot of regression data for cumulative plastic rotation for non-RBS connections (ATC, 2010)	244
A.10	Moment-rotation relationship for various RBS component tests [a) Popov et al., 1997; b) Moore and Engelhardt, 2000; c) Gilton and Uang, 2002; d) Engelhardt and Sabol, 1994; f) Chi and Uang, 2002; g) Engelhardt and Sabol, 1994; h) Engelhardt and Sabol, 1994], (i) skeleton curve of each component test	247
A.11	Moment-Rotation relationships for component tests of beam sections used in archetype frames (Chi and Uang (2002), Engelhardt and Sabol (1994), Moore and Engelhardt (2000), Popov and al (1997))	249
A.12	(a) Backbone curves for component tests of beam sections used in archetype frames	250
A.13	(a) Comparison of moment-rotation relationship of W24 component test and analytical model, (b) backbone curves of W24 component tests of beam sections used in archetype frames, of ATC-72 regression values and of final IMK model, (c) skeleton curves of component tests of beam sections used in archetype frames and of final IMK model	253
A.14	(a) Comparison of moment-rotation relationship of W24 component test and analytical model, (b) backbone curves of W24 component tests of beam sections used in archetype frames, of ATC-72 regression values and of final IMK model, (c) skeleton curves of component tests of beam sections used in archetype frames and of final IMK model	255

A.15 (a) Comparison of moment-rotation relationship of W24 component test and analytical model, (b) backbone curves of W24 component tests of beam sections used in archetype frames, of ATC-72 regression values and of final IMK model, (c) skeleton curves of component tests of beam sections used in archetype frames and of final IMK model	256
A.16 Impact of n-factor on pushover behaviour and dynamic period of component test model	259
A.17 Isometric view of a SHJ connection	261
A.18 (a) Idealized AFC only Moment-Rotation behaviour of SHJ connection (after Khoo et al. 2012), (b) Experimental component results for SHJ connection, (c) Effective Moment-Rotation behaviour of SHJ connection (after Khoo et al. 2012), , and (d) Bilinear-dominated moment-rotation behaviour at low rotations	263
A.19 (a) Division of moment-rotation behaviour, (b) Idealized moment-rotation behaviour of Steel02 and Hysteretic materials, (c) Key SHJ connection model parameters, and (d) Analytical and experimental SHJ component tests	267
A.20 Isometric view of a SCSHJ connection	270
A.21 (a) Idealized moment-rotation contribution of self-centering ring spring, and (b) Experimental component results for SCSHJ connection	271

A.22 (a) Idealized moment rotation behaviour of Steel02 and SelfCentering materials, (b) Key SCSHJ connection model parameters, and (c) Comparison of analytical and experimental SCSHJ component test	274
A.23 Connection model for SHJ and SCSHJ connection	277
B.1 Deaggregation plots at 2% in 50 year hazard level for (a) PGA, (b) 1 second period and (c) 2 second period (USGS, 2008)	284
B.2 Conditional mean spectra for shallow crustal hazard for (a) three story frame, (b) six story frame and (c) 12 story frame	286
B.3 Conditional mean spectra for subduction hazard for (a) three story frame, (b) six story frame and (c) 12 story frame	286
B.4 Comparison of collapse fragility of an 8 story structure using four MS-AS sequence types (from Shokrabadi et al (2018))	289
B.5 Deaggregation plots for varying hazard levels	292
B.6 Demonstration of MS-AS linking on deaggregation	293
B.7 Boore & Atkinson attenuation model relating PGA to Magnitude for varying rupture distances	294
B.8 Process for the selection and scaling of MS-AS intensity stripes	296
B.9 (a) Site hazard curve, (b) Collapse performance of six-story frame under main-shock only	298
B.10 Collapse of main-shock after-shock combinations of six-story frame	299
B.11 Contribution of added collapse frequency from After-Shocks	301
C.1 Screen Shot of Owner Parameter Step	360
C.2 Screen Shot of Structural Component Population Step	361
C.3 Screen Shot of Site Parameters Step	362
C.4 Screen Shot of Non-Structural Component Population Step	363

C.5	Screen Shot of Building Analysis Step	365
C.6	Screen Shot of Location of Calculation Sheets	366

List of Tables

2.1	Summary (Number) of Frame Heights, Connection Types, Seismic Hazard Types, EDPs and Performance Objectives . . .	32
2.2	Component test sections and major IMK parameters for pre-qualified connections	39
2.3	Component test sections and major parameters for SHJ and SCSHJ connections	42
3.1	Component Test Sections Used for Connection Models	82
3.2	Parameters of IMK Models to Match Cyclic Envelope Curves of Component Tests	83
3.3	Parameters of all SCSHJ models (From Chapter 2)	83
3.4	Annual probability of connection exceeding 0.017 rad.	89
3.5	DDBD Values for Isolation Floor Designs	103
4.1	Component test sections and major parameters for SHJ and SCSHJ connections	131
4.2	Component test sections and major parameters for SHJ and SCSHJ connections	133
5.1	Summary of Upgrade Strategies and assumed Level 1 Q_θ values	194
5.2	Summary of nonstructural normalized repair and upgrade costs for case study structure	194
5.3	Summary of structural repair and upgrade costs for Level 2 . . .	198
5.4	Calculated Q_θ values for Level 2 of MSP method	199
5.5	Summary of change in <i>EAL</i> for each structural upgrade and net positive nonstructural upgrade	203
A.1	Summary of pre-qualified connections	234

A.2	Selection of component test for connection model calibration . . .	250
A.3	Comparison of IMK values	256
A.4	Parameters for SHJ model	268
A.5	Parameters for SCSHJ model	274
B.1	Proposed MS-AS sequence type (summarized from Shokrabadi et al (2018))	287
B.2	Example of MS-AS scaling process	295
B.5	Spectra for Period 0.87, Amp 0.1	305
B.6	Details for Period 0.87, Amp 0.1	306
B.5	Spectra for Period 0.87, Amp 0.5	307
B.6	Details for Period 0.87, Amp 0.5	308
B.6	Spectra for Period 0.87, Amp 0.75	309
B.7	Details for Period 0.87, Amp 0.75	310
B.7	Spectra for Period 0.87, Amp 1.0	311
B.8	Details for Period 0.87, Amp 1.0	312
B.8	Spectra for Period 0.87, Amp 1.25	313
B.9	Details for Period 0.87, Amp 1.25	314
B.9	Spectra for Period 0.87, Amp 1.5	315
B.10	Details for Period 0.87, Amp 1.5	316
B.10	Spectra for Period 0.87, Amp 2.0	317
B.11	Details for Period 0.87, Amp 2.0	318
B.11	Spectra for Period 0.87, Amp 3.0	319
B.12	Details for Period 0.87, Amp 3.0	320
B.15	Spectra for Period 1.3, Amp 0.1	321
B.16	Details for Period 1.3, Amp 0.1	322
B.15	Spectra for Period 1.3, Amp 0.25	323

B.16 Details for Period 1.3, Amp 0.25	324
B.12 Spectra for Period 1.3, Amp 0.5	325
B.13 Details for Period 1.3, Amp 0.5	326
B.13 Spectra for Period 1.3, Amp 0.75	327
B.14 Details for Period 1.3, Amp 0.75	328
B.14 Spectra for Period 1.3, Amp 1.0	329
B.15 Details for Period 1.3, Amp 1.0	330
B.15 Spectra for Period 1.3, Amp 1.25	331
B.16 Details for Period 1.3, Amp 1.25	332
B.16 Spectra for Period 1.3, Amp 1.5	333
B.17 Details for Period 1.3, Amp 1.5	334
B.17 Spectra for Period 1.3, Amp 2.0	335
B.18 Details for Period 1.3, Amp 2.0	336
B.18 Spectra for Period 1.3, Amp 3.0	337
B.19 Details for Period 1.3, Amp 3.0	338
B.22 Spectra for Period 2.8, Amp 0.1	339
B.23 Details for Period 2.8, Amp 0.1	340
B.20 Spectra for Period 2.8, Amp 0.25	341
B.21 Details for Period 2.8, Amp 0.25	342
B.19 Spectra for Period 2.8, Amp 0.5	343
B.20 Details for Period 2.8, Amp 0.5	344
B.20 Spectra for Period 2.8, Amp 0.75	345
B.21 Details for Period 2.8, Amp 0.75	346
B.21 Spectra for Period 2.8, Amp 1.0	347
B.22 Details for Period 2.8, Amp 1.0	348
B.22 Spectra for Period 2.8, Amp 1.25	349

B.23 Details for Period 2.8, Amp 1.25	350
B.23 Spectra for Period 2.8, Amp 1.5	351
B.24 Details for Period 2.8, Amp 1.5	352
B.24 Spectra for Period 2.8, Amp 2.0	353
B.25 Details for Period 2.8, Amp 2.0	354
B.25 Spectra for Period 2.8, Amp 3.0	355
B.26 Details for Period 2.8, Amp 3.0	356

NOTATION AND ABBREVIATIONS

Notation

A_h	Area of the stabilized hysteretic cycle
a_1, a_3	Isotropic hardening stiffness in sliding hinge joint beam connection model (positive, negative)
a_2, a_4	Isotropic hardening activation in sliding hinge joint beam connection model (positive, negative)
AM	Amortization conversion
BCR	Benefit cost ratio
BV	Building value
CC_c	Consequence cost of building collapse
DM	Damage measure
DR	Rate of death caused by collapse
DV	Decision variable
D_r	Cyclic deterioration ratio
E	Young's modulus
EAD_O	Expected annual deaths of original building
EAD_U	Expected annual deaths of upgraded building

EAI_O	Expected annual injuries of original building
EAI_U	Expected annual injuries of upgraded building
EAL	Expected annual loss
EAL_C	Expected annual loss caused by building collapse
$EAL_{accel.}$	Expected annual loss caused by acceleration sensitive non-structural components
EAL_{drift}	Expected annual loss caused by drift sensitive non-structural components
EAL_O	Expected annual loss of original building
EAL_R	Expected annual loss caused by building non-recoverable residual drifts
EAL_U	Expected annual loss of upgraded building
EAT_O	Expected annual time lost of original building
EAT_U	Expected annual time lost of upgraded building
EDP	Engineering Demand Parameter
$EDP_{n,k}$	Engineering Demand Parameter for the n^{th} component k^{th} damage state
$f(EDP_{n,k})$	Annual frequency of occurrence of floor hazard engineering demand parameter $EDP_{n,k}$ for k^{th} damage state of component n

$F(EDP_{n,k})$	Annual frequency of exceedance of floor hazard engineering demand parameter $EDP_{n,k}$ for k^{th} damage state of component n
$f(IM)$	Annual frequency of occurrence of ground motion intensity measure IM
$F(IM)$	Annual frequency of exceedance of ground motion intensity measure IM
F_i	Maximum force in stable cycle of isolation floor
F_j	Applied force at j^{th} floor
$F_{SDR,j}$	j^{th} force at connection strength degradation rotation moment
H_e	Effective height of single degree of freedom
h_d	Height of isolation story
IM	Ground motion intensity measure
IR	Rate of Injury caused by collapse
i	Isolation floor
j	Floor number
k	damage state number
$K_{initial}$	Initial connection stiffness
K_{post}	Post yield/activation connection stiffness
L_j	Bay length of j^{th} floor

m	Ground motion intensity stripe
M_{AB}	Activation moment of sliding hinge joint or self centering sliding hinge joint beam connection
M_{Bilin}	Initial moment increase in bilinear portion of sliding hinge joint connection
M_d	First dependable moment of sliding hinge joint or self centering sliding hinge joint beam connection
M_r	Residual moment of beam connection
M_y	Yield moment
m_j	Mass at j^{th} floor
NP	Maximum number of occupants
NPV	Net present value
OHW	Average worker occupied hours
OWY	Average worker occupied weeks
P_F	Pinching Force in sliding hinge joint beam connection model
P_{RS}	Percentage of self-centering sliding hinge joint beam connection moment capacity provided by ring spring
PV	Present value
PV_O	Present value of seismic losses of original building
PV_U	Present value of seismic losses of upgraded building

$p(DS_k|IM)$ Probability of occurrence of damage state k , given ground motion intensity measure IM

$p(DS_k|NDS_{k+1}, IM)$ Probability of occurrence of damage state k , given non-occurrence of damage state $k + 1$ and ground motion intensity measure IM

$p(DS_{n,k}|EDP_{n,k})$ Probability of occurrence of damage state k of n component, given engineering demand parameter $EDP_{n,k}$

$p(DS_{O,n,k}|EDP_{n,k})$ Probability of occurrence of damage state k of original n component, given engineering demand parameter $EDP_{n,k}$

$p(DS_{U,n,k}|EDP_{n,k})$ Probability of occurrence of damage state k of upgraded n component, given engineering demand parameter $EDP_{n,k}$

$p(C|IM)$ Probability of collapse, given ground motion intensity measure IM

$p(ND|IM)$ Probability of non-demolition, given ground motion intensity measure IM

$p(ND_O|IM)$ Probability of non-demolition of original building, given ground motion intensity measure IM

$p(ND_U|IM)$ Probability of non-demolition of upgraded building, given ground motion intensity measure IM

$p(NR|IM)$ Probability of non-repairable residual drifts, given ground motion intensity measure IM

$p(NR|NC, IM)$ Probability of non-repairable residual drifts, given non-collapse NC and ground motion intensity measure IM

$P(EDP_{n,k}|ND, IM_m)$ Probability of occurrence of engineering demand parameter $EDP_{n,k}$ for k^{th} damage state of component n , given non-demolition ND and ground motion intensity measure IM_m

$P(EDP_{n,k}|ND, IM_m)$ Probability of exceedance of engineering demand parameter $EDP_{n,k}$ for k^{th} damage state of component n , given non-demolition ND and ground motion intensity measure IM_m

$Q_{\beta,C}$ Change in lognormal standard deviation β of building collapse

$Q_{\theta,C}$ Change in median θ of building collapse

$Q_{\beta,EDP,n,k}$ Change in lognormal standard deviation β of engineering demand parameter EDP of damage state k of n component

$Q_{\theta,EDP,n,k}$ Change in median θ of engineering demand parameter EDP of damage state k of n component

$Q_{\beta,NR}$ Change in lognormal standard deviation β of building non-repairable residual drifts

$Q_{\theta,NR}$	Change in median θ of building non-repairable residual drifts
r	Internal rate of return
$Rank_{Casualties}$	Ranking function associated with casualty target metric
$Rank_{Economic}$	Ranking function associated with economic target metric
$Rank_{Downtime}$	Ranking function associated with downtime target metric
$RC_{n,k}$	Repair cost for k^{th} damage state of component n
S	Sequence upgrade time factor
S_n	Maximum number of structural strategies
S_{MS}	risk based maximum considered earthquake, 5% damped, spectral acceleration at short periods adjusted for site class effects
S_{M1}	risk based maximum considered earthquake, 5% damped, spectral acceleration at 1 second period adjusted for site class effects
t	Expected occupancy time
T	Modal Period
T_1	First Modal Period
$T_{e,sys}$	Effective period
UC	Upgrade Cost
UT	Upgrade Time

V_b	Base shear
V_j	Shear of j^{th} floor
VSI	Value of a statistical injury
VSL	Value of a statistical life
α_1	First post yield strain hardening ratio
α_2	Second post yield strain hardening ratio
α_3	Third post yield strain hardening ratio
β	Lognormal standard deviation
$\beta_{C,O}$	Lognormal standard deviation of original building collapse
$\beta_{C,U}$	Lognormal standard deviation of upgraded building collapse
$\beta_{EDP,n,k,O}$	Lognormal standard deviation of EDP of damage state k of component n in original building
$\beta_{EDP,n,k,U}$	Lognormal standard deviation EDP of damage state k of component n in upgraded building
β_m	Lognormal standard deviation of $EDP_{n,k}$ for k^{th} damage state of component n from ground motion intensity stripe m
β_k	Lognormal standard deviation of damage state k
$\beta_{n,k}$	Lognormal standard deviation of damage state k for component n

$\beta_{NR,O}$	Lognormal standard deviation of original building non-repairable residual drifts
$\beta_{NR,U}$	Lognormal standard deviation of upgraded building non-repairable residual drifts
β_{SC}	Forward-Reverse activation ratio of self-centering sliding hinge joint model
$\Delta(x)$	Change of variable x
Δ_{DS}	Change due to modification of damage state probability
$\Delta_{DS\&H}$	Change due to modification of both damage state probability and hazard occurrence
$\Delta_{d,sys}$	Total displacement of equivalent single degree of freedom system
Δ_H	Change due to modification of hazard occurrence
Δ_i	Design displacement of isolation floor
Δ_j	Displacement of j^{th} floor
$\Delta_{y,j}$	Yield displacement of j^{th} floor
$\Delta_{y,sys}$	Yield displacement of system
ϵ	Number of standard deviations observed ground motion logarithmic spectral acceleration exceeds target
$\lambda(x)$	Mean annual frequency of occurrence of x

λ_C	Mean annual frequency of collapse
$\lambda_{n,k}$	Mean annual frequency of damage state k of component n
λ_{NR}	Mean annual frequency of non-repairable residual drifts
λ_{SC}	Self-centering ratio of self-centering sliding hinge joint model
ϕ	Standard Guassian probability distribution function
Φ	Standard Guassian cumulative distribution function
$\theta_{C,O}$	Median intensity of original building collapse
$\theta_{C,U}$	Median intensity of upgraded building collapse
$\theta_{EDP,n,k,O}$	Median engineering demand parameter EDP of damage state k of component n in original building
$\theta_{EDP,n,k,U}$	Median engineering demand parameter EDP of damage state k of component n in upgraded building
θ_m	Median engineering demand parameter EDP for k^{th} damage state of component n from ground motion intensity stripe m
θ_k	Median intensity measure of damage state k
$\theta_{NR,O}$	Median intensity of original building non-repairable residual drifts
$\theta_{NR,U}$	Median intensity of upgraded building non-repairable residual drifts
θ_p	Plastic rotation

θ_{pc}	Post-capping rotation
θ_{SC}	Rotation at final stiffness of self-centering sliding hinge joint model
θ_u	Ultimate rotation
θ_y	Yield inter-story drift
$\theta_{y,j}$	Yield inter-story drift of j^{th} floor
ξ_e	Elastic damping of structure
$\xi_{e,sys}$	Equivalent viscous damping of the single degree of freedom system
ξ_{hyst}	Hysteretic damping of isolation floor

Abbreviations

AFC	asymmetrical friction connection
BRB	buckling restrained brace
BV	building value
CDF	cumulative distribution function
CFM	cubic feet per minute
CMR	collapse margin ratio
Crustal	shallow crustal ground motion

DE	design earthquake
DDBD	displacement based design
EAL	expected annual economic loss
EAT	expected annual time loss
EDP	engineering demand parameter
g	gravitational constant
GA	genetic algorithm
IDA	incremental dynamic analysis
IMK	Ibarra-Medina-Krawinkler
km	kilometers
kN	kilonewton
LF	linear feet
m	meters
mm	millimeter
MCE	maximum considered earthquake
MCE_R	risk-targeted maximum considered earthquake
MLE	maximum likelihood estimation
MPa	megapascal
MRF	moment resisting frame

MSA	multiple stripe analysis
MSP	median shift probability
MSPIT	iterative median shift probability
MS-AS	main-shock-after-shock series of ground motions
NLTHA	non-linear time history analysis
PACT	performance assessment calculation tool
PBEE	performance based earthquake engineering
PEER	pacific earthquake engineering research
PDF	probability distribution function
PFA	peak floor acceleration
PRA	peak roof acceleration
PRENORTH	pre-Northridge moment resisting connection
QDA	qualifying inter-story drift angle
rad	rotation radian
RBS	reduced beam section moment resisting connection
RSS	residual sum of squares
s or sec	second(s)
SCSHJ	self-centering sliding hinge joint moment resisting connection
S_D	design spectral acceleration

SDOF	single degree of freedom
SDR	strength degradation rotation
SF	square feet
SFRS	seismic force-resisting systems
SHJ	sliding hinge joint moment resisting connection
Sub.	subduction ground motion
USGS	United States geological survey
VD	viscous damper
Vs30	average shear wave velocity in the top 30 meters of soil

Chapter 1

INTRODUCTION

1.1 Motivation for Improvements in Seismic Resiliency

The risk posed by earthquakes increases with the urbanization of human society and its prevalence has therefore been increasing with the growth of human population living in urban centers. The quotation "earthquakes don't kill people - buildings do" provides a symbolic representation of this relationship as combining earthquakes with the built environment shifts the impact of a seismic event from a naturally occurring outlying event to a potentially catastrophic disaster. However, with the introduction of modern building codes, which began emphatically identifying strategies to resist earthquake forces after the 1908 Messina earthquake in Italy (Pino et al. 2009), a decoupling occurred in the relationships between the increase in urbanization and the extent of earthquake damage. This is particularly true when measuring human casualties, which have seen a dramatic decrease in countries having implemented modern building codes over the previous half century (Vaughan and Turner 2013). This improvement in casualty reduction due to the avoidance of catastrophic collapse was historically well timed as the pace of urbanization accelerated further throughout the same time period. Societies in developed countries can now take some level of comfort

with the knowledge that the construction boom resulting from the recent increase in urbanization was administered using building codes which ensured a reliable level of collapse avoidance performance for the first time in human history.

However, with the casualty reduction objective having been substantially achieved by modern building codes (Vaughan and Turner 2013), the occupants and owners of buildings began to question the seismic resiliency of their environment at objective levels beyond life safety. This shift in the definition of acceptable and more stringent performance objectives was accelerated following several damaging earthquakes affecting cities built using the aforementioned modern building codes. One such event was the 2011 Christchurch earthquakes which struck an urban center where the majority of the building population were constructed using such modern codes and standards. While the number of casualties was relatively small at 185 in comparison to preceding events of similar magnitude and level of urbanization exposure, such as the 2006 Yogyakarta earthquake in Indonesia which caused more than 5800 casualties (USGS 2009), the extent of damage observed in Christchurch was economically devastating (Potter et al. 2015). In the North American market, a study of earthquake repair and rehabilitation in the United States has estimated annual costs at five billion dollars, concentrated in the three west coast states (Folger, 2013). The main cause of the dichotomy between the achievement of the reduction in casualties but not of losses can be attributed to the prevailing reliance on ductility provided by material deformations as the primary strategy for seismic force resisting systems in modern building codes. The lack of damage cost reduction is attributed to the implementation of this ductility as the

conventional building design consists of computing the expected seismic forces applied to a structure, designing certain elements to yield at forces lower than these levels, and ensuring all other elements to remain elastic. This allows a concentration of ductile detailing to specific elements where displacement capacity can be expected so as to provide reliable collapse prevention performance (AISC 2016a, CSA 2014). However, as these ductile elements are expected to undergo large displacements, typically within the plastic range of their respective materials, permanent damage to the structure is expected. In summary, the quote "Ductility is damage" summarizes the negative attribute of this traditional approach, and loss evaluations using the performance based earthquake engineering (PBEE) (Miranda and Aslani 2003) methodology provide numerical examples of the economic vulnerability of even code conforming buildings. This shift in objective has continued to motivate the development of alternative earthquake damage mitigation strategies and their improvement to include the protection of property, within the scope of creating a more resilient society. This goal has been echoed across several research and development fields centered on disaster response as the population becomes increasingly aware of both their risk exposure beyond life safety, and the potential economic benefits of improved seismic resiliency (ADB 2013, Nikellis et al. 2019).

Several research projects and industry strategies have addressed these desired increases in seismic resiliency earnestly since the beginning of the 21st century, resulting in the development of seismic force resisting systems whose performance exceeds the minimums mandated by building codes. This tier of systems is categorized as "low-damage" and/or "high performance" and

includes strategies such as seismic isolation, low-damage energy dissipation elements, and/or self-centering behaviour. As several of these strategies have only recently been developed, much of the existing building stock has not benefited from these improvements. Structures located in the center of urban environments, a majority of which were constructed between the 1950's and 1980's (USCB 2019), are expected to be vulnerable to the same economic damage as was observed in Christchurch. This is particularly true for the west coast of North America, which has not experienced a significant ground motion in an urban center since the development of these high performance systems, limiting their appeal and introduction (Fuller et al. 2019). While several of the proposed low-damage options are available for use in the retrofit of structures, building owners must be convinced of the viability of the investment when considering such significant capital projects, a current challenge facing professionals in the earthquake engineering industry. The recent development of methodologies for quantifying loss, such as the FEMA P-58 (FEMA 2012) or the REDI program (Almufti 2013), provide design engineers with tools to quantify expected seismic losses at the individual building level. Two recent examples of buildings designed by considering reductions in loss estimation are the Long Beach Civic Center (Haselton and Hamburger 2018), where expected losses were reduced by 6.8% and re-occupancy time was reduced by 27.5 weeks for a 10% probability of occurrence in 50 year ground motion, and the Watson Land Company building, where immediate occupancy was achieved for a 10% probability of occurrence in 50 year ground motion. However, both these methodologies require advanced modeling tools and extensive design experience, often necessitating a significant pro-active investment by the building owner.

Therefore, the following work aims to provide some guidance on addressing this challenge. While the focus is primarily on the seismic upgrading of a building typology identified as being particularly vulnerable to economic damage, the steel moment resisting frame (MRF) with pre-Northridge connections, the goal is to provide a framework for the broader consideration of improvements in seismic resiliency as a viable investment option for building owners, ultimately encouraging further investments in a more resilient society.

1.2 Seismic Resiliency of Steel Moment Resisting Frames

1.2.1 Post-Northridge Investigations and Pre-Qualified Connections

The design of steel moment resisting frames has undergone a series of shifts in the decades since their initial implementation at the beginning of the 20th century (Bennett 1995). These frames were initially constructed using moment resisting connections at all beam-column joints, where rivets were used for fasteners (McGuire 1988). This construction method resulted in flexible frames with redundant seismic force resisting elements, and their ductile performance was praised following multiple earthquakes (Freeman 1932, Bronson 1959). With the introduction of welding as a preferred fastening method in the 1970s, and the increase in construction labor costs, the design philosophy of MRFs

shifted to concentrate the seismic forces in a limited number of larger beam-column connections as welds provided the ability to transfer a large percentage of the member forces (Hamburger et al. 2009). This resulted in a lower cost implementation of MRFs while retaining the belief that the system provided high ductility. Factors such as the architectural flexibility provided by MRFs, as well as the aforementioned increase in urbanization and particularly in the west coast region of North America during the 1970s and 1980s, resulted in large quantities of these welded steel MRFs being erected in locations with moderate to high levels of seismic hazard.

However, investigations summarized in Youssef et al. (1995), Biddah and Heidebrecht (1999), and Bertero et al. (1994) following the 1994 Northridge earthquake revealed multiple cases of fractured MRF connections, caused by a lower than anticipated ductility of these welded connections. These discoveries resulted in significant research efforts (Tsai et al. 1995, Tremblay et al. 1995, FEMA 2000a, FEMA 2000b, among many) to understand the behaviour of these connections and to provide alternatives which would have more reliable ductility. These alternative connections were developed in the years following the Northridge earthquake, with several connections being identified as pre-qualified by a series of design codes (CISC 2015, AISC 2016b). A summary of these connections is discussed in Appendix A and an isometric view of each connection is shown in Figure 1.1. The process for pre-qualification required specific component quasi-static testing of the beam-column connections and a large library of the results of these tests is now available for multiple connections using a variety of section sizes (Lignos and Al-Shawwa 2013). Current design procedures select a pre-qualified connection for use at all moment resisting beam-column connections, and

rely on the beam-column joints as the location of hysteretic energy dissipation in the form of plastic yielding, while all other elements are designed to remain elastic (AISC 2016a, CSA 2014). To surpass the standards prescribed in the building codes mentioned, research is ongoing to develop higher performing connections which exceed the performance of these pre-qualified connections. Nevertheless, the development of the pre-qualified connections and their implementation in current design specifications do not alleviate the issue of the existing structures constructed before the development of these connections.

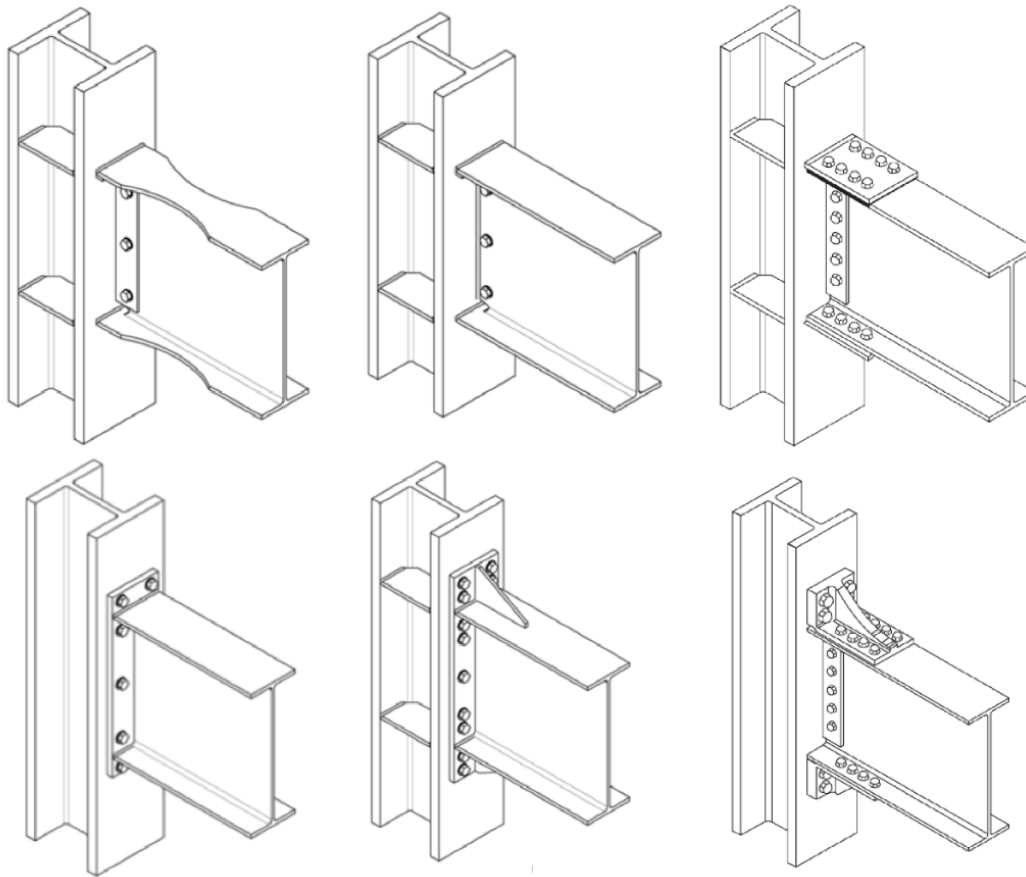


Figure 1.1: Isometric view of pre-qualified connections (from top left, clockwise: Reduced Beam Section (RBS), Welded Unreinforced Flange (WUF), Bolted Flange Plate (BFP), Kaiser Bolted Bracket (KBB), Welded Stiffened End Plate (WSEP), Welded Unstiffened End Plate (WUEP) (AISC 2016b))

1.2.2 Continued Development of High-Performing MRF Connections

While the use of these current pre-qualified connections provides reliable ductile response in the beam-column joints of the frame, the reliance on hysteretic energy dissipation and the resulting plastic deformation of these connections can result in large non-recoverable residual displacements. This

property of the system, combined with the inherent flexibility of a MRF, can have a detrimental effect on the overall economic resiliency of the structure (Erochko et al. 2011). Several research efforts have been undertaken to alleviate the issues surrounding the plastic deformations of the pre-qualified connections. Ricles et al. (2001) and Christopoulos et al. (2002) both proposed connections with post-tensioned tendons, providing the ability to self-center after an earthquake and resulting in a reduction to the probability of a ground motion causing non-recoverable residual displacements. However, these connections resulted in the development of gap openings at the beam-column intersection which would require diaphragm detailing to avoid damage, among other global performance issues (MacRae and Clifton 2013). Clifton (2005) introduced a sliding hinge joint (SHJ) moment connection which uses a friction surface placed at the bottom flange to dissipate energy. The addition of a ring spring allows for some self-centering behaviour, converting the SHJ connection to a self-centering sliding hinge joint (SCSHJ) connection (Khoo et al. 2012). The fixed point of rotation in the SHJ and SCSHJ connections alleviates the frame expansion and gap opening issues of previous self-centering MRF connections (MacRae and Clifton 2013). Isometric views of both the SHJ and SCSHJ connections, as well as the pre-Northridge connection, are shown in Figure 1.2. Component testing of these SCSHJ connections (Khoo et al. 2013) indicates the connection provides reliable ductile behaviour, and variants of these connections have been used in construction projects in New Zealand (e.g. Gledhill et al. 2008). While extensive local component testing has indicated the reliability of the SHJ and SCSHJ connections, their impact on the global performance of the MRF has not yet been quantified. As these connections provide ductility

with friction sliding instead of plastic yielding, the global performance improvements provided by these connections may be more apparent in performance objectives other than casualty reduction. These improvements across different performance objectives could relate directly to increasing a building’s seismic resiliency.

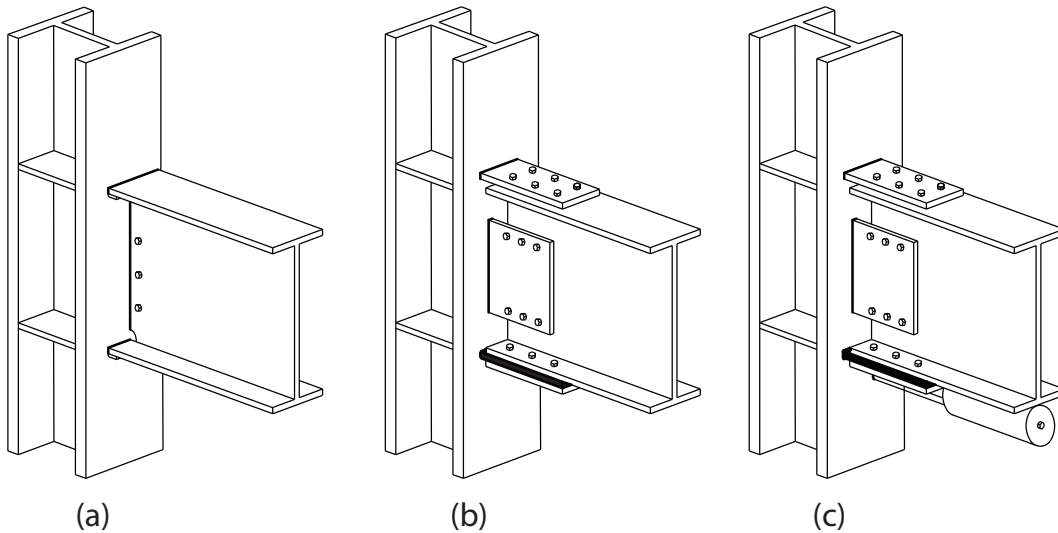


Figure 1.2: Isometric View of (a) Pre-Northridge, (b) SHJ, and (c) SCSHJ connections

1.2.3 Addressing Existing Vulnerable MRF Buildings And Improving MRF Designs

The existence of buildings which were constructed before the Northridge earthquake and still have connections which can experience the same brittle failures documented in the post-Northridge investigations has encouraged the development of multiple strategies to improve their performance. These strategies are summarized in FEMA-351 (2000b) and listed below:

1. Connection modification

2. Supplemental energy dissipation
3. Global Stiffening
4. Global Strengthening
5. Seismic Isolation
6. Mass Reduction
7. Removal of irregularities

Several of these strategies have undergone continuous and more detailed investigations and examples of the implementation of most of these strategies exists in practice. Furthermore, while the specification of pre-qualified connections in building standards has ensured that MRFs constructed after the Northridge earthquake have connections with reliably ductile performance, these pre-qualified connections provide ductile performance using the aforementioned plastic deformations causing the performance concerns mentioned earlier. Therefore, many of the proposed upgrade strategies are also being considered to enhance the performance of MRF frames beyond the code conforming designs with pre-qualified connections, potentially providing the desired increases in seismic resiliency beyond reliable casualty reduction.

Connection Modification

Initially, the immediate strategy developed for retrofitting existing frames with pre-Northridge connections consisted of modifications of the connections to a version of the reduced beam section (RBS) connection by removing

flange width from the bottom flange of the beam, targeting a connection behaviour similar to the reduced beam section (RBS) pre-qualified connection (Uang et al 1998). However, tests conducted by Civjan et al. (2000) revealed that a more rigorous approach to achieve the desired ductility was required since the welds connecting the beam-column joint also needed replacement to achieve the full desired ductile connection behaviour provided by the pre-qualified connections, increasing the cost of intervention and potentially reducing the appeal of this retrofit to the building owner as the replacement of pre-Northridge connections with pre-qualified connection does not improve the resiliency of the frame substantially (see previous comments on plastic deformations). A potential strategy to overcome this shortfall in performance is the replacement of either pre-Northridge or pre-qualified connections with high performing and more ductile alternatives such as the newly developed low-damage SHJ connection and self-centering SCSHJ connection, which both maintain the architectural flexibility provided by MRFs as this retrofit does not involve the introduction of diagonal members so as to keep the structural bays free of permanent obstructions. This can be an important factor to building owners as this design consideration is often the reason for the selection of MRFs as the seismic force resisting system in the early stages of the original building's design.

Supplemental Energy Dissipation

As an alternative to connection focused retrofit solutions for pre-Northridge frames, the addition of supplemental energy dissipation as a retrofit strategy has seen significant attention in recent research and its implementation in buildings has increased in the previous decade (MacRae and Clifton 2013).

The design of these systems has undergone several layers of refinement and is summarized concisely in Christopoulos and Filiatrault (2006) and further examples of their implementation are shown in Terzic and Mahin (2017). Supplemental energy dissipation is most commonly provided in two forms: hysteretic and viscous.

The implementation of hysteretic dampers has proven to be an economical strategy for many building owners, as summarized in Kasai et al. (1998), Mirtaheri et al. (2011), and Monir and Zeynali (2013). These dampers are typically designed in a bracing configuration and the most common energy dissipation behaviour of these elements uses non-linear hysteretic deformations which are typically idealized as having elastic perfectly plastic behaviour (Christopoulos and Filiatrault 2006). The most advanced hysteric damping designs allow for a decoupling of the strength and stiffness parameters, where an activation force can be selected independently of the stiffness of the element, providing the required energy dissipation without potentially large modifications to the dynamic behaviour of the frame since the elements can be designed to activate at low force levels.

The implementation of viscous dampers as a supplemental damping system in MRFs has also been developed since first being proposed in the late 1990's (Uriz and Whittaker 2001). The system uses large liquid dampers which dissipate energy based on the velocity of their axial strain (Soong and Dargush 1997). In contrast to the hysteretic dampers, the velocity dependence of the viscous dampers allows them to dissipate energy while not increasing the elastic stiffness or strength of the structure. However, the elements of this system are often more expensive than the hysteretic damping alternative (Pollini et al. 2018), resulting in the hysteretic dampers

being a preferred strategy by cost sensitive building owners.

Increases in Global Strength and Stiffness

Increases in global strength and stiffness are often provided in tandem with one another, typically with the introduction of additional lateral force resisting elements, such as shear walls or various diagonal bracing designs. A notable strategy used for steel MRFs is the buckling restrained brace (BRB) (Sabelli et al. 2003 and Kiggins and Uang 2006) which has become a popular choice of either a supplemental hysteretic damper, or an independent SFRS in some design standards (AISC 2016a). In contrast to traditional concentrically braced frame braces, the BRB consists of a steel section placed inside a concrete shell which prevents the global buckling of the member, allowing the BRB to have a similar force-displacement behaviour in both tension and compression. This bracing system has shown to be both an economical option for owners, as well having shown reliable performance in past seismic events.

Seismic Isolation

The development of seismic isolation as a rehabilitation strategy is ongoing and several notable implementations of the system indicates its increased popularity in high seismic areas. This system has seen widespread implementation in new construction in Japan (Nakamura and Okada 2019) as the economic costs of the system become more viable when exposed to the high frequency of ground motions occurring in Japan. However, due to its high cost of implementation, this strategy tends to see limited use in North America, focused mostly on buildings with the highest importance level or

heritage structures (Christopoulos and Filiatrault 2006). At the time of writing, no current or existing implementations of seismic isolation as a retrofit strategy for steel moment resisting frames with pre-Northridge connections in North America were identified.

Mass Reduction and Removal of Irregularities

Finally, the remaining two retrofit strategies proposed in FEMA 351 involve changes to the structure which are not directly related to the local behaviour of the seismic force resisting systems. Therefore, the reduction in seismic mass and the removal of structural irregularities are not included in this work.

1.3 Objectives and Organization

As stated, the primary goal of this study is the optimization of strategies to improve the seismic resilience of buildings with steel moment resisting frames. Initially, the study is focused on improving the resilience of MRFs by upgrading the connection detailing with newly developed low-damage connections. Subsequently, the scope of upgrade options is expanded to allow a comparison of this connection upgrade strategy to other strategies. In order to move towards the stated goal, the thesis seeks to answer the following questions:

1. What global frame performance benefits are provided by replacing either pre-Northridge or pre-qualified connections with low-damage and high-performance connections?

2. Can these benefits to the global frame performance be achieved by upgrading only a select subset of the MRF connections?

Next, the scope of considered upgrade strategies is expanded to also include other structural alternatives for existing buildings with steel MRFs, as well as seismic upgrades to non-structural components. Considering such a broad scope for seismic design requires the following question to be addressed:

3. How can a designer determine the optimal upgrade strategy when considering alternative upgrades to both structural and non-structural components?

Finally, continuing to consider this expanded scope of seismic design, the overall design process is examined to answer the final question:

4. How can the relationship between a structure and its non-structural components be delineated to quickly assess and identify viable upgrade strategies?

Each of these questions is addressed in the following thesis chapters, as outlined in more detail below:

Chapter 2 This chapter starts with the development of non-linear connection models for both the SHJ and SCSHJ connections, which had not yet been developed at the time of writing, in order to permit a comparison of the global performance of steel MRFs with varying connection detailing. The connection modification upgrade strategy, either applied as a retrofit replacement in an existing building or as a

connection redesign during the design of a new building, allows for a minimal disturbance in the architectural appeal of steel MRFs and can have a relatively small design requirement beyond traditional MRF design since global performance increases are achieved through modifications of local connection detailing and not through redesigns of the structural layout. Frames with either pre-Northridge connections or pre-qualified RBS connections are compared with otherwise identical frames having low-damage SHJ or SCSHJ connections. The global performance of these frames is compared using multiple hazard types (short or long duration ground motions as well as main-shock-after-shock ground motion sequences) and multiple engineering demand parameters (displacements, accelerations, and residual inter-story drifts) to identify key differences in system level performance when using these low-damage connections.

Chapter 3 This chapter focuses on the efficient use of low damage connections by implementing these connections only at a subset of floor levels while still seeking to maintain the benefit in global system level performance achieved with the uniform connection upgrade, as determined in the previous chapter. This subset of locations is referred to as critical connections, and a method for identifying them based on non-linear time history analysis is proposed. A simplified identification process, based on nonlinear static analysis, is also proposed. Finally, the location of these connections is selected and imposed using a direct displacement based design process (DDBD) (Priestley et al. 2007). The ability to concentrate the application of detailing resources at the

critical connections ensures that it provides the largest increase in global performance.

Chapter 4 This chapter presents an optimization methodology which widens the scope of considered upgrade strategies, allowing for the comparison of the connection modification upgrade strategy to other structural upgrade strategies proposed in FEMA-351 (2000b), such as increases in strength/stiffness and supplemental damping, as well as the inclusion of upgrades to non-structural components as recommended in FEMA E-74 (FEMA 2011). This expansion in scope also introduces consideration of the cost of upgrade implementation, so as to measure and compare the life-cycle viability of each upgrade strategy. The optimization of the overall upgrade strategy uses a genetic algorithm, which evaluates the change in losses using the Monte Carlo PBEE methodology, and assess the benefits provided by the upgrade options using different decision metrics such as economic cost, downtime, and casualties.

Chapter 5 This chapter presents an overall framework to assess the viability of competing structural upgrades in combination with accompanying upgrades to non-structural components. The framework outlines three levels of analysis, each with increasing analytical resources required, where the first level consists of an approximation of the required upgrade performance based on its assumed cost of implementation, the second is a validation of the assumed upgrade performance using structural analysis, and the third is the detailed

optimization of the upgrade strategies presented in Chapter 4. The rapid assessment of the upgrade viability completed in the first two levels of the framework is possible using a proposed modification to the PBEE methodology, the Median Shift Probability (MSP) method. Once introduced, the first two levels of the framework are used to identify the viability of several possible structural upgrades for a case study structure, as well as to estimate the optimal combination of accompanying non-structural upgrades. The results obtained using the MSP method are compared to the results obtained in Chapter 4.

Chapter 6 This chapter summarizes the findings of this research and concludes the thesis by addressing each of the questions posed in this Introduction. Outlines of proposed future research are also included in this chapter.

As presented, each chapter examines and compares optimal upgrade strategies with potentially increasing scope. Figure 1.3 provides a schematic representation of the scope of upgrade strategies of each chapter, where the larger circles represent a larger scope, encompassing the smaller circles. While each chapter is its own self-contained study, the theme of improving the performance of both existing MRFs with pre-Northridge connections, as well as current MRF code compliant design, is maintained throughout the entire study. As each chapter is submitted as an independent research article as specified in the sandwich thesis model, some repetition of content is unavoidable.

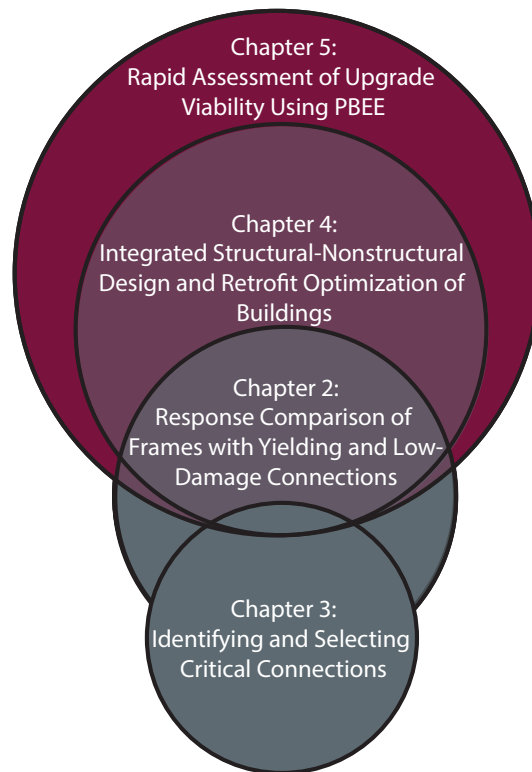


Figure 1.3: Scope of upgrades addressed in each chapter

1.4 References

- ADB, (2013). “Investing in Resilience Ensuring a Disaster-Resistant Future”, Asian Development Bank, Manila, Philippines.
- AISC, (2016a). “Seismic Provisions for Structural Steel Buildings.” *AISC 341-16*, American Institute of Steel Construction, Chicago, IL, US.
- AISC, (2016b). “Prequalified Connections for Special and Intermediate Steel Moment Frames for Seismic Applications.” *AISC 358-16*, American Institute of Steel Construction, Chicago, IL, US.
- Almufti, I., and Willford, M., (2013) ”REDI Rating System: Resilience-Based Earthquake Design Initiative for the Next Generation of Buildings” ARUP Advanced Technology and Research.
- Bennett, D., (1995). ”Skyscrapers”, Simon and Schuster, New York, NY.
- Bertero, V., Anderson, J., and Krawinkler, H., (1994). “Performance of Steel Building Structures During the Northridge Earthquake”, *Report No. UCB/EERC-94/09*. Berkeley, California.
- Biddah, A., and Heidebrecht, A. C., (1999). “Evaluation of the Seismic Level of Protection Afforded to Steel Moment Resisting Frame Structures Designed for Different Design Philosophies,” *Canadian Journal of Civil Engineering*, 26(1), pp. 35–54.
- Bronson, W., (1959). “The Earth Shook, The Sky Burned” 1st Edition, Chronicle Books, San Francisco, CA.

- Christopoulos, C., Filiatrault, A., Uang, C., and Folz, B., (2002). "Posttensioned Energy Dissipating Connections for Moment-Resisting Steel Frames", *Journal of Structural Engineering*, 128(9), 1111-1120.
- Christopoulos, C., and Filiatrault, A., (2006). "Principles of Passive Supplemental Damping and Seismic Isolation", IUSS Press, Pavia, Italy.
- CISC, (2015). "Moment Connections for Seismic Applications", 2nd, Canadian Institute of Steel Construction.
- Civjan, S., Engelhardt, M., and Gross, J., (2000). "Retrofit of Pre-Northridge Moment-Resisting Connections" *Journal of Structural Engineering*. 126(4), 445-452.
- Clifton, G.C. (2005). "Semi-Rigid Joints For Moment-Resisting Steel Framed Seismic-Resisting Systems." *Doctoral Dissertation, Department of Civil and Environmental Engineering*, University of Auckland, New Zealand.
- CSA, (2014). "Design of Steel Structures", S16-14, Canadian Standards Association.
- Erochko, J., Christopoulos, C., Tremblay, R., and Choi, H. (2011). "Residual Drift Response of SMRFs and BRB Frames in Steel Buildings Designed according to ASCE 7-05." *Journal of Structural Engineering*, 137(5), 589–599.
- FEMA, (2000a). "Recommended Seismic Design Criteria for New Steel Moment-Frame Buildings" *Report FEMA-350*, Federal Emergency Management Agency Washington, D.C.

FEMA, (2000b). “Recommended Seismic Evaluation and Upgrade Criteria for Existing Welded Steel Moment-Frame Buildings” *Report FEMA-351*, Federal Emergency Management Agency Washington, D.C.

FEMA, (2011). “Reducing the Risks of Nonstructural Earthquake Damage-A Practical Guide” *Report E-74*, Federal Emergency Management Agency, Washington, DC.

FEMA, (Federal Emergency Management Agency). (2012). “Seismic Performance Assessment of Buildings.” *Federal Emergency Management Agency Report P-58*, Washington, D.C.

Folger, P., (2013). ”Earthquakes: Risk, detection, warning and research.” *CRS Report for Congress*.

Freeman, J., (1932). “Earthquake Damage and Insurance” 1st Edition, McGraw-Hill.

Fuller, T., Singhvi, A., Grondahl, M., and Watkins, D., (2019). “Buildings Can Be Designed to Withstand Earthquakes. Why Doesn’t the U.S. Build More of Them?” *The New York Times*, June 7th, 2019.

Gledhill, S., Sidwell, G., and Bell D., (2008). “The Damage Avoidance Design of Tall Steel Frame Buildings – Fairlie Terrace Student Accommodation Project, Victoria University of Wellington” *New Zealand Society for Earthquake Engineering Conference*, Wairakei, NZ.

Haselton, C., and Hamburger, R., (2018). ”Resilient Design and Risk Assessment using FEMA P-58 Analysis” *Structure magazine*.

- Hamburger, R., Krawinkler H., Malley J., and Adan, S., (2009). “Seismic Design of Steel Special Moment Resisting Frames: A Guide for Practicing Engineers” *NEHRP Brief No. 2*, Gaithersburg, Maryland.
- Kasai, K., Fu, Y., and Watanabe, A., (1998). “Passive Control Systems for Seismic Damage Mitigation” *Journal of Structural Engineering*, 124(5), 501-512.
- Khoo, H.-H., Clifton, C., Butterworth, J., MacRae, G., Gledhill, S., and Sidwell, G., (2012). “Development of the Self-centering Sliding Hinge Joint with Friction Ring Springs.” *Journal of Constructional Steel Research*, 78, 201–211.
- Khoo, H. H., Clifton, C., Butterworth, J., and MacRae, G., (2013). “Experimental Study of Full-scale Self-centering Sliding Hinge Joint Connections with Friction Ring Springs.” *Journal of Earthquake Engineering*, 17(7), 972–977.
- Kiggins, S., and Uang, C., (2006). “Reducing Residual Drift of Buckling-Restrained Braced Frames as a Dual System” *Engineering Structures*, 25(5), 655-666.
- Lignos, D., and Al-Shawwa, N., (2013). “Web-Based Interactive Tools for Performance-Based Earthquake Engineering”, <http://resslabtools.epfl.ch/steel/>, Accessed September 2015.
- MacRae, G., and Clifton, C., (2013). “Low Damage Design of Steel Structures” *Steel Innovations Workshop*, Christchurch, New Zealand.

- McGuire, W., (1988). “Introduction to Issue” *Journal of Constructional Steel Research*, 10(1), 1-35.
- Miranda, E., and Aslani, H., (2003). “Probabilistic Response Assessment for Building-Specific Loss Estimation” *Pacific Earthquake Engineering Research Center Report No. 2003/03*, University of California Berkeley, California.
- Mirtaheri, M., Zandi, A., Samadi, S. and Samani, H., (2011). “Numerical and Experimental Study of Hysteretic Behavior of Cylindrical Friction Dampers”, *Engineering Structures*, 33, 3647-56.
- Monir, H., and Zeynali, K., (2013). “A Modified Friction Damper for Diagonal Bracing of Structures” *Journal of Constructional Steel Research*, 65, 159-176.
- Nakamura, Y., and Okada, K., (2019). “Review on Seismic Isolation and Response Control Methods of Buildings in Japan” *Geoenvironmental Disasters*, 6(7), 1-10.
- Nikellis, A., Sett, K., and Whittaker, A., (2019). “Multihazard Design and Cost-Benefit Analysis of Buildings with Special Moment-Resisting Steel Frames” *Journal of Structural Engineering*, 145(5).
- Pino, N., Piatanesi, A., Valensise, G., and Boschi, E., (2009). “The 28 December 1908 Messina Straits Earthquake (MW 7.1): A Great Earthquake throughout a Century of Seismology” *Seismological Research Letters*, 80(2), 243-259.
- Pollini, N., Lavan, O., and Amir, O., (2018). “Optimization-based

Minimum-cost Seismic Retrofitting of Hysteretic Frames with Nonlinear Fluid Viscous Dampers” *Earthquake Engineering & Structural Dynamics*, 47(15), 2985-3005.

Potter, S., Becker, J., and Rossiter, K., (2015). “An Overview of the Impacts of the 2010-2011 Canterbury Earthquakes” *International Journal of Disaster Risk Reduction* , 14, 6-14.

Priestley, M.J.N., Calvi, G.M. and Kowalsky, M.J., (2007). Direct Displacement-Based Seismic Design of Structures. IUSS Press, Pavia.

Ricles, J., Sause R., Garlock M., and Zhao C., (2001). ”Post-Tensioned Seismic-Resistant Connections for Steel Frames.” *Journal of Structural Engineering*, 127(2), 113–121.

Sabelli, R., Mahin, S., and Chang, C., (2003). “Seismic Demands on Steel Braced Frame Buildings with Buckling Restrained Braces” *Engineering Structures*, 25, 655-666.

Soong, T., and Dargush, G., (1997) ”Passive Energy Dissipation Systems in Structural Engineering”, John Wiley & Sons, Chichester, England.

Terzic, V., and Mahin, S., (2017). “Using PBEE to Assess and Improve Performance of Different Structural Systems for Low-Rise Steel Buildings” *International Journal of Safety and Security Engineering*, 7(4), 532-544.

Tsai, K., Wu, S., and Popov, E., (1995). “Experimental Performance of Seismic Steel Beam-Column Moment Joints” *Journal of Structural Engineering*, 121(6), 925-931.

Tremblay, R., Timler, T., Bruneau, M., and Filiatrault, A., (1995). “Performance of Steel Structures During the January 17, 1994, Northridge Earthquake” *Canadian Journal of Civil Engineering*, 23(3), 757-770.

Uang, C., Yu, Q., and Noel, S., (1998). “Rehabilitating pre-Northridge Steel Moment Frame Connections: RBS and Haunch Approaches Considering Slab Effects” *Procedure of the 6th U.S. National Conference on Earthquake Engineering*, Oakland, California.

Uriz, P., and Whittaker, A., (2001). “Retrofit of Pre-Northridge Steel Moment-Resisting Frames Using Fluid Viscous Dampers” *Structural Design of Tall Buildings*, 10(5), 371-390.

USCB, (2019). “Urban and Rural Areas - History” *United States Census Bureau*, Washington D.C.

USGS, (2009). *PAGER-CAT Earthquake Catalog*, Version 2008 06.1, United States Geological Survey.

Vaughan, E., and Turner, J., (2013). “The Value and Impact of Building Codes” *Environmental and Energy Study Institute - White Paper*, September, 2013.

Youssef, N., Bonowitz, D., and Gross, J., (1995). “A Survey of Steel Moment-Resisting Frame Buildings Affected by the 1994 Northridge Earthquake” *National Institute of Standards and Technology*, Gaithersburg, Maryland.

Chapter 2

SEISMIC RESPONSE COMPARISON OF STEEL MRFS WITH YIELDING AND LOW-DAMAGE CONNECTIONS

2.1 Abstract

The development of low-damage steel moment resisting connections for seismic applications provides designers with techniques to dissipate energy without relying on plastic deformations of beam sections, thus avoiding connection strength and stiffness deterioration and providing the opportunity of adding a self-centering mechanism to avoid residual displacements. In this paper, the system-level performance of two low-damage connections, the sliding hinge joint (SHJ) connection and the self-centering sliding hinge joint (SCSHJ) connection, is evaluated using analytical models. New component models are first developed for each of the connections and validated using available experimental results. The global performance of three steel frames of different heights, using either the SHJ connection or SCSHJ connection, are then compared to otherwise identical frames with either pre-Northridge (PRENORTH) connections or reduced beam section (RBS) connections. The benefits of these new connections for the global performance of the frames are presented through fragility curves for 27 response indices, comprising three

engineering demand parameters (maximum inter-story drift, residual drifts, and accelerations) under three earthquake hazard types (shallow crustal, subduction, and main-shock-after-shock combinations) for three performance objectives. The global performance of the frames with the SHJ connection is similar to that of frames with the RBS connection, while avoiding yielding and damage in the connections. The SCSHJ connections further enhance the good performance of the SHJ connection by also reducing residual drifts and peak floor accelerations. This improvement in performance translates directly to reductions in the expected annual loss, particularly for structures exposed to longer duration ground motions or main-shock-after-shock sequences.

2.2 Introduction

The investigations following the 1994 Northridge Earthquake in California demonstrated the lower than expected performance of welded connections in steel moment resisting frames (MRFs) (Engelhardt and Sabol 1994). These observations resulted in the development of pre-qualified connections for use in seismic areas (FEMA 2000a), which included the reduced beam section (RBS) connection. Designers may select among these pre-qualified connections since extensive component testing has demonstrated that they can undergo large amounts of plastic hinging and provide a reliable amount of hysteretic energy dissipation (AISC 2016). However, this plastic hinging can also result in irrecoverable deformations in the beams, leading to the frame having significant residual displacements (Erochko et al. 2011), which can translate into large economic losses and significant delays in the operating capability of the structure (FEMA 2012). To mitigate this issue,

several low-damage alternative connections have been proposed. Examples of such connections include post-tensioned seismic-resistant connections (Ricles et al. 2001, Christopoulos et al. 2002), connections using high-force-to-volume dissipaters (Mander et al. 2009), the double split tee connection (Latour et al. 2015), and the sliding hinge joint (SHJ) connection and its self-centering (SCSHJ) variant (Clifton 2005 & Khoo et al. 2012). Isometric views of the SHJ and SCSHJ connections are shown in Figure 2.1. The SHJ connection, initially proposed by Clifton (2005), allows a moment resisting frame to dissipate energy via friction rather than plastic hinging by using an asymmetric friction connection placed at the bottom flange of the beam. These connections have been implemented in several buildings in practice (Gledhill et al. 2008; Tait et al. 2013). The addition of a ring spring (Filiatrault et al. 2000) below the asymmetrical friction connection converts a SHJ connection to a SCSHJ connection by providing self-centering capability (Clifton 2005). The activation load and stiffness of the connection can be configured by modifying the friction surface properties, while the degree of self-centering capability can be configured by modifying the properties of the ring spring. A series of full scale cyclic tests of these connections conducted by Khoo et al. (2013) demonstrated their consistent energy dissipation and self-centering capabilities. While the research surrounding the component performance of these low-damage connections has continued over more than a decade, the system-level analysis of the global performance of these connections in steel MRFs has only been recently undertaken. Some global performance analyses have been conducted on the aforementioned post-tensioned MRF connections, which have a similar flag shaped hysteretic behavior as the SCSHJ. Rojas et al. (2005) examined the

seismic performance of a six-story frame having post-tensioned connections with friction devices, while Dimopoulos et al. (2016) compared the probabilistic economic seismic loss of a five-story frame with either conventional connections, conventional connections and viscous dampers, post-tensioned connections, or post-tensioned connections and viscous dampers. Yeow et al. (2018) demonstrated that frames installed with SHJ connections reduced expected repair costs when compared to frames with pre-qualified MRF connections, but the benefits were heavily dependent on the specific site hazard.

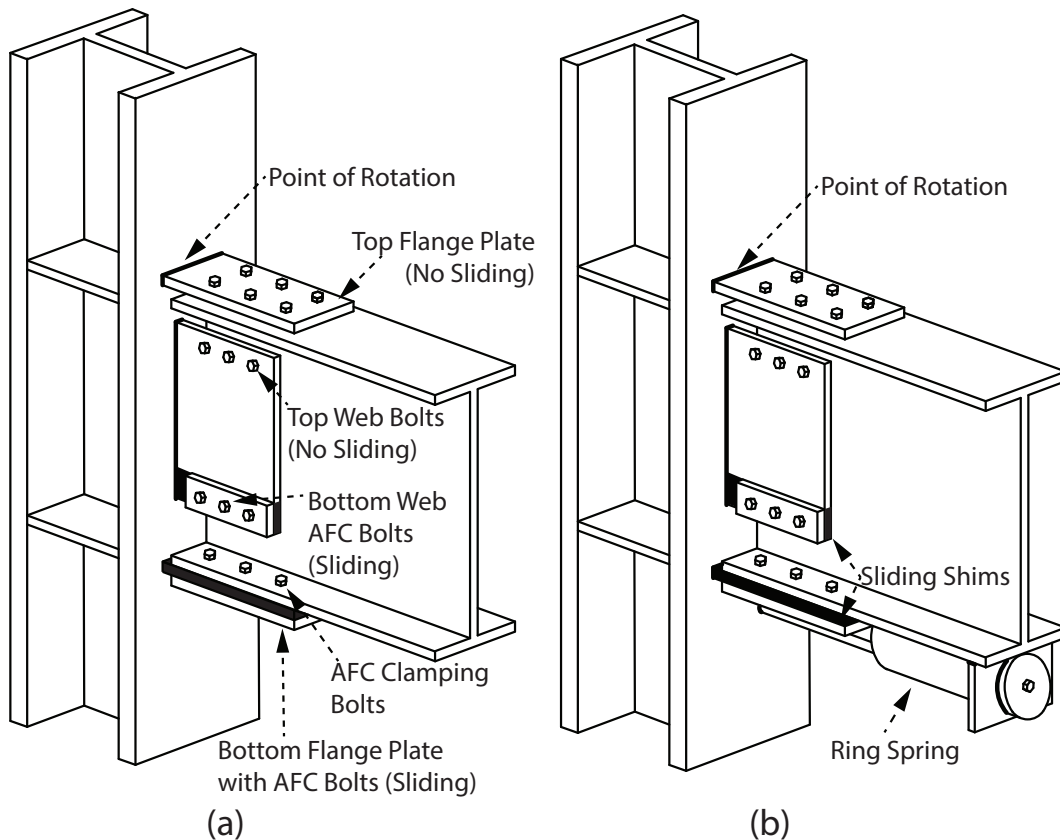


Figure 2.1: Isometric views of (a) SHJ connection and (b) SCSHJ connection

With the recent shift towards performance-based design and to seismic resiliency of structures, the low-damage SHJ and SCSHJ connections provide

designers with alternatives that may enhance the overall performance of MRFs. The objective of this paper is to evaluate the potential benefits of using these newly developed low-damage connections across multiple response indices. The initial steps involve the creation and calibration of non-linear models to replicate the moment-rotation behavior observed during cyclic tests. Following this calibration, the design of three archetype steel MRFs of different heights (three stories, six stories and 12 stories) is presented and four versions of each of these archetype frames are modelled, each with a different connection configuration: pre-Northridge (PRENORTH), pre-qualified reduced beam section (RBS), sliding hinge joint (SHJ), and self-centering sliding hinge joint (SCSHJ). All of the frame versions are studied based on nonlinear time-history dynamic analyses, considering three seismic hazard types at the chosen site, three engineering demand parameters (EDPs), and three performance objectives. Table 2.1 summarizes the scope of the analyses.

Table 2.1: Summary (Number) of Frame Heights, Connection Types, Seismic Hazard Types, EDPs and Performance Objectives

Frame Heights (3)	3, 6, 12
Connection Types (4)	PRENORTH, RBS, SHJ, SCSHJ
Seismic Hazard Types (3)	Shallow Crustal Earthquakes, Main-Shock-After-Shock of Shallow Crustal Earthquakes, Subduction Earthquakes
EDPs (3)	Maximum Inter-story Drifts, Maximum Residual Drifts, Peak floor accelerations
Performance Objectives (3)	Collapse Prevention (Hazard Reduction for acceleration EDP), Life Safety, Immediate Occupancy (Position Retention for acceleration EDP)
Total Number of Fragility Curves	324

2.3 Frame Designs and Modeling Approach

Three frame heights were selected for this study: three stories, six stories, and 12 stories, as shown in Figure 2.2. Each frame was selected from previous literature and the design was updated to satisfy the ASCE 7-16 (ASCE 2016) design requirements for the same location in Seattle, Washington on a site class B/C boundary with modified spectral response parameters $S_{MS}=1.4g$ and $S_{M1}=0.6g$. The frame with three stories, taken from Gupta and Krawinkler (1999), has an updated fundamental period of 0.87 seconds and a design spectral acceleration of 0.46g; the frame with six stories, taken from Hall (1995), has a fundamental period of 1.3 seconds and a design spectral acceleration of 0.31g; and the frame with 12 stories, taken from NIST (2010), has an updated fundamental period of 2.8 seconds and design spectral acceleration of 0.14g. The frames were all designed with an importance factor of one. Each frame was initially designed with RBS connections and a verification was conducted to ensure that the use of any of the other connection types would still satisfy the strong column/weak beam design principle at all locations. To provide a consistent baseline for comparison, no sections were modified with the different connection types, such that the initial periods of the frames were within 5% across the different connection types. As the beam sections were not modified, the SHJ and SCSHJ connections were designed to ensure the full non-linear behavior of each connection was achieved before beam yielding. For the SHJ connection, the activation moment (M_{AB}) was designed as 40% of the yield moment of

the beam, while the first activation moment of the SCSHJ connection was designed as 30% of the yield moment. The self-centering for the SCSHJ connection is quantified by the percentage of joint moment capacity developed by the ring springs (P_{RS}), and was set to 52.4%, following the design ratios of the connection used for Test #7 in Khoo et al. (2013).

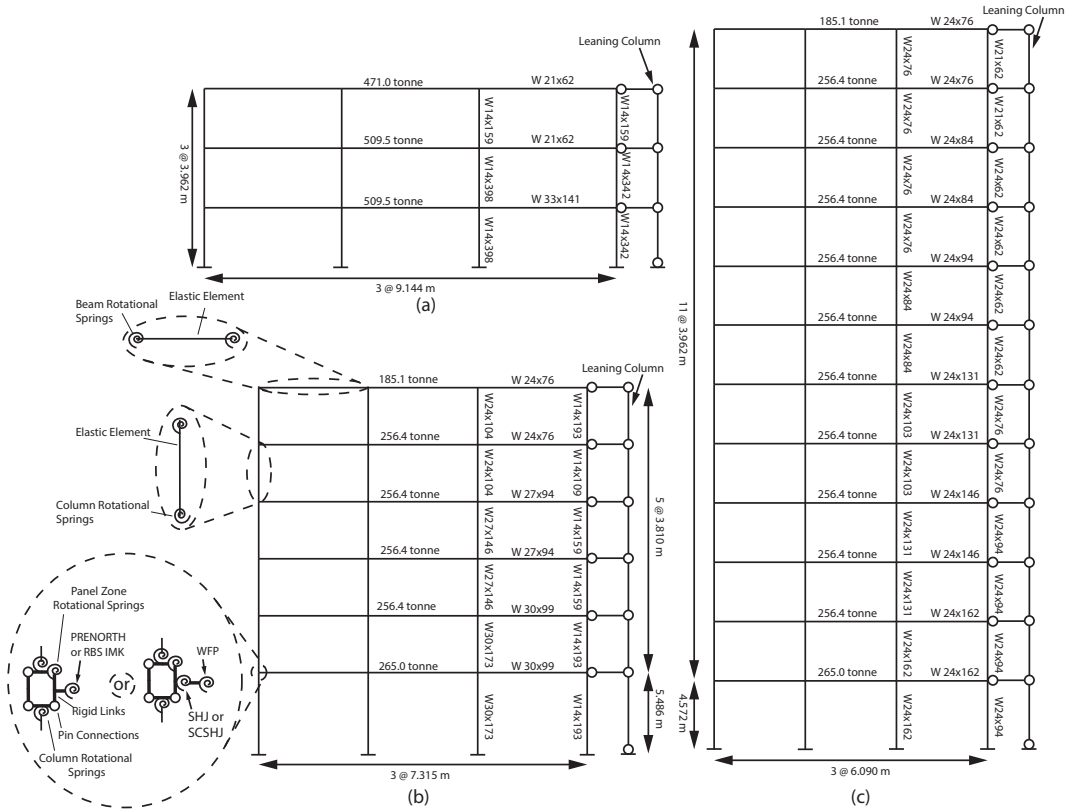


Figure 2.2: Layout of (a) 3-story frame, (b) 6-story frame with modeling detail and (c) 12-story frame

The frame models were assembled in OpenSees (McKenna et al. 2000) and consisted of elastic beam and column elements with concentrated rotational hinges at the ends. Each beam to column joint was modeled to capture panel zone yielding using the Krawinkler spring box model (Gupta and Krawinkler 1999), shown in Figure 2.2 (b), with a trilinear behavior (Charney and Pathak

2008). The beam connections were modeled using material models presented in the next section. The columns are assumed well braced at the top and bottom of every story, had a maximum axial gravity load less than 20% of the axial capacity, and therefore satisfied the modeling recommendations outlined in ATC-72 (ATC 2010). For modeling using the Ibarra-Medina-Krawinkler (IMK) model (Ibarra et al. 2005). The tributary seismic mass at each floor level for each frame is shown in Figure 2.2. Rayleigh damping of 2% was applied to each frame in the first and second elastic modes using a combination of mass proportional and constant stiffness proportional damping based on initial conditions. However, to avoid unrealistic and spurious damping forces, the stiffness proportional damping was applied using the approach of Zareian and Medina (2010). The second order P- Δ effects were modeled with vertical loads equal to the gravity forces within the frame's lateral tributary area at each floor level. These loads were applied to a pin-connected gravity column shown in Figure 2.2. No other contributions from the gravity system were included.

2.3.1 Calibration of PRENORTH and RBS beam hinge models

The non linear moment-rotation spring models for the PRENORTH and RBS connections were calibrated using component test results obtained from the library developed by Lignos and Al-Shawwa (2013) and selected beam-column assemblies with steel sections similar in size to those used in the frames, as specified by modeling option #2 in ATC-72 (ATC 2010). No floor slabs were present in the experimental component tests and their effect

was not included in the model. To determine the parameters of the IMK models (Ibarra et al. 2005) that were used for the PRENORTH and RBS connections, values were initially set using the general regression equations provided in ATC-72 (ATC 2010) and were then calibrated using component test data for beam sections of identical depth for each beam size. The target metric for calibration was minimizing the difference in total absorbed energy (i.e. cumulative areas of hysteretic loops) between the experimental results and analytical models, while matching the experimental moment-rotation skeletal curve. The procedure outlined by Ibarra and Krawinkler (2005) was used to account for the additional degrees of freedom and consequently the extra flexibility introduced by the zero-length hinges. Table 2.2 summarizes key IMK parameters for the PRENORTH and RBS connections, and Figure 2.3 (a) and (b) shows the influence of each of these IMK parameters on the moment-rotation hysteretic behavior. The calibrated beam-column connection models are shown in detail in Figure 2.3 (a) for the PRENORTH and Figure 2.3 (b) for the RBS connections with a W24x131 beam made of grade A36 steel and a W24x103 column with grade A572 steel. Both analytical models replicate the backbone moment-rotation behavior to within 2% measured using the residual sum of squares (RSS), although each model overestimates the unloading stiffness portion of the moment-rotation response. This leads to an overestimation of the total absorbed energy of 5% for the PRENORTH connection and 7% for the RBS connection and this is shown in Figure 2.3 (a) and (b), respectively. These differences were deemed acceptable for the evaluation of the global seismic performance of the frames. More details regarding the calibration of the beam hinges are described in Steneker et al. (2018). Each connection model was placed in the

beam-column assembly as shown in Figure 2.2 (b).

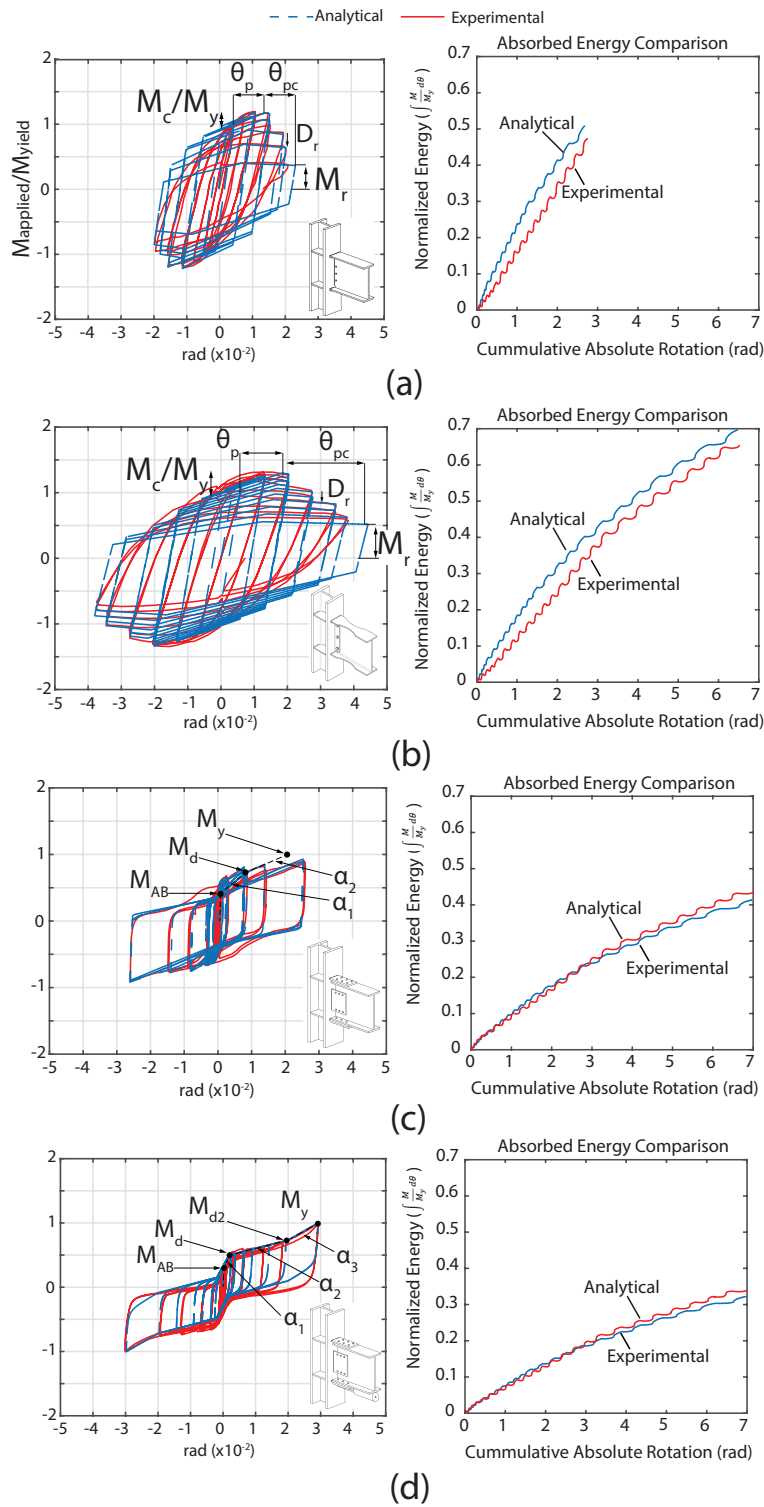


Figure 2.3: Hysteretic model calibration, major model parameters and energy comparison for (a) PRENORTH IMK model (Engelhardt and Sabol 1994), (b) RBS IMK model (Lee et al. 2004), (c) SHJ model (Khoo et al. 2013), and (d) SCSHJ model (Khoo et al. 2013)

Table 2.2: Component test sections and major IMK parameters for pre-qualified connections

IMK Parameter	Calibrated		RBS	ATC-72 Values for RBS Connections (Option 3)
	PRENORTH Connections	Calibrated Connections (Option 2)		
Size of Test Beam/ Test Column	W610x195/W610x153 (W24x131/W24x103)	W610x195/W610x153 (W24x131/W24x103)		W610x195/W610x153 (W24x131/W24x103)
Analytical Model Used	Bilinear IMK	Bilinear IMK		N/A
Strain Hardening Ratio M_c/M_y)	1.15	1.1		1.06
Plastic Rotation (θ_p)	0.013 rad	0.02 rad		0.04 rad
Post-Capping Rotation (θ_{pc})	0.1 rad	0.2 rad		0.2 rad
Ultimate Rotation (θ_u)	0.025 rad	0.05 rad		0.05
Residual Strength Ratio (M_r)	0.2	0.3		N/A
Cyclic Deterioration Ratio (D_r)	0.8	0.5		N/A

2.3.2 Calibration of SHJ and SCSHJ beam hinge models

As presented in Khoo et al. (2012), and shown in Figure 2.3 (c), the SHJ connection’s moment-rotation behavior has three distinct characteristics, all of which are taken into account in the analytical model: 1) a dominant bilinear hysteretic behavior at small rotations, 2) a dominant trilinear hysteretic behavior at large rotations, and 3) a degradation of both stiffness and strength as the cycle number and amplitude increase. To replicate the bilinear and trilinear behaviors and provide a similar degree of modeling adjustability when compared to the adjustability of the connection design, the model uses a parallel combination of the Hysteretic and Steel02 materials

in OpenSees. The Steel02 material provides the initial bilinear behavior and the Hysteretic material is used to capture the trilinear behavior segments of the pinched moment-rotation behavior that occur due to the sliding of the first and second interface surfaces (Khoo et al. 2012). A negative isotropic hardening parameter in the Steel02 material is used to representing the decrease in clamping force of the bolts in the asymmetrical friction connection due to their initial plasticity, and leads to the transition from a bilinear moment-rotation behavior into a trilinear Hysteretic material at larger rotations. The Fatigue uniaxial material (Uriz and Mahin 2008) in OpenSees was applied to the Steel02 material to capture the cyclic deterioration caused by the further reduction in the clamping force of the bolts when they undergo larger levels of plasticity (Khoo et al. 2012). Table 2.3 summarizes the model parameters and Figure 2.3 (c) provides a visual indicator of these parameters for the SHJ connection. The SHJ model was validated using component test results from MacRae et al. (2010) with a W14x30 beam section and W12x106 column section. The model replicates almost exactly the moment-rotation backbone curve observed in component tests and results in an underestimation of the energy absorbed per cycle of less than 2%. The parameters in Table 2.3 were used for all connections as they provide the chosen design ratio of activation moment to yield moment for each of the beam sizes. Khoo et al. (2012) also present three distinct moment-rotation behavior characteristics of the SCSHJ connection: 1) a quadrilinear hysteretic behavior, 2) the self-centering mechanism, and 3) the elimination of stiffness and strength degradation, shown in Figure 2.3 (d). To capture the quadrilinear behavior, the SCSHJ analytical model used three material models in OpenSees in parallel: SelfCentering (Erochko 2013),

Steel02 (Filippou and Popov 1983), and ElasticPPGap models. The combination of the three materials provides the model with the ability to capture the stiffness contributions from both sliding surfaces and the ring spring. As mentioned in Khoo et al. (2012), the use of the ring spring reduces the degradation of the connection’s elastic stiffness, removing the need to include a Fatigue model for this connection. The input model parameters are summarized in Table 2.3, and their influences on the hysteretic response are shown in Figure 2.3 (d). The SCSHJ model was validated using component test results obtained from Khoo et al. (2013) with a W14x38 beam section and a W18x50 column section. While the moment-rotation behavior in the positive and negative loading directions are well captured, the asymmetric unloading behavior of the SCSHJ component test results is not perfectly captured by the analytical model. This experimental asymmetric behavior data is caused by the presence of a floor slab used throughout the series of component tests that preceded the one used for calibration, which did not include a floor slab and was selected for consistency with the PRENORTH and RBS component tests. This led to an RSS in absorbed energy of 3% between the analytical and experimental results when this asymmetry is corrected, shown in Figure 2.3 (d).

To provide a limit on the capacity of the SHJ and SCSHJ connections at large drifts, both connection models consist of two zero-length rotational springs in series, as shown in Figure 2.2 (b). One spring at the column face represents the desired friction activation, as discussed above, while the other spring represents the beam yielding behavior at the end of the flange plate. While this plastic hinging is not desired, it is expected to occur at large rotations after the bolts reach the ends of the slotted holes in the sliding

interfaces, causing the connection to lock up for larger rotations. This modeling approach was used as no test results were available for SHJ and SCSHJ connections beyond rotations of 0.03 rad (Khoo et al. 2013), whereas larger rotations are anticipated at near-collapse level seismic events, requiring that the beam plastic hinging be captured. The beam model used for the plastic hinging occurring at large deformations was an IMK material calibrated to component tests results for a flange-plate connection (WFP) (Kim et al. 2000). This connection type was selected as it has similar geometry to a SHJ connection past the "lock-up" rotation of 0.03 rad, and the consequence function associated with the WFP connection was used for both the SHJ and SCSHJ connections while accounting for the extra rotational capacity.

Table 2.3: Component test sections and major parameters for SHJ and SCSHJ connections

Parameter	SHJ	SCSHJ
Size of Test Beam/Test Column	W360x45/W310x158 (W14x30/W12x106)	W360x57/W460x74 (W14x38/W18x50)
Analytical Model Used	SHJ	SCSHJ
Activation Moment (M_{AB})	$0.4 \times M_y$	$0.3 \times M_y$
Dependable Moment (M_d)	$1.5 \times M_{AB}$	$2.0 \times M_{AB}$
First Post-Activation Stiffness (α_1)	0.1	0.5
Second Post-Activation Stiffness (α_2)	0.02	0.004
Third Post-Activation Stiffness (α_3)	N/A	0.01
Pinching Displacement (P_D)	0.5	N/A
Pinching Force (P_F)	0.3	N/A
Isotropic Hardening Stiffness (a_1, a_3)	-0.02	N/A
Isotropic Hardening Activation (a_2, a_4)	1.0	N/A
Self-Centering Ratio (λ_{SC})	N/A	0.05
Forward-Reverse Activation Ratio (β_{SC})	N/A	0.0001
Deformation at Final Stiffness (θ_{SC})	N/A	0.02

2.4 Response Indices

To understand the influence of each connection type on the overall system performance, the three frames described above were evaluated using a total of 27 different response indices: three distinct engineering demand parameters (EDPs) for three different performance objectives across three different seismic hazard types. The three different EDPs used were the maximum inter-story drifts, the residual inter-story drifts and the peak absolute floor accelerations. The three different seismic hazard types were defined as shallow crustal motions, main-shock-after-shock sequence of shallow crustal motions, and subduction motions, and were selected to determine the effects of duration and repetitive exposure on the performance of each type of frame. The three performance objectives considered are taken from ASCE 41 (ASCE 2017) and can be categorized into two parts, structural performance objectives listed as collapse prevention (S-5), life safety (S-3), and immediate occupancy (S-1); and nonstructural performance objectives listed as hazards reduced (N-D), life safety (N-C), and position retention (N-B). The combined performance objectives are listed in ASCE 41 as 1-B, 3-C and 5-D. Each response index was evaluated using a multiple stripe analysis having seven intensity stripes, where each stripe consisted of 40 individual ground motion components (Baker 2015). For each stripe of each response index, the percentage of the 40 ground motions causing the EDP in question to exceed the limits corresponding to each of the three performance objectives was determined. The maximum likelihood estimation (MLE) approach was then used to fit a lognormal cumulative distribution function (CDF) between the probability values of each stripe for each

performance objective. As discussed in Baker (2015), fitting a lognormal distribution using the MLE approach is suitable for estimating the CDF parameters in this case, as multiple stripe analysis does not directly indicate the sample moments (i.e. mean, variance, etc.). To numerically summarize these CDFs, the median and lognormal standard deviation (β) values were extracted, where the median values indicate the intensity corresponding to a probability of exceedance of 50% and the β values reflect the record-to-record variability across the ground motions used at each stripe (NIST 2010). The median intensity values are used throughout the discussion of results as a comparative value, as the cumulative distribution functions within each response index and performance objective generally have similar β values, unless noted otherwise.

2.4.1 Seismic Hazard Types

Three different seismic hazard types were identified based on the deaggregation information for the Seattle site (Lat: 47.6, Long: -122.3). The seismic hazard deaggregation plots are shown in Figure 2.4 (a) to (c) (USGS, 2014) for peak ground accelerations and 5% damped spectral accelerations at periods of 1 second and 2 seconds, respectively. The first seismic hazard type is from shallow crustal (including intraslab) earthquakes caused by the various Puget Sound faults (USGS, 2014), and the horizontal acceleration time histories for this hazard source were selected from the NGA-West2 Database (PEER 2013). The components at each intensity stripe were selected and scaled to match a conditional spectrum at a target spectral acceleration at the first-mode period for each frame (Baker and Lee 2017).

Furthermore, the ground motions were filtered to have magnitudes between 6 and 7, rupture distances of 5 km to 50 km (USGS, 2014), ϵ values of 0.47 to 1.30 (where ϵ is the number of standard deviations by which the observed ground motion's logarithmic spectral acceleration exceeds the target (Baker and Lee 2017), a V_{s30} (the average shear wave velocity in the top 30 meters of the soil) value of 760m/s for the B/C boundary site class, and a maximum scale factor of 3. The range of considered periods for matching was from 0.1 seconds to 5 seconds. The selected shallow crustal earthquakes had a mean 90% Arias intensity (Arias 1970) duration of 45 seconds. The median spectrum for each intensity stripe, as well as the spectrum for each of the 40 ground motion components for the MCE intensity, defined as a probability of exceedance of 2% in 50 years (ASCE 2016), is shown in Figures 2.5 (a), (b) and (c) for the three-story, six-story, and 12-story frames, respectively.

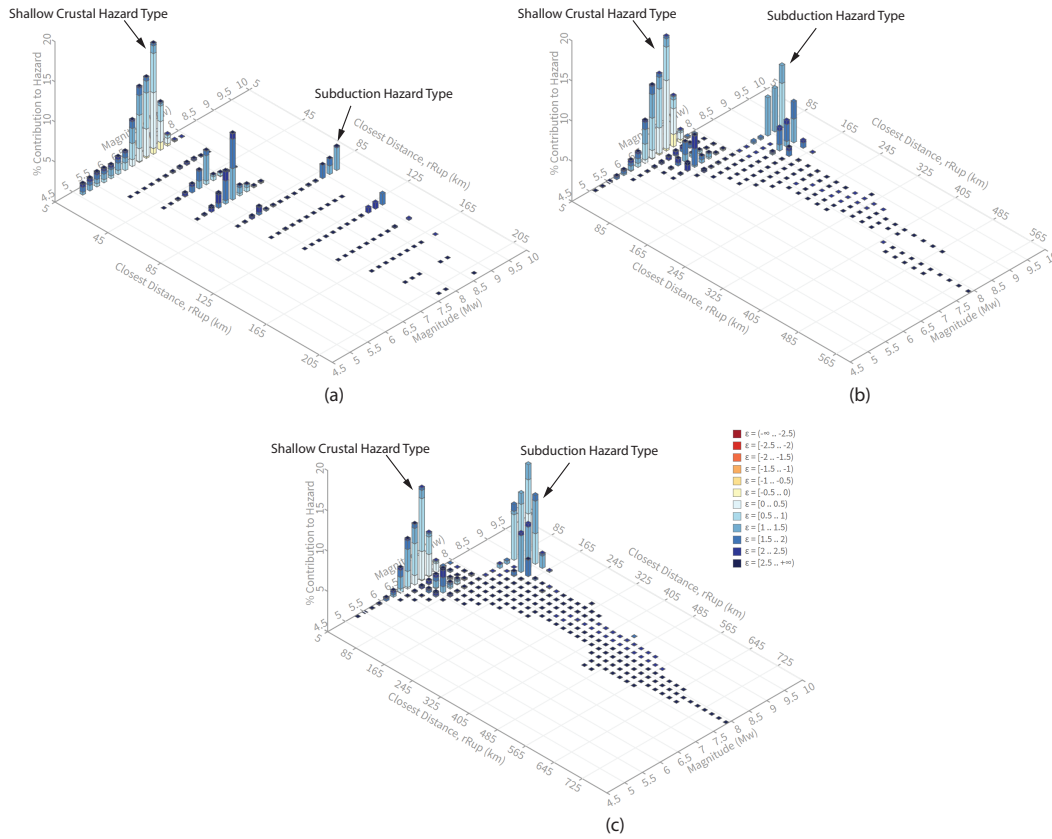


Figure 2.4: Deaggregation of seismic hazard for Seattle site (Lat: 47.6, Long: -122.3) for (a) Peak Ground Acceleration, and 5% damped spectral acceleration at period of (b) 1 second and (c) 2 seconds (Modified from USGS 2014)

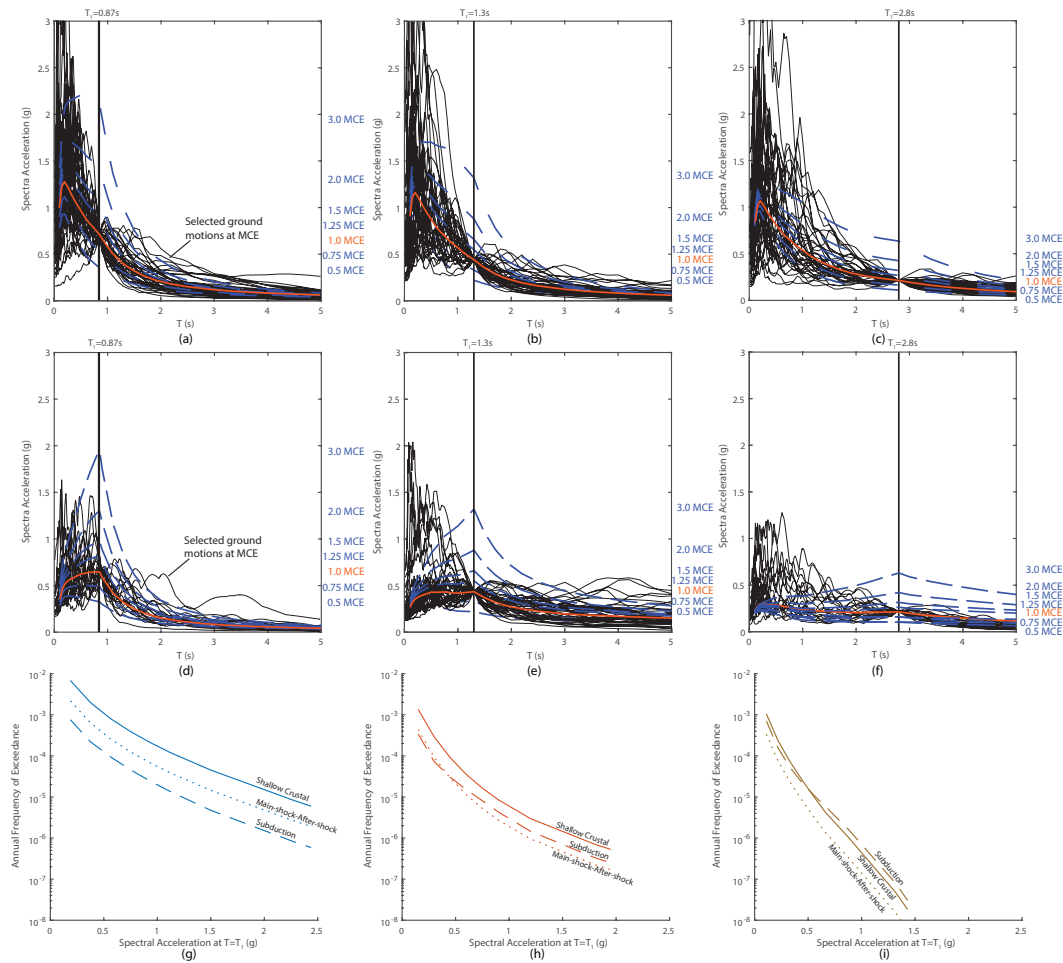


Figure 2.5: Shallow crustal hazard conditional mean spectra for (a) three-story frame, (be) six-story frame and (c) 12-story frame, Subduction hazard conditional mean spectra for (d) three-story frame, (e) six-story frame and (f) 12-story frame, and Hazard curves for (g) three-story frame, (h) six-story frame and (i) 12-story frame

The second seismic hazard type represents a main-shock-after-shock (MS-AS) series of shallow crustal earthquakes. Two different shallow crustal ground motions were selected and scaled to represent a sequence of MS-AS events. The set of main-shock motions consisted of the same shallow crustal motions selected as described above. For each main-shock, the after-shock motion was selected using the targeted main-shock procedure (TG MS MS)

outlined in Shokrabadi et al. (2018), Goda (2012) and Hatzigeorgiou and Beskos (2009), which selects the after-shock ground motion to be a single magnitude unit lower than the main-shock and at an opposing rupture distance. Each after-shock record was selected and scaled to match a new conditional spectrum having the specific after-shock ground motion characteristics and a target first-mode spectral acceleration that was reduced from the initial main-shock target acceleration by the amount calculated due to the change in magnitude according to the Boore and Atkinson (2008) attenuation model. Full details regarding this process and a complete listing of the selected ground motions are provided in Appendix B.

The third seismic hazard type identified for this site was subduction earthquakes, as shown in the deaggregation plots in Figure 2.4 and caused by the location of the frames within 90 km of the Cascadia fault (USGS 2014). The subduction ground motions were selected from the K-NET database (Fujiwara et al. 2004) because it had a higher prevalence of records originating from subduction motions when compared to the NGA-West2 database (PEER 2013). The selected subduction ground motions were scaled to a conditional spectrum with different characteristics, having magnitudes between 8.5 and 9.5, distances of 85 to 150 km (USGS 2014), and ϵ values of 1.07 to 1.80. Each subduction record had a 90% Arias intensity duration longer than 120 seconds. The individual spectra of the 40 subduction ground motions scaled to MCE for the three, six and 12-story frames are shown in Figure 2.5 (d), (e) and (f), respectively. The median spectra for intensity stripes varying from $0.5 \times \text{MCE}$ to $3.0 \times \text{MCE}$ are also shown in each figure.

Frequency intensity curves for the three hazard types are shown in Figure 2.5 (g) for the period of the three-story building, (h) for the six-story building,

and (i) for the 12-story building, where the frequency values for both fault types were obtained from the deaggregation information provided by the USGS (2014) and the values for the frequency of after-shocks was obtained using a combination of Båth’s and Omori’s laws (Reasenberg and Jones 1989, Utsu and Ogata 1995). Further details are available in Appendix B.

2.4.2 EDPs and Performance Objectives

The first of the three EDPs considered was the maximum inter-story drift, with values of 5.0% for collapse prevention (S-5), 2.5% for life safety (S-3) and 0.5% for immediate occupancy (S-1). The second EDP considered was the residual inter-story drifts following the seismic event with limits of 2.5% for collapse prevention (S-5), 1% for life safety (S-3) and 0.1% for immediate occupancy (S-1). The limits for both drift-based EDPs were based on the guidance provided in Table C2-4 of ASCE-41 (ASCE 2017) and FEMA 356 (FEMA 2000b) with some adjustments such as a value of 0.1% used as “negligible”, and a value of 2.5% instead of 5% for the collapse prevention residual drift limit. The third EDP considered was the peak floor acceleration along the height of the frames, with limits set to 2g for hazards reduced (N-D), 0.75g for life safety (N-C) and 0.25g for position retention (N-B) (ASCE 2017). These acceleration values were determined based on the approximate locations of changes in slope of the story loss function for acceleration sensitive non-structural office components, as shown in Figure 2.6. These story loss functions were defined using component quantity, repair cost, and fragility data from an office occupancy type and specific floor area, as defined using the FEMA P-58 Normative Quantity Estimating Tool and

Loss Estimation methodology (FEMA 2012).

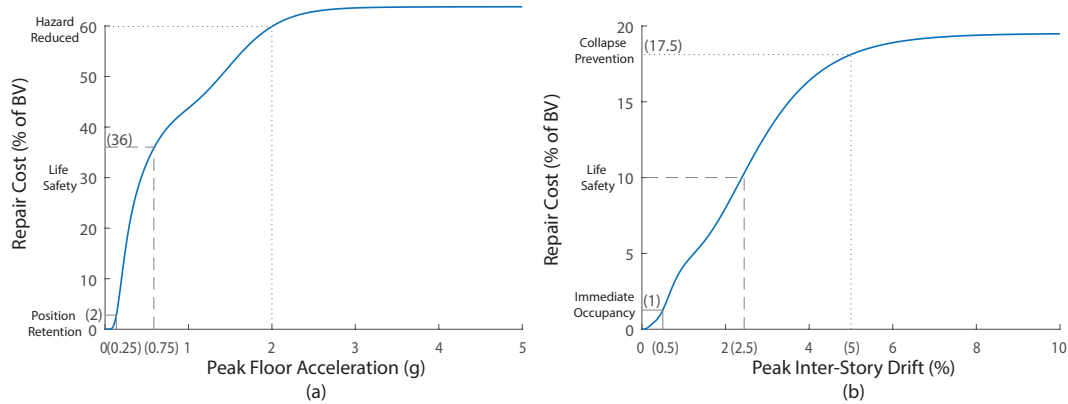


Figure 2.6: Non-Structural component story loss functions for office archetype for (a) acceleration sensitive and (b) drift sensitive components

2.5 Results and Discussion

2.5.1 Maximum Inter-story Drifts

For each frame, Figure 2.7 shows fragility curves indicating the probability of exceeding the maximum inter-story drift limits associated with the collapse performance objective, defined above, as functions of the ground motion intensities for the three seismic hazard types. The maximum inter-story drifts during shallow-crustal ground motions for the three-story frames are shown in the top left plot in Figure 2.7. In this figure, the PRENORTH frame has a 20% reduction in median collapse intensity when compared to the code-compliant RBS frame, while the SHJ and SCSHJ frames have a 7% and 10% increase in median collapse intensity, respectively. The poor performance of the PRENORTH frame is a result of the lower rotational capacity of the connections when compared to the frame incorporating RBS connections, inducing fracture and leading to a loss of stiffness of the frame,

ultimately causing large inter-story drifts. In contrast, the frames with SHJ and SCSHJ connections provide more energy dissipation capacity by activating at smaller values of moment before the beam yields, and the low-damage connections increase the rotational capacity of the beam section before deterioration. This hierarchy of performance is consistent across all of the 27 response indices (see Section 2.3.0).

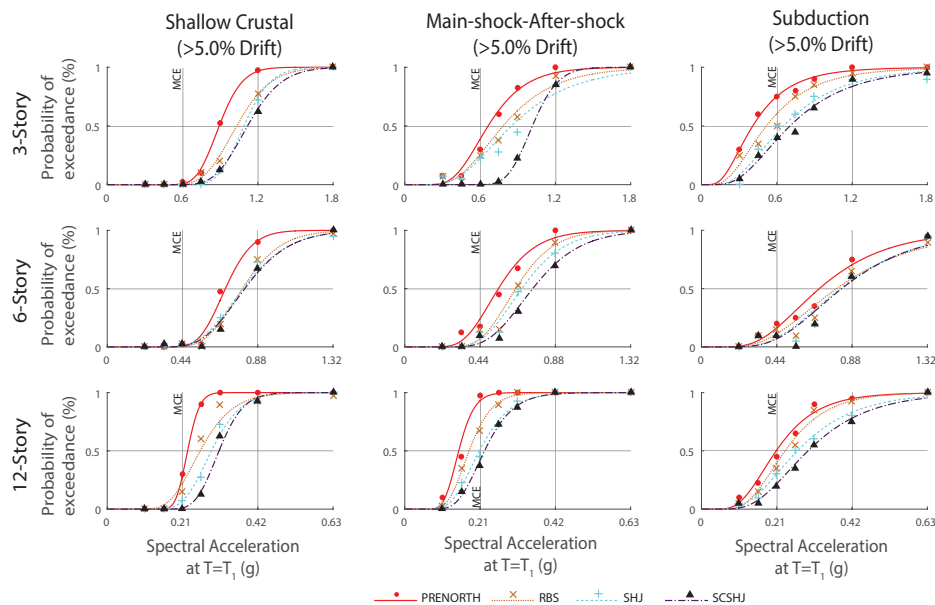


Figure 2.7: Fragility curves for maximum inter-story drifts associated with collapse prevention performance objective for all considered frame types, heights and seismic hazard types

For the taller frames, the difference in performance between connection types is similar, except that the improvement in median collapse intensity from the RBS to SHJ and SCSHJ connections is not as apparent with the six-story frame. This is because the majority of the inelastic action is concentrated at the first floor, previously identified as a soft-story (Hall 1995), especially with the reduced activation moment of the SHJ and SCSHJ connections relative to the RBS yield moment. Once the stiffness provided

by the SCSHJ connection decreases due to the intended friction mechanism, stronger components such as the panel zone and column hinges begin to yield, limiting the ability of the SCSHJ connection to re-center the frame. Larger differences in inter-story drift performance are observed for different seismic hazard types. For the main-shock-after-shock performance of the three-story frame, the frames incorporating RBS and SHJ connections exhibit respectively a median collapse intensity of only 13% and 17% higher than that of the PRENORTH frame. The frame with SCSHJ connections, however, shows an increase in median collapse intensity of approximately 50% compared to that of the PRENORTH frame. This performance improvement of the frames with SCSHJ connection is most apparent at lower intensities and for the shorter frames, where the inelastic action is limited to the low-damage self-centering mechanics and does not spread to the panel zones or column hinges. This allows the SCSHJ frames to undergo almost full re-centering at lower intensities before undergoing the second ground motion. A similar trend in performance differences is observed for the subduction hazard type, where the RBS frame has an 18% average increase in the median collapse intensity over the PRENORTH frame, while the SHJ and SCSHJ frames have 49% and 57% higher median collapse intensities, respectively. As the subduction motions have a duration that is three to four times longer than the shallow crustal motions, the avoidance of strength and stiffness degradation and the low-damage energy dissipation provided by the SHJ and SCSHJ connections provides more significant benefits over the PRENORTH and RBS connections.

2.5.2 Residual Inter-story Drifts

For each frame, Figure 2.8 shows the fragility curves indicating the probability of exceeding the residual inter-story drift limits associated with the life safety performance objective, defined above as 1.0%, as functions of the ground motion intensities for the three seismic hazard types. This performance objective is highlighted in the results as it is a traditional threshold value used when selecting building replacement instead of building repair (FEMA 2012). Considering the three-story frame during shallow crustal ground motions, the overall hierarchy of performance for this EDP is the same as for the maximum drift EDP, where the PRENORTH frame has the lowest median intensity, followed by the RBS and SHJ frames with increases in median intensities of 1.4% and 14%, respectively, and finally the SCSHJ frame with an increase in median collapse intensity of 34%. The SHJ connections are benefiting from the seismic shake-down effect, defined as the ability to partially re-center during the last cycles of the ground motion and free vibration of the frame, when compared to the PRENORTH connections as the SHJ connections have a slightly pinched hysteretic behavior, providing a lower unloading stiffness and increasing re-centering capability during the free vibration of the frames. The additional improvement in residual drifts of the frames incorporating the SCSHJ connections, over that of the frames with SHJ connections, is a result of the self-centering capability of the connections that directly reduces the residual drifts. The same trends across frame heights as observed for the maximum inter-story drift EDP were observed for the residual drifts, where large differences in performance are observed in the three and 12-story frames, while the six-story frame was

affected by a soft-story response. The other seismic hazard types resulted in generally poorer performance of the frames but no variation in the relative ranking in performance from one frame type to the others. The main-shock-after-shock sequence caused the SCSHJ frames to have a median intensity 17% higher than their RBS counterparts, while the frames incorporating SHJ connections had a gain in median intensity of less than 5% relative to the RBS frames for all heights. The subduction hazard led to much larger residual drifts, particularly in the shorter frames, and more variability (indicated by larger β values in the lognormal fragility curves). For this hazard type, the PRENORTH and RBS frames had median intensity values that were much closer to each other when compared to the other hazard types, particularly at the six- and 12-story frames. Overall, the SCSHJ frames still had the highest performance for this hazard type, surpassing the median intensity of the RBS frame by an average of 23%.

For each frame, Figure 2.8 shows the fragility curves indicating the probability of exceeding the residual inter-story drift limits associated with the collapse performance objective, defined above, as functions of the ground motion intensities for the three seismic hazard types. Considering the three-story frame during shallow crustal ground motions, the overall hierarchy of performance for this EDP is the same as for the maximum drift EDP, where the PRENORTH frame has the lowest median collapse intensity, followed by the RBS and SHJ frames with increases in median collapse intensities of 36% and 44%, respectively, and finally the SCSHJ frame with an increase in median collapse intensity of 68%. The RBS and SHJ connections are benefiting from the seismic shake-down effect, defined as the ability to partially re-center during the last cycles of the ground motion and

free vibration of the frame, when compared to the PRENORTH connections. The RBS connections, with a higher ductility capacity, allow a further decrease in unloading force and stiffness before fracture when compared to the PRENORTH connections, thereby increasing the probability that the frames can re-center during their free vibrations. Similarly the SHJ connections have a slightly pinched hysteretic behavior, providing a lower unloading stiffness and increasing re-centering capability during the free vibration of the frames. The additional increase in performance of the frames incorporating the SCSHJ connections, over that of the frames with SHJ connections, is a result of the self-centering capability of the connections that directly reduces the residual drifts.

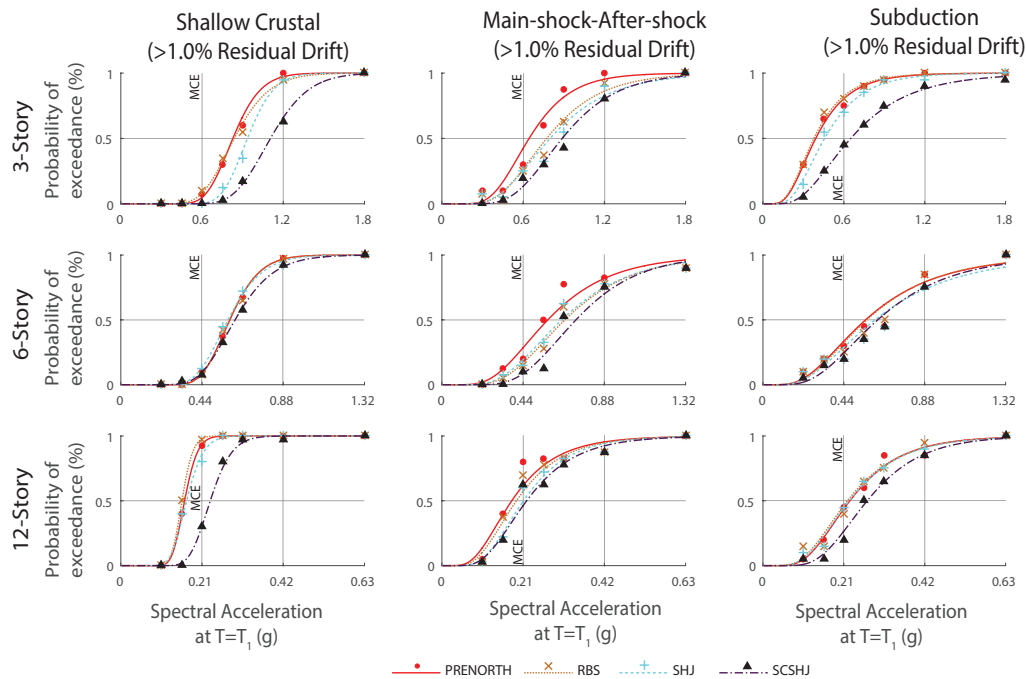


Figure 2.8: Fragility curves for residual inter-story drifts associated with life safety performance objective for all considered frame types, heights and seismic hazard types

The same trends across frame heights as observed for the maximum inter-story drift EDP were observed for the residual drifts, where large differences in performance are observed in the three and 12-story frames, while the six-story frame was affected by a soft-story response as described previously. The other seismic hazard types resulted in generally poorer performance of the frames but no variation in the relative ranking in performance from one frame type to the others. The main-shock-after-shock caused the SCSHJ frames to maintain median collapse intensities approximately 30% higher than their RBS counterparts, while the frames incorporating SHJ connections had a gain in median collapse intensity of less than 10% relative to the RBS frames for all heights. The subduction hazard led to much larger residual drifts, particularly in the shorter frames, and more variability (defined by larger β values in the lognormal fragility curves). For this hazard type, the PRENORTH and RBS frames had median collapse intensity values that were much closer to each other when compared to the other hazard types, particularly at the six- and 12-story frames. Overall, the SCSHJ frames still had the highest performance for this hazard type, surpassing the median collapse intensity of the RBS frame by an average of 32%.

2.5.3 Peak Floor Accelerations

For each frame, Figure 2.9 shows the fragility curves indicating the probability of exceeding the peak floor acceleration limits associated with the life safety performance objective, defined above as 0.75g, as functions of the ground motion intensities for the three seismic hazard types. Since the elastic properties were approximately identical for all connection types in a given

frame, the differences in floor accelerations are attributed to the differences in yield/activation moment and the non-linear behavior of the connections. The same hierarchy of performance is observed in Figure 2.9 as for the structural EDPs in Figures 2.7 and 2.8, where the frames incorporating the PRENORTH have the worst performance, followed by the RBS, then SHJ, and finally the SCSHJ frames. Considering the shallow crustal hazard type across the frame heights, some differences in trends are observed when compared to the previous two structural EDPs: the six- and 12-story SCSHJ frames have increases of 33% and 40% in median intensity relative to the PRENORTH connections, respectively, while the shorter three-story frame median intensity only increased by 6%. For the other hazard types, the results are generally similar but with the response of the frames with RBS or SHJ connections being even closer to the response of the PRENORTH frames in most cases. The frames with SCSHJ connections continue to have the best performance for all considered combinations of frames and hazard types.

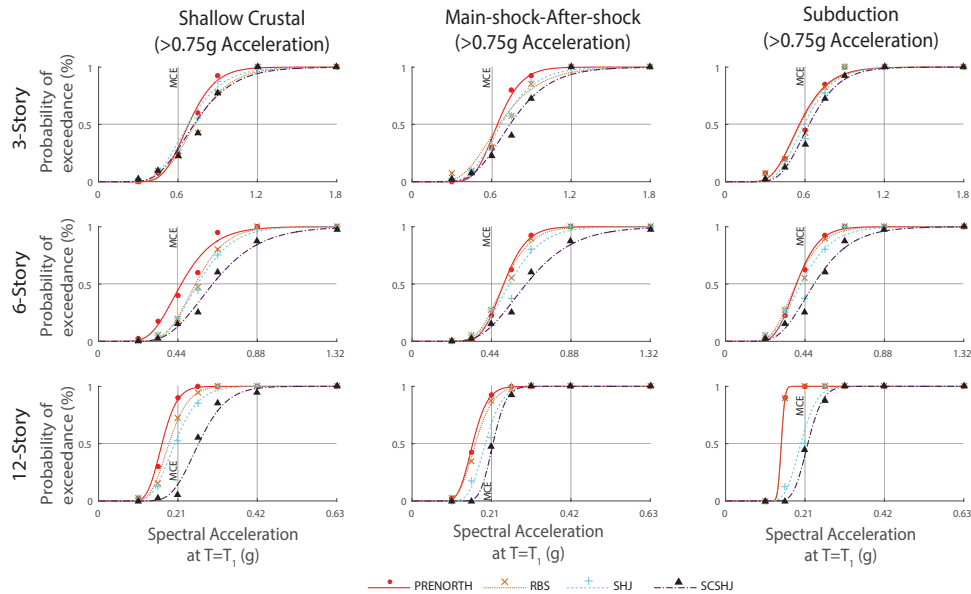


Figure 2.9: Fragility curves for peak floor accelerations associated with life safety performance objective for all considered frame types, heights and seismic hazard types

2.5.4 Comparisons of Response Index Performance Improvements

Radar plots showing the median capacities obtained for all 27 response indices are shown in Figure 2.10, where the median intensity from each probability of exceedance curve for each index is identified on radial scales with markers identifying three different ground motion intensities: design earthquake (DE), maximum considered earthquake (MCE), and $2 \times \text{MCE}$. A larger perimeter indicates that a frame has higher median capacities across all the different response indices.

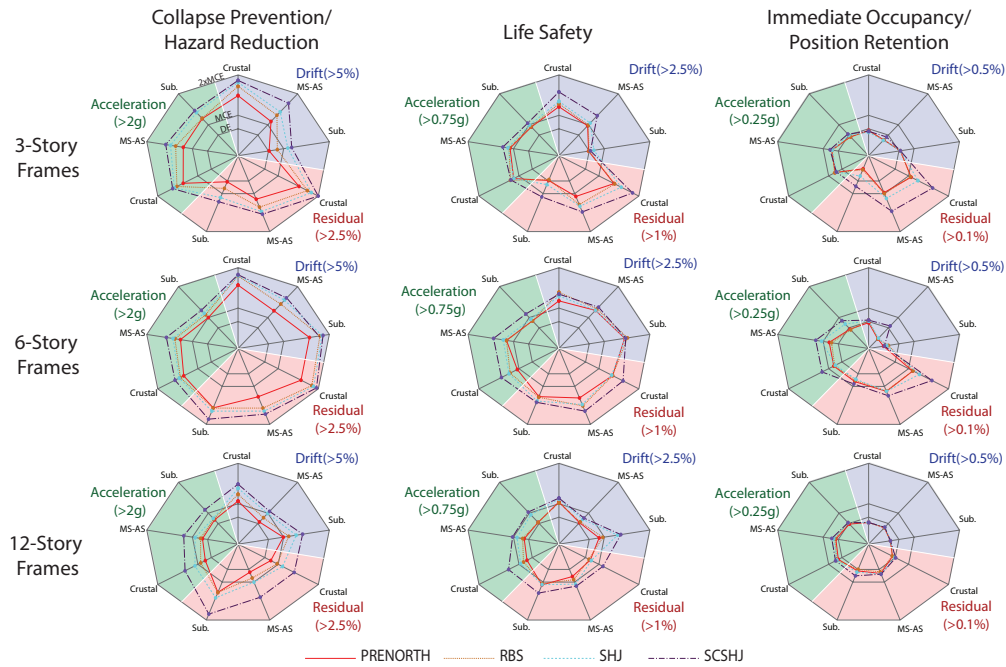


Figure 2.10: Radar plots of median intensities for all response indices of all three frames

As expected, the RBS frames either equaled or exceeded the performance of the PRENORTH frames throughout all of the response indices. For all three hazard types and frame heights, the differences are largest for the collapse prevention/hazard reduction performance objectives and for the maximum inter-story drift EDP. The frames incorporating SHJ connections exhibited performance that closely resembled that of the RBS frames. The most significant gains when using the SHJ connections rather than RBS connections are apparent in the acceleration EDP for all hazard types because of the lower activation loads. Even though the performance improvements are minimal for the other EDPs when using SHJ connections instead of RBS connections, the energy dissipation mechanism used to obtain this similar performance is mostly low-damage friction instead of plastic yielding. The frames using SCSHJ connections have the highest median

intensity values across all 27 response indices, with the largest gains observed for the residual displacement and acceleration EDPs at all performance objectives, and are generally more apparent for the main-shock after-shock and subduction hazard type ground motions because of their longer durations relative to the shallow crustal ground motions. The gains in performance are independent of frame height but are impacted by vertical irregularities such as soft stories. Furthermore, the frames using SCSHJ connections obtain the most well-balanced performance among the response indices at the collapse prevention/hazard reduction and life safety performance objectives. An example of this balance in performance is the six-story frame with SCSHJ connections at the life safety performance level, where each response index has a median capacity of approximately $1.5 \times \text{MCE}$. However, while the frames using SCSHJ connections still maintain the highest level of performance at the immediate occupancy/position retention performance objectives, they demonstrate a poorly balanced performance in the three- and six-story frames. For both of these frames, the residual inter-story drift EDP has median capacities that are more than twice the median capacity for the maximum drifts, indicating that the frames do not fully utilize their capacities to reduce residual inter-story drifts before exceeding the other targets of these performance objectives for either maximum inter-story drifts or peak floor accelerations.

2.5.5 Loss Analysis

Finally, annual frequency of exceedance of loss curves for each hazard type are shown in Figure 2.11 for all three heights and include the expected

annual loss (EAL) for each frame. These are determined by considering each performance level of each EDP as sequential and exclusive damage states with consequence costs determined from the story loss functions (Figure 2.6) for the peak floor acceleration and maximum inter-story drift EDPs. In addition, for the collapse prevention performance level of the drift EDP and the life safety performance level of the residual drift EDP, the consequence cost consisted of a building replacement with a cost of 100% of the building value (BV). Other residual drifts were not associated with consequence costs, as the associated losses were already considered through the maximum inter-drift and peak floor acceleration EDPs. The hazard return periods were obtained from the frequency-intensity curves shown in Figure 2.5.

These frequency-loss curves indicate the same performance hierarchy across the connection types as was previously identified. Most notable, the value of using SCSHJ connections is indicated by the reduction in annual frequency of exceeding the full range of losses. The reduction in the frequency of exceeding relatively large losses is mostly caused by the reduction in residual drifts that lead to building replacement, while reductions in annual frequency of exceedance of losses less than 50% of BV are mostly attributed to the increase in median ground motion intensities required to exceed a given peak floor acceleration, both of which are shown in Figure 2.11. Overall, the economic benefits provided by the SCSHJ connections are greatest in taller structures and/or during longer duration hazards.

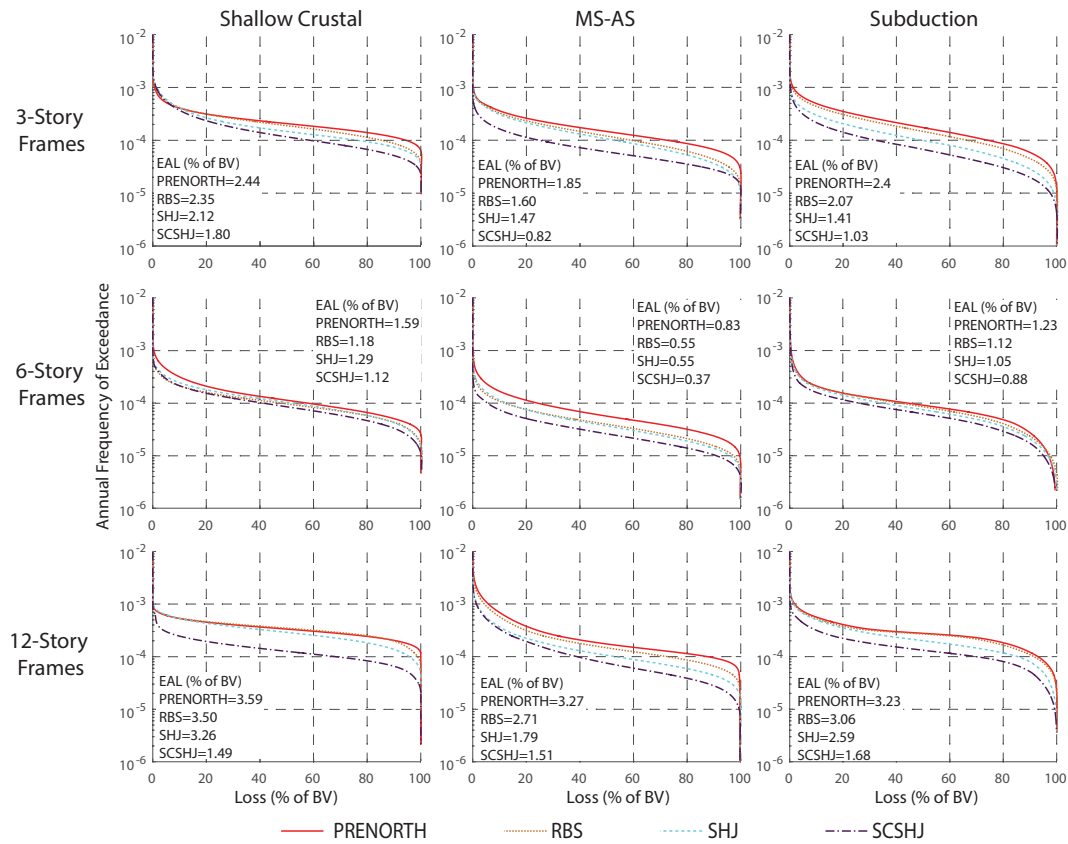


Figure 2.11: Loss Curves for each structure for each hazard

2.6 Conclusions

This paper began by calibrating hysteretic models for two newly developed low-damage connections, the sliding hinge joint (SHJ) and the self-centering sliding hinge joint (SCSHJ). For comparison, existing hysteretic models were calibrated for a pre-Northridge (PRENORTH) connection and for a pre-qualified reduced beam section (RBS) connection. These hysteretic models were used to determine the influence of each of these connections on the global performance of three-, six-, and 12-story moment resisting frames for 27 different response indices. The response indices consisted of three different engineering demand parameters for three seismic hazard types at

three different performance objectives for all three frame heights. The system level performance of the frames using SHJ and SCSHJ connections was compared to that of frames using the PRENORTH and RBS connections across all response indices. The PRENORTH frames exhibited the worst performance across all 27 response indices, while the frames using RBS connections had higher median capacities. The median capacities of the frames using SHJ connections were only marginally better than those of the frames using RBS connections, but the friction energy dissipation mechanism in the SHJ connection means that the level of yielding damage in the SHJ frames would be less than for the RBS frames, even with similar response indices. The frames using SCSHJ connections had the highest overall performance across all frame heights, performance objectives and response indices, but experienced unequal performance improvement across the different response indices, having the greatest gains for residual inter-story drift and peak floor acceleration EDPs. Finally, larger gains in performance for the frames using SHJ and SCSHJ connections were observed when considering seismic hazard types with longer durations, as these connections dissipated energy using low-damage mechanisms that had less cyclic degradation. The impact of these connections on the expected losses associated with using these frames was similarly largest in taller structures and under longer duration or sequential ground motions, indicating that hazard types should be considered when considering these low-damage and high performing connections. The numerical results obtained herein illustrate the importance of considering multiple EDPs and seismic hazard scenarios when evaluating the potential advantages of using high-performance seismic force-resisting systems, such as steel MRFs with SCSHJ connections, as the

largest improvements in performance were for indices other than the maximum inter-story drifts during shallow crustal motions. While this study focused on the implementation of high-performing connections at all moment resisting connections in the structure, an opportunity to achieve the same increases in global frame performance while only installing these connections at a subset of locations could increase the efficiency of the implementation of high-performance connections. Further work should validate these global performance trends in other frame configurations, which should include irregularities, various heights and section sizes. The comparisons of performance for different hazard types and EDPs should also be extended to other high-performance systems to allow for a more complete understanding of the benefits of such systems. Finally, more laboratory testing to failure is recommended for the SHJ and SCSHJ connections to better quantify the behavior of these connections at large rotations.

2.7 Acknowledgments

The authors would like to acknowledge the assistance of Dr. Charles Clifton, Dr. Greg MacRae and Dr. Hsen-Han Khoo for providing component test data for the SHJ and SCSHJ connections used in this paper. The authors would also like to acknowledge the National Science and Engineering Research Council (NSERC) for funding this research.

2.8 References

- AISC, (2016). “Prequalified Connections for Special and Intermediate Steel Moment Frames for Seismic Applications.” *American Institute of Steel Construction 358-16*, Chicago, IL, US.
- ASCE, (2016). “Minimum Design Loads and Associated Criteria for Buildings and Other Buildings.” *American Society of Civil Engineers 7-16*, Reston, VA, US.
- ASCE, (2017). “Seismic Evaluation and Retrofit of Existing Buildings.” *American Society of Civil Engineers 41-17*, Reston, VA, US.
- Arias, A., (1970). “A measure of earthquake intensity.” *Seismic design for nuclear power plants*, MIT Press, Cambridge MA, 438-483.
- ATC, (2010). “ATC-72-1: Modeling and acceptance criteria for seismic design and analysis of tall buildings” *Applied Technology Council/Pacific Earthquake Engineering Research Center Report No. 72-1*, Richmond, CA, US.
- Baker, J. W., (2015). “Efficient analytical fragility function fitting using dynamic structural analysis.” *Earthquake Spectra*, 31(1), 579–599.
- Baker, J. W., and Lee, C., (2017). “An Improved Algorithm for Selecting Ground Motions to Match a Conditional Spectrum.” *Journal of Earthquake Engineering*, 22 (4), 708-723.
- Boore, D. and Atkinson, G., (2008). “Ground-motion prediction equations for the average horizontal component of PGA, PGV, and 5%-damped PSA

at spectral periods between 0.01s and 10.0s” *Earthquake Spectra*, 24 (1), 99-138.

Charney, F. and Pathak, R., (2008). “Sources of elastic deformation in steel frame and framed-tube structures: Part 1: Simplified subassemblage models.” *Journal of Constructional Steel Research*, 64(1), 87–100.

Christopoulos, C., Filiatrault, A., Uang, C.-M., and Folz, B., (2002). “Posttensioned Energy Dissipating Connections for Moment-Resisting Steel Frames.” *Journal of Structural Engineering*, 128(9), 1111–1120.

Clifton, G.C., (2005). “Semi-Rigid Joints For Moment-Resisting Steel Framed Seismic-Resisting Systems.” *Doctoral Dissertation, Department of Civil and Environmental Engineering*, University of Auckland, New Zealand.

Dimopoulos, A., Tzimas, A., Karavasilis, T., and Vamvatsikos, D., (2016). “Probabilistic Economic Seismic Loss Estimation in Steel Buildings Using Post-Tensioned Moment-Resisting Frames and Viscous Dampers” *Earthquake Engineering and Structural Dynamics*, 45 (11)

Engelhardt, M. D. and Sabol, T. A., (1994). “Testing of welded steel moment connections in response to the Northridge earthquake.” *AISC Northridge Steel Update*.

Erochko, J., Christopoulos, C., Tremblay, R., and Choi, H., (2011). “Residual Drift Response of SMRFs and BRB Frames in Steel Buildings Designed according to ASCE 7-05.” *Journal of Structural Engineering*, 137(5), 589–599.

Erochko, J., (2013). *Improvements to the Design of Use of Post-Tensioned*

Self-Centering Energy-Dissipative (SCED) Braces, University of Toronto, Canada.

FEMA, (Federal Emergency Management Agency). (2000a). “Recommended Seismic Design Criteria for New Steel Moment-Frame Buildings.” *Federal Emergency Management Agency Report 350*, Washington, D.C.

FEMA, (Federal Emergency Management Agency). (2000b). “Prestandard and Commentary for the Seismic Rehabilitation of Buildings.” *Federal Emergency Management Agency Report 356*, Washington, D.C.

FEMA, (Federal Emergency Management Agency). (2012). “Seismic Performance Assessment of Buildings.” *Federal Emergency Management Agency Report P-58*, Washington, D.C.

Filiatrault, A., Tremblay, R. and Kar, R., 2000. “Performance Evaluation of Friction Spring Seismic Damper”, *Journal of Structural Engineering*, 126(4), 491-499.

Filippou, F. C. and Popov, E. P., (1983). “Effects of Bond Deterioration on Hysteretic Behaviour of Reinforced Concrete Joints.” *Earthquake Engineering Research Center Report EERC 83-19*, University of California, Berkeley, CA, US.

Fujiwara, H., Aoi, S., Kunugi, T., and Adachi, S., (2004). “Strong-motion observation networks of NIED: K-NET and KIK-net,” *Cosmos Report*, National Research Institute for Earth Science and Disaster Prevention, Japan.

Gledhill, S., Sidwell, G., and Bell D., (2008). “The Damage Avoidance

Design of Tall Steel Frame Buildings – Fairlie Terrace Student Accommodation Project, Victoria University of Wellington” *New Zealand Society for Earthquake Engineering Conference*, Wairakei, NZ

Goda, K., (2012). “Nonlinear response potential of Mainshock-Aftershock sequences from Japanese earthquakes” *Bulletin of the Seismological Society of America*, 102 (5), 2139-2156.

Gupta, A. and Krawinkler, H., (1999). “Seismic Demands for Performance Evaluation of Steel Moment Resisting Frame Structures.” *Stanford University Department of Civil and Environmental Engineering Report No. 132*, 1–379.

Hall, J., (1995) “Parameter Study of the Response of Moment -Resisting Steel Frame Buildings to Near-Source Ground Motions.” *SAC95-05: Parametric Analytical Investigation of Ground Motion and Structural Response, Northridge Earthquake of January 17, 1994*, Sacramento, CA, US.

Hatzigeorgiou, G. and Beskos, D., (2009). “Inelastic displacement ratios for SDOF structures subjected to repeated earthquakes” *Engineering Structures*, 31(11), 2744-2755.

Ibarra, L., and Krawinkler, H., (2005). “Global Collapse of Frame Structures under Seismic Excitations” *Pacific Earthquake Engineering Research Report No. 2005/06*, University of California, Berkeley, CA, US.

Ibarra, L., Medina, R., and Krawinkler, H., (2005). “Hysteretic Models That Incorporate Strength and Stiffness Deterioration” *Earthquake Engineering and Structural Dynamics*, 34, 1489-1511.

- Khoo, H.-H., Clifton, C., Butterworth, J., MacRae, G., Gledhill, S., and Sidwell, G., (2012). “Development of the self-centering Sliding Hinge Joint with friction ring springs.” *Journal of Constructional Steel Research*, 78, 201–211.
- Khoo, H. H., Clifton, C., Butterworth, J., and MacRae, G., (2013). “Experimental study of full-scale self-centering sliding hinge joint connections with friction ring springs.” *Journal of Earthquake Engineering*, 17(7), 972–977.
- Kim, T., Whittaker, A. S., Gilani, A. S. J., Bertero, V. V., and Takhirov, S. M., (2000). “Cover Plate and Flange-Plate Reinforced Steel Moment-Resisting Connections.” *Pacific Earthquake Engineering Research Center Report 2000/07*, University of California, Berkley, CA, US.
- Latour, M., Piluso, V., and Rizzano, G., (2015) “Free from Damage Beam-to-Column Joints: Testing and Design of DST Connections with Friction Pads” *Engineering Structures*, 85. 219-233.
- Lee, C.-H., Jeon, S.-W., Kim, J.-H., Kim, J.-H., and Uang, C.-M., (2004). “Effects of panel zone strength and beam web connection method on seismic performance of reduced beam section steel moment connections.” *Journal of Structural Engineering-Asce*, 131(12), 1854–1865.
- Lignos, D. and Al-Shawwa, N., (2013). *Web-Based Interactive Tools for Performance-Based Earthquake Engineering*. URL: <http://resslabtools.epfl.ch/steel/>.
- MacRae, G., Clifton, G., Mackinven, H., Mago, N., Butterworth, J. and Pampanin, S., (2010). “The Sliding Hinge Joint Moment Connection.”

Bulletin of the New Zealand Society for Earthquake Engineering, 43(3), 202-212.

Mander, T.J., Rodgers, G.W., Chase, J.G., Mander, J.B. and MacRae, G.A., (2009). “Damage avoidance design steel beam-column moment connection using high-force-to-volume dissipaters.” *University of Canterbury Research Repository*, 962.

McKenna, F., Fenves, G. L., and Scott, M., (2000). *Open System for Earthquake Engineering Simulation*. University of California, Berkeley, CA, US.

NIST, (2010). “Evaluation of the FEMA P-695 Methodology for Quantification of Building Seismic Performance Factors” *NEHRP Report GCR 10-917-8*, National institute of Standards and Technology, US Department of Commerce, Gaithersburg, MD.

PEER, (2013). “PEER NGA-West2 Database.” *Pacific Earthquake Engineering Research Center Report No. 2012/03*, Berkeley, CA, US.

Reasenberg, P., and Jones, L., (1989) “Earthquake Hazard After a Mainshock in California” *Science*, 243(4895), 1173-1176.

Ricles, J., Sause, R., Garlock, M. and Krawinkler, H., (2001). “Posttensioned Seismic-Resistant Connections for Steel Frames.” *Journal of Structural Engineering*, 127(2), 113–121.

Rojas, P., Ricles J. M., and Sause R., (2005). “Seismic Performance of Post-Tensioned Steel Moment Resisting Frames with Friction Dampers” *Journal of Structural Engineering*, 131 (4).

- Shokrabadi, M., Burton, H., and Stewart, J., (2018). “Impact of Sequential Ground Motion Pairing on Mainshock-Aftershock Structural Response and Collapse Performance Assessment” *Journal of Structural Engineering*, 144(10).
- Steneker, P., Wiebe, L., and Filiatrault, A., (2018). “A Comparison of Recently Developed Analytical Models for Steel Moment-Resisting Frame Connections” *CSCE Conference*, Fredericton, NB, Canada.
- Tait, J., Sidwell, G., and Finnega, J., (2013). “Case Study – Elevate Apartments – A Rocking 15 Storey Apartment Building” *Steel Innovations Conference*, Christchurch, NZ
- USGS, (2014). “Unified Hazard Tool” United States Geological Survey Dynamic v4.2.0 (Lat: 47.6, Long: -122.3, T: 1.0 Sec), URL: <https://earthquake.usgs.gov/hazards/interactive/>.
- Uriz, P, and Mahin, S., (2005). “Towards Earthquake Resistant Design of Concentrically Braced Steel-Frame Structures,” *Pacific Earthquake Engineering Research Center Report No. 2008/08*, Berkeley, CA, US.
- Utsu, T., and Ogata, Y., (1995) “The centenary of the Omori formula for a decay law of after-shock activity”, *textit Physics of the Earth*, 43 (1): 1–33
- Yeow, T., Orumiyehi, A., Sullivan, T., MacRae, G., Clifton, G., and Elwood, K., (2018) “Seismic Performance of Steel Friction Connections Considering Direct-Repair Costs” *Bulletin of Earthquake Engineering*, 16, 5963-5993.

Zareian, F., and Medina, R., (2010). “A practical method for proper modeling of structural damping in inelastic plane structural systems.” *Computers and Structures*, 88(1), 45-53.

Chapter 3

IDENTIFYING AND SELECTING CRITICAL CONNECTIONS FOR SEISMIC RESPONSE OF STEEL MOMENT RESISTING FRAMES

3.1 Abstract

This paper examines the differences in seismically induced deformation demands on beam-column connections in steel Moment Resisting Frames (MRFs), with the goal of identifying critical beam-to-column connections for which changes to their local hysteretic behavior result in a significant change in the global probability of collapse of the frame. First, collapse fragility curves are developed for three-, six- and 12-story MRFs using reduced beam section (RBS) connections, representing current practice. The maximum rotation demands on the beam-to-column connections at each floor are examined, and connections that undergo a high annual frequency of exceeding the rotation at which their strength begins to degrade are defined as critical to the global performance of the frame. Next, to confirm the definition of these connections as critical, collapse fragility curves are developed for a set of frames that have high-performance low-damage self-centering sliding hinge joint (SCSHJ) connections at only the locations

defined as critical, while having low-ductility pre-Northridge (PRENORTH) connections with lower rotational capacity at all other locations. Even with a limited number of connections with high ductility, these mixed connection frames surpass the performance of the frames with only RBS connections and achieve essentially the same system collapse performance as frames with SCSHJ connections at all locations. A simplified pushover analysis method for identifying critical connections is proposed and compared to the results obtained from the non-linear time history dynamic analyses. Finally, a process for selecting these critical connections is introduced, using a Direct Displacement-Based Design (DDBD) procedure to give a designer control over their locations. This paper is useful to both researchers and practitioners who seek to identify or select particular connections where increases in rotation capacity would have the greatest influence on the overall frame performance, whether for retrofit applications or to maximize the benefit of selectively applying emerging connection details that offer enhanced performance.

3.2 Introduction

Current seismic design provisions for moment resisting frames (MRFs) intend to provide energy dissipation through the formation of plastic hinges in the beams as they yield in flexure (AISC 2016a). These provisions have undergone significant revisions since the investigations following the 1994 Northridge earthquake. These investigations identified fractured connections among steel MRFs, highlighting both the lower than anticipated ductility capacity of MRF connections at the local component level and the unequal

distribution of seismic demands across floor levels at the global system level (Hall 1995). At the local component level, a research effort was undertaken following the Northridge earthquake to develop moment resisting connections that provided a dependable moment-rotation behavior by ensuring a larger minimum rotation at which strength degradation or failure occurs (Popov et al. 1998, FEMA 2000a), referred to as the strength degradation rotation (SDR). When detailing steel MRFs, designers may select among pre-qualified connections having undergone component tests (AISC 2016a) that have ensured that they can exceed a minimum SDR and undergo large amounts of plastic hinging, providing a reliable amount of hysteretic energy dissipation. However, this plastic hinging can also result in irrecoverable inelastic deformations in the beams, leading to significant residual displacements (Erochko et al. 2011). These residual displacements can cause large economic losses and significant delays in the operating capability of the structure (FEMA 2012). To mitigate this issue, several low-damage alternative connections have been proposed, including post-tensioned energy dissipating connections (Ricles et al. 2001, Christopoulos et al. 2002), connections using high-force-to-volume-dissipaters (Mander et al. 2009), and the sliding hinge joint (SHJ) and its self-centering (SCSHJ) variant (Clifton 2005 & Khoo et al. 2013). Each of these low-damage connections provides alternative energy dissipation capabilities but may require increases in detailing complexity when compared to pre-qualified yielding connections. The benefits of using low-damage connections, specifically the SHJ and SCSHJ connections, were demonstrated in previous research (Steneker et al. 2019) that compared the performance of frames using the SHJ, SCSHJ, the reduced beam section connection (RBS) or pre-Northridge (PRENORTH) connections. An average

gain of 20% in the collapse margin ratio (CMR) (FEMA 2009) was observed when shifting from the RBS to the SCSHJ frame. At the system level, current seismic design provisions assume the simultaneous formation of plastic hinges at each floor (Gupta and Krawinkler 1999), as illustrated in Figure 3.1 (a) for a six-story MRF, where a single set of local detailing requirements is normally used for all connections within a frame, as each floor is expected to contribute a similar amount to the overall system ductility. However, the post-Northridge investigations demonstrated that the majority of MRFs suffered fractures in less than 50% of their connections (Youssef et al. 1995). Although no clear pattern was identified for the story levels of fractured connections, it was observed that if a fractured connection was discovered during inspections, additional fractured connections at the same floor elevation were extremely likely (Li and Ellingwood 2008). These observations suggest that connections at some floor levels underwent larger rotational demands than others within the same frame, and that the rotational demands at different floors were not equal, as discussed by Gupta and Krawinkler (1999). An illustration of this behavior is shown in Figure 3.1 (b) for a six-story MRF. Thus, using a constant connection type at all levels of an MRF may lead to some inefficiency by applying a relatively uniform rotation capacity to a non-uniform rotational demand across the frame.

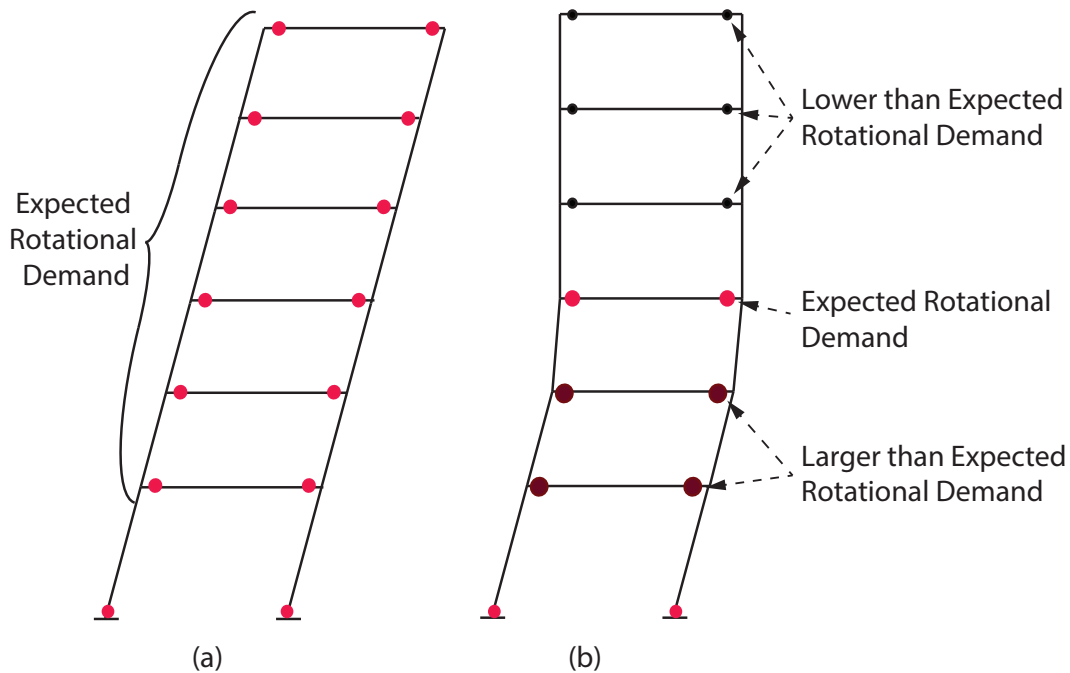


Figure 3.1: (a) Idealized deformation of six-story MRF, (b) Example of typical deformation of six-story MRF.

While the development of low-damage connections have provided designers with different ranges of connection ductility, energy dissipation mechanisms, and self-centering capability at the local level, no formal modifications to the system level design procedure have been proposed to benefit from the discrepancy in unequal rotation demands described above. This limits the opportunity to concentrate desirable but potentially more costly resources, such as low-damage connections, in areas with the greatest influence on performance. The identification of connections whose local component performance is critically linked to the global performance of the MRF would provide designers with such an opportunity. This paper proposes a method of identifying the location of critical connections in MRFs using a probabilistically based approach by defining a limit on the annual frequency of exceedance of rotations causing connection strength degradation, followed

by a simplified method of identifying these connections using static pushover analysis. Finally, a direct displacement-based design (DDBD) process is introduced to select the location of the critical connections by modifying the local connection hysteretic parameters. The systematic identification or selection of these critical connections would permit valuable detailing resources to be concentrated at the most critical connections, limiting implementation costs to specific floor levels while providing efficient performance benefits beyond minimum code requirements.

3.3 Definition of Critical Connections

The pre-qualification standards provided in AISC 341 (2016b), derived from the research summarized in FEMA 350 (2000a), specify a single target for pre-qualifying connections: a qualifying inter-story drift angle (QDA) of 4% before strength degradation or failure occurs. As mentioned in AISC 341 (2016b), the onset of strength degradation in the connection can increase rotation demands from P- Δ effects and increase frame instability, leading to collapse. A direct link is therefore formed between a connection rotation surpassing its SDR, the corresponding QDA, and unacceptable global performance of the frame. In this paper, to quantify the annual frequency of a connection exceeding its SDR, the maximum rotation of the connection is specified as an engineering demand parameter (*EDP*) of interest, and this rotation exceeding its SDR is specified as the damage measure (*DM*) of interest in the performance based earthquake engineering (PBEE) methodology (Miranda and Aslani 2003):

$$v(DV) = \int \int G(DM|EDP)G(EDP|IM)\lambda(IM) \quad (3.3.1)$$

where $\lambda(IM)$ represents the annual frequency of occurrence of ground motions measured using an intensity measure (IM), $G(EDP|IM)$ is the probability of exceeding a specific maximum connection rotation given a specific IM , and $G(DM|EDP)$ is the probability of exceeding a damage measure (DM) given a specific EDP . In this way, the frequency of a connection surpassing its SDR is expressed as an annual frequency of occurrence, allowing for a connection within a frame to be identified as critical when its annual frequency of exceeding its SDR value surpasses a limit. In this paper, the SDR limit is defined based on a 10% acceptable probability of collapse in an earthquake with a return period of 2475 years (FEMA 2009), resulting in a SDR annual frequency limit of 4×10^{-5} per year.

3.4 Application to Archetype Frames

3.4.1 Model Details

Three previously studied frames were selected as archetypes for this study, with three, six, and 12 stories, as shown in Figure 3.2. Each building was upgraded to satisfy ASCE 7-16 design requirements for the same location in Seattle, Washington on a site class B, which has spectral response parameters S_{MS} of 1.4g and S_{M1} of 0.6g (ASCE 2016). The building with three stories, based on a frame studied by Gupta and Krawinkler (1999), has an updated fundamental period of 0.87 seconds and a corresponding design spectral acceleration (S_D at $T = T_1$) of 0.46g; the building with six stories, based on a frame studied by Hall (1995), has an updated period of 1.3 seconds and a design spectral acceleration of 0.31g; the building with 12 stories, based on a frame described in NIST

(2010), has an updated fundamental period of 2.8 seconds and corresponding design spectral acceleration of 0.14g. Each building was initially designed with RBS connections and a verification was conducted to ensure that the use of the pre-Northridge or low-damage connection types would still satisfy the strong column/weak beam design principle at all locations. The seismic mass at each floor level for each frame is shown in Figure 3.2.

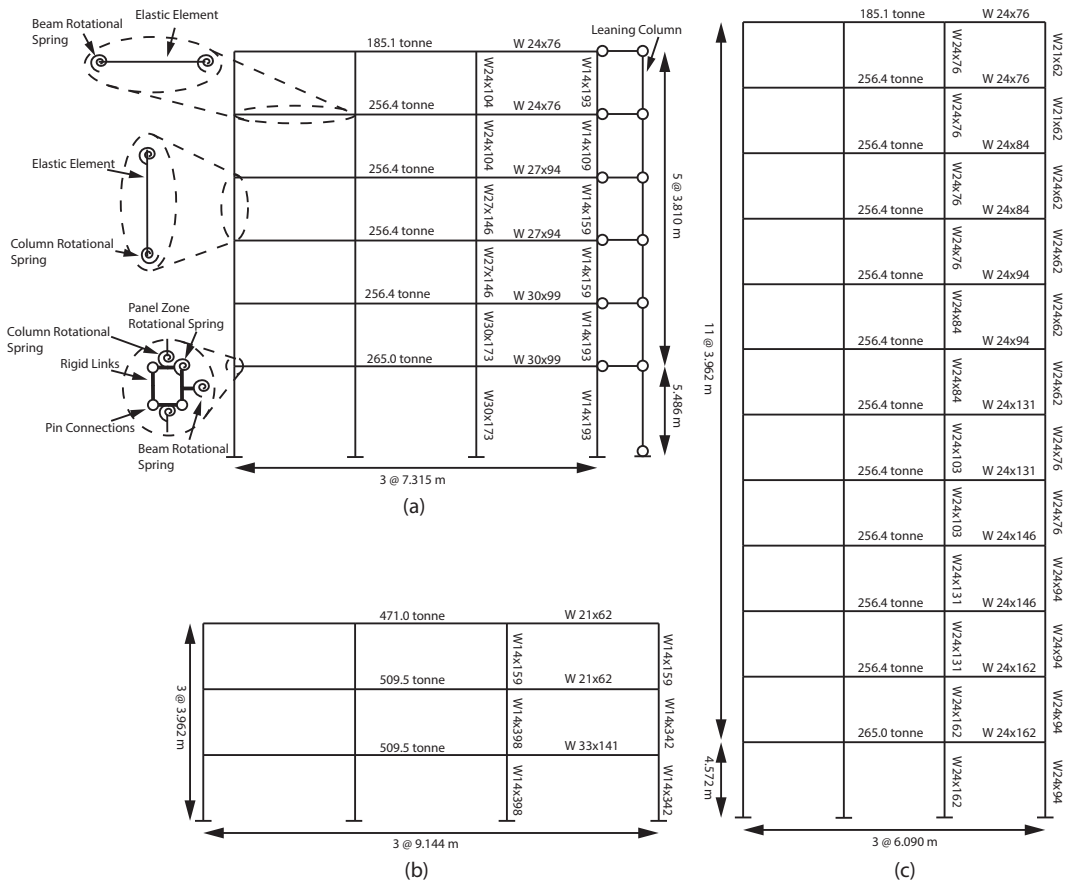


Figure 3.2: Frame layout of (a) 3 story building, (b) 6 story building with modeling detail and (c) 12-story building.

The frame models were assembled in OpenSees (McKenna et al. 2000) and consisted of elastic beam-column elements with concentrated rotational hinges at the ends. Each beam-to-column joint was modeled to capture panel

zone yielding using the Krawinkler spring box model (Gupta and Krawinkler 1999), as shown in Figure 3.2 (a), with a trilinear behaviour (Charney and Pathak 2008). For the PRENORTH and RBS connections, the beam and column hinges were modeled using the Ibarra-Medina-Krawlinker (IMK) model (Ibarra et al. 2005), calibrated to match the cyclic envelope curve of existing component test data, summarized in Table 3.1, as per the analytical modeling guidelines in ATC-72 (ATC 2010). The SCSHJ beam connections were modeled using existing material models and matched to the cyclic envelope curve of available component test data (Khoo et al. 2013), as described in Steneker et al. (2019). A comparison of the hysteretic behavior of a characteristic component test and a corresponding analytical model is shown for each connection type in Figure 3.3. The IMK properties for each beam depth size for both the PRENORTH and RBS connections are summarized in Table 3.2, using the same nomenclature as in ATC-72 (ATC 2010), while the model properties for all the SCSHJ connection models are summarized in Table 3.3. Since the axial forces in the column do not exceed 20% of their capacity, the same IMK properties were used in the column hinges as recommended in ATC-72 (ATC 2010). As the PRENORTH and RBS connection component tests did not include concrete floors, they were also not included in any beam rotational hinge behaviour. Rayleigh damping of 2% was applied to each frame in the first and second elastic modes. The Rayleigh damping was defined using a constant stiffness proportional component based on initial conditions. However, to avoid unrealistic and spurious damping forces, the stiffness proportional damping was applied using the approach described by Zareian and Medina (2010). The second order $P-\Delta$ effects were modeled with a pin-connected gravity column, shown

in Figure 3.2, carrying the loads within the frame’s lateral tributary area at each floor level.

Table 3.1: Component Test Sections Used for Connection Models

Modeled Connection	Componnet Test (Reference)		Location in Archetype Frames
	PRENORTH	RBS	
W33x141 & W14x398	W36X150 & W14X455 (Engelhardt and Sabol 1994)	W33x130 & W36x280 (Popov et al. 1997)	1st floor, three-story frame
W21x62 & W14x398	W21X44 & W14X176 (Tsai and Popov 1988)	W21x62 & W14x176 (Lee et al. 2004)	2nd floor, three-story frame
W21x62 & W14x159	W21X44 & W14X176 (Tsai and Popov 1988)	W21x62 & W14x176 (Lee et al. 2004)	3rd floor, three-story frame
W30x99 & W30x173	W30X99 & W14X176 (Choi et al. 2003)	W30x99 & W14x176 (Chi and Uang 2002)	1st and 2nd floors, six-story frame
W27x94 & W27x146	W24X68 & W14X120 (Choi et al. 2003)	W27x194 & W27x194 (Gilton and Uang 2002)	3rd and 4th floors, six-story frame
W24x76 & W24x104	W24X68 & W14X120 (Choi et al. 2003)	W24x62 & W14x176 (Gilton and Uang 2002)	5th and 6th floors, six-story frame
W24x162 & W24x162	W24X68 & W14X120 (Choi et al. 2003)	W24x62 & W14x176 (Gilton and Uang 2002)	1st and 2nd floors, 12-story frame
W24x146 & W24x131	W24X68 & W14X120 (Choi et al. 2003)	W24x62 & W14x176 (Gilton and Uang 2002)	3rd and 4th floors, 12-story frame
W24x131 & W24x103	W24X68 & W14X120 (Choi et al. 2003)	W24x62 & W14x176 (Gilton and Uang 2002)	5th and 6th floors, 12-story frame
W24x94 & W24x84	W24X68 & W14X120 (Choi et al. 2003)	W24x62 & W14x176 (Gilton and Uang 2002)	7th and 8th floors, 12-story frame
W24x84 & W24x76	W24X68 & W14X120 (Choi et al. 2003)	W24x62 & W14x176 (Gilton and Uang 2002)	9th and 10th floors, 12-story frame
W24x76 & W24x76	W24X68 & W14X120 (Choi et al. 2003)	W24x62 & W14x176 (Gilton and Uang 2002)	11th and 12th floors, 12-story frame

Table 3.2: Parameters of IMK Models to Match Cyclic Envelope Curves of Component Tests

IMK Parameters	W21		W24		W27		W30		W33	
	PRE-NORTH	RBS	PRE-NORTH	RBS	PRE-NORTH	RBS	PRE-NORTH	RBS	PRE-NORTH	RBS
Strain Hardening Ratio M_c/M_y	1.15	1.1	1.15	1.1	1.15	1.1	1.15	1.1	1.15	1.1
Pre-Capping Plastic Rotation (θ_p) (+ and -)	0.017	0.028	0.013	0.020	0.013	0.020	0.013	0.020	0.013	0.020
Post-Capping Rotation (θ_{pc}) (+ and -)	0.11	0.20	0.11	0.20	0.11	0.18	0.10	0.16	0.08	0.16
Ultimate Rotation (θ_u) (+ and -)	0.025	0.050	0.025	0.050	0.025	0.050	0.025	0.050	0.025	0.050
Cyclic Deterioration Ratio (D_r)	0.80	0.50	0.80	0.50	0.80	0.49	0.76	0.46	0.70	0.43

Table 3.3: Parameters of all SCSHJ models (From Chapter 2)

SCSHJ Parameters	W21, W24, W30, and W33
Analytical Models Used in Parallel	Self-Centering/Steel02/EPP (Elastic Perfectly Plastic)
Activation Moment (M_{AB})	$0.3M_y$
Dependable Moment (M_d)	$2.0 M_{AB}$
Second Dependable Moment (M_{d2})	$3.0 M_{AB}$
First Post-Activation Stiffness (α_1)	0.5
Second Post-Activation Stiffness (α_2)	0.004
Third Post-Activation Stiffness (α_3)	0.01
Self-Centering Ratio (λ_{SC})	0.05
Forward-Reverse Activation Ratio (β_{SC})	0.0001
Deformation at Final Stiffness (θ_{SC})	0.02

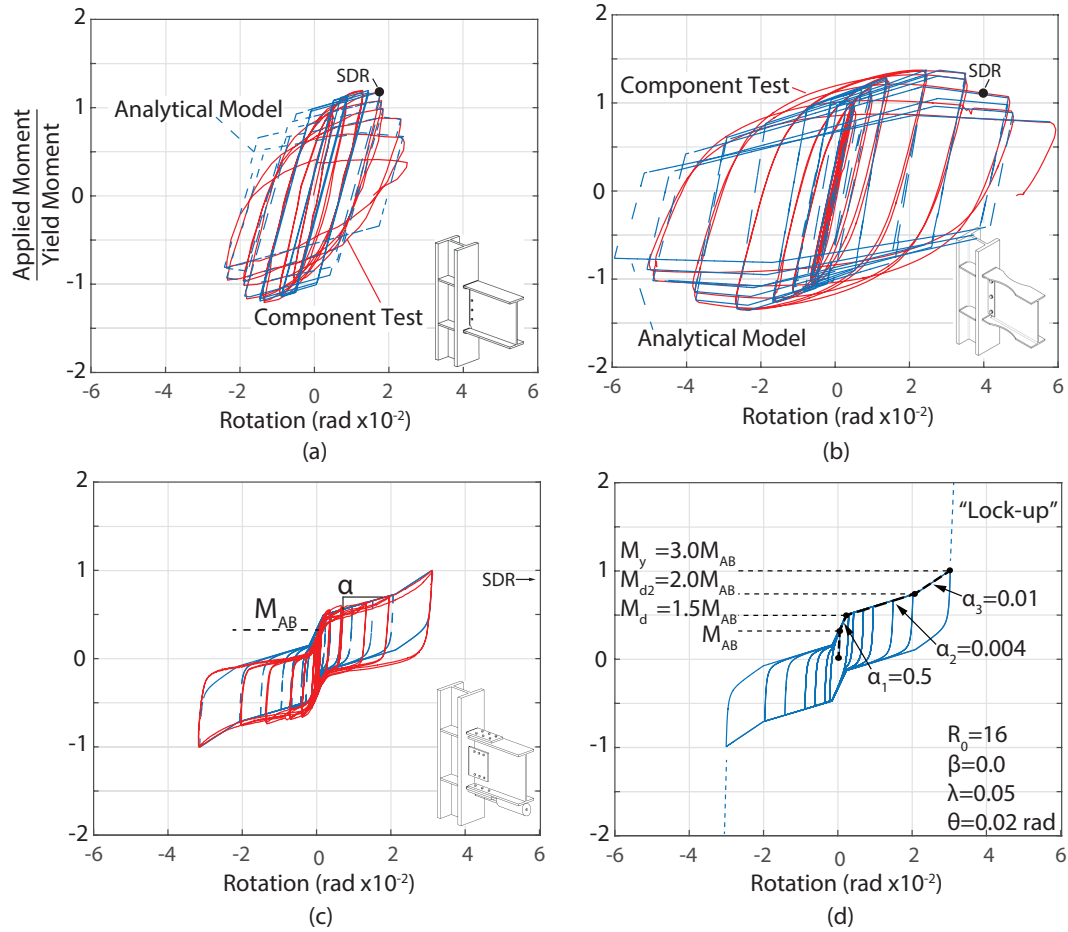


Figure 3.3: Analytical and experimental moment-rotation behavior for (a) PRENORTH (Choi et al. 2003), (b) RBS (Lee et al. 2004), (c) SCSHJ (Khoo et al. 2013); and (d) SCSHJ model parameters.

3.4.2 Seismic Intensity Measures

The three buildings were assessed based on non-linear time history analyses (NLTHA) at seven intensity stripes from 0.5 MCE_R to 3.0 MCE_R , where MCE_R is the risk-targeted maximum considered earthquake. At each intensity stripe, 40 ground motion components were selected (PEER 2013) to match values obtained from the USGS (2014) for magnitude (6-7), distance, ϵ values (where

ϵ is the number of standard deviations by which the observed ground motion's logarithmic spectral acceleration exceeds the target (Baker and Cornell 2005)), and a time-averaged shear-wave velocity to 30 m depth (V_{s30}) value of 760m/s. The ground motions were then scaled to match a conditional spectrum at the target spectral acceleration of the first-mode period for each frame (Baker and Lee 2017). The range of considered periods for matching was from 0.1 to 5 seconds. The median spectrum for each intensity stripe, as well as the spectrum for each of the 40 ground motion components for the MCE_R intensity, are shown in Figures 3.4 (a), (b) and (c) for the three-story, six-story, and 12-story frames, respectively. The corresponding hazard curve for each of the three building periods provides the annual frequency of exceedance for each of the seven intensity stripes, which are used to determine the annual frequency of occurrence in the (IM) portion of Equation 3.3.1.

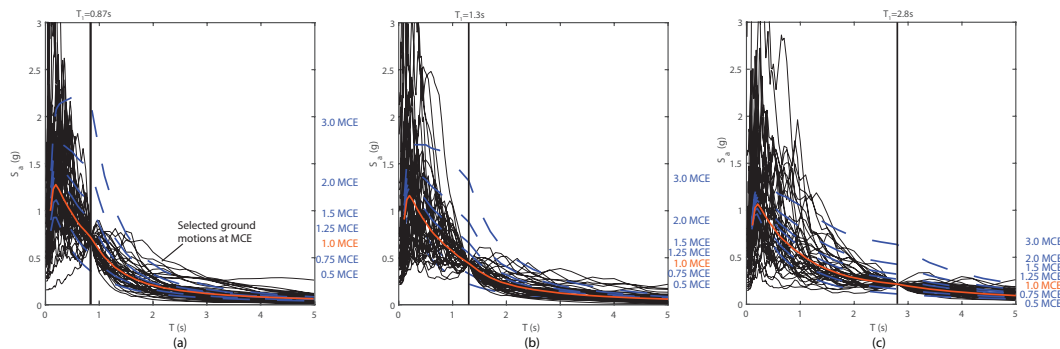


Figure 3.4: Conditional spectra for the first mode period of (a) three-story, (b) six-story and (c) 12-story frames. Ground motion spectra chosen for 1.0 MCE intensity are also shown.

3.4.3 Identification of Critical Connections in Archetype Frames

As noted in Figure 3.3, each of the three connection types considered has a different value of SDR. The PRENORTH connection is non-code compliant with an SDR value of 0.017 rad. The pre-qualified RBS connection (RBS) is code compliant with an SDR of 0.04 rad. The low-damage SCSHJ connection surpasses code minima for local component level ductility performance with an assumed SDR value of 0.06 rad when including the rotation of the adjacent beam section after the sliding mechanism has reached full stroke. These convert to inter-story drift ratios of 2.3%, 4%, and greater than 5% for frames incorporating PRENORTH, RBS and SCSHJ connections, respectively (FEMA 2000a). The initial analysis to identify the critical connections was conducted using the frames with only RBS connections, representing current design practice. Figure 3.5 shows the maximum connection rotations recorded at each floor of all three archetype frames during each of the 40 ground motions at each of the seven intensity stripes. These graphs are the visual representation of the $(EDP|IM)$ portion of Equation 3.3.1. The solid line in each plot indicates the median maximum connection rotation at each floor, while the two dashed lines indicate rotations of 0.017 rad and 0.04 rad, corresponding to the SDR of the PRENORTH and RBS connection, respectively. As the intensity of the ground motions increases, the three-story frame experiences the largest rotations at the third and then second floors because the first floor incorporates much heavier beam sections. The six-story frame experiences large rotations at the first, then second, then third and fourth floors, in

decreasing amounts. Finally, the 12-story frame has pronounced higher mode effects, particularly at intensities near MCE_R , where the largest rotations occur at the fifth, sixth, and seventh floors, with smaller rotations at the first, second and third floors. These graphs demonstrate that the rotation demand is not uniform for these three MRFs designs, and is not located at specific floor levels, but depends on design choices within each frame and on the earthquake intensity.

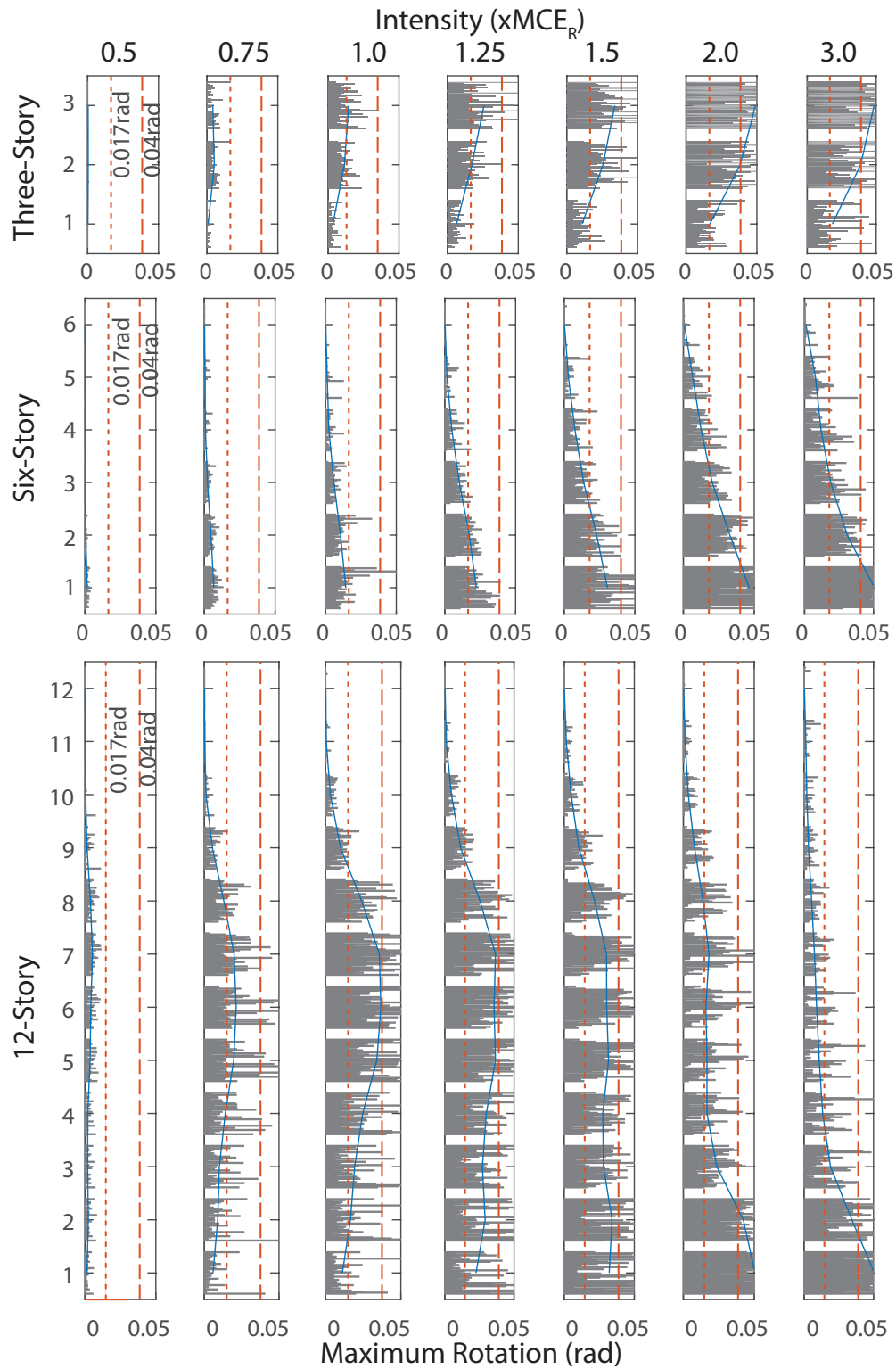


Figure 3.5: Maximum connection rotations for each ground motion at each floor of each archetype frame.

The annual frequency of connection rotations exceeding 0.017 rad at each floor of the three archetype frames as function of the ground motion intensities are shown in Figure 3.6. The value of 0.017 is used to determine which connections would benefit from an improvement in rotation capacity relative to a PRENORTH connection. The annual frequency of exceeding a rotation of 0.017 rad for each floor level in each frame is determined through integration with the site hazard curve using Equation 3.3.1 and results in a hierarchy of importance of the connections, summarized in Table 3.4. All floors with annual frequency of exceeding 0.017 rad larger than 4×10^{-5} are identified as critical, while the floors with annual frequency smaller than 4×10^{-5} are identified as non-critical. As described in Section 3.2, this annual frequency limit is selected as it corresponds to 10% of the annual frequency of exceedance of MCE_R ground motion intensities. Defined this way, the critical connections are located in all three floors in the three-story frame, the first three floors in the six-story frame, and the first eight floors in the 12-story frame. A second, less conservative limit on the annual frequency of exceedance was defined as 10×10^{-5} and used as a sensitivity analysis on the threshold for critical connections. This less conservative limit value was used because each of the three frames has connections with annual frequency of exceedance values between the two limits.

Table 3.4: Annual probability of connection exceeding 0.017 rad.

Floor number	Three-Story	Six-Story	12-Story
1	$4.33 \times 10^{-5*}$	$12.34 \times 10^{-5*,+}$	$8.00 \times 10^{-5*}$
2	$10.55 \times 10^{-5*,+}$	$7.88 \times 10^{-5*}$	$10.73 \times 10^{-5*,+}$
3	$13.01 \times 10^{-5*,+}$	$5.29 \times 10^{-5*}$	$13.73 \times 10^{-5*,+}$
4		0.88×10^{-5}	$15.48 \times 10^{-5*,+}$

Continued on the next page

Continued from previous page

Floor number	Three-Story	Six-Story	12-Story
5		0.21×10^{-5}	$21.96 \times 10^{-5*}, +$
6		0.00×10^{-5}	$23.71 \times 10^{-5*}, +$
7			$24.96 \times 10^{-5*}, +$
8			$14.73 \times 10^{-5*}, +$
9			$3.74 \times 10^{-5*}$
10			$0.00 \times 10^{-5*}$
11			$0.00 \times 10^{-5*}$
12			$0.00 \times 10^{-5*}$

*Critical connection identified using the 4×10^{-5} limit,
 + Critical connection identified using the 10×10^{-5} limit

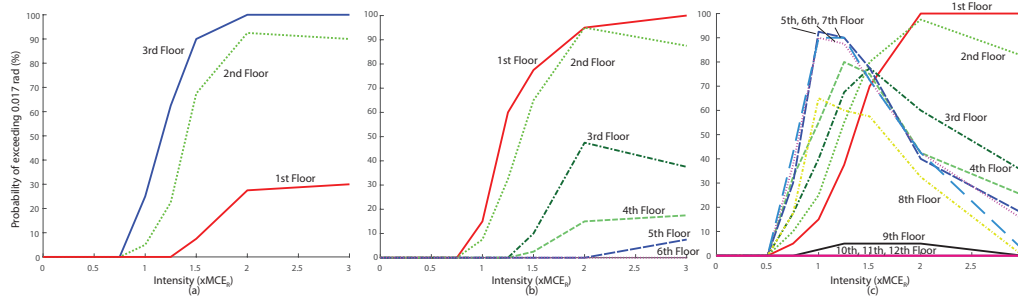


Figure 3.6: Probability of exceeding 0.017 rad rotation at each floor for (a) 3 story building, (b) 6 story building, and (c) 12-story building.

3.4.4 Collapse Analysis

To evaluate the effectiveness of the definition of critical connections as described above, a multiple stripe analysis (Baker 2015) of all three archetype frames was conducted using five connection configurations. Three connection configurations applied a single connection type throughout the whole frame: the PRENORTH connections to provide a lower-bound collapse performance, the RBS connection to provide the code compliant collapse performance, and the SCSHJ connection to provide an upper bound collapse performance. The

other two connection configurations consisted of mixed connections, using SCSHJ connections in locations defined as critical using either the $4 \times 10^{-5}/\text{yr}$ or $10 \times 10^{-5}/\text{yr}$ limit, while using PRENORTH connections in all other locations. For all frames, collapse was defined as an inter-storey drift exceeding 5% during the ground motion. The resulting collapse fragility curves for the five different connection configurations are shown in Figure 3.7 (a), (b) and (c) for the three-, six- and 12-story frames, respectively.

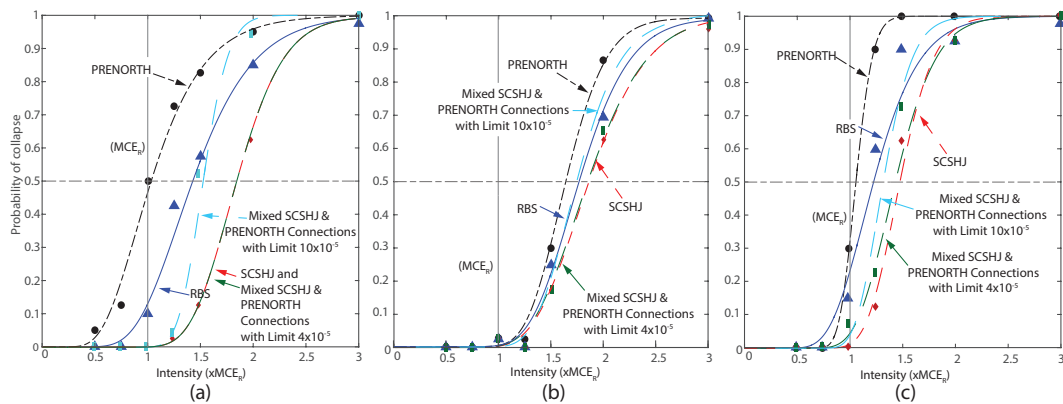


Figure 3.7: Collapse fragility curves for three-story, six-story, and 12-story frame for frames with PRENORTH, RBS, SCSHJ, and both mixed connections configurations.

Among the three single-type connection configurations, as expected, the frames using only SCSHJ connections had the highest collapse capacity, followed by the frames using only RBS connections, and finally the frames using only PRENORTH connections. For all three archetype frames, the improvement in CMR between the frames incorporating only PRENORTH and only SCSHJ connections is approximately twice as large as the improvement between the frame incorporating only PRENORTH and only RBS connections. For the mixed connection frames using SCSHJ connections only at critical locations and PRENORTH connections elsewhere, the critical

connections identified using the annual frequency of exceedance limit of 4×10^{-5} led to CMR values identical to the SCSHJ frames for the three-story frame (since all floors were identified as critical), 0.5% lower for the six-story frame, and 2.7% lower for the 12-story frame. Furthermore, these mixed connection frames exhibit a CMR 30% larger than the CMR for the three-story RBS frame, 5% larger for the six-story RBS frame, and 20% larger for the 12-story RBS frame. For the mixed connection frames using the less conservative critical connection selection criteria of $10 \times 10^{-5}/\text{yr}$, the CMR of the three-story mixed connection frame is 21% lower than that of the SCSHJ only frame, 6% lower for the six-story frame, and 13% lower for the 12-story frame. However, the mixed connection frames using the less conservative selection criteria still outperformed the frames using RBS connections at intensities less than $1.5 \times \text{MCE}_R$. These collapse analyses indicate that the presence of low ductility connections, such as the PRENORTH, does not necessarily lead to a frame having poor performance, as long as low damage connections with higher ductility, such as the SCSHJ connections, are located at all floor levels with a high annual frequency of exceeding the low ductility connection's SDR.

3.5 Identification of Critical Connections

Using Pushover Analysis

During preliminary design stages when multiple options may be considered, it may be desirable to identify the critical connections in a MRF without conducting the extensive NLTHA used in the previous section. A pushover

analysis method could be a good alternative for this purpose. While numerous pushover analysis methods and lateral loading patterns have been proposed to capture nonlinear behavior (e.g. Gupta and Krawinkler 1999, FEMA 2000b, Chopra 2012), two common methods in current literature are the standard inverted triangular force configuration and a configuration based on the classical modal combinations (Chopra 2012). The normalized force vectors obtained for both pushover methods are shown in Figure 3.8 (a) for the three archetype MRFs considered in this study. The pushover curves obtained from the force distributions are shown in Figure 3.8 (b), (c), and (d) for the three-, six-, and 12- story archetype frames, respectively. The maximum base shear value is also identified for all curves in these plots.

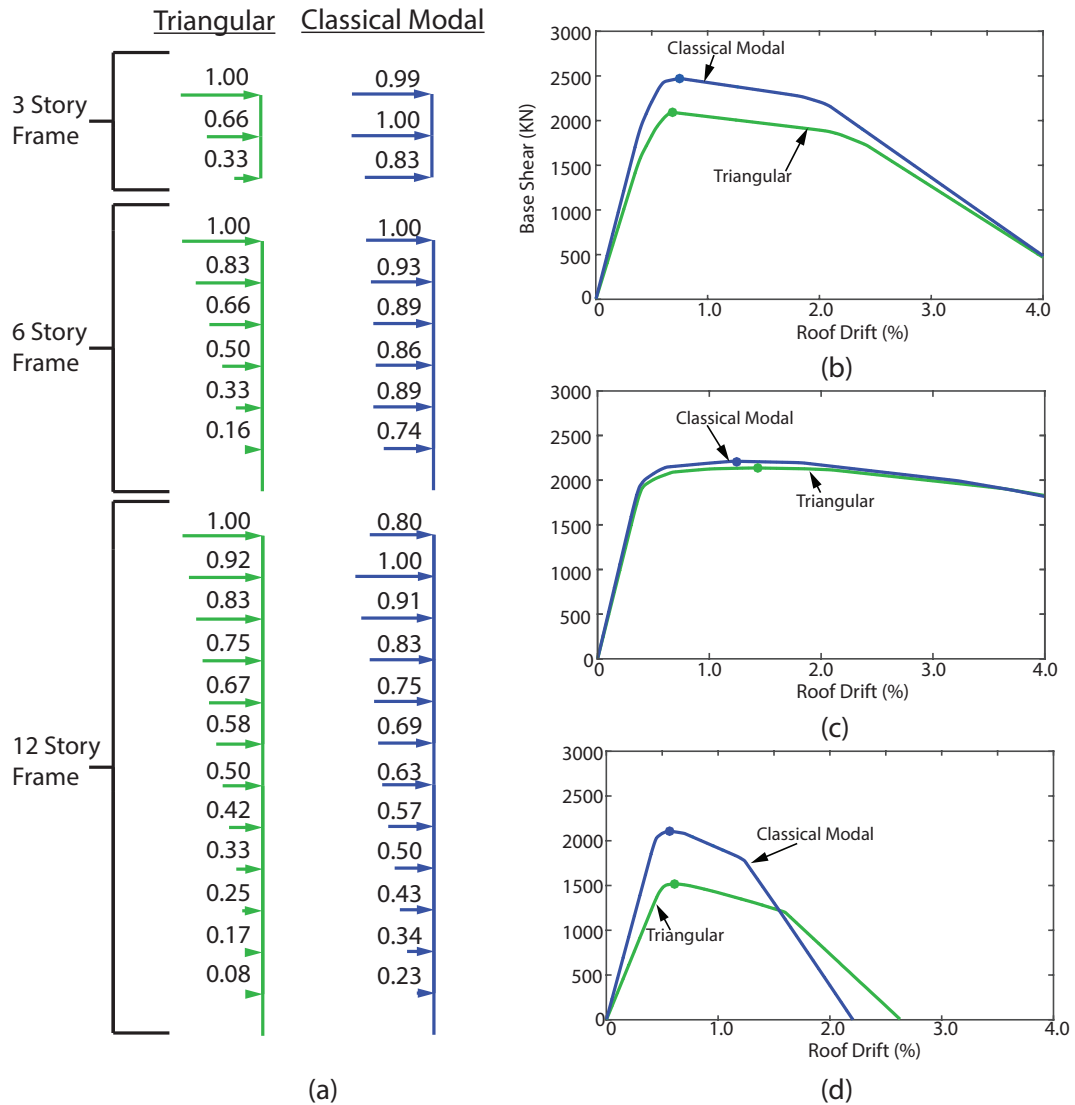


Figure 3.8: (a) Triangular and classical modal pushover force vectors; Pushover curves for (b) three-story, (c) six-story, and (d) 12-story archetype frames.

Figure 3.9 shows the relationship between the beam rotations measured for each floor at maximum pushover base shear and the annual frequency of exceedance of these rotations obtained in Section 3.3. These numerical values are normalized by the maximum value at any floor to determine a rank between 0 and 1 that is plotted in Figure 9 (a) and (b) for the three-story

triangular and classical modal pushovers, Figure 3.9 (d) and (e) for the six-story triangular and classical modal pushovers, and Figure 3.9 (g) and (h) for the 12-story triangular and classical modal pushovers. The mean ranks from both normalized pushover results are compared to the results of the annualized value, in Figure 3.9 (c), (f), and (i) for the three-, six- and 12- story buildings.

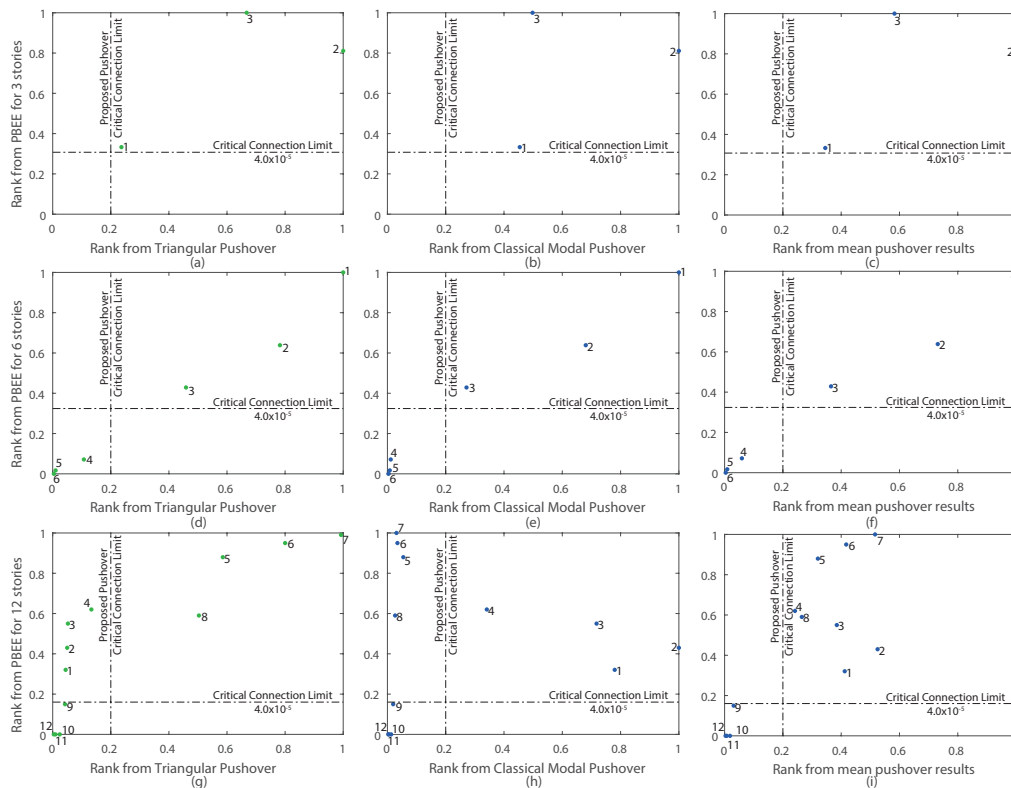


Figure 3.9: Comparison of pushover beam rotation values to annual frequency of exceedance values

The comparison shown in Figure 3.9 indicates that both pushover methods identify the same relative floor connection rotations when compared to the annual frequency of exceedance calculated from the PBEE values in Table 3.4 in both the three- and six-story buildings. In both the triangular and classical modal pushovers for both structures, the relative rotations have a similar trend in value as the relative annual frequency of exceedance for Table

3.4. However, both pushover vectors provide a less accurate implication of the annualized frequency values when applied to the 12-story building. This is likely caused by the pushover analyses being unable to properly capture higher mode effects, which were identified as contributing factor to the maximum beam rotations of this frame, as observed in Figure 3.5. Figure 3.9 (i) shows that the mean ranks from these two pushover force vectors provide a higher degree of accuracy than either pushover taken independently. Force adaptive pushover analyses (Abbasnia et al. 2014) were also considered, but did not provide any increase in connection identification accuracy. The limit on the annual frequency of exceedance used for defining critical connections of 4×10^{-5} per year (see Section 3.3) was also normalized using the maximum annual frequency of exceedance value from Table 3.4 for each building and is included in Figure 3.9 for all three archetype frames. For the pushover methods, a proposed limit of 20% of the maximum beam rotation is also included in each plot of Figure 3.9. The proposed limit of 20% of the maximum beam rotation rank identifies all of the same connections as being critical when considering the mean pushover rank (Figure 3.9 (d, f, and i)) as compared to floors identified using the PBEE based limit, and thus appears to be an acceptable approach for initial design identification before undertaking more advanced analysis.

3.6 Selection of Critical Connections

Having identified the location of critical connections within existing frames, this section explores how these connections may be selected through providing SCSHJ connections with reduced activation moment (M_{AB}) and/or second post-activation stiffness (α_2) (see Figure 3.3) at a single floor, referred to as

an isolation floor. The friction mechanism of the SCSHJ connections allows for large ranges of possible values for these two parameters without changing the frame stiffness (Khoo et al. 2013). This study was conducted based on upgrading PRENORTH six story frames, with the isolation floor selected at either the first or second floor and the goal of making the connections at all other floors non-critical. While this approach may appear to have similarities to that proposed by Fintel and Khan (1969), which was not pursued due to the disadvantages of generating a “soft-story” mechanism, the use of SCSHJ connections may provide more reliable performance at large displacements than the traditional connections that have been considered previously. Of course, this would also require displacement compatibility to be maintained with the rest of the structure, an important issue that is outside the scope of this work. Since larger displacement demands will be applied to the SCSHJ connections placed at the isolation floor, the lock up rotation of the SCSHJ connections was modified from the original value of 0.03 rad to 0.05 rad.

3.6.1 Direct Displacement-Based Design Approach

As a design method to determine the properties described above, direct displacement-based design (DDBD) is used as a basis following the steps outlined by Priestley et al. (2007). A summary of the DDBD process is shown in Figure 3.10. This begins with the selection of the intended isolation floor, a targeted performance level and a corresponding design displacement, as shown in Figure 3.10 (a). Since the goal of the isolation floor design is preventing all other connections from exceeding the limit of 4×10^{-5} annual frequency of exceeding their SDR of 0.017 rad, the design displacement is

taken as 5% inter-story drift at the isolation floor for a ground motion intensity corresponding to an annual frequency of exceedance of 4×10^{-5} for the site, while the design displacement at all other floors is taken as the displacement corresponding to the yielding of the beam connections. These design values were chosen to ensure that the connections at the other floors would only have an opportunity of exceeding their SDR at ground motions with an annual frequency of exceedance below 4×10^{-5} , resulting in the connections not being identified as critical according to limit defined in Section 3.2. Using these floor displacements, the equivalent SDOF is then computed to determine the equivalent height using Equation (3.6.1) from Priestley et al. (2007).

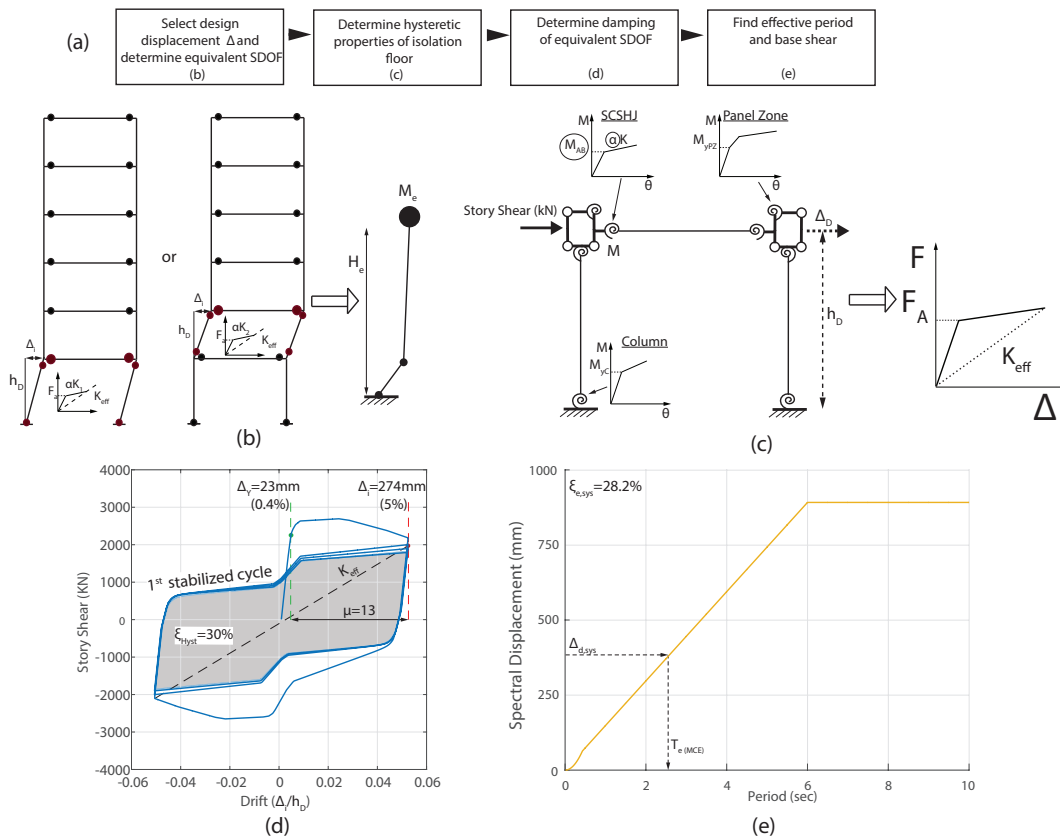


Figure 3.10: Outline of DDBD Process

$$H_e = \frac{\sum_{j=i+1}^J m_j \Delta_{y,j} H_j}{\sum_{j=i}^J m_j \Delta_{y,j}} \quad (3.6.1)$$

where H_e is the effective height of the equivalent SDOF, m_j is the mass at the j^{th} floor, H_j is the height of the j^{th} floor, $\Delta_{y,j}$ is the yield displacement of the j^{th} floor, and i is the isolation floor. The yield displacement of the j^{th} floor is determined using Equations 3.6.2 and 3.6.3 from Priestley et al. (2007).

$$\theta_{y,j} = 0.65 \frac{f_y L_j}{E H_j} \quad (3.6.2)$$

$$\Delta_{y,j} = \theta_{y,j} H_j \quad (3.6.3)$$

where f_y is the yield strength of the beam, E is the Young's modulus, L_j is the bay length of the j^{th} floor, H_j is the floor height of the j^{th} floor, and $\theta_{y,j}$ is the yield drift of the j^{th} floor. To determine the effective stiffness and hysteretic damping of the isolation floor, initial values of activation moment (M_{AB}) and second post activation stiffness (α_2) for the SCSHJ connections are selected and the hysteretic behavior of the single floor system is then determined using the sub-assembly shown in Figure 3.10 (c) subjected to a push-pull analysis. Because all the other nonlinear elements (e.g. column ends, panel zones) affect the overall hysteretic response of the isolation floor, this push-pull analysis must be conducted within the DDBD process when determining the behavior of the equivalent SDOF system. As the hysteretic shape varies with the connection design, and did not generally match any of the common hysteretic shapes provided in Priestley et al. (2007) for determining equivalent viscous damping, the hysteretic damping was calculated from the

force-displacement response of the isolation floor using Equation 3.6.4.

$$\xi_{hyst} = \frac{A_h}{2\pi F_i \Delta_i} \quad (3.6.4)$$

where A_h is the area of the stabilized hysteretic cycle defined as the first hysteretic cycle occurring without significant loss in strength or stiffness (Priestley et al. (2007)), shown in Figure 3.10 (d), F_i is the maximum force in the stable cycle and Δ_i is the design displacement of the isolation floor. The hysteretic damping of the isolation floor is combined with the elastic damping of the system in Equation 3.6.5, resulting in an equivalent viscous damping of the SDOF.

$$\xi_{e,sys} = \frac{\xi_e \Delta_{y,sys} + \xi_{hyst} \Delta_i}{\Delta_{y,sys} + \Delta_i} \quad (3.6.5)$$

where $\xi_{e,sys}$ is the equivalent viscous damping of the SDOF system, ξ_e is the elastic damping of the frame structure, $\Delta_{y,sys}$ is the system yield displacement of the structure above the isolation floor, ξ_{hyst} is the hysteretic damping from Equation 3.6.2, and Δ_i is the displacement of the isolation floor. As mentioned in Priestley et al. (2007), for shorter frame structures dominated by first mode response, the yield displacement $\Delta_{y,sys}$ can be computed as:

$$\Delta_{y,sys} = \theta_y H_e \quad (3.6.6)$$

where θ_y is the yield inter-story drift of any of the floors above the isolation floor since each have identical geometric distances. The corresponding displacement spectrum for the system equivalent damping is determined and shown in Figure 3.10 (e) for the intensity corresponding to an annual frequency of exceedance

of 4×10^{-5} . The total displacement of the system is then determined by adding the large displacement of the isolation floor and the elastic displacement of the structure above the isolation floor, as shown in Equation 3.6.7.

$$\Delta_{d,sys} = \Delta_{y,sys} \Delta_i \quad (3.6.7)$$

where $\Delta_{d,sys}$ is the total displacement of the equivalent SDOF system and the other variables are defined above. The effective mass (m_e) of the SDOF is then determined using Equation 3.6.8.

$$m_e = \frac{\sum_{j=i}^J m_j \Delta_j}{\Delta_{d,sys}} \quad (3.6.8)$$

Finally, the design base shear (V_b) is determined from the effective mass and the effective period ($T_{e,sys}$) obtained at the design displacement on the displacement spectra, using Equation 3.6.9.

$$V_b = \frac{4\pi^2 m_e \Delta_{d,sys}}{T_{e,sys}^2} \quad (3.6.9)$$

The base shear is then used to compute the applied forces at the floors above the isolation floor using Equation 3.6.10:

$$F_j = \frac{V_b m_j \Delta_{y,j}}{\sum_{j=1}^J m_j \Delta_j} \quad (3.6.10)$$

The accumulation of these shear values (V_j) at the j^{th} floor are then compared with the maximum allowable floor shear values of that floor, defined as the shear force calculated from the connection SDR moment ($F_{SDR,j}$) determined using a single floor sub-assembly model similar to Figure 3.10 (c), to ensure that the connections in the other floors do not

exceed their SDR at all intensities. This comparison is shown in Equation 3.6.11:

$$V_j = \sum_j^J F_j < F_{SDR,j} \quad (3.6.11)$$

where J is the total number of floors. A final verification of the design process is conducted using the pushover methods described in Section 3.4.0.

3.6.2 Application to Archetype Frames

Table 3.5 presents key values from the DDBD procedure described above for both isolation floor frames, and the values without any isolation floor are also included for comparison. For the first isolation floor design, the DDBD procedure described above led to a solution with an activation moment five times smaller than the original PRENORTH beam connection yield moment and a post-activation stiffness of 0.001 times the initial stiffness. For the second floor isolation floor design, the DDBD procedure lead to solution with an activation moment 7.5 times smaller than the original PRENORTH yield moment and a post-activation stiffness of 0.001 times the initial stiffness. Both isolation floor designs were analysed using the same pushover methods presented in Section 3.4.0 to conduct a preliminary identification of the critical connection location and both designs resulted in a concentration of rotations occurring at their respective floors during the pushover analysis while the relative rotations at all other floors remained below the 20% threshold. Following this confirmation from the preliminary analysis, the performance of the frames with isolation floors designed using the DDBD process described above was evaluated using the same process outlined in

Section 3.3.4. The collapse fragility curves for the original six-story frame using only PRENORTH connections, only SCSHJ connections and both isolation floor configurations are shown in Figure 3.11 for the 1st and 2nd floor designs. The same collapse criterion of 5% inter-storey drift was used in this analysis.

Table 3.5: DDBD Values for Isolation Floor Designs

Isolation Floor Level	Δ_i	Δ_j	H_e	m_e	ξ_{hyst}	$\xi_{e,sys}$	$\Delta_{d,sys}$	$T_{e,sys}$	V_b
PRENORTH only	0	$0.017H_j$	16.8m	$87\%m_t$	0	15.5%	323mm	1.50sec	7295kN
1	275mm	$\theta_{y,j}H_j$	14.7m	$95\%m_t$	30%	28.2%	293mm	2.62sec	207kN
2	190.5mm	$\theta_{y,j}H_j$	16.7m	$85\%m_t$	30%	23.2%	251mm	2.31sec	2333kN

Note: M_t = Total mass of structure

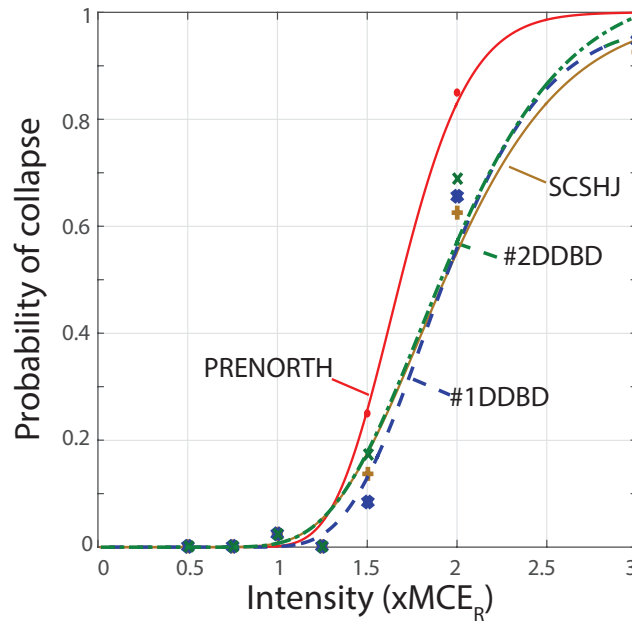


Figure 3.11: Fragility curves for 1st and 2nd isolation floor designs.

The first and second floor DDBD parameter configurations had a collapse performance which was essentially identical to the frame using only SCSHJ

connections, demonstrating that the isolation floor design is not limited to the floor with the largest original frequency of exceedance. Collapse occurred in the isolation floor designed buildings shortly after to the lock up rotation being reached in the SCSHJ connections at the isolation floors. Once the rotation of 0.05 rad was achieved in the SCSHJ connections, the stiffness of the SCSHJ hysteretic model increased to essentially rigid, and the other non-linear elements at the floor began yielding, leading to interstorey drifts exceeding the collapse criteria. While the collapse performance of the frames with an isolation floor did not surpass the collapse performance of the frames using SCSHJ connections, the design of the isolation floor did increase the CMR of the frame by 12% over the frame using only PRENORTH connections for both the first and second floor isolation floor designs. This seems to indicate that the replacement of PRENORTH connections at even a single floor can have a significant benefit on the collapse performance of the frame by following the principles of capacity design at a global level. However, the mechanism for displacement in the isolation floor requires large rotations in both the beam hinges and the column hinges at the isolation floor. Since this study of isolation floors designed using DDBD included modifications to only the beam connections with the addition of SCSHJ connections as a theoretical support to the discussion of critical connections, no modifications to the other elements were considered and displacement compatibility in all elements was assumed. True design implementations of an isolation floor concept should consider modifications to the columns at these floors to provide a more reliable hysteretic behavior at large displacements, among other detailing.

3.6.3 Parametric Study on Connection Rotation

Demands

While the DDBD procedure resulted in distinct activation moments and post-activation stiffnesses for both the first and second floor isolation design, a parametric study was conducted to determine if other combinations of these two parameters are also possible. To measure the effectiveness of the concentration and isolation of large rotations at the isolation floor, the same collapse analysis described in Section 3.3.4 is applied to the isolation floor designs with varying combinations of modified parameters. Each occurrence of a connection surpassing the SDR value of the PRENORTH connection (0.017 rad) is recorded during all of the ground motions in the collapse analyses. The percentages of those occurrences located at the isolation floor is measured, with the goal of obtaining nearly 100% of the large rotations occurring at the isolation floor. For the parametric study, three values were selected for the post-activation stiffness and six values for the activation moment for the SCSHJ connection at the isolation floor, including values obtained from both DDBD designs, which are identified. The percentages of connection rotations exceeding 0.017 rad that occurred at the isolation floors are summarized in Figure 3.12 (a) for the first floor and Figure 3.12 (b) for the second floor for all considered combinations of post-activation stiffness and activation moment, plotted against the activation moment for the SCSHJ connections at the isolation floor for all floors. Figure 3.12 demonstrates that, for both the first and second isolation floor designs, a variety of combinations of activation moments and post-activation stiffnesses can concentrate the large inelastic displacements at a single floor. In Figure

3.12 (a), the original PRENORTH frame from Section 3.4 begins with only 46% of the connections that surpass 0.017 rad being located at the first floor. As the first floor’s activation moment is decreased, the proportion of connections that surpassing a rotation of 0.017 rad at the first floor increases. Reducing the post-activation stiffness further contributes to the large rotation. Figure 3.12 (b) indicates that 30% of all beams surpassing 0.017 rad are located at the second floor in the original structure. The same overall trend is observed as with the first isolation floor, where a decreasing value of the activation moment at the second floor leads to a greater concentration of connection rotations at that floor. However, when compared to the first isolation floor implementation, a further reduction of activation moment and post-activation stiffnesses were required to achieve similar levels of concentration of large rotations.

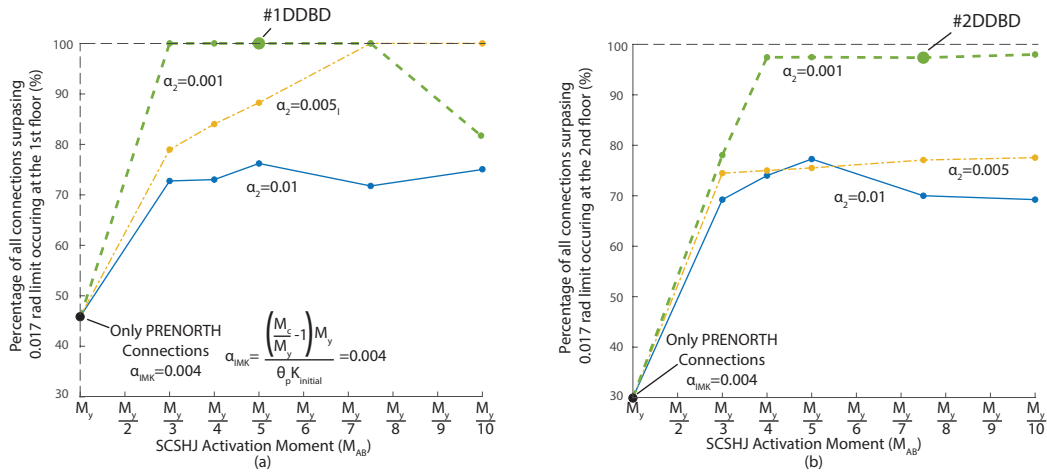


Figure 3.12: Parametric study of large inelastic rotation concentration for (a) 1st isolation floor design and (b) 2nd floor isolation design.

3.7 Conclusions

This paper aimed to identify the connections in moment-resisting frames (MRFs) whose local component ductility was critical to the seismic performance of the complete system. The definition of a critical connection used the maximum rotation occurring at each floor as the engineering demand parameter (EDP) within the PBEE framework to determine an annual frequency of exceeding a connection's strength degradation rotation (SDR). An annual limit of 4×10^{-5} was set, where any connection exceeding this limit was defined as critical to the behavior of the frame. The collapse performance of frames using only one kind of connections (pre-Northridge (PRENORTH), RBS, or self-centering sliding hinge joint (SCSHJ)), was compared to that of frames using SCSHJ connections only at locations defined as critical and PRENORTH connections at locations not defined as critical. The frames with this combination of PRENORTH and SCSHJ connections matched the performance of the frame with SCSHJ connections at all locations. Based on analysis of the same frames, an empirical method was provided to identify critical connections at the preliminary design phase using only pushover analysis. This paper also discussed how to select the locations of critical connections. Direct displacement-based design (DDBD) was proposed as a design method to select connection properties at a single isolation floor and its effectiveness was verified through NLTHA, before a parametric study indicating that additional designs could also achieve the same goal. This ability to select the critical connections within a frame allows designers to choose the location of resource concentration, applying low-damage and self-centering behavior while avoiding soft-story collapse.

With the current proliferation of high-performing and low damage components, the possibility of applying displacement and self-centering at select levels within a building has applications beyond steel MRFs. Further research work should examine the modification of relative yield forces and post-yield stiffnesses for other systems. The influence of the gravity framing, particularly continuous columns spanning multiple levels, should also be examined.

3.8 Acknowledgments

The authors would like to acknowledge the assistance of Dr. Andre Filiatrault for his contribution and early revisions of this paper. The authors would also like to acknowledge the National Science and Engineering Research Council (NSERC) for funding this research

3.9 References

- Abbasnia, R., Tajik Davoudi, A., and Maddah, M., (2014) “An Improved Displacement-Based Adaptive Pushover Procedure Based on Factor Modal Combination Rule.” *Earthquake Engineering and Engineering Vibration*, 13(2), 223-241.
- AISC, (2016a). “Prequalified Connections for Special and Intermediate Steel Moment Frames for Seismic Applications.” *American Institute of Steel Construction 358-16*, Chicago, IL, US
- AISC, (2016b). “Seismic Provisions for Structural Steel Buildings.” *American Institute of Steel Construction 341-16*, Chicago, IL, US

ASCE, (2016). “Minimum Design Loads and Associated Criteria for Buildings and Other Buildings.” *American Society of Civil Engineers 7-16*, Reston, VA, US

ATC, (2010). “ATC-72-1: Modeling and acceptance criteria for seismic design and analysis of tall buildings” *Applied Technology Council/Pacific Earthquake Engineering Research Center Report No. 72-1*, Richmond, CA, US.

Baker, J. W., (2015). “Efficient analytical fragility function fitting using dynamic structural analysis.” *Earthquake Spectra*, 31(1), 579–599.

Baker, J. W., and Lee, C., (2017). “An Improved Algorithm for Selecting Ground Motions to Match a Conditional Spectrum.” *Journal of Earthquake Engineering*, 22 (4), 708-723.

Baker, J. W. and Cornell, C. A., (2005). “A Vector-Valued Ground Motion Intensity Measure Consisting of Spectral Acceleration and Epsilon.” *Earthquake Engineering & Structural Dynamics*, 34 (10), 1193-1217.

Charney, F. and Pathak, R., (2008). “Sources of elastic deformation in steel frame and framed-tube structures: Part 1: Simplified subassembly models.” *Journal of Constructional Steel Research*, 64(1), 87–100.

Chi, B. and Uang, C.-M., (2002). “Cyclic Response and Design Recommendations of Reduced Beam Section Moment Connections with Deep Columns” *Journal of Structural Engineering*, 128(4), 464–473.

Choi, J., Stojadinovic, B., and Goel, S., (2003). “Design of Free Flange Moment Connection” *American Institute of Steel Construction*

Engineering Journal, 40(1), 25-41

Chopra, A., (2012). *Dynamics of Structures.*, Pearson, 4th edition.

Christopoulos, C., Filiatrault, A., Uang, C.-M., and Folz, B., (2002).
“Posttensioned Energy Dissipating Connections for Moment-Resisting
Steel Frames.” *Journal of Structural Engineering*, 128(9), 1111–1120.

Clifton, G.C., (2005) “Semi-Rigid Joints For Moment-Resisting Steel Framed
Seismic-Resisting Systems.” *Doctoral Dissertation, Department of Civil
and Environmental Engineering*, University of Auckland, New Zealand

Engelhardt, M. D. and Sabol, T. A., (1994). “Testing of welded steel moment
connections in response to the Northridge earthquake.” *AISC Northridge
Steel Update*, (1).

Erochko, J., Christopoulos, C., Tremblay, R., and Choi, H., (2011). “Residual
Drift Response of SMRFs and BRB Frames in Steel Buildings Designed
according to ASCE 7-05.” *Journal of Structural Engineering*, 137(5),
589–599.

FEMA(Federal Emergency Management Agency)., (2000a). “Recommended
Seismic Design Criteria for New Steel Moment-Frame Buildings.” *Federal
Emergency Management Agency Report 350*, Washington, D.C.

FEMA(Federal Emergency Management Agency)., (2000b). “Prestandard
and Commentary for the Seismic Rehabilitation of Buildings” *Federal
Emergency Management Agency Report 356*, Washington, D.C.

FEMA(Federal Emergency Management Agency) (2009). “Quantification of
Building Seismic Performance Factors” *Federal Emergency Management*

Agency Report P-695, Washington, D.C.

FEMA(Federal Emergency Management Agency) (2012). “Seismic Performance Assessment of Buildings.” *Federal Emergency Management Agency Report P-58*, Washington, D.C.

Fintel, M., and Khan, F., (1969) “Shock-Absorbing Soft Story Concept for Multistory Earthquake Structures.” *Journal of the American Concrete Institute*, 66(5), 381-390.

Gilton, C. and Uang, C.-M., (2002). “Cyclic Response and Design Recommendations of Reduced Beam Section Moment Connections with Deep Columns” , *Journal of Structural Engineering*, 128(4), 452–463.

Gupta, A. and Krawinkler, H., (1999). “Seismic Demands for Performance Evaluation of Steel Moment Resisting Frame Structures.” *Stanford University Department of Civil and Environmental Engineering Report No. 132*, 1–379.

Hall, J., (1995). “Parameter Study of the Response of Moment -Resisting Steel Frame Buildings to Near-Source Ground Motions.” *SAC95-05: Parametric Analytical Investigation of Ground Motion and Structural Response, Northridge Earthquake of January 17, 1994*, (1).

Ibarra, L., Medina, R., and Krawinkler, H., (2005). “Hysteretic Models That Incorporate Strength and Stiffness Deterioration” *Earthquake Engineering and Structural Dynamics*, 34, 1489-1511.

Khoo, H. H., Clifton, C., Butterworth, J., and Macrae, G., (2013). “Experimental study of full-scale self-centering sliding hinge joint

connections with friction ring springs.” *Journal of Earthquake Engineering*, 17(7), 972–977.

Lee, C.-H., Jeon, S.-W., Kim, J.-H., Kim, J.-H., and Uang, C.-M., (2004). “Effects of panel zone strength and beam web connection method on seismic performance of reduced beam section steel moment connections.” *Journal of Structural Engineering*, 131(12), 1854–1865.

Li, Q., and Ellingwood, B. R., (2008). “Damage inspection and vulnerability analysis of existing buildings with steel moment-resisting frames.” *Engineering Structures*, 30(2), 338–351.

Lignos, D., and Al-Shawwa, N., (2013). “Web-Based Interactive Tools for Performance-Based Earthquake Engineering”.

Mander, T.J., Rodgers, G.W., Chase, J.G., Mander, J.B. and MacRae, G.A., (2009). “Damage avoidance design steel beam-column moment connection using high-force-to-volume dissipaters.” *University of Canterbury Research Repository*, 962.

McKenna, F., and Fenves, G. L., and Scott, M., (2000). *Open System for Earthquake Engineering Simulation*. University of California Berkeley, CA.

Miranda, E., and Aslani, H., (2003). “Probabilistic Response Assessment of Building-Specific Loss Estimation” *PEER Report No. 2003/03*, Berkeley, California.

NIST(2010). “Evaluation of the FEMA P-695 Methodology for Quantification of Building Seismic Performance Factors.” *NIST GCR 10-917-8*

- PEER, (2013) “PEER NGA-West2 Database.” *Pacific Earthquake Engineering Research Center Report No. 2012/03*, Berkeley, California.
- Popov, E., Balan, T., and Yang, T. S., (1998). “Post-Northridge Earthquake Seismic Steel Moment Connections.” *Earthquake Spectra*, 14(4), 659–677.
- Priestley, M.J.N., Calvi, G.M. and Kowalsky, M.J., (2007). *Direct Displacement-Based Seismic Design of Structures*. IUSS Press, Pavia.
- Ricles, J., Sause, R., Garlock, M. and Krawinkler, H., (2001). “Posttensioned Seismic-Resistant Connections for Steel Frames.” *Journal of Structural Engineering*, 127(2), 113–121.
- Steneker, P., Wiebe, L., and Filiatrault, A., (2019) “Steel Moment Resisting Frames with Sliding Hinge Joint Connections: Seismic Evaluation Using Various Response Indices” *12th Canadian Conference on Earthquake Engineering (12CCEE)*, Quebec City, Canada, 9 p
- Tsai, K.C., and Popov, E., (1988), “Steel Beam-Column Joints in Seismic Moment Resisting Frames” Report No. UCB/EERC-88/19 Earthquake Engineering Research Center, Berkeley, CA.
- USGS, (2014). “Unified Hazard Tool” United States Geological Survey (Lat: 47.6, Long: -122.3, T: 1.0 Sec)
- Youssef, N. F., Bonowitz, D., and Gross, J. L., (1995). “NISTIR 5625: A Survey of Steel Moment-Resisting Frame Buildings Affected by the 1994 Northridge Earthquake.” *Building and Fire Research Laboratory, National Institute of Standards and Technology*, NISTIR 562, 173.

Zareian, F., and Medina, R., (2010). “A practical method for proper modeling of structural damping in inelastic plane structural systems.” *Computers and Structures*, 88(1), 45-53.

Chapter 4

INTEGRATED STRUCTURAL–NONSTRUCTURAL PERFORMANCE-BASED SEISMIC DESIGN AND RETROFIT OPTIMIZATION OF BUILDINGS

4.1 Abstract

The assessment of anticipated losses due to damage of both structural and nonstructural components is now recognized to be a key component in the performance-based seismic design or retrofit of buildings. Current performance-based seismic loss estimation procedures are building case specific, and they do not easily allow for the integrated optimization of structural and nonstructural interventions in a particular building. The main objective of this paper is to develop a general optimization procedure within the Performance-Based Earthquake Engineering (PBEE) framework developed by the Pacific Earthquake Engineering Research (PEER) Center and implemented through the FEMA P-58 methodology. Available optimization procedures that can be applied to the PEER-PBEE framework are first reviewed, leading to the selection of the genetic algorithm for this

purpose. The implementation of the genetic algorithm within the PEER-PBEE framework, considering integrated structural and nonstructural seismic upgrades, is described. The seismic retrofit case-study of a three-story steel moment-resisting frame archetype building is then conducted for the three different target metrics included in the PEER-PBEE framework: 1) an economic target metric, 2) a downtime target metric and, 3) a casualty reduction target metric. The results of the case study indicate how this optimization process, based on the genetic algorithm, quickly and reliably converges to different allocations of resources for structural and nonstructural components depending on the target metric selected. Finally, a parametric study on the effects of the owner’s expected internal rate of return and building occupancy time on the optimum retrofit solutions illustrates the utility of the optimization process beyond the single case study.

4.2 Introduction

The development of the Performance-Based Earthquake Engineering (PBEE) framework by the Pacific Earthquake Engineering Research Center (PEER) (Cornell and Krawinkler 2000; Miranda and Aslani 2003; Moehle and Deierlein 2004) and its implementation through the FEMA P-58 methodology (FEMA 2012a) provide designers and building owners with tools to describe the seismic performance of building systems, including both structural and nonstructural components. The PEER-PBEE framework includes four stages, with hazard analysis, structural analysis, and damage analysis being conducted to provide information for a final loss analysis, which determines decision variables. The importance of considering both

structural and nonstructural seismic losses in a seismic design or retrofit situation is now recognized and has been discussed extensively in the last decades (Miranda and Taghavi 2003; Bradley et al. 2009; Molina et al. 2016). More recently, procedures to conduct cost-benefit analyses to reduce economic losses have been developed (Hofer et al. 2018; Sousa and Monteiro 2018). The PEER-PBEE framework is based on evaluating a specific building case, thereby limiting the selection of a seismic upgrade strategy to a trial-and-error approach, typically aided by some guidance from experienced designers. This building case specific approach does not easily allow the optimization of integrated structural–nonstructural interventions. Only a few studies have considered optimization procedures for the seismic design or retrofit of buildings. Most of these strategies involved the use of genetic algorithms as the optimization process but were limited in scope to structural design decisions. For example, Rojas et al. (2011) used a genetic algorithm focused on the optimal weight of steel members in a steel moment resisting frame (MRF) to reduce the expected annual loss (EAL). Apostolakis et al. (2014) used a genetic algorithm to select the optimal design parameters of self-centering connections in a steel MRF building that minimizes the EAL, by controlling the tradeoff between maximum (and residual) inter-story displacements and maximum floor accelerations. Farhat et al. (2009) used a single cost-objective genetic algorithm to optimize the seismic upgrade of an existing structure with buckling restrained braced frames. Wongprasert and Symans (2004) used a genetic algorithm to determine the optimal distribution of viscous dampers in a steel MRF to reduce building drifts and accelerations. Gidaris and Taflanidis (2015) optimized the design of a viscous damping retrofit in a reinforced concrete

MRF by using a kriging metamodel that accounts for the upfront installation cost of the dampers and the associated reduction in seismic losses. Finally, Pollini et al. (2017, 2018) explored the use of various optimization processes, including genetic algorithms, to minimize the retrofit cost of a building equipped with viscous dampers. None of the optimization studies described above included a process to determine the optimal resource allocation between structural and nonstructural upgrades with the purpose of minimizing seismic losses. The main objective of this study is to develop such a general process within the PEER-PBEE framework using various decision variables as target optimization metrics. The results obtained from this optimization process can be used by building owners and non-engineering professionals to better conduct investment planning and risk mitigation analysis throughout their asset's life cycle.

4.3 Review of Optimization Procedures

Applicable to PEER-PBEE Framework

As discussed by Rojas et al. (2011) and Hofer et al. (2018), among others, the probabilistic nature of the PEER-PBEE framework requires that the selection of any single component (structural or nonstructural) upgrade must be considered within the context of a full system-level analysis. This is required because of deterministic and probabilistic interconnected factors influencing the decision variables. An example of a deterministic interconnected factor is an individual component upgrade cost being reduced by combination with other related upgrades, such as the cost savings when

upgrading both ceiling tiles and piping systems due to common work tasks. An example of a probabilistic influencing interconnected factor is the influence of structural changes to a building on the change in demand on nonstructural components, such as when the stiffening of a building with braces increases the likelihood of damage to acceleration-sensitive nonstructural components. Therefore, an optimization process implemented within the PEER-PBEE framework needs to include a building case specific stochastic optimization solution, such as those considered by Wongprasert and Symans (2004), and Apostolakis et al. (2014). Several stochastic methods are available for this purpose, such as the genetic algorithm, swarm algorithm, simulated annealing, and ant colony algorithm (Kirmayaz et al. 2014). The genetic algorithm optimization strategy (Golberg 1989; Mitchell 1999) was selected herein for implementation in the PEER-PBEE framework. This decision was based on three main reasons: 1) the genetic algorithm is available in many commercial software packages (Carroll 2004; MathWorks 2018), 2) the genetic algorithm is easier to implement than other stochastic optimization methods (Kirmayaz et al. 2014), and 3) recent research works have explored the use of genetic algorithms for structural upgrades, as discussed in the previous section.

4.4 Overview of Genetic Algorithm and Implementation in the PEER-PBEE Framework

The genetic algorithm is based on the principles of evolutionary biology and has been applied to various areas of engineering, including structural design (Golberg 1989; Camp et al. 1998). It replicates natural evolutionary selection theory with the use of repetitive iterations, where individuals within a population who have a higher fitness have a higher degree of propagation to the following generation. Both probabilistic-based crossovers of individuals forming the next generation and random mutations are used to ensure some population diversity as the algorithm converges towards an optimal solution. A genetic algorithm can be summarized into five main steps, as illustrated in Figure 4.1: 1) the formulation of the genetic code defining each individual within the population; 2) the evaluation of the performance of each individual using a ranking function for a specific target metric; 3) the selection and mixing of individuals to form a new generation seeking higher performing individuals; 4) the mutation of individuals to ensure genetic diversity; and 5) the determination of an optimum solution using single or multiple convergence criteria.

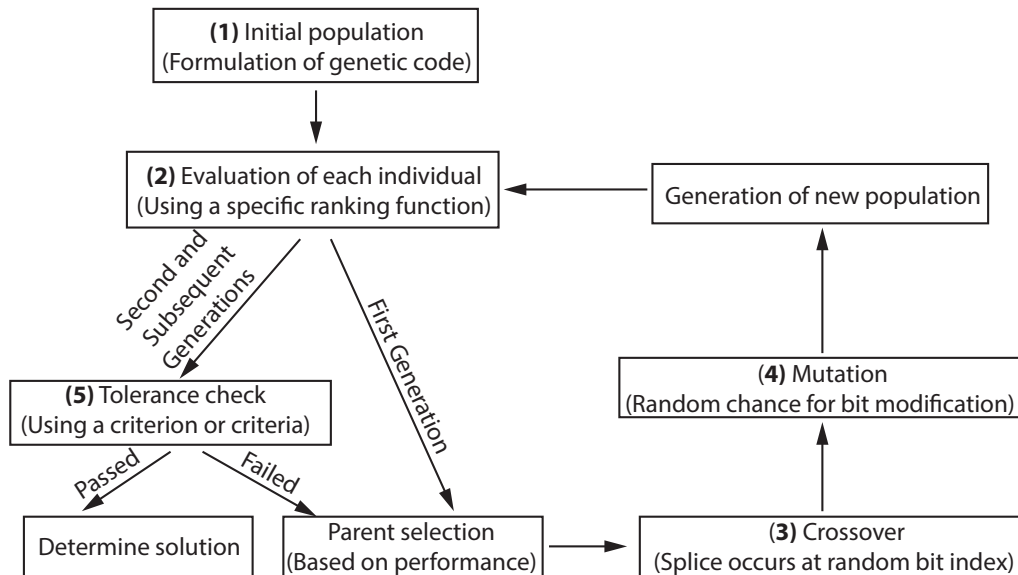


Figure 4.1: Flow chart for genetic algorithm

The components of the genetic algorithm must be adapted to ensure that all considered upgrade options are evaluated within the PEER-PBEE framework. Implementing the PEER-PBEE framework requires the formulation of the genetic code (i.e. string of bits) of each individual within the population with a sufficient number of bits to represent each component’s upgrade, forming step (1) of Figure 4.1. As shown in Figure 4.2, each nonstructural component is represented with its own binary bit, where a zero bit represents a non-upgraded status, and a unity bit represents an upgraded status, which is accompanied by an improvement of its fragility curves, as defined in FEMA P-58 (FEMA 2012a). The identification of a particular structural upgrade strategy is made by two separate bits. The value of the first “structural upgrade option” bit varies from unity to S_n , where S_n is the maximum number of structural upgrade strategies being considered. The implementation of the structural upgrade strategy is then represented by one “structural upgrade implementation” binary bit for each floor of the building

(with a value of unity indicating an upgrade at that floor). This procedure provides more flexibility to structural upgrades on a floor-by-floor basis, rather than limiting the decision to the entire building at once. The introduction of a particular unity bit at a given floor requires nonlinear time history analyses conducted at multiple intensity stripes both to generate the collapse fragility curve of the upgraded building and to determine the engineering demand parameters (EDPs) for each floor, which are needed to evaluate the nonstructural damage from the initial or upgraded fragility curves. An example of a population of four individuals within a given generation is shown in Figure 4.2 for a three-story building considering four different structural upgrade options and 26 different nonstructural component typologies. The total number of bits composing the string of a particular individual of this building is 30: 26 nonstructural bits, 1 “structural upgrade option” bit with four different structural upgrade options and 3 “structural upgrade implementation” bits (one for each of the three floors). The string of an individual could be constructed for any number of different structural upgrade types (S_n) or building floors and could consider any number of nonstructural components as desired. Furthermore, the optimization procedure allows for the possible inclusions of component or system level constraints.

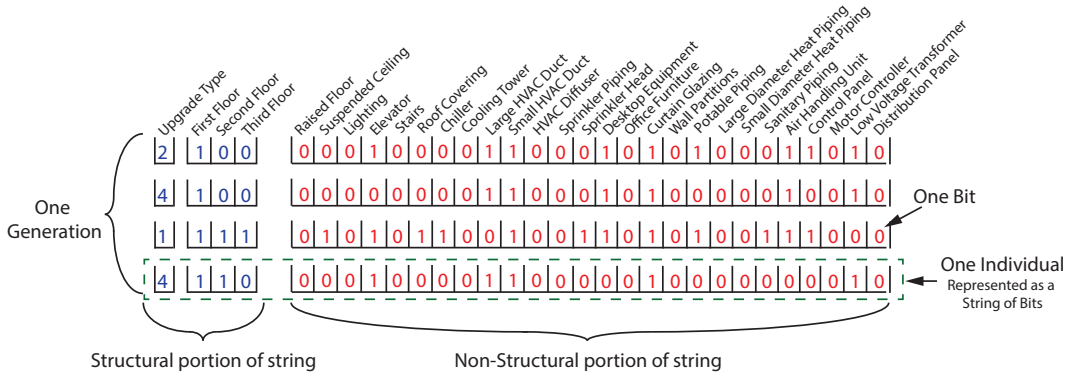


Figure 4.2: Example of population formulation in genetic algorithm

Following the formation of the genetic code of the individuals of the initial population, the fitness of each individual within a population is evaluated and ranked using a ranking function for each target metric considered, identified as step (2) in Figure 4.1. Each ranking function uses results obtained from the application of the FEMA P-58 methodology to the individual. The three target metrics included in the PEER-PBEE framework were selected herein, with each potentially leading to a different optimal upgrade solution. These three target metrics are: 1) an economic target metric, 2) a downtime target metric and, 3) a casualty reduction target metric. These three target metrics and their associated ranking functions are described in the next sections. The initial population described above is formed by individuals having randomly assigned bit values. This provides an initial diversity to the population, before selective optimizing begins. After the fitness of each individual is evaluated and ranked, a crossover is conducted (step (3) in Figure 4.1), where two individuals are randomly selected with a weighted preference according to their rank. The strings of these highly ranked individuals are spliced and mixed to form a new generation of the same population size as the previous generation. A carryover percentage is used to guarantee the existence of a certain number

of the best performing individuals from the previous generation moving into the next generation without undergoing splicing. Once the new generation is formed, each bit can mutate based on a pre-determined mutation rate (step (4) in Figure 4.1). If a bit mutates, its value is randomly reassigned using a uniform distribution. The new generation is then evaluated and ranked again. The optimization process is deemed to have reached a solution once a set of convergence criteria is satisfied (step 5 in Figure 4.1). Finally, since the genetic algorithm is a heuristic searching algorithm, multiple algorithm runs are needed to increase the confidence in the solution obtained for each target metric.

4.4.1 Economic Target Metric

The first target metric considered in this study is an economic target metric, which compares the total cost of each integrated structural and nonstructural upgrade strategy to the benefits derived from a reduction of seismically induced economic loss over the occupancy time. The ranking function ($Rank_{Economic}$) associated with this economic target metric is given by:

$$Rank_{Economic} = (PV_O - PV_U) - UC \quad (4.4.1)$$

where PV_O is the present value of the seismic losses of the original (non-upgraded) building, PV_U is the present value of the seismic losses of the upgrade case being considered (i.e. an individual in a generation), and UC is the total cost of the combination of chosen upgrades. The equation for the

present value (PV) used in Eq. 4.4.1 is calculated as:

$$PV = \frac{EAL}{r} \left(1 - \frac{1}{(1+r)^t}\right) \quad (4.4.2)$$

where r is the internal rate of return required by the owner, t is the expected occupancy time of the building in years, and EAL is the expected annual loss obtained from the FEMA P-58 methodology. A positive rank for an individual indicates that the economic gain due to the risk reduction outweighs the upgrade cost. Therefore, maximizing the positive rank represents the optimal design objective for the economic target metric.

4.4.2 Downtime Target Metric

The second target metric considered is the reduction in operational downtime throughout the projected occupancy time of the building. The function considers both the time required to implement the desired upgrades and the reduction in estimated annual time lost due to earthquake damage. The ranking function ($Rank_{Downtime}$) associated with this downtime target metric is given by:

$$Rank_{Downtime} = (EAT_O - EAT_U)(t) - \frac{UT}{S} \quad (4.4.3)$$

where EAT_O is the expected annual time lost due to seismic events in days per year for the original building, EAT_U is the expected annual time lost due to seismic events in days per year for the upgrade strategy being considered, t is the expected occupancy time in years and UT is the time required to conduct the particular set of upgrades being considered in days. For a retrofitting situation, S is a sequencing factor that reflects the ability to

reduce the operational impact of construction through planned sequencing strategies, such as conducting upgrade work during non-operational hours or while completing other architectural upgrades, in contrast to unprepared post-earthquake repairs. Again here, maximizing the ranking fitting function for the downtime target metric represents the optimum upgrade solution.

4.4.3 Casualty Reduction Target Metric

The reduction of casualties is the third target metric considered in this study. This target metric is associated with the longstanding primary objective of maintaining life safety considered by modern building codes. The ranking function ($Rank_{Casualties}$) associated with this casualty reduction target metric is given by:

$$Rank_{Casualties} = (EAD_O - EAD_U)(VSL) + (EAI_O - EAI_U)(VSI) \quad (4.4.4)$$

where EAD_O is the expected annual number of deaths per year for the original building, EAD_U is the expected annual number of deaths per year for the individual being considered, VSL is the monetary statistical value assigned to a human life, EAI_O is the expected annual number of serious injuries per year for the original building, EAI_U is the expected annual number of serious injuries per year for the individual being considered, and VSI is the statistical monetary value assigned to a statistical human injury. A reduction of the number of injuries and deaths would lead to a larger rank value and, thereby, an optimal upgrade strategy. Values of VSL and VSI recommended in the current literature (DOT, 2016) were used in this study.

While structural collapse is the main source of casualties, damage states of some of the nonstructural components can also lead to localized casualties in the immediate affected area. These nonstructural related casualties could affect the optimization of structural upgrades.

4.5 Retrofit Case Study

A retrofit case study was developed to demonstrate the capabilities of the genetic algorithm optimization process in influencing the decision-making within the PEER-PBEE framework. An archetype building was selected, and an owner profile was defined in terms of internal rate of return (r) and building occupancy time (t). It consisted of a 4% internal rate of return with a 40-year occupancy time, and is representative of a long-term building owner having a low-risk investment strategy and targeting value-added real estate returns typical of the Western United States (Shilling and Wurtzebach, 2012).

4.5.1 Archetype Building and Modeling of Structural Response

The original (non-upgraded) archetype building in this case study is an existing three-story office type building (FEMA 2012b), to be retrofitted in Seattle, Washington. The seismic force-resisting system is a steel moment resisting frame (MRF) with pre-Northridge Earthquake beam-to-column connections. This archetype frame was designed according to the seismic provisions contained in the 1994 edition of the Uniform Building Code (UBC

1994) for a Site Class B. With the exception of the use of pre-Northridge connections, the archetype frame satisfies current ASCE 7-16 seismic design requirements (ASCE 2016, AISC 2016). Its computed fundamental period is 0.87s. The frame model was assembled in the OpenSees software (McKenna et al. 2000) and consisted of elastic beam-to-column elements with concentrated rotational plastic hinges, using the Ibarra-Medina-Krawinkler model (Ibarra et al. 2005), at the element ends. Each beam-to-column joint was modeled to capture panel zone yielding using the Krawinkler Spring Box model illustrated in Figure 4.3 (a) (Gupta and Krawinkler 1999), and was modeled using a trilinear backbone curve (Charney and Pathak 2008). The building was assumed to have no irregularities causing torsional effects and, thus, its seismic response was obtained independently in the North-South and East-West directions (see Figure 4.3(b)).

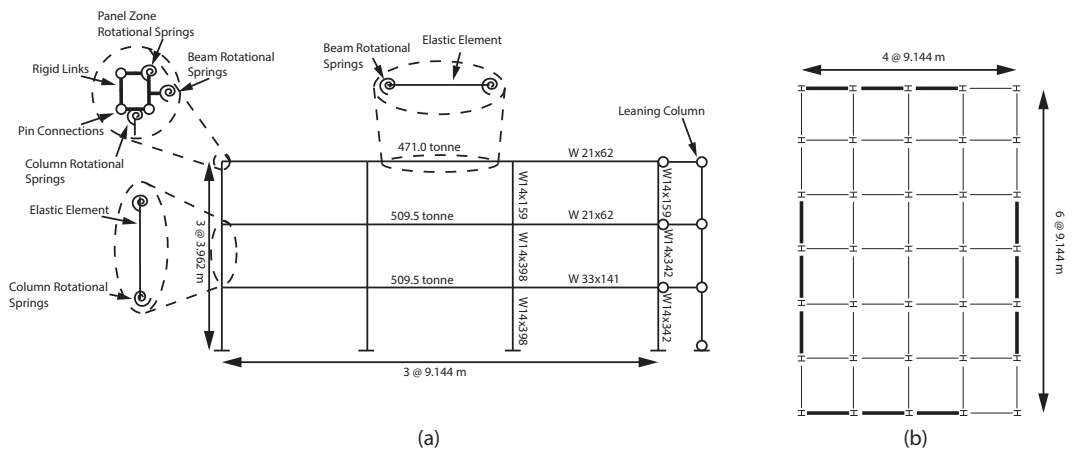


Figure 4.3: (a) Elevation view and modeling details of seismic force-resisting system of three-story steel office type archetype building, (b) Plan view of archetype building

The collapse performance of the archetype frame was evaluated by a multiple stripe analyses using nine different intensity stripes (Baker 2015). For each stripe, 40 ground motion component pairs were selected and scaled

to match a conditional spectrum with a target spectral acceleration at the first-mode period of the building (Baker and Lee 2017). The motions were selected from the far-field NGA-West2 Database (PEER 2013). The conditional mean spectrum for each stripe, as well as the spectrum for each of the 40 ground motions selected at a maximum considered earthquake (MCE) intensity level (2475 years return period) for the building site, are shown in Figure 4.4.

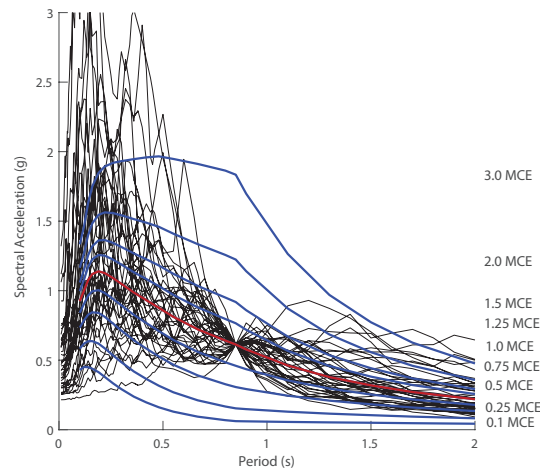


Figure 4.4: Conditional spectra for archetype building

Structural Upgrade Options

Four structural upgrade options were considered in this case study, all selected with a goal of reducing structural damage. The design of each option was performed considering an implementation across all floors. The first option consisted of replacing the pre-Northridge moment resisting connections of the archetype frame with newly developed self-centering sliding hinge joint connections (SCSHJ) (Khoo et al. 2012, Khoo et al. 2013). This type of connection dissipates energy using a sliding interface instead of relying on deformations within the beam-to-column connections.

When coupled with a ring spring (Filiatrault et al. 2000) above and/or below the beam flanges, this connection is able to self-center. The second and third retrofit options consisted of the installation of linear viscous dampers (Christopoulos and Filiatrault 2006) diagonally across a bay opening within the frame. Non-linear viscous dampers were not considered as recent research has demonstrated their potential to increase floor accelerations beyond values obtained in the original structure (Chalarca et al. 2020). The targeted first modal viscous damping ratios were 10% and 25% of critical for the second and third retrofit options, respectively. The fourth structural retrofit option considered in this case study was the installation of diagonal buckling restrained braces (BRB) (Black et al. 2004) across a bay opening within the frame. These braces were designed to replace the MRF as the seismic force-resisting system of the building, while the existing MRF became a secondary system. Details of the implementation of these four structural retrofit options for each floor of the archetype building are summarized in Table 4.1. Clearly, the four retrofit options would not produce the same performance levels. However, the unique costs of each retrofit are also included in the optimization considerations, as summarized in **Upgrade Costing** further in this section.

Table 4.1: Component test sections and major parameters for SHJ and SCSHJ connections

Floor Number	<i>Self-Centering Sliding Hinge</i>			
	<i>Joints at each MRF Connection (100% Self-Centering Ratio)</i>	<i>Linear Viscous Dampers (10% first modal damping)</i>	<i>Linear Viscous Dampers (25% first modal damping)</i>	<i>Buckling Restrained Braces (Yield Strength: 350 MPa)</i>
1	Activation Moment: $M_{ybeam}/3$	Damping Constant: 7,400 kNs/m	Damping Constant: 19,500 kNs/m	Cross-Sectional Area: 4300mm ²
2	Activation Moment: $M_{ybeam}/3$	Damping Constant: 3,900 kNs/m	Damping Constant: 10,200 kNs/m	Cross-Sectional Area: 2800mm ²
3	Activation Moment: $M_{ybeam}/3$	Damping Constant: 1,270 kNs/m	Damping Constant: 3,300 kNs/m	Cross-Sectional Area: 2800mm ²

Note: M_{ybeam} = Yield moment of beam

Nonstructural Upgrade Options

Table 4.2 summarizes both the original and upgraded FEMA P-58 fragility specifiers used for each of the 26 nonstructural component typologies included in the archetype building. Each of these fragility specifiers includes fragility curves and consequence functions for each damage state identified for the specific component. Where more recent nonstructural research results were identified, the associated fragility specifiers were updated, as identified by superscripts in Table 4.2. When specification of capacities was to be provided by a designer, such as anchorage for mechanical equipment, typical design details were obtained from relevant manufacturers' product catalogs. All downtime consequence functions included the repair time from FEMA P-58 and impedance time from RSMMeans for equivalent tasks. These impedance times included design, financing, permitting, and mobilization, but did not explicitly capture environmental factors. In addition, seven of the 26 component consequence functions were modified from those in FEMA P-58. The first six were for each of the piping systems, where the consequence function for the C3021.001a component (Generic Floor Covering - Flooding of floor caused by failure of pipe - Office - Dry) was added to include water damage to surrounding flooring based on estimated affected areas. These areas were determined using both the description of damage in FEMA P-58 and the pipe sizes, where small leaks and smaller diameter pipe breaks caused only a fraction of floor area to be damaged in comparison to breaks in large diameter pipes. The seventh modified consequence function was for the stairs, where the consideration of non-collapse casualty across the affected floor area was added as a consequence if all stair components were

damaged and rendered unusable at that floor, thereby preventing a proper egress path. A proper means of egress was deemed a priority when optimizing for the reduction of casualties, leading to the addition of probabilistic non-collapse casualties as a modification to the stair component consequence function.

Table 4.2: Component test sections and major parameters for SHJ and SCSHJ connections

Component	<i>Original FEMA</i>	<i>Upgraded FEMA</i>	<i>RSMMeans Estimation Itemized Task</i>
	<i>P-58 Fragility Specification</i>	<i>P-58 Fragility Specification</i>	
Chiller	D3031.011c	D3031.013h	236419101160, 15436501700, 51223400672, 50519208575
Cooling Tower	D3031.021c	D3031.023i	236419101160, 15436501700, 51223400672, 50519208575
Air Handling Unit	D3052.011d	D3052.013l	2237433102100, 220548100640, 20548100740, 50519208575, 15436501700
Control Panel	D3067.011a	D3067.12c	262413300600, 50519208575, 50523251350, 51223200200
Motor Controller	D5012.013a	D5012.013d	262413300600, 50519208575, 50523251350, 51223200200,
Low Voltage Transformer	D5012.021b	D5012.023f	261219100300, 51223200200, 50519208575, 15436501700
Distribution Panel	D5012.031b	D5012.033f	262413300600, 50519208575, 50523251350, 51223200200
Potable Piping	D2021.011a D2021.011b	D2021.014a D2021.014b	92226138800, 51223200200, 50519208575, 220548100470, 220548100130, 221113141160
Large Diam. Heat Piping	D2022.023a D2022.023b	D2022.024a D2022.024b	92226138800, 51516051530, 50519208575, 51516051640, 51516052350, 221113231260, 220548100130

Continued on the next page

Continued from previous page

Component	<i>Original FEMA</i>		<i>Upgraded FEMA</i>
	<i>P-58 Fragility Specification</i>		<i>P-58 Fragility Specification</i>
	<i>RSMeans Estimation Itemized Task</i>		
Small Diam. Heat Piping	D2022.011a D2022.011b	D2022.014a D2022.014b	92226138800, 51223200200, 50519208575, 220548100470, 220548100130, 221113141160
Sanitary Piping	D2031.021a D2031.021b	D2031.024a D2031.024b	92226138800, 51516051530, 50519208575, 51516051640, 51516052350, 220548100130, 221113141160, 220548100470
Sprinkler Piping ¹	D4011.021a	D4011.022a	92226138800, 220548100150, 50519208575, 221113231260
Sprinkler Head ²	D4011.031a	D4011.053a	92226138800, 211313504520, 221119140160
Lighting	C3034.001	C3034.002	92226138800, 51516051530, 51516051640, 51516052350
Desktop Equipment	E2022.023	E2022.022	50523300200
Office Furniture ³	E2022.001	E2022.001	102219432100, 50519208575, 51223200200, 50523300200
Suspended Ceiling	C3032.001b	C3032.004b	92226138800, 51516500560, 51516603100, 51223180300, 50523300020
Raised Floor	C3027.001	C3027.002	96913100105, 51223200200, 50523300200, 96913100105
Curtain Glazing ⁴	B2022.001	B2022.002	84413100020, 84413100200
Wall Partitions ⁵	C1011.001a	C1011.001c	92226138800, 28213440250, 51223200200, 51223200200, 50519208575, 50523300200, 92116339200
Roof Covering	B3011.013	B3011.011	50519208575
Large HVAC Duct	D3041.012a	D3041.012d	92226138800, 220548100190
Small HVAC Duct	D3041.011a	D3041.011c	92226138800, 220548100190
HVAC Diffuser	D3041.031a	D3041.32d	92226138800, 51516051530, 51516051640, 51516052350
Stairs ⁶	C2011.021b	C2011.021a	34123500300, 51223200200, 50519208575, 50523251750

Continued on the next page

Continued from previous page

Component	<i>Original FEMA</i>	<i>Upgraded FEMA</i>	<i>RSMMeans Estimation Itemized Task</i>
	<i>P-58 Fragility Specification</i>	<i>P-58 Fragility Specification</i>	
Elevator	D1014.012	D1014.011	50519208575, 51223200200, 51223200200

Superscript indicate that the component fragility curves were updated according to: ¹, ²[Soroushian et al., 2015], ³[Filiatrault et al., 2004], ⁴[Behr, 2001], ⁵[Retamales et al., 2013], ⁶[Bull, 2011]

Upgrade Costing

Costs and downtime estimates for the upgrade work were obtained from the commercial estimation software RSMMeans (2018). The work required for the various upgrade options was documented using existing guidelines for structural upgrades according to ASCE 41-17 (ASCE 2017), and for nonstructural upgrades according to FEMA E-74 (FEMA 2011). The upgrade work was then translated to itemized cost data included in RSMMeans, which provided monetary costs and daily outputs per pre-set work crews for each upgrade. Included in these costs are large items such as heavy equipment rentals, demolition of existing components, as well as design and management overhead costs. Particularly relevant for structural upgrade costing, values for tasks not explicitly identified in RSMMeans were either obtained from tasks with similar scope and activity, such as the installation of specialized connections, or obtained from unit costing provided by third party manufactures, such as prices for viscous dampers. A list of estimation numbers used in the commercial estimation software RSMMeans for each individual non-structural component upgrade is shown in Table 4.2. This list

does not include the overhead costs that are tabulated separately from the total upgrade cost. Each unit cost was also randomly adjusted for each upgrade case using a corresponding normal or lognormal distribution function, provided by RSMMeans, to account for local labor costs and downtime variations. All costs were indexed to 2011-dollar values for the Seattle area, to maintain consistency with the default FEMA P-58 values. The costs of procuring and installing all of the structural elements were included for the cases involving structural retrofits.

4.5.2 Sample Optimization Results

Sample optimization runs using the genetic algorithm for each of the three target metrics considered are summarized in this section. The objective is to show the types and formats of optimization results that can be generated and how they can be used by stakeholders to make investment decisions. In the genetic algorithm, a carryover percentage of 10% and a mutation rate of 2% were used for each of these sample runs. Two convergence criteria were used for this study: 1) a change of less than 1% in the rank of the optimal solution (individual) between the current and the previous generation and, 2) the population of the current generation consists of at least 25% of individuals having the highest ranked genetic code (i.e. 25% of optimal individuals). These stringent convergence criteria were used to ensure the termination of the algorithm at the global optimum solution. To aid in the integration of the FEMA P-58 loss estimation process within the optimization algorithm, the FEMA P-58 program was rewritten as a Monte Carlo loss analysis in Matlab (Mathworks 2018) and example structures were used to verify its accuracy.

The number of realizations used in the Monte Carlo analysis for the original archetype building was set to 2000 to ensure that the coefficient of variation was less than 1%. All other individuals with any upgraded components used 500 realizations, as recommended by FEMA P-58 for loss estimations that include building collapse and casualties (FEMA 2012a). Due to the heuristic searching nature of the genetic algorithm and the variability within the PEER-PBEE framework, 100 optimization runs were conducted for each of the three target metrics to ensure the true global optimized solutions were achieved. The cumulative optimal results obtained from the 100 runs are discussed in a later section. To further validate the termination of the algorithm at the global optimum, the rank results were verified with an optimization run conducted for a minimum of 1000 generations for each target metric.

Optimization for Economic Target Metric

The values of the economic ranking functions obtained over 25 generations for the first owner profile (i.e. a 4% internal rate of return and an occupation time of 40 years) are shown in Figure 4.5 (a). The ranks of the first generation, whose individuals were constructed randomly, exhibit large variabilities. The ranks of the subsequent generations trend to larger ranking values, as is desired for this target metric. Deviations from this trend in subsequent generations are a result of random factors such as: the random variation in the loss estimation obtained from the FEMA P-58 methodology, the probabilistic selection of lower ranked parents mating during the crossover component of the genetic algorithm, and/or the probabilistic occurrence of a mutation within the genetic algorithm, as described earlier. The baseline, shown in Figure 4.5 (a) with a rank of zero, is associated with

the original (non-upgraded) archetype building. The “locked” rank value shown in Figure 4.5 (a) indicates the rank associated with the fully upgraded individual (i.e. including the structural upgrade type with the best collapse performance and all nonstructural upgrades) in each generation. The optimal rank value is first obtained in the 13th generation and no substantial increases in rank values are observed after this generation. Figure 4.5 (b) shows the evolution over 25 generations of the two convergence criteria described previously.

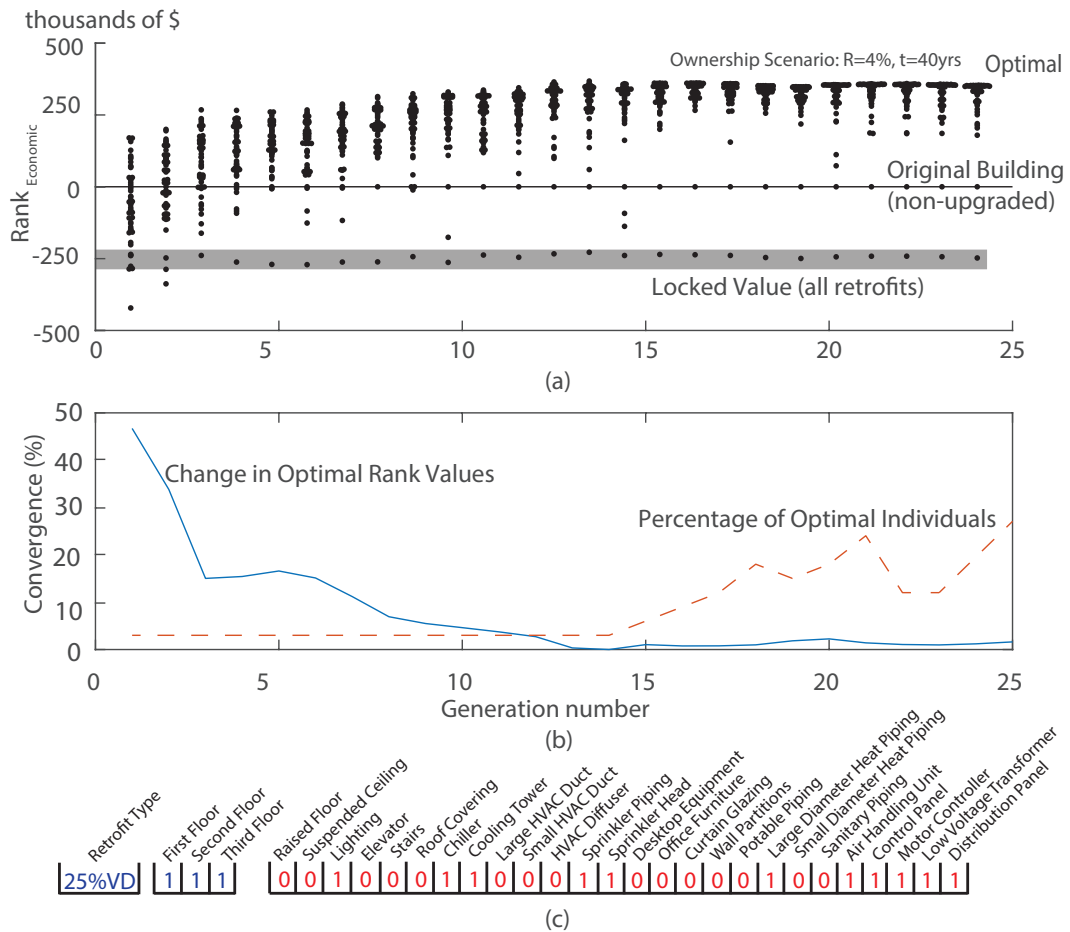


Figure 4.5: (a) Ranking functions for economic target metric, (b) Changes in convergence criteria, (c) Genetic code of optimal solution

The genetic code of the optimal individual obtained for this run is shown

in Figure 4.5 (c), and consists of upgrading the structure with viscous dampers at all floors to target 25% of critical viscous damping (25%VD in Figure 4.5 (c)) and upgrading 11 of the 26 nonstructural typologies included in the building. The main nonstructural upgrades included in the optimal solution are for large mechanical and electrical systems, such as the chiller, sprinkler systems, and large HVAC equipment, for which damage translates into large *EAL* values. The optimal solution obtained reduces the EAL of the original archetype building by 89% with a *PV* loss reduction of 25% of the building value and a corresponding upgrade cost equal to 13% of the building value. The structural and nonstructural components selected for upgrade in the optimal solution is discussed in more detail later.

Optimization for Downtime Target Metric

The results of a single optimization run for the second downtime target metric are shown in Figure 4.6 (a). The same owner profile of 4% internal rate of return and a 40-year occupancy time was considered and a sequencing factor *S* of 6.0 was used in Equation 4.4.3. Again, the baseline rank shown in Figure 4.6 (a) indicates the downtime calculated from the original archetype building. The main cause of the persistence of high variability in the ranks shown in Figure 4.6 (a) compared to that in Figure 4.5 (a) is the larger variations in *EAT* (compared to *EAL*) obtained from the FEMA P-58 methodology (FEMA 2012a), especially when quantifying the variability of the recovery time required for a collapsed structure. The maximum rank (i.e. optimum solution) is achieved for the first time in the 7th generation. However, as observed previously, the stringent optimal population percentage portion of the convergence criteria forces the genetic algorithm to continue

up to the 25th generation before both convergence criteria are met. The results shown in Figure 4.6(a) demonstrate the importance of considering both convergence criteria simultaneously, as the change in optimal rank value from the 3rd to 4th generation does not exceed 1%, which would have resulted in a convergence at a local maximum and a termination of the genetic algorithm, had the second convergence criterion of 25% of optimum individuals in a population not been included. Figure 4.6 (b) shows the genetic code of the optimum individual, which consists of upgrading the structure with viscous dampers to target 25% viscous damping at all floors and upgrading 9 of the 26 nonstructural typologies included in the building. For this downtime target metric, the structural solution is the same as for the economic metric, but the nonstructural upgrades focus mainly on nonstructural typologies requiring large repair times, such as roof coverings, wall partitions, curtain glazing, and large HVAC equipment. The optimal solution reduces the *EAT* by 84% relative to the original (non-upgraded) building, leading to a reduction of 43 days in total downtime over the building occupancy time and an upgrade downtime of 20 days.

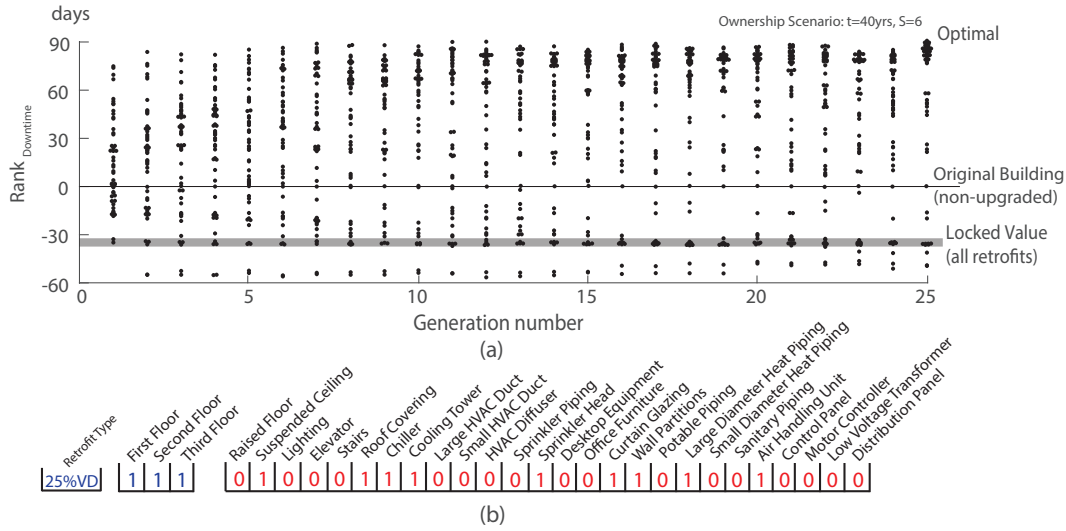


Figure 4.6: (a) Ranking functions for downtime target metric, (b) Genetic code of optimal solution

Optimization for Casualty Reduction Target Metric

The results of a single optimization run for the third casualty reduction target metric are shown in Figure 4.7 (a). In this case, the bits representing casualty-neutral nonstructural components were locked at a value of zero, thereby removing their consideration from the optimization process. As discussed above, the optimization results for this target metric were expected to be trivial. The solution for this target metric is first achieved in the first generation and the genetic algorithm rapidly converges within five generations. The genetic code of the optimal individual is shown in Figure 4.7 (b) and again consists of upgrading the structure with viscous dampers to target 25% viscous damping at all floors but, this time, upgrading only the stairs, curtain glazing, hot water piping, office furniture, and lighting, which are the nonstructural element typologies in the building that cause the majority of possible injuries and casualties.

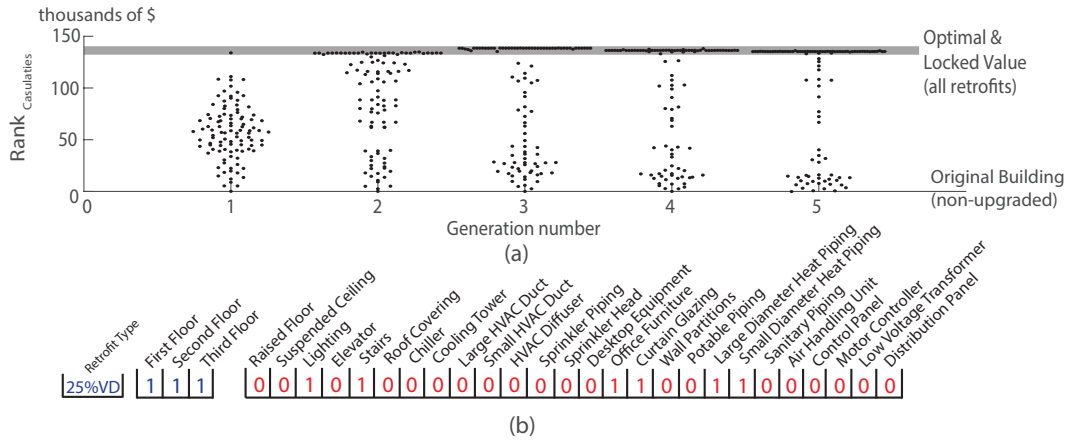


Figure 4.7: (a) Ranking functions for casualty reduction targeted metric, (b) Genetic code of optimal solution

4.5.3 Prioritization of Structural and Nonstructural Upgrades

The sample optimization runs described above were repeated 100 times for each target metric to ensure the global optimum was being achieved. The components selected for upgrade in the optimal solution for each of the three different target metrics are compared in Figure 4.8 for the same owner profile of a 4% internal rate of return r , a 40-year occupancy time t , and a sequencing factor S of 6.0. The upgrade priority of a particular component is expressed in Figure 4.8 by the number of optimization runs in which it was upgraded in the optimal solution. The upgrade of a component has the highest priority (100) when it is selected in all optimized solutions and has the lowest priority (0) when it is not part of any optimized solution. Figure 4.8 also shows results for a “combined” target metric of each component, defined as the average upgrade priority across the three target metrics. Note that while a simple combination is used herein for illustration, other combination rules can be used depending

on the importance that a specific owner assigns to each of the three target metrics. Nevertheless, the numerical prioritization format shown in Figure 4.8 can be a useful tool to building owners and non-engineering professionals to better rationalize building upgrades given limited resources.

Category	Component	Economic	Downtime	Casualty Reduction	Combined
No Structural Upgrades	First Floor Structural	10	6		4
	Second Floor Structural	10	6		4
	Third Floor Structural	30	20		12
Structural SCSHJ	First Floor Structural				
	Second Floor Structural				
	Third Floor Structural				
Structural 10% VD	First Floor Structural				
	Second Floor Structural				
	Third Floor Structural				
Structural 25% VD	First Floor Structural	90	94	100	96
	Second Floor Structural	90	94	100	96
	Third Floor Structural	70	80	100	88
Structural BRB	First Floor Structural				
	Second Floor Structural				
	Third Floor Structural				
Mech. Equip.	Chiller	100	100		66
	Cooling Tower	100	60		48
	Air Handling Unit	77	55		35
	Control Panel	100	24		40
	Motor Controller	100			30
	Low Voltage Transformer	75			24
	Distribution Panel	100			33
Plumbing	Potable Piping	35			
	Large Diam. Heat Piping	100	70	31	65
	Small Diam. Heat Piping	35		16	16
	Sanitary Piping	35			11
	Sprinkler Piping	70	33		33
	Sprinkler Head	70	70		44
Contents	Lighting	100	35	16	50
	Desktop Equipment		43		15
	Office Furniture		42	16	20
Finishes	Suspended Ceiling		70		23
	Raised Floor				
	Curtain Glazing		100	100	65
	Wall Partitions		100		33
	Roof Covering		81		26
HVAC	Large HVAC Duct		26		8
	Small HVAC Duct		31		10
	HVAC Diffuser				
	Stairs		35	100	44
	Elevator				

Figure 4.8: Prioritization of structural and nonstructural upgrades for economic, downtime, casualty reduction and combined target metrics for first owner profile

The optimum structural upgrade across all three target metrics is the installation of 25% damped viscous dampers in all floors of the building. This is to be expected since the incorporation of highly damped viscous devices

substantially reduces both peak inter-story drifts and peak floor accelerations (Christopoulos and Filiatrault, 2006), which are the two EDPs used in the nonstructural fragility curves. Also, the downtime required to install large viscous dampers is not significantly different from the installation times of the other three structural retrofit upgrades considered. The “no structural upgrades” in these figures represents the original structure with no upgrades. These were included such that the sum should equal 100%. The nonstructural upgrades, however, vary significantly across the three different target metrics considered. The components with the highest upgrade priority for the economic target metric include the lighting system, some of the piping, and the majority of the mechanical equipment. For the downtime target metric, the highest nonstructural upgrade priorities were shifted from the mechanical equipment to the glazing systems, partition walls, and the piping systems. These nonstructural components were avoided by the optimization process based on the economic target metric because of their high upgrade costs, but had very large downtime consequences upon failure. Finally, the trivial solution for the casualty reduction target metric includes the highest upgrade priorities to the nonstructural components whose failures could lead to larger quantities of deaths or injuries to occupants located in their vicinities, such as the stairs and curtain glazing. The components with intermediate upgrade priority values (i.e. which are not 0% or 100%) result from the combined effects of 1) the variability of the cost of the component upgrade, 2) the probability of failure of a component, defined in FEMA P-58 by fragility curves, and 3) the variation in repair cost of a component once failure is achieved, defined in FEMA P-58 by consequence functions. These “medium-priority” nonstructural components, such as the sprinkler piping

system or air handling unit, may need to be reviewed on a case-by-case basis, including more specific information on their upgrade costs, before a final upgrade decision can be made. These medium-priority nonstructural components were only selected in the optimal solution for the economic target metric when their cumulative consequence costs were relatively high and/or their upgrade costs were relatively low. The overlapping combination of individual component consequence functions and upgrade costs is not the only deciding factor when determining a component's upgrade priority. The use of a full PBEE analysis for each optimization run ensures that only components whose damage states occur before the collapse of the structure are identified as important for upgrade. Components that might have a favorable upgrade cost/consequence function relationships are maintained at a low priority if their damage states do not occur before collapse of the structure. An example of this is the HVAC diffuser, which is never selected in the optimum solution because building collapse is predicted before the damage state of this component. Some low priority components were identified in the casualty reduction target metric, such as the heat piping, lighting, office furniture, and HVAC diffusers, as their consequence functions resulted in a small but non-zero probability of casualties or injuries.

4.5.4 Parametric Studies for Internal Rate of Return and Occupancy Time

Economic target metric optimization runs using different internal rates of return in Equation 4.4.2 were conducted to determine its impact on the optimal cost of upgrade. Figure 4.9 (a) shows the relationship between the

total mean upgrade cost of the optimum solutions (as a fraction of building value) and the internal rate of return. This relationship indicates how much upgrade investment should be made by an owner in order to maintain a desired internal rate of return. The results shown in Figure 4.9 (a) were obtained from the optimal solutions of 100 genetic algorithm runs, at each of the selected internal rates of return, using an occupancy time of 40 years. The results show that an increase of the internal rate of return from 2% to 6% results in a rapid decrease in the total mean upgrade cost from 25% to 5% of building value. Further increases in internal rate of return beyond 6% result in relatively little change in upgrade cost, with a minimum level of investment maintained at 1.5% of the building value for internal rates of return between 12% and 16%. Figure 4.9 (b) shows that as the internal rate of return is increased, certain components are excluded from the optimal solution. For an internal rate of return of 16%, the upgrade investment is limited only to larger equipment items, such as the chiller and cooling tower, with no structural upgrade. Note that the seismic performance, and associated losses, of each optimum solution obtained in Figure 4.9 will be poorer for lower mean upgrade costs.

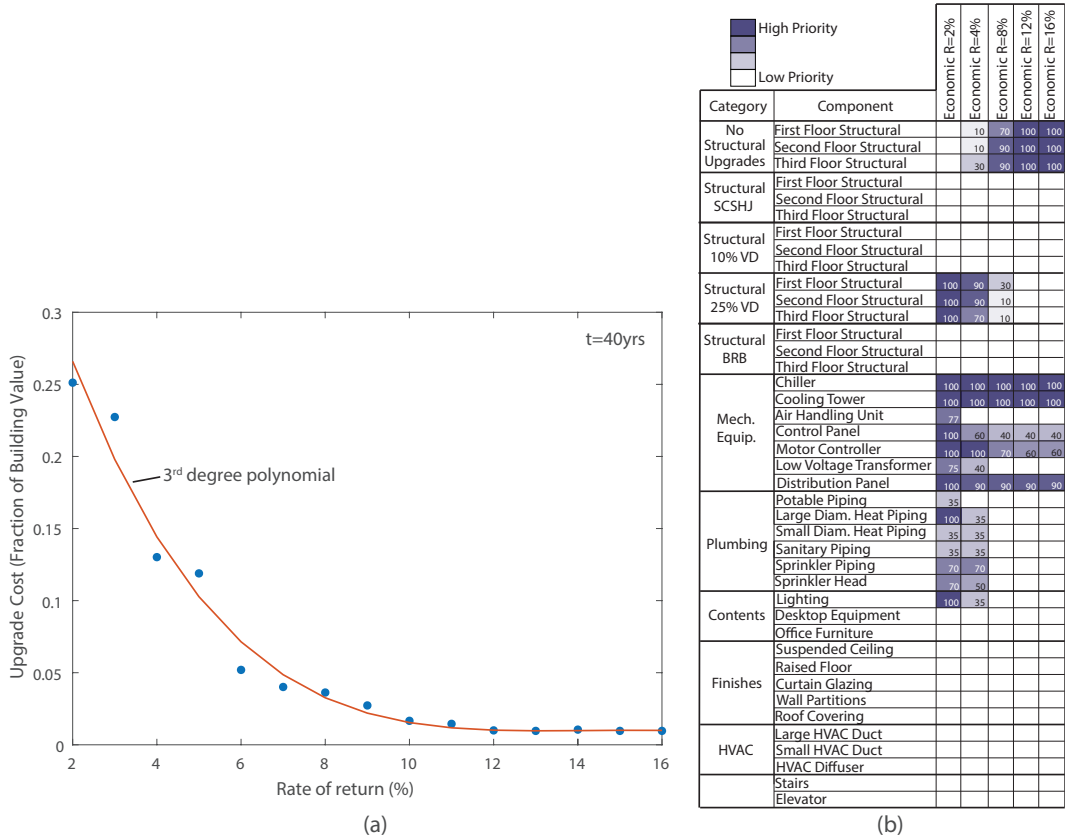


Figure 4.9: a) Upgrade cost of optimal solution vs internal rate of return, b) Component prioritization for specific rates of return

A similar parametric study was conducted to identify how the expected occupancy time of the archetype building would affect the optimal downtime solution with a downtime target metric, while maintaining a sequencing factor of 6.0 in Equation 4.4.3. The resulting relationship shown in Figure 4.10 (a) indicates that when the expected occupancy time increases, the optimal amount of downtime spent upgrading also increases. Figure 4.10 (b) demonstrates the additional components that are a priority to upgrade as the occupancy time is increased, with almost all components having some level of upgrade priority when considering long occupancy time horizons.

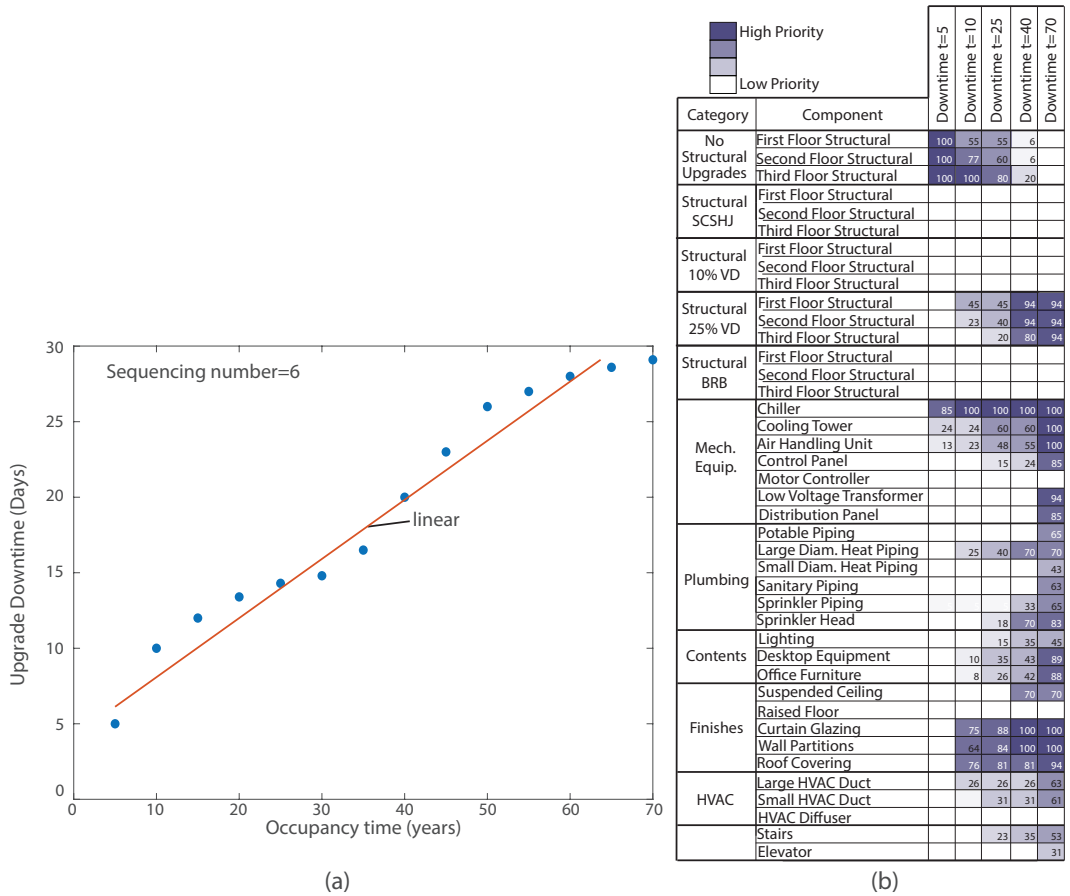


Figure 4.10: a) Occupancy time vs upgrade time of optimal solution, b) Component prioritization at specific occupancy time

4.5.5 Influence of Building Owner Profiles

Results such as those of the case study described above would provide the owner of the archetype building with different recommendations for seismic upgrades depending on that owner’s priorities. As described in detail above, for an owner having a 4% rate of return and an occupancy time of 40 years, a focus on the economic target metric leads to a recommendation to spend 13% of the building’s value on a combination of structural and nonstructural upgrades. With a focus on a reduction of downtime, the optimization results

suggest an upgrade downtime of 20 days, again including both structural and nonstructural work. The optimization of the casualty reduction target metric led to the same structural system upgrade as for the economic and downtime target metrics, but with nonstructural upgrades to only the glazing and stairs. The retrofit recommendations are substantially different for a different owner profile. For example, a 12% internal rate of return and a 10-year occupancy time is considered to represent a high-yield and short-term owner with a higher acceptable risk level, such as a real-estate investor/developer. For this owner profile and the economic target metric, the recommendation is to spend only 1.2% of the building value, focused only on nonstructural upgrades to the chiller, cooling towers and distribution panel. For the same owner focused on reducing downtimes over the 10-year occupancy time, only 10 days (sequenced in six parts) should be spent on nonstructural upgrades to the chiller, glazing and partition walls. To optimize the casualty target metric, the same trivial solution is obtained as for the previous owner profiles. These differences in optimized upgrade solutions are important for various types of owner objectives and profiles, and would be very difficult to identify using the FEMA P 58 methodology with only a small number of upgrade cases based on engineering judgement. The consideration of all possible genetic codes (i.e. brute-force solution) to identify the optimum individual for each target metric would have required over 2 billion different loss estimation analyses. In contrast, the genetic algorithm converged to each optimal solution with only 1250 loss estimation analyses.

4.6 Conclusions

This study implemented a genetic algorithm for the integrated optimum seismic design or retrofit of buildings within the Pacific Earthquake Engineering Research (PEER) Performance-Based Earthquake Engineering (PBEE) framework. This algorithm integrates the consideration of both structural and nonstructural upgrades based on system-level performance and loss estimations. The capabilities of the optimization procedure were illustrated through the seismic retrofit case-study of a three-story steel moment-resisting frame archetype building and for the three different target metrics used in the PEER-PBEE framework: 1) an economic target metric, 2) a downtime target metric and, 3) a casualty reduction target metric. Although the results of the case study indicated the same structural upgrade (incorporation of 25% damped linear viscous dampers) across the three target metrics, significant variations in nonstructural upgrade priorities were obtained. Furthermore, the structural and nonstructural optimization priorities differed significantly for different owners' risk tolerances and building occupancy times. Whereas these differences in optimized upgrade solutions would be very difficult to identify using only a small number of upgrade cases based mainly on engineering judgement, the optimum solution for each target metric was achieved by the genetic algorithm by evaluating only a small fraction of all possible cases. The parametric study conducted on the effects of the owner's expected internal rate of return and building occupancy time on the optimum retrofit solutions illustrates the flexibility of the genetic algorithm optimization process in accommodating different owner profiles. This optimization process can also be extended to any number of

other variables, including the consideration of component or system level constraints.

4.7 Acknowledgments

The authors gratefully acknowledge the supports of Mr. Craig Winters from Taylor Devices for providing viscous damper costing data, the engineering department at RSMeans for providing statistical cost estimation information, Dr. Vladimir Mahalec for his preliminary guidance on various optimization methods, and Dr. Charles Clifton, Dr. Greg MacRae and Dr. Hsen-Han Khoo for providing component test data for the SCSHJ connections. The authors would like to acknowledge the financial support of the Natural Sciences and Engineering Research Council of Canada. The optimization methodologies presented in this study are included in a patent pending application submitted by the 1st two authors.

4.8 References

- AISC(American Institute of Steel Construction). (2016). “Specification for Structural Steel Buildings.” *AISC 360-16*, Chicago, IL, US
- ASCE(American Society of Civil Engineers). (2016). “Minimum Design Loads and Associated Criteria for Buildings and Other Buildings.” *ASCE 7-16*, Reston, VA, US
- ASCE(American Society of Civil Engineers). (2017). “Seismic Evaluation and Retrofit of Existing Buildings.” *ASCE 41-17*, Reston, VA, US

- Apostolakis, G., Dargush, G., and Filiatrault, A. 2014. “Computational Framework for Automated Seismic Design of Self-Centering Connections in Steel Frames.” *Journal of Computing in Civil Engineering*, 28(2), 170-181.
- Baker, J. W. (2015). “Efficient Analytical Fragility Function Fitting Using Dynamic Structural Analysis.” *Earthquake Spectra*, 31(1) 579–599.
- Baker, J. W., and Lee, C. (2017). “An Improved Algorithm for Selecting Ground Motions to Match a Conditional Spectrum.” *Journal of Earthquake Engineering*, 22 (4), 708-723.
- Behr, R. (2001) “Architectural Glass for Earthquake-resistant Buildings.” *Glass Processing Days*, Vol. 14, 18-21.
- Black, C. J., Makris, N., and Aiken, I. D. (2004). ”Component Testing, Seismic Evaluation and Characterization of Buckling-Restrained Braces.” *Journal of Structural Engineering*, 130(6), 880-894.
- Bradley, B., Dhakal, R., Cubrinovski, M., MacRae, G., and Lee, D. (2009) “Seismic Loss Estimation for Efficient Decision Making.” *Bulletin of the New Zealand Society for Earthquake Engineering*, 42 (2), 96-110.
- Bull, D., (2011) “Stairs and Access Ramps Between Floors in Multi-story Buildings.” *Report to the Royal Commission*, Vol. 1, 1-8.
- Camp, C., Pezeshk, S., and Cao, G. (1998) “Optimized Design of Two-Dimensional Structures Using a Genetic Algorithm.” *Journal of Structural Engineering*, 124 (5), 551-559.

Carrol, D. (2004) *FORTRAN Genetic Algorithm Driver*, CU Aerospace, Champaign, IL.

Chalarca, B., Filiatrault, A., and Perrone, D. (2020). “Seismic Demand on Acceleration-Sensitive Nonstructural Components in Viscously Damped Braced Frames” *Journal of Structural Engineering*, 146(9).

Charney, F., and Pathak, R. (2008). “Sources of Elastic Deformation in Steel Frame and Framed-Tube Buildings: Part 1: Simplified Subassemblage Models.” *Journal of Constructional Steel Research*, 64(1), 87–100.

Christopoulos, C., and Filiatrault, A. (2006) *Principles of Passive Supplemental Damping and Seismic Isolation*, IUSS Press, Pavia, Italy

Cornell, C. A., and Krawinkler, H. (2000) “Progress and Challenges in Seismic Performance Assessment.” *PEER News*, April

DOT(Department of Transportation) (2016) “Guidance on Treatment of the Economic Value of a Statistical Life (VSL) in U.S. Department of Transportation Analyses – 2016 Adjustment.” *U.S. Department of Transportation Office of the Secretary of Transportation, Memorandum to Secretarial Officers*, August 8th, 2016, Washington, D.C.

Farhat, F., Nakamura, S., and Takahashi, K. (2009) “Application of Genetic Algorithm to Optimization of Buckling Restrained Braces for Seismic Upgrading of Existing Structures.” *Computers and Structures*, 87, 110-119

FEMA(2011). “Reducing the Risks of Nonstructural Earthquake Damage-A Practical Guide.” *Report E-74 Federal Emergency Management Agency*,

Washington, D.C.

FEMA(2012a). “Seismic Performance Assessment of Buildings - methodology.” *Report P-58 Federal Emergency Management Agency*, Vol. 1, 1-278, Washington, D.C.

FEMA(2012b). “Seismic Performance Assessment of Buildings - Normative Quantity Estimating Tool.” *Report P-58 Federal Emergency Management Agency*, Vol. 3.3, Washington, D.C.

Filiatrault, A., Tremblay, R., and Kar, R. (2000) “Performance Evaluation of Friction Spring Seismic Damper.” *Journal of Structural Engineering*, 126(4), 491-499.

Filiatrault, A., Kuan, S., and Tremblay, R. (2004) “Shake Table Testing of Bookcase-partition Wall Systems.” *Canadian Journal of Civil Engineering*, 31, 664-676.

Gidaris, I., and Taflanidis, A. (2015) “Performance Assessment and Optimization of Fluid Viscous Dampers Through Life-cycle Cost Criteria and Comparison to Alternative Design Approaches.” *Bulletin of Earthquake Engineering*, 13, 1003-1028.

Golberg, D. (1989) *Genetic Algorithms in Search, Optimization and Machine Learning*, Addison-Wesley, Boston, MA

Gupta, A., and Krawinkler, H. (1999). “Seismic Demands for Performance Evaluation of Steel Moment Resisting Frame Buildings.” *Department of Civil and Environmental Engineering*, Stanford University, Report No. 132.

Hofer, L., Zanini, M., Faleschini, F., and Pellegrino, C. (2018) “Profitability Analysis for Assessing the Optimal Seismic Retrofit Strategy of Industrial Productive Processes with Business-Interruption Consequences.” *Journal of Structural Engineering*, 144 (2)

Ibarra, L., Medina, R., and Krawinkler, H. (2005). “Hysteretic Models That Incorporate Strength and Stiffness Deterioration” *Earthquake Engineering and Structural Dynamics*, 34, 1489-1511.

Khoo, H. H., Clifton, C., Butterworth, J., and MacRae, G. (2013). “Experimental Study of Full-scale Self-centering Sliding Hinge Joint Connections with Friction Ring Springs.” *Journal of Earthquake Engineering*, 17(7), 972–977.

Khoo, H.-H., Clifton, C., Butterworth, J., MacRae, G., Gledhill, S., and Sidwell, G. (2012). “Development of the Self-centering Sliding Hinge Joint with Friction Ring Springs.” *Journal of Constructional Steel Research*, 78, 201–211.

Kirmayaz, S., Ince, T., and Gabbouj, M. (2014) *Multidimensional Particle Swarm Optimization for Machine Learning and Pattern Recognition*, Springer, Berlin, Germany, 15th Printing.

MathWorks(2018). “Global Optimization Toolbox” *Matlab Documentation*

McKenna, F., Fenves, G. L., and Scott, M. (2000). *Open System for Earthquake Engineering Simulation*. University of California Berkeley, CA.

Miranda, E., and Aslani, H. (2003) “Probabilistic Response Assessment for

Building-Specific Loss Estimation.” *Pacific Earthquake Engineering Research Center Report No. 2003/03*, University of California Berkeley, California.

Miranda, E., and Taghavi, S. (2003) “Estimation of Seismic Demands on Acceleration-sensitive Nonstructural Components in Critical Facilities.” *Proceedings of ATC-29-2 Seminar on Seismic Design, Performance, and Retrofit of Nonstructural Components in Critical Facilities, ATC-29-2 Report*, Applied Technology Council, California

Mitchell, M. (1999). *An Introduction to Genetic Algorithms*, MIT Press, Cambridge, Massachusetts, 5th Printing.

Moehle, J., and Deierlein, G. (2004). “A Framework Methodology for Performance-Based Earthquake Engineering.” *Proceedings of the 13th World Conference on Earthquake Engineering (WCEE)*, Vancouver, BC, Canada

Molina, C., Almufti, S., Wilford, M., and Deierlein, G. (2016) “Seismic Loss and Downtime Assessment of Existing Tall Steel-Framed Buildings and Strategies for Increased Resilience.” *Journal of Structural Engineering*, 142 (8),

PEER(Pacific Earthquake Engineering Research Center) (2013) “PEER NGA-West2 Database.” *Pacific Earthquake Engineering Research Center Report No. 2012/03*, Berkeley, California.

Pollini, N., Lavan, O., and Amir, O. (2017) “Minimum-cost Optimization of Nonlinear Fluid Viscous Dampers and their Supporting Members for

Seismic Retrofitting.” *Earthquake Engineering and Structural Dynamics*, 46, 1941-1961.

Pollini, N., Lavan, O., and Amir, O. (2018) “Optimization-based Minimum-cost Seismic Retrofitting of Hysteretic Frames with Nonlinear Fluid Viscous Dampers.” *Earthquake Engineering and Structural Dynamics*, 47, 2958-3005.

Retamales, R., Davies, R., Mosqueda, G., and Filiatrault, A. (2013) “Experimental Seismic Fragility of Cold-Formed Steel Framed Gypsum Partition Walls.” *Journal of Structural Engineering*, 139 (8), 1285-1293.

Rojas, M., Foley, C., and Pezeshk, S. (2011) “Risk-based Seismic Design for Optimal Structural and Nonstructural System Performance.” *Earthquake Spectra*. 27 (3), 857-880

RSMeans(2018) “Commercial Renovation Cost Data.” *Reed Construction Data*, Norwell, MA,

Shilling, J. and Wurtzebach, C. (2012) “Is Value-Added and Opportunistic Real Estate Investing Beneficial? If So, Why?” *Journal of Real Estate Research*, 34 (4), 429-461.

Soroushian, S., Zaghi, A., Maragakis, M., Echevarria, A., Tian, Y., and Filiatrault, A. (2015) “Analytical Seismic Fragility Analyses of Fire Sprinkler Piping Systems with Threaded Joints.” *Earthquake Spectra*, 31 (2), 1125-1155.

Sousa, L., and Monteiro, R. (2018) “Seismic Retrofit Options for Nonstructural Building Partition Walls: Impact on Loss Estimation and Cost-benefit

Analysis.” *Engineering Structures*, 161, 8-27

UBC(Uniform Building Code) (1994) *Structural Engineering Design Provisions vol. 2*, International Conference of Building Officials, Lansing, Michigan.

Wongprasert, N., and Symans, D. (2004) “Application of a Genetic Algorithm for Optimal Damper Distribution within the Nonlinear Seismic Benchmark Building.” *Journal of Engineering Mechanics*, 130, (4), 401-406.

Chapter 5

A FRAMEWORK FOR THE RAPID ASSESSMENT OF SEISMIC UPGRADE VIABILITY USING PERFORMANCE BASED EARTHQUAKE ENGINEERING

5.1 Abstract

The Performance Based Earthquake Engineering (PBEE) methodology allows designers to deaggregate expected seismic losses in a building to a component level. This deaggregated information provides the opportunity to tailor upgrade strategies to individual structures based on sources of losses. However, the optimization of an upgrade strategy becomes difficult because of the relationship between a structure and its nonstructural components; hence, multiple competing upgrade options must be considered. To address this obstacle, this paper proposes a framework to guide the assessment of the viability of both structural and nonstructural upgrade strategies, while accounting for limited design resources likely encountered in the early stages of the design process. The framework utilizes the median shift probability (MSP) method, a modified version of the PBEE method introduced in this paper, to rapidly summarize the effects of structural upgrades on nonstructural components by considering the impacts of structural

modifications on the floor hazards. While accounting for this relationship, the MSP method utilizes the deaggregation of loss across different source categories to identify the benefit of combined structural and nonstructural upgrades, increasing a designer’s understanding of the impact of structural upgrades on losses and allowing for the rapid determination of optimized upgrade strategies unique to the owner’s conditions. A case study example of the implementation of the framework is provided, and the results obtained from the MSP method are compared with those obtained from more rigorous but resource-intensive optimization analysis. An implementation of the MSP method in Microsoft Excel is provided with this paper.

5.2 Introduction

5.2.1 Current Methods for Seismic Upgrade

Evaluation and Viability

The development of the Performance-Based Earthquake Engineering (PBEE) methodology by the Pacific Earthquake Engineering Research (PEER) Center (Cornell and Krawinkler 2000; Miranda and Aslani 2003) has provided a process for quantifying earthquake-induced losses using metrics beyond structural performance. This methodology has highlighted the importance of considering both structural and nonstructural seismic losses in seismic design and retrofit (Miranda and Taghavi 2003; Bradley et al. 2009). In parallel with general loss reduction considerations, seismic design guidelines such as ASCE 41 (ASCE 2017) and the Resilience-based Earthquake Design Initiative (REDi) rating system (Almufti and Willford

2013) have been developed based on seismic performance targets, ranging from collapse prevention to immediate occupancy, and are applied to both structures and nonstructural components. However, while the performance of the structure and the nonstructural components is often treated independently in these design guidelines, the PBEE methodology captures the relationships between them (Bradley et al. 2009; Günay and Mosalam 2013, Perrone et al. 2019; O’Reilly and Calvi 2020). These relationships must be considered when evaluating seismic upgrades to a building, as the effect of these relationships can include: a reduction of expected benefits from the implementation of higher performing seismic force-resisting systems (SFRS) if seismic upgrades to the nonstructural components are not considered; the benefits provided by upgrading the nonstructural components not being wholly achieved if the structure is not similarly robust; and changes in the dynamic properties of a structure due to structural upgrades impacting the engineering demand parameters (EDPs) imposed on the nonstructural components. Current PBEE evaluation methodologies capture these relationships implicitly through scenario-based evaluations, but do not facilitate the implementation of an integrated and optimized upgrade strategy because they require a trial-and-error approach aided only by guidance from experienced designers. A further challenge facing decision makers when attempting to reduce exposure to seismic loss is optimizing the upgrade investment. Recently, several studies have presented methods for comparing the costs and benefits of structural upgrades and have shown that implementing a high-performing SFRS can provide a net positive benefit. Galanis et al. (2018) used the PBEE methodology to evaluate the cost-benefit of structural seismic upgrades and demonstrated its use on two

case-study residential buildings in Europe. Hofer et al. (2018) applied the PBEE methodology to determine a profitability index associated with various seismic retrofit strategies for an industrial facility. Most studies that use life cycle assessment to determine the viability of a seismic upgrade use as their metric either a net present value (NPV) or a benefit-cost ratio (BCR) calculation:

$$NPV = (EAL_O - EAL_U)AM - UC \quad (5.2.1)$$

$$BCR = \frac{EAL_O - EAL_U}{UC} AM \quad (5.2.2)$$

where EAL_O is the expected annual loss of the original (non-upgraded) building, EAL_U is the expected annual loss of the upgraded building, UC is the upgrade cost, and AM is an amortization conversion expressed by:

$$AM(R, t) = \left(1 - \frac{1}{(1+r)^t}\right) r^{-1} \quad (5.2.3)$$

where r is the internal rate of return or discount rate, and t is the expected occupancy time of the building in years. Both the NPV and BCR equations compare the reduction in loss and the upgrade cost, where a positive value of NPV or a BCR value exceeding unity indicates that the proposed upgrade strategy yields a reduction in seismic losses that exceeds the implementation cost and is, therefore, viable. However, the studies described above limit the scope of the upgrade strategy to structural modifications, neglecting the effect of upgrading the nonstructural components. In Chapter 4, a methodology was developed to systematically

determine optimal upgrade strategies when considering both structural and nonstructural components. For this purpose, a genetic algorithm was used to define each “individual” in a potential upgrade generation as a string of bits. Both structural and nonstructural upgrades were considered in each individual, and each change of a bit from a value of 0 to 1 corresponded to a component being seismically upgraded, resulting in a change to both the capital cost and estimated building loss. The flexibility of the algorithm allowed multiple target metrics, such as minimizing economic costs or downtime, including both upgrade costs and reduction in seismic losses. While a genetic algorithm provides a systematic way of determining optimal seismic upgrades and significantly reduces the computational effort when compared to a brute force approach, its implementation can still be onerous during the preliminary phases of an upgrade feasibility study, where the full scope of the possible upgrade strategies is not yet defined. Furthermore, previous work has mostly measured the gains obtained from various upgrade strategies by comparing the reduction in the final loss value obtained from the PBEE methodology, using either a scenario- or time-based assessment (FEMA 2012). This comparison of final values only indicates overall viability of the proposed upgrade strategy and does not provide detailed reasoning on the design and selection of the combination of structural and nonstructural upgrades. Such guidance would be valuable at the preliminary stages of decision-making. To address these needs, this paper presents a framework to guide decision-making when contemplating seismic upgrades. The goal is to provide a more formalized and accessible evaluation framework for practicing engineers and stakeholders who use PBEE to evaluate the viability of an upgrade through increasing layers of analytical complexity. The paper first

introduces a three-level framework for assessing the viability of seismic upgrades. The first two levels of this framework utilize a novel and rapid modification to the PBEE evaluation process, referred to as the median shift probability (MSP) method. The MSP is introduced in this paper along with a summary of the required PBEE equations. The third level of this framework is implemented using the genetic algorithm optimization presented in Chapter 4. Finally, a case study is presented to illustrate the application of the framework and MSP method by initially assessing the viability of several potential structural upgrade strategies, before comparing the results of this assessment with the results obtained from the more rigorous Level 3 optimization process utilizing the genetic algorithm.

5.2.2 Overview of Proposed Framework

The proposed framework divides the upgrade design and viability assessment into three distinct levels, as shown in Figure 5.1, where each level has increasing analytical refinement. Information on the original conditions of the structure, such as probability distributions describing the collapse, residual and floor hazard curves, are required to serve as a point of comparison. In Level 1, an approximate cost of a structural upgrade is used to determine the required changes to each of these curves according to the anticipated structural upgrade behaviour until a positive NPV is obtained. These required changes are then assessed by the designer to determine if they are likely to be achievable based on the proposed upgrade type. If so, the investment of the engineering resources required for a Level 2 analysis is justified, and a design of each upgrade and the development of corresponding analytical models is used to refine each upgrade

curve. The results of this structural analysis are then used to confirm the positive *NPV* result for the structural upgrade before deciding whether to invest the additional resources required to fully optimize the upgrade strategy in Level 3.

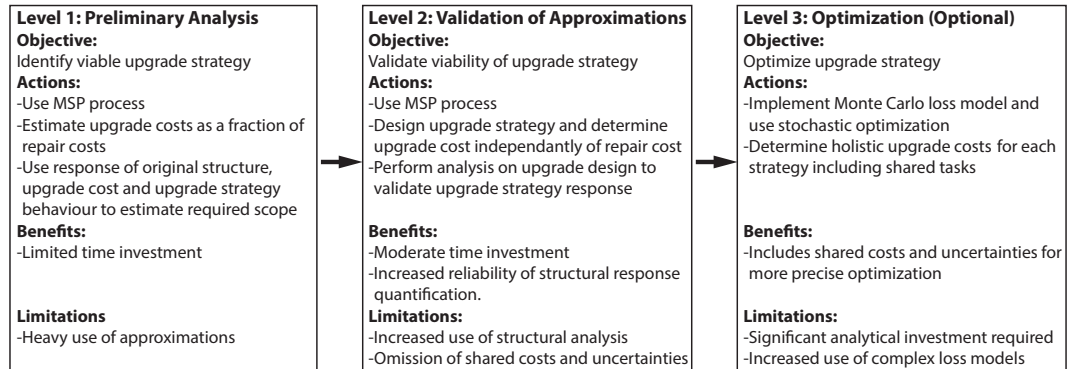


Figure 5.1: Levels of assessment of proposed framework to determine upgrade viability and optimization

A modified PBEE method, the MSP method, is used for Level 1 and 2 as it summarizes the change in structural performance by defining explicitly the relationship between changes to a structure and the resulting demands on nonstructural components. This provides an alternative to either the end-to-end total probability theorem (Günay and Mosalam 2013) or Monte Carlo PBEE approaches (FEMA 2012). The MSP method allows the viability of different upgrade strategies to be approximately quantified early in the decision-making process based on changes to single parameters of the probabilistic functions that describe key performance indicators. In particular, the relationship between changes to the behaviour of the structure and the performance of the nonstructural components, defined as changes to the floor hazard curves, are expressed using these shifts in probabilistic functions. The importance of this relationship is further demonstrated by

deaggregating the total change in loss with a particular upgrade strategy into distinct source categories.

5.3 Key Parameters of MSP Method

5.3.1 Performance of Structures and Non-Structural Components

The seismic performance of either structural systems or nonstructural components is often quantified using a fragility curve that is represented by a lognormal cumulative distribution function (CDF):

$$p(DS_k|x) = \Phi \left(\frac{\ln \left(\frac{x}{\theta_k} \right)}{\beta_k} \right) \quad (5.3.1)$$

where $p(DS_k|x)$ is the probability of occurrence of a specific damage state k (DS_k) given a hazard intensity x (e.g. ground spectral acceleration at first mode period, peak floor acceleration), Φ is the standard Gaussian CDF, θ_k is the median intensity of x , and β_k is the standard deviation of the lognormal CDF. For structures, collapse fragility curves are used to define the probability of occurrence of structural collapse given a site hazard intensity measure (IM), typically represented by the spectral acceleration at the first-mode period (FEMA 2009). This can be done based on incremental dynamic analysis (Vamvatsikos and Cornell 2001) or more computationally efficient alternatives, such as multiple stripe analysis (Baker 2015), which generates the same two parameters that define the lognormal CDF (θ_k , β_k) using the maximum likelihood estimation (MLE) method (Baker 2015). For

nonstructural components, similar lognormal CDFs are used to define the probability of occurrence of specific damage states given an *EDP*, instead of an *IM*. An extensive library of these curves for nonstructural components is included in the performance assessment calculation tool (PACT), developed as part of the FEMA P-58 project (FEMA 2012). While some nonstructural components may be exposed to multiple simultaneous damage states (e.g. both guide rails and operational machinery being damaged for elevators), each with an independent probability of occurrence, the structural system and most nonstructural components have sequential and exclusive damage states whose definition requires conditional probabilities. Capturing this exclusivity using the lognormal CDF functions is expressed as:

$$p(DS_k | NDS_{k+1}, x) = \Phi \left(\frac{\ln \left(\frac{x}{\theta_k} \right)}{\beta_k} \right) \left(1 - \Phi \left(\frac{\ln \left(\frac{x}{\theta_{k+1}} \right)}{\beta_{k+1}} \right) \right) \quad (5.3.2)$$

where $p(DS_k | NDS_{k+1}, x)$ is the probability of occurrence of damage state k conditional on intensity measure x and the non-occurrence of damage state $k + 1$. The MSP method stores these curves and uses two parameters of the lognormal CDF (θ_k, β_k) for each k damage state, as well as a specification indicating simultaneous or exclusive damage states.

5.3.2 Site Hazards and Floor Hazards

The seismic hazard at the site of a structure is defined by a frequency-intensity “site hazard curve” determined from probabilistic seismic hazard analysis and available from a national geological survey service (e.g. USGS 2014). The

annual frequency of occurrence ($f(IM)$) is given by:

$$f(IM) = \left| \frac{dF(IM)}{dIM} \right| \quad (5.3.3)$$

where $F(IM)$ is the annual frequency of exceedance of a ground motion intensity measure (IM).

The process for determining the hazard for a nonstructural component located at a floor level of the structure is not as well defined as for the site hazard but has received some attention in recent years. Bradley et al. (2009) and Günay and Mosalam (2013) defined the probability of exceedance of the peak floor acceleration and interstory drift ratio *EDPs* using total probability theorem within the PBEE methodology. O'Reilly and Monteiro (2019) used approximate methods developed from Welch et al. (2014) for obtaining frequency-intensity *EDP* “floor hazard curves”, which provide the annual frequency of exceedance of the floor *EDP*. In contrast to these preceding works, the floor hazard curves used in this paper are obtained from a multiple stripe analysis, defined as:

$$f(EDP_{n,k}) = \sum_{g=1}^G p(EDP_{n,k}|ND, IM_m) p(ND|IM_m) f(IM_m) \quad (5.3.4)$$

where $f(EDP_{n,k})$ is the annual frequency of occurrence of the *EDP* for the n^{th} component's k^{th} damage state, $p(EDP_{n,k}|ND, IM_m)$ is the probability of occurrence of the *EDP* at the m^{th} ground motion intensity stripe conditional on non-demolition, $p(ND|IM_m)$ is the probability of non-demolition of the building at the m^{th} ground motion intensity stripe, and $f(IM_m)$ is the annual

frequency of occurrence of the m^{th} ground motion intensity stripe. Figure 5.2 summarizes the inputs required to determine a floor hazard curve, where the *EDPs* obtained from the structural analysis of the building at various ground motion intensity levels are shown in Figure 5.2 (a), the probability of non-demolition is shown in Figure 5.2 (b), and the frequency of exceedance of the ground motion intensity, determined from the site hazard curve, is shown in Figure 5.2 (c).

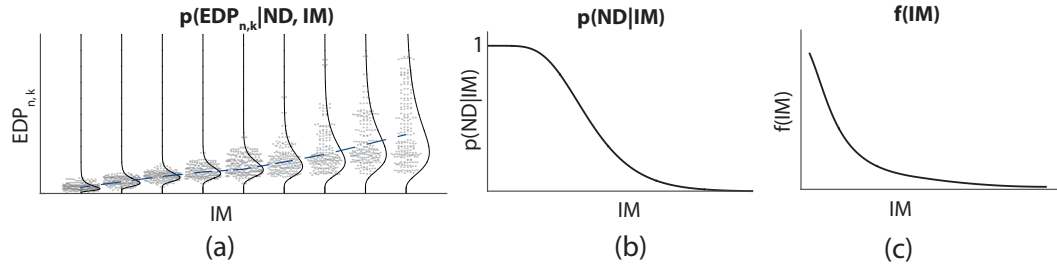


Figure 5.2: Input to the construction of a floor hazard curve: (a) Maximum *EDP* results obtained for different intensity stripes, (b) probability of non-demolition of structure, (c) site hazard curve

The probability of non-demolition is determined from the combined probability of non-collapse and reparable residual drifts as:

$$p(ND|IM) = 1 - p(C|IM) - p(NR|NC, IM)(1 - p(C|IM)) \quad (5.3.5)$$

where $p(ND|IM)$ is the probability of non-demolition of the structure at a specific ground motion intensity (IM), $p(C|IM)$ is the probability of collapse of the structure at a specific ground motion intensity (IM), and $p(NR|NC, IM)$ is the probability of occurrence of non-reparable residual drifts at a specific ground motion intensity conditional on the non-collapse of the structure. Finally, $p(EDP_{n,k}|ND, IM_m)$ is the probability of occurrence

of the $EDP_{n,k}$ at the m^{th} ground motion intensity conditional on non-demolition can be fitted using a lognormal PDF, given as:

$$p(EDP_{n,k}|ND, IM_m) = \phi \left(\frac{\ln \left(\frac{EDP_{n,k}}{\theta_{EDP,n,k,m}} \right)}{\beta_{EDP,n,k,m}} \right) \quad (5.3.6)$$

where $\theta_{EDP,n,k,m}$ is the median EDP value occurring at the ground motion intensity m among non-demolished structures, and $\beta_{EDP,n,k,m}$ is the lognormal standard deviation for the same PDF.

In order to quickly compare the change in floor hazards caused by structural upgrades, useful in the MSP method (Levels 1 and 2 of the framework in Figure 5.1), the $f(EDP_{n,k})$ curve is approximated using a single lognormal PDF for each EDP with parameters consisting of a median ($\theta_{EDP,n,k}$) and lognormal standard deviation value ($\beta_{EDP,n,k}$) determined using the same MLE process as was used for the structural performance curves in the previous section. This curve is expressed as:

$$f(EDP_{n,k}) \approx \phi \left(\frac{\ln \left(\frac{EDP_{n,k}}{\theta_{EDP,n,k}} \right)}{\beta_{EDP,n,k}} \right) \int p(ND|IM) f(IM) dIM \quad (5.3.7)$$

To assess the upgrade viability, values of $\theta_{EDP,n,k}$ and $\beta_{EDP,n,k}$ are required for each EDP used for a fragility curve, typically consisting of peak floor interstory drifts and accelerations. The integration of Equation 5.3.7 provides the annual frequency of exceedance CDF of the $EDP_{n,k}$, providing a curve with similar properties to a site hazard curve which is likely more

familiar:

$$F(EDP_{n,k}) \approx \left(1 - \Phi \left(\frac{\ln \left(\frac{EDP_{n,k}}{\theta_{EDP,n,k}} \right)}{\beta_{EDP,n,k}} \right) \right) \int p(ND|IM) f(IM) dIM \quad (5.3.8)$$

5.3.3 Annual Frequency of Damage and Mean Annual Loss

The expected annual loss (EAL) for a single component (or structure) n can be defined as:

$$EAL_{O,n} = \sum_{k=1}^K CC_{n,k} \lambda(DS_{O,n,k}) \quad (5.3.9)$$

$$EAL_{U,n} = \sum_{k=1}^K CC_{n,k} \lambda(DS_{U,n,k}) \quad (5.3.10)$$

where $CC_{n,k}$ is the consequence cost of damage state k of component n , K is the total number of damage states considered, and $\lambda(DS_{O,n,k})$ and $\lambda(DS_{U,n,k})$ are the mean annual frequency of occurrence of the damage state k of component n in its original and upgraded condition, respectively. The mean annual frequency of occurrence of damage is the integral of the function defining the annual frequency of occurrence of damage (DS) as a function of the hazard, defined as x for either IM or EDP , dependent on the component type:

$$\lambda(DS_{O,n,k}) = \int p(DS_{O,n,k}) f_O(x) dx \quad (5.3.11)$$

$$\lambda(DS_{U,n,k}) = \int p(DS_{U,n,k}|x) f_U(x) dx \quad (5.3.12)$$

where $p(DS_{O,n,k}|x)$ and $p(DS_{U,n,k}|x)$ are the probability of occurrence of damage state k of the original and upgraded component n , respectively, defined by the aforementioned fragility curves, and $f_O(x)$ and $f_U(x)$ are the annual frequency of occurrence of hazard (x) of the original or upgraded component, respectively.

5.3.4 Deaggregation of Change in Loss By Hazard

Intensity

The change in mean annual frequency of occurrence of damage state k of the component n can be computed from the integral of the change in the annual frequency of occurrence of damage at each hazard value x , which can be a result of a change in the probability of occurrence of damage (Δ_{DS}), a change in the frequency of occurrence of the hazard (Δ_H), or a change in both ($\Delta_{DS\&H}$). These are shown in Figure 5.3 and are expressed as:

$$\Delta_{DS} (\lambda(DS_{n,k})) = \int \Delta (p(DS_{n,k}|x)) f(x) dx \quad (5.3.13)$$

$$\Delta_H (\lambda(DS_{n,k})) = \int p(DS_{n,k}|x) \Delta (f(x)) dx \quad (5.3.14)$$

$$\begin{aligned} \Delta_{DS\&H}(\lambda(DS_{n,k})) &= \int (\Delta(p(DS_{n,k}|x) + p(DS_{O,n,k}|x))\Delta(f(x)))f_o(x) \\ &\quad - \Delta(p(DS_{n,k}|x))\Delta(f(x))dx \end{aligned} \tag{5.3.15}$$

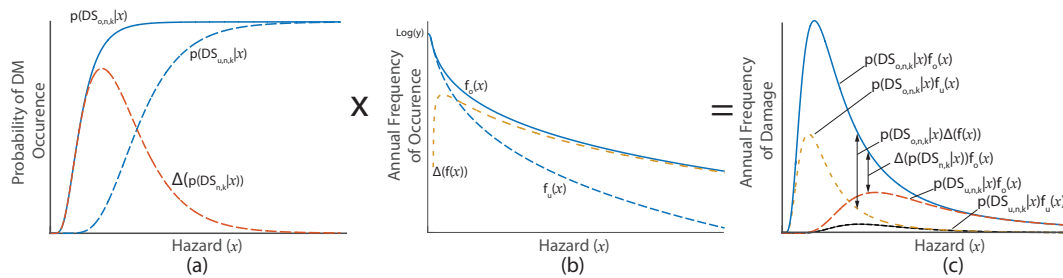


Figure 5.3: Change in frequency of occurrence of damage

A particularly useful application of the deaggregation of change in damage functions shown above is when determining the *BCR* of the upgrade of a component whose upgrade has no other effects on the overall building loss, as when determining the viability of an individual nonstructural component upgrade in a structure with a given floor hazard curve. In these simplified cases, Equation (5.3.13) can be substituted into Equation (5.2.3) to define the *BCR* of component n as a function of hazard intensity ($bcr_n(EDP_{n,k})$):

$$\begin{aligned} BCR_n &= \int bcr_n(EDP_n)dEDP_n \\ &= \int \sum_1^K \frac{RC_{n,k}}{UC_n} \Delta(p(DS_{n,k}|EDP_{n,k})) f(EDP_{n,k}) AM dEDP_{n,k} \end{aligned} \tag{5.3.16}$$

Equation 5.3.16 can be used to identify the hazard values where the change in component performance provided by the component upgrade has the largest benefit, and inversely, the hazard values where performance improvements would have the greatest influence.

5.4 Deaggregation of Change In Loss From Upgrades

To quickly assess the upgrade viability, it is convenient to evaluate the change in *EAL* from an upgrade strategy across four categories: 1) change in loss caused by the changes to the collapse fragility of the structure, 2) change in loss caused by changes to the probability of demolition of the structure due to non-reparable residual drifts, 3) change in loss caused by changes to the floor EDPs that impact the nonstructural components, and 4) change in loss caused by changes to the nonstructural component fragilities. Each of these is characterized below.

5.4.1 Changes to the Collapse Fragility of the Structure

To quantify the change in annual frequency of collapse caused by modifications to the structural performance, the parameters of the lognormal CDFs of the original and upgraded collapse curves are required. Also using the site hazard

curve ($f(IM)$), this change in annual frequency of occurrence is expressed as:

$$\begin{aligned}\Delta_{DS}(\lambda_C) &= \int \Delta(p(C|IM))f(IM)dIM \\ &= \int \left(\Phi \left(\frac{\ln \left(\frac{IM}{\theta_{C,O}} \right)}{\beta_{C,O}} \right) - \Phi \left(\frac{\ln \left(\frac{IM}{\theta_{C,U}} \right)}{\beta_{C,U}} \right) \right) f(IM)dIM\end{aligned}\quad (5.4.1)$$

where $\Delta_{DS}(\lambda_C)$ is the change in mean annual frequency of collapse caused by a change in structural performance, $\theta_{C,O}$ and $\theta_{C,U}$ are the median collapse intensity measure values for the original and upgraded structure, respectively, and $\beta_{C,O}$ and $\beta_{C,U}$ are the lognormal standard deviation of the collapse lognormal CDF of the original and upgraded structure, respectively. The consequence cost of collapse is a combination of the building replacement value and the loss from the average number of casualties caused by collapse, which can be obtained using an equivalent continuous occupancy approximation (Comerio, 2000):

$$CC_c = BV + \left(\frac{OHW}{168} \right) \left(\frac{OWY}{52} \right) (NP)((DR)(VSL) + (IR)(VSI)) \quad (5.4.2)$$

where BV is the building replacement value, OHW is the occupied hours per week for an average building occupant, OWY is the occupied weeks per year for an average building occupant, NP is the maximum number of occupants in the building, DR and IR are the death rate and injury rate per occupant, respectively, and VSL and VSI are the value of a statistical life and value of a statistical injury, respectively. Values for each of these variables can be obtained from a variety of sources (DHS/FEMA 2007,

FEMA 2012, DOT 2016), or using information provided by the building owner. This results in the change to the EAL contributed by the collapse of the structure to be:

$$\Delta(EAL_C) = CC_C(\Delta_{DS}(\lambda_C)) \quad (5.4.3)$$

The changes in EAL_C resulting from changes to the lognormal fragility curve defining structural collapse can be summarized by the change (ratio) in both the median ($Q_{\theta,C}$) and lognormal standard deviation ($Q_{\beta,C}$) of the original to the upgraded curve, as shown:

$$Q_{\theta,C} = \frac{\theta_{C,U}}{\theta_{C,O}} \quad (5.4.4)$$

$$Q_{\beta,C} = \frac{\beta_{C,U}}{\beta_{C,O}} \quad (5.4.5)$$

Since structural upgrades are not expected to cause large changes in β_C (Liel et al. 2009, FEMA 2012), most of the change in EAL_C can be captured by $Q_{\theta,C}$.

5.4.2 Changes to the Non-Recoverable Residual Drift Fragility of the Structure

Similar to changes in collapse performance, the change in loss caused by non-reparable residual drifts resulting from a structural upgrade can be expressed

as:

$$\begin{aligned} \Delta_{DS}(\lambda_{NR}) = & \int \Phi \left(\frac{\ln \left(\frac{IM}{\theta_{NR,O}} \right)}{\beta_{NR,O}} \right) \left(1 - \Phi \left(\frac{\ln \left(\frac{IM}{\theta_{C,O}} \right)}{\beta_{C,O}} \right) \right) \\ & - \Phi \left(\frac{\ln \left(\frac{IM}{\theta_{NR,U}} \right)}{\beta_{NR,U}} \right) \left(1 - \Phi \left(\frac{\ln \left(\frac{IM}{\theta_{C,U}} \right)}{\beta_{C,U}} \right) \right) f(IM) dIM \end{aligned} \quad (5.4.6)$$

where $\Delta_{DS}(\lambda_{NR})$ is the change in mean annual frequency of occurrence of non-recoverable residual drifts from a change in performance, $\theta_{NR,O}$ and $\theta_{NR,U}$ are the median non-repairable residual drifts intensity measures for the original and upgraded structure, respectively, and $\beta_{NR,O}$ and $\beta_{NR,U}$ are the lognormal standard deviation of the non-repairable residual drift lognormal CDF of the original and upgraded structure, respectively. Since a building with non-repairable residual drifts is not expected to have caused any casualties, but a building replacement is still required, the consequence cost for this damage state is simply the building value, and thus the change in EAL is given by:

$$\Delta(EAL_{NR}) = BV \int \Delta(p(NR|IM)) f(IM) dIM \quad (5.4.7)$$

Similar to the representation of the change in EAL_C using $Q_{\theta,C}$, the change in EAL_{NR} can be captured using $Q_{\theta,NR}$ and $Q_{\beta,NR}$, where $Q_{\theta,NR}$ is the change in median non-repairable residual drifts intensity value and $Q_{\beta,NR}$ is the change in lognormal standard deviation non-repairable residual drifts intensity value,

given by:

$$Q_{\theta,R} = \frac{\theta_{R,U}}{\theta_{R,O}} \quad (5.4.8)$$

$$Q_{\beta,R} = \frac{\beta_{R,U}}{\beta_{R,O}} \quad (5.4.9)$$

5.4.3 Changes to the Floor Hazard

Upgrades to the structural system can modify the dynamic properties of the structure, resulting in changes to the losses caused by damage to nonstructural components. Since the MLE method was used to define the floor hazard curves using a lognormal distribution, as discussed in Section 5.3.2, the change in annual frequency of occurrence of a damage state k of a component n as a function of the change in corresponding EDP is expressed as:

$$\Delta_H(\lambda_{n,k}) = \int p(DS_{n,k}|EDP_{n,k}) \Delta(f(EDP_{n,k})) dEDP_{n,k} \quad (5.4.10)$$

$$\begin{aligned} \Delta(f(EDP_{n,k})) = & \phi \left(\frac{\ln \left(\frac{EDP_{n,k}}{\theta_{EDP,n,k,O}} \right)}{\beta_{EDP,n,k,O}} \right) \int p(ND_O|IM) f(IM) dIM \\ & - \phi \left(\frac{\ln \left(\frac{EDP_{n,k}}{\theta_{EDP,n,k,U}} \right)}{\beta_{EDP,n,k,U}} \right) \int p(ND_U|IM) f(IM) dIM \end{aligned} \quad (5.4.11)$$

where $\Delta_H(\lambda_{n,k})$ is the change in median annual frequency of occurrence of

the k^{th} damage state of the n^{th} component from a change in floor hazard, ϕ is the standard Gaussian probability distribution function (PDF), $p(ND_O|IM)$ and $p(ND_U|IM)$ are the probability of non-demolition of the original and upgraded structure, respectively, $\theta_{EDP,n,k,O}$ and $\theta_{EDP,n,k,U}$ are the original and upgraded median EDP values of the floor hazard curves, respectively, and $\beta_{EDP,n,k,O}$ and $\beta_{EDP,n,k,U}$ are the lognormal standard deviation of the original and upgraded floor hazard curves, respectively. The consequence cost associated with each of these changes is the repair cost (RC) associated with the k^{th} damage state of the n^{th} nonstructural component, and thus the total change to the EAL caused by a structural upgrade can be defined by the summation of the change in annual loss across all components N , expressed as:

$$\Delta_H(EAL_{NS}) = \sum_{n=1}^N \sum_{k=1}^K RC_{n,k} \Delta_H(\lambda_{n,k}) \quad (5.4.12)$$

In a similar way to the change in EAL_C and EAL_{NR} , the change in EAL_{NS} of either acceleration or displacement sensitive nonstructural components from a change in their respective EDP floor hazard curves can be expressed by $Q_{\theta,EDP,n,k}$ and $Q_{\beta,EDP,n,k}$ factors given by :

$$Q_{\theta,EDP,n,k} = \frac{\theta_{EDP,n,k,U}}{\theta_{EDP,n,k,O}} \quad (5.4.13)$$

$$Q_{\beta,EDP,n,k} = \frac{\beta_{EDP,n,k,U}}{\beta_{EDP,n,k,O}} \quad (5.4.14)$$

5.4.4 Changes to the Fragility of the Nonstructural Components

The change in loss caused by an improvement to the performance of a nonstructural component $\Delta_{DS}(\lambda_{n,k})$ can be expressed as:

$$\Delta_{DS}(\lambda_{n,k}) = \int (p(DS_{O,n,k}|EDP_{n,k}) - p(DS_{U,n,k}|EDP_{n,k})) f(EDP_{n,k}) dEDP_{n,k} \quad (5.4.15)$$

Equation (5.4.15) can be used when contemplating an upgrade strategy limited only to the nonstructural components, which will not modify the dynamic behaviour of the structure. However, when considering an upgrade strategy that includes both structural and nonstructural components, the possibility of simultaneous changes to the component performance and to the floor hazard $\Delta_{DS\&H}(\lambda_{n,k})$ must be considered by:

$$\begin{aligned} \Delta_{DS\&H} = & \int (p(DS_{O,n,k}|EDP_{n,k})\Delta(f(EDP_{n,k}))) \\ & + \Delta(p(DS_{n,k}|EDP_{n,k}))f_O(EDP_{n,k}) \\ & - \Delta(p(DS_{n,k}|EDP_{n,k}))\Delta(f(EDP_{n,k})))dEDP_{n,k} \end{aligned} \quad (5.4.16)$$

Thus, the change in expected annual loss from nonstructural component damage when including both structural and nonstructural upgrades becomes:

$$\Delta(EAL_{NS}) = \sum_{n=1}^N \sum_{k=1}^K RC_{n,k} \Delta_{DS\&H}(\lambda_{n,k}) \quad (5.4.17)$$

5.5 Multiple Framework Levels

As mentioned in Section 5.2, the use of multiple levels in the framework for assessing upgrade viability allows for increasing analytical accuracy by differing loss estimation analysis methods. The lower effort associated with the first two levels of the framework requires the organization of the equations outlined in Section 5.4 into the MSP method, which quickly quantifies the approximate effect of a structural upgrade on the expected losses. This MSP method is explained in greater detail in this section, and aspects of this method are compared to the Level 3 PBEE Monte Carlo optimization.

5.5.1 Level 1 MSP Method for Feasibility Study of Upgrade Strategy

Both Level 1 and Level 2 use the MSP method to determine the viability of an upgrade strategy. The MSP method relies on the assumption that the seismic structural responses presented in Section 5.3 are lognormally distributed and uses the deaggregated changes in the performance curves presented in Section 5.4. While the MSP method used in Level 1 or Level 2 is identical, as shown in Figure 5.4, the objective of the analysis and the quality of data used for each level differ. For a Level 1 analysis, the MSP method includes the following steps:

1. Identify original building conditions including structural system, nonstructural population, owner parameters, and site hazard to determine θ and β values for collapse, residual drift, and floor hazard curves for the original structure.

2. Select an upgrade strategy and estimate whether each associated Q_θ is greater than or less than one and approximate the structural upgrade cost as a fraction of the building value.
3. Determine the required Q_θ value for each performance curve to obtain the required change in EAL , using Equations (5.4.7) to (5.4.4) for collapse and Equations (5.4.6) to (5.4.8) for non-repairable residual drift.
4. Identify the nonstructural components to upgrade by using Equation (5.3.16) with the updated floor hazard curve, adjusted with the Q_θ value for each EDP . Update the upgrade cost in Step 3 as needed and continue modifying the Q_θ values and the selection of nonstructural upgrades until the required change in EAL is obtained, determined using Equations (5.4.10) to (5.4.17) for nonstructural components, as applicable.
5. Estimate if the final Q_θ values are attainable with the proposed upgrade strategy.

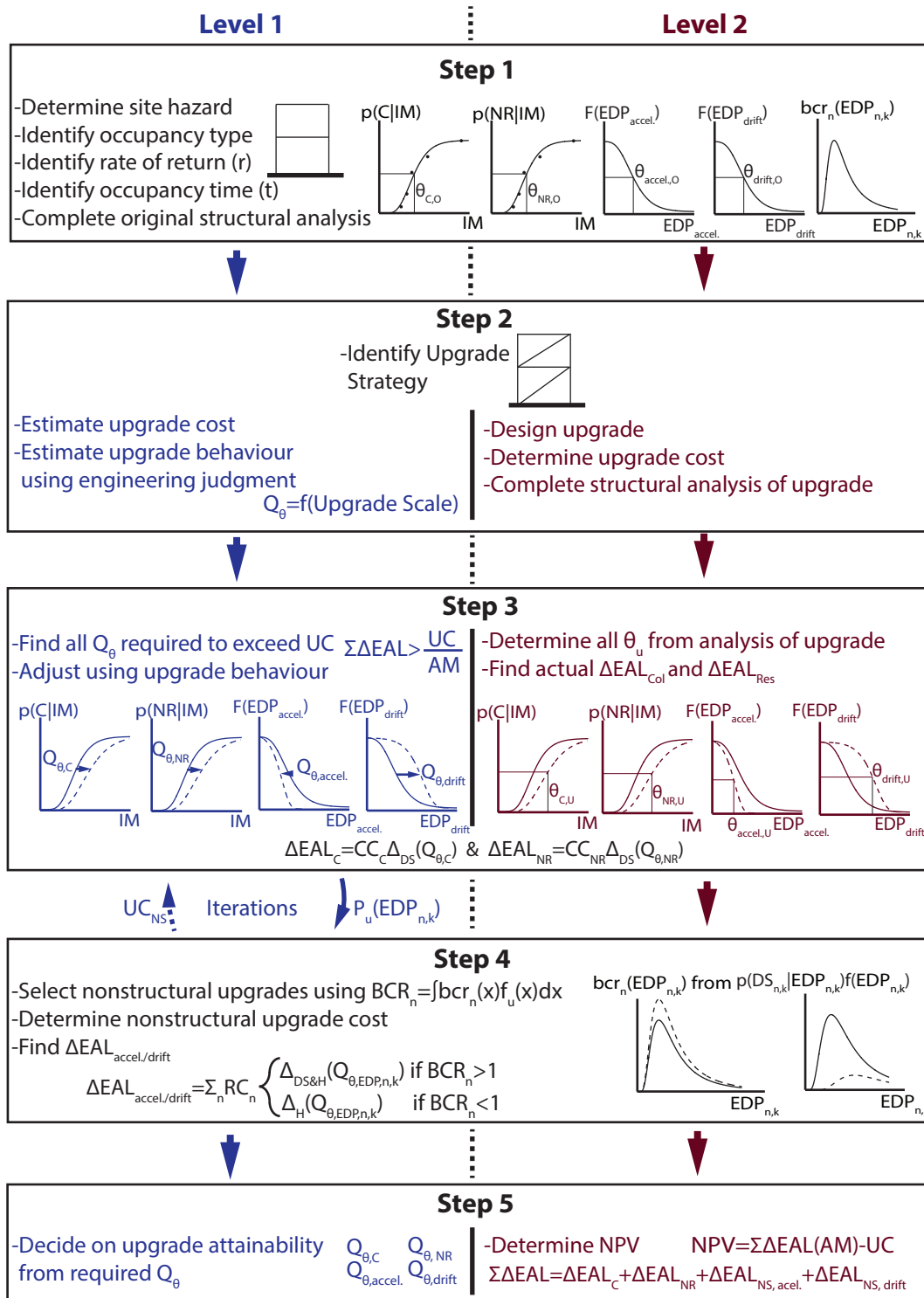


Figure 5.4: Flow Chart for Levels 1 and 2 of MSP method of Assessment of Upgrade Viability

While it is recommended that the θ and β values for the collapse and residual drift curves in Step 1 be determined based on a nonlinear time history analysis (NLTHA), approximate methods to determine the collapse performance of a structure are available (e.g. Chopra 2012, Moon et al. 2012) and could be used in a Level 1 type analysis. Similarly, θ and β for the floor hazard curve can either be fitted from NLTHA results or by using various approximate methods (e.g. Welch et al. 2014, Sullivan et al. 2014, Merino et al. 2019, O'Reilly and Calvi 2020). A tool implemented in Microsoft Excel has been developed to quickly iterate between Steps 3 and 4 of the method and is included as a supplementary file to this thesis.

5.5.2 Level 2 MSP Method for Verification of Schematic Design of Upgrade Strategy

If the obtained Q_θ values for the upgrade strategy have been deemed achievable in the Level 1 of the MSP method, the use of more resource-intensive tools can be justified to determine the viability of the upgrade strategy in a Level 2 analysis. The verification of viability is completed using the same MSP method, but replacing the approximations in Step 2 with more detailed cost estimates and the results in Step 3 from a NLTHA. The steps for this method are summarized as follows:

1. Same step as in Level 1 but potentially utilizing more accurate models to determine θ and β values.
2. Design structural upgrade, obtain structural upgrade cost estimate, and perform NLTHA.

3. Determine actual curve parameters (θ and β) for the upgraded structure to determine change in collapse and non-reparable residual deformation *EALs*.
4. Determine nonstructural component upgrades using floor hazard curves obtained from NLTHA and determine change in nonstructural *EAL*.
5. Find NPV from Equation 5.2.1 using both the structural and non-structural upgrade costs.

5.5.3 Level 3: Optimization using Monte Carlo PBEE Evaluation

The goal of a Level 3 analysis is to apply an end-to-end scenario-based PBEE method to further verify and optimize the upgrade strategies beyond the components identified using the MSP method in the Level 2 analysis. The genetic algorithm (GA) in Chapter 4, used to optimize the seismic upgrade of a building using the Monte-Carlo-based PBEE method, is an example of a Level 3 analysis. The Monte Carlo scenario evaluation allows for the inclusion of several factors not considered in the MSP method, as discussed next.

First, by simultaneously considering all components selected for upgrade when determining the overall upgrade cost, the individual cost of the component upgrades can be reduced by identifying common tasks. Furthermore, as the Monte Carlo approach typically subdivides each component quantity into multiple subdivisions evaluated independently, the ability to capture both shared consequence functions across components and to determine economies-of-scale cost reductions is possible in Level 3. These

are not reflected in the MSP method of the Level 2 analysis, as the *EAL* and *BCR* of all individual nonstructural components are evaluated with a single function for the entire component quantity. An iterative version of the MSP method (MSPIT) is introduced in the case study example to attempt to overcome this shortcoming of the MSP method, and is discussed in Section 5.6.2.6.

Second, since the GA developed in Chapter 4 used a Monte Carlo implementation of PBEE, the consequence function and upgrade cost were defined using probabilistic distributions that captured variability in repair and upgrade costs. This factor, in combination with the randomness of the GA selection process, results in variation in the final optimal upgrade solution, as components with *BCR* values close to one are selected in a fraction of the repeated iterations. To identify these components, the optimization run is repeated several times, and the rate at which components are selected in the optimal solution at each value is recorded. In contrast, the MSP method produces a single deterministic selection of components in the optimal upgrade strategy.

5.6 Case Study Example

The case study example used to demonstrate the framework described above is the same scenario considered in Chapter 4 to illustrate a Level 3 analysis with GA. This section focuses on the implementation of Level 1 and Level 2 analyses, while results from the Level 3 analysis are summarized to allow comparisons.

5.6.1 Level 1 Analysis:

Step 1: Original Conditions

The original archetype structure is a three-story steel moment resisting frame (MRF) with an office type occupancy, located in Seattle, Washington, on site class B soil. The owner profile used for the analysis is assumed to have a 2% rate of return and 40-year occupancy time, representative of a typical institutional building owner (Shilling and Wurtzebach 2012). The population of nonstructural components included in this archetype structure consists of all 26 components identified by the FEMA P-58 Normative Quantity Tool (FEMA 2012). The structure was designed according to the seismic provisions of the 1994 Uniform Building Code (UBC 1994) and, with the exception of pre-Northridge Earthquake beam-to-column connections, satisfies current seismic design requirements (ASCE 2016, AISC 2016). Plan and elevation views for this frame are shown in Figure 5.5. The building was assumed to have no torsional irregularities. The frame model for both the MSP method Level 1 and Level 2 analysis of this original structure was assembled in OpenSees (McKenna et al. 2000), with concentrated zero-length springs capturing element nonlinearity using the Ibarra-Medina-Krawinkler hysteretic model (Ibarra et al. 2005). The nonlinear behaviour of the panel zones was also modeled using the Krawinkler Spring Box model with a trilinear backbone curve (Gupta and Krawinkler 1999). The computed fundamental period of the frame was 0.87 seconds. Details of the modelling of the archetype structure are provided in Chapter 2.

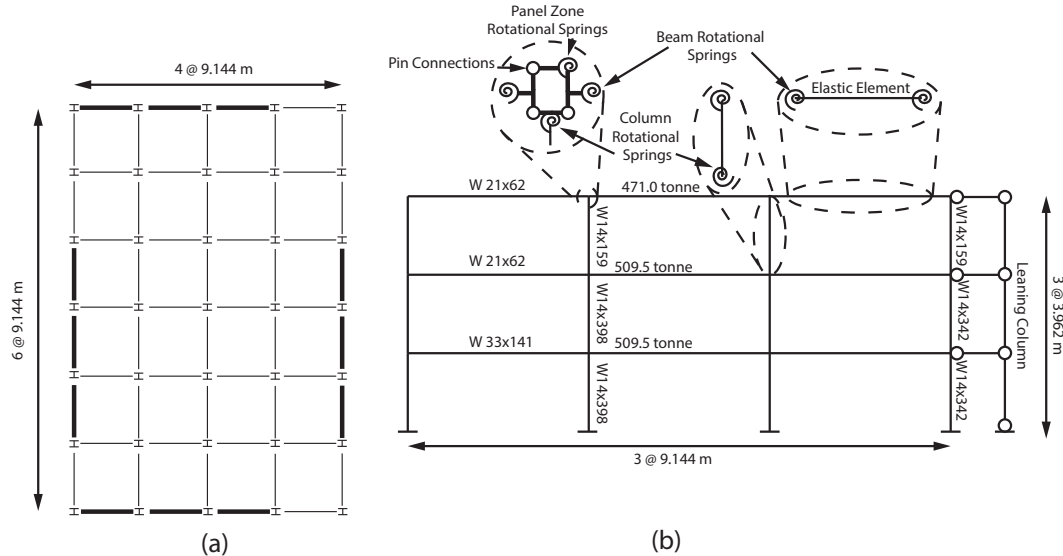


Figure 5.5: (a) Plan view of archetype building, (b) Elevation view of archetype building with modeling details

The seismic hazard analysis for the archetype building’s site was obtained using the USGS Uniform Hazard Tool (USGS 2014). A frequency-intensity curve was obtained for the original structure’s fundamental period, as shown in Figure 5.6 (a). A multiple stripe analysis (Baker 2015) was used to evaluate the structural performance of the frame, with nine intensity stripes, each with 40 ground motions selected and scaled to match different conditional mean spectra (Baker and Lee 2017). For each stripe, ground motions were selected from the far-field NGA-West2 Database (PEER 2013) to match rupture parameters identified by the site seismic hazard deaggregation information corresponding to the frequency of occurrence of each stripe’s intensity. Details on the ground motion selection are provided in Appendix B.

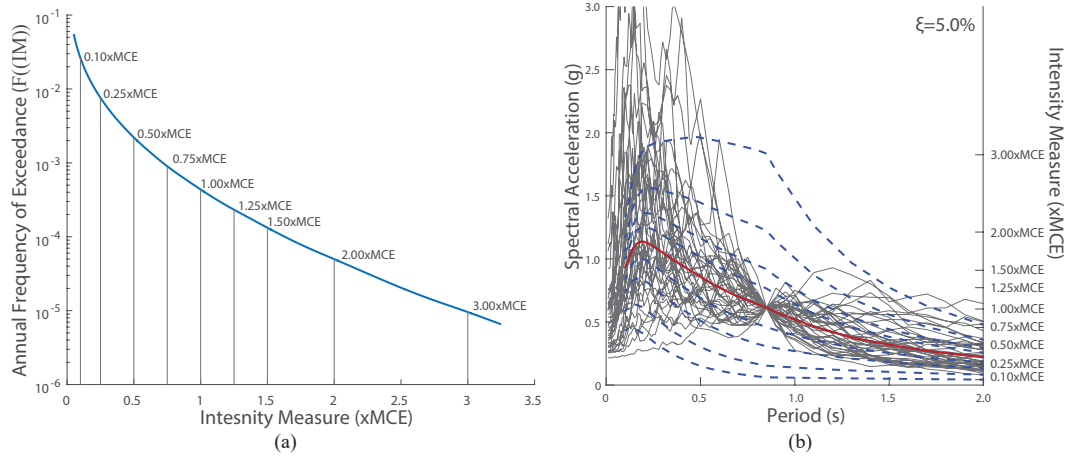


Figure 5.6: (a) Arhceytp building's site frequency-intensity curve, (b) Conditional mean spectra for multiple stripe analysis

The results of the multiple stripe analysis were represented by five lognormal CDFs whose parameters were determined using the MLE method. The fragility curves for collapse and for non-reparable residual drifts conditional on non-collapse are shown in Figure 5.7 (a). The probability of building demolition, $p(D|IM)$, and the probability of non-reparable residual drifts are also included. Figure 5.7 (b) shows the peak floor and roof acceleration hazard curves and includes the values obtained directly from the NLTHA results, as well as the approximate lognormal CDF fitted to the NLTHA results using the MLE method. Two acceleration curves were used since the floor and roof levels have different populations of nonstructural components. The distinctive drops in values of the acceleration hazard curves in Figure 5.7 (b) are caused by the increasing probability of demolition of the original building at larger intensity stripes. Finally, Figure 5.7 (c) shows the floor hazard curve for the peak interstory drifts before collapse. In all instances, the assumption of lognormality of the floor hazards obtained from the sample of NLTHA at all intensities passed the one-sample

Kolmogorov-Smirnov test having an alpha value of 5% (Chakravarti et al. 1967).

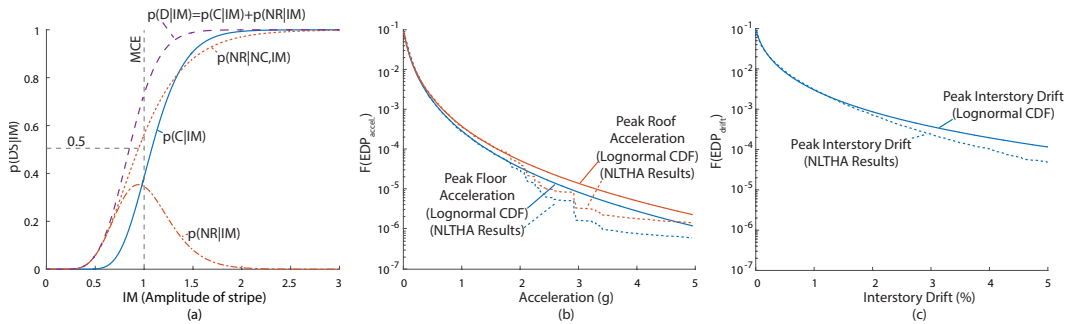


Figure 5.7: Performance curves for original structure: (a) Structural fragility curves, (b) Roof and floor acceleration hazard curves, and (c) Floor drift hazard curve

Step 2: Upgrade Cost and Structural Behaviour

This case study example considered three structural upgrade strategies of the archetype building and one strategy that limited upgrades to the nonstructural components only. All three structural strategies are commonly recommended in practice for steel MRFs with pre-Northridge connections (FEMA 2000, ASCE 2017). A short description of the assumed effect of each strategy on the four loss categories is provided below and an estimate of cost is listed in Table 5.1. This step required the most assumptions in Level 1 of the MSP method, and a more accurate estimation of cost and behaviour is considered in Level 2.

Structural Upgrade Strategy 1: Increase Strength and Stiffness.

This strategy is typically achieved with the addition of seismic force-resisting elements, such as braces. The main objectives of this strategy are to increase collapse resistance and reduced residual drifts.

This characteristic also typically results in smaller interstory drifts but higher floor accelerations (e.g. Flores et al. 2015, Mayes et al. 2013).

Structural Upgrade Strategy 2: Increase Ductility and/or Self-Centering.

This strategy is typically achieved by modifying the beam-column connections to provide greater displacement capacity. This strategy increases the collapse resistance and may reduce residual drifts. However, the increase in the probability of non-demolition at higher ground motion intensities also increases the frequency of occurrence of both large accelerations and interstory drift EDPs (Yeow et al. 2018, Steneker et al. 2019).

Structural Upgrade Strategy 3: Addition of Supplemental Viscous Damping.

This strategy is typically achieved with the addition of viscous dampers. This strategy increases the collapse resistance and may reduce residual drifts. The addition of viscous dampers usually also reduces both interstory drifts and floor accelerations (Mayes et al. 2013).

Structural Upgrade Strategy 4: Upgrades to Non-Structural Components.

This strategy consists of upgrading all nonstructural components with a BCR_n value larger than one (Equation 5.3.16) in the original structural condition. The strategy was not considered to change any of the Q_θ values but still reduced the EAL .

Step 3 & Step 4: Required Change in EAL and Approximation of Q_θ Values

A required minimum change in EAL was determined based on the estimated upgrade cost for each strategy and the amortization value obtained for the building owner profile. The changes in EAL obtained from shifts in Q_θ value were evaluated using Equations (5.4.1) to (5.4.4) for collapse and Equations (5.4.6) to (5.4.8) for non-reparable residual drifts. Each shift in Q_θ values for either the floor acceleration (PFA) or floor interstory drift $EDPs$ in Equation (5.4.13) was considered in Step 4 to determine all accompanying nonstructural component upgrades, and any modification in upgrade cost of these components was included in the upgrade cost used in Step 3 through an iterative process. Table 5.1 lists all the Q_θ values assumed in Level 1 of the MSP method based on engineering judgement. Using the Excel tool provided as a supplementary file, a nonstructural component n was upgraded when the integral of the product of $bcr_n(EDP)$ from Equation (5.3.16) and the upgraded floor hazard resulting from the Q_θ value $\Delta(f(EDP_{n,k}))$ exceeded 1, leading to the change in EAL for component n being evaluated using Equation (5.4.16) instead of Equation (5.4.10). The relevant nonstructural repair and upgrade costs used in Equation (5.3.16) are summarized in Table 5.2 as a fraction of the total building value for all 26 component types. The nonstructural upgrades followed the FEMA E-74 guidelines (FEMA 2011) and the upgrade costing was determined using the RSMeans commercial software estimating tools (RSMeans 2018). The iterative process was completed once the total change in EAL exceeded the upgrade cost divided by the amortization conversion.

Table 5.1: Summary of Upgrade Strategies and assumed Level 1 Q_θ values

Upgrade Strategy	Structural Cost Estimate (% of BV)		Structural and Non-Structural Cost Estimate (% of BV)	Collapse Q_θ	Residual Drift Q_θ	Floor Acceleratio Q_θ	Floor Drift Q_θ
1. Increase in Strength and Stiffness	5%		11%	1.4	1.2	1.4	0.4
2. Increase in Ductility/ Self-Centering	10%		14%	1.6	1.8	1.1	1.1
3. Addition of Supplemental Damping	Viscous	15%	17%	1.0	1.0	0.7	0.8
4. Upgrade of Nonstructural Components	0%		6.6%	1.0	1.0	1.0	1.0

Table 5.2: Summary of nonstructural normalized repair and upgrade costs for case study structure

Component (n)	Quantity (Unit)	Demand Parameter	Source of Fragility Function	Consequence Function	RC_n (% of BV)	Upgrade	UC_n (% of BV)
Chiller	1300 Ton	PRA* (g)	FEMA P-58	Replacement	11.00	Reseating on Seismic Snubbers	1.48
Cooling Tower	1300 Ton	PRA (g)	FEMA P-58	Replacement	11.00	Reseating on Seismic Snubbers	1.48
Air Handling Unit	12800 CFM	PRA (g)	FEMA P-58	Repair attaching ducts	0.40	Installation of flexible coupling	1.04
				Replacement	15.00	Reseating on Seismic Snubbers	1.025
Motor Controller	13 units	PRA (g)	FEMA P-58	Replacement	0.40	Proper anchorage	0.11
Low Voltage Transformer	6 units	PRA (g)	FEMA P-58	Replacement	1.50	Proper anchorage	0.07
Distribution Panel	3 units	PRA (g)	FEMA P-58	Replacement	0.70	Proper anchorage	0.067
Control Panel	5 units	PFA* (g)	FEMA P-58	Replacement	0.15	Proper anchorage	0.10
Lighting	1900 units	PFA (g)	FEMA P-58	Replacement	13.5	Safety Cable	1.00
Desktop Equipment	450 units	PFA (g)	FEMA P-58	Replacement	4.78	Proper anchorage	1.10

Continued on the next page

Continued from previous page

Component (<i>n</i>)	Quantity (Unit)	Demand Parameter	Source of Fragility Function	Consequence Function	RC_n (% of BV)	Upgrade	UC_n (% of BV)
Office Equipment	450 units	PFA (g)	Filiatrault et al. 2004	Replacement	4.78	Proper anchorage	0.81
Large HVAC Duct	1285 LF	PFA (g)	FEMA P-58	Repair support Replace section	0.02 0.22	Installation of bracing or trapeze	0.58
Small HVAC Duct	4815 LF	PFA (g)	FEMA P-58	Repair support Replace section	0.05 0.60	Installation of bracing or trapeze	0.73
HVAC Diffuser	580 units	PFA (g)	FEMA P-58	Replacement	1.35	Safety Wires	1.33
Cold Piping	5390 LF	PFA (g)	FEMA P-58	Repair Replace (flooding)	0.16 5.05	Installation of bracing or trapeze	0.61
Large Diameter Piping	1925 LF	PFA (g)	FEMA P-58	Repair Replace (flooding)	0.10 1.84	Installation of bracing or trapeze	0.50
Small Diameter Piping	5390 LF	PFA (g)	FEMA P-58	Repair Replace (flooding)	0.16 5.05	Installation of bracing or trapeze	0.90
Sanitary Piping	3660 LF	PFA (g)	FEMA P-58	Replace (flooding)	3.50	Installation of bracing	0.71
Sprinkler Piping	12840 LF	PFA (g)	Soroushian et al. 2015	Repair Replace (flooding)	0.26 12.00	Installation of bracing or trapeze	1.54
Sprinkler Head	580 units	PFA (g)	Soroushian et al. 2015	Repair Replace (flooding) Replace (flooding)	0.02 0.30 5.27	Installation of flexible piping	1.04
Suspended Ceiling	57780 SF	PFA (g)	FEMA P-58	Repair 5% Repair 30% Repair 100%	0.71 5.57 11.50	Installation of wire bracing, cross runners	5.04
Raised Floor	481 SF	PFA (g)	FEMA P-58	Repair	0.47	Pedestal Bracing	0.28
Curtain glazing	19260 SF	Drift (%)	Behr 2001	Replace cracked glass Replace broken glass	10.00 10.00	Replace with shatter proof glass	6.80
Wall Partitions	6420 LF	Drift (%)	Retamales et al. 2013	Re-tape joints Replace 10% Replace 50%	1.55 3.10 4.77	Partial heights, Installation of lateral bracing	3.16
Roofing Tiles	21850 SF	PFA (g)	FEMA P-58	Minor reinstall	3.70	Installation of	4.48

Continued on the next page

Continued from previous page

Component (<i>n</i>)	Quantity (Unit)	Demand Parameter	Source of Fragility Function	Consequence Function	RC_n (% of BV)	Upgrade	UC_n (% of BV)
				Major reinstall	10.10	vener anchor	
Concrete Stairs	24 units	Drift (%)	Bull 2011	Repair cracks	0.17	Installation of proper seismic joint at landing	1.16
				Major repair	0.92		
				Replacement	6.78		
Elevator	6 units	PRA (g)	FEMA P-58	Repair controls	0.37	Proper anchorage of rails and equipment	0.56
		and		Repair rails	1.59		
		PFA (g)		Repair car	0.21		

*PRA=Peak Roof Acceleration

*PFA=Peak Floor Acceleration

Step 5: Determination of Attainability of Q_θ Values

Relevant engineering experience and further research would have provided more accurate guidance on estimating Q_θ for each upgrade strategy. Owner profiles with shorter occupancy times and higher rates of return lead to a need for larger Q_θ values for a viable retrofit, which would be deemed less attainable. However, in this case study, the values shown in Table 5.1 were considered achievable based on engineering judgment, so each upgrade strategy was considered for a Level 2 analysis.

5.6.2 Level 2 Analysis

Step 1: Original Conditions

Since a detailed model of the original building was used in the Level 1 analysis, the same model was used for the Level 2 method. No further refinement of the numerical results was required.

Step 2: Upgrade Design, Cost, and Performance

The increase in stiffness and strength was implemented using the installation of buckling restrained braces (BRBs) in the MRFs. The design process for the BRB structural upgrade used an iterative implementation of the equivalent lateral force procedure as outlined in ASCE 7-16, where the design period of the structure was determined from modal analysis of the combined MRF/BRB system, but with the BRBs designed to take 100% of the lateral loads. The increase in ductility and the addition of self-centering behaviour was implemented by replacing the pre-Northridge connections with low-damage self-centering sliding hinge joint (SCSHJ) connections (Khoo et al. 2012) without changing the beam section. The design of the SCSHJ connections targeted 100% self-centering capability in each beam-column connection, and the activation moment was set to allow for the full connection mechanism to develop before yielding of the existing beam (Steneker et al. 2019). The addition of supplemental damping was realized using diagonal linear viscous dampers (VD) that were designed to provide either 10% or 25% damping in the first mode of the structure using the process outlined in Christopoulos and Filiatrault (2006). In both the 10% and 25% VD designs, the number of dampers in each frame was minimized to provide the required damping level, but the size of the dampers was limited to avoid yielding in adjacent original structural elements. The implementation of all structural upgrades, with the exception of the BRBs, was also considered with the possibility of an incremental floor implementation where the upgrades was installed at only the first floor, or only the first two floors, or at all three floors. Since the installation of the

BRBs at only a limited number of floors would cause a vertical stiffness and strength irregularity, its implementation at a subset of floors was not considered. The design details for each upgrade option for a single frame of the structure are presented in Chapter 4, and the estimated costs for all ten structural upgrade options are summarized in Table 5.3.

Table 5.3: Summary of structural repair and upgrade costs for Level 2

Component (<i>n</i>)	Quantity (Unit)	Demand Parameter	Source of Fragility Function	Consequence Function	RC_n (% of BV)	Upgrade	UC_n (% of BV)
Total Building	1 unit	Drift (%)	Structural Analysis	Building	100+250	1, 2 & 3 BRB	6.6
				Replacement		1 10% VD	7.9
				and Casualties		1 & 2 10% VD	8.9
		Residual Drift (%)	Structural Analysis	Building	100	1 25% VD	7.5
				Replacement		1 & 2 25% VD	10.3
						1, 2 & 3 25% VD	12.2
PRENORTH MRF Connections	72 units	Rotation (rad)	FEMA P-58	Repair	11	1 SCSHJ 1 & 2 SCSHJ 1, 2 & 3 SCSHJ	7.3 9.0 10.0
Gravity Connections	276 units	Rotation (rad)	FEMA P-58	Repair	33		

Step 3: Analysis of Upgrade Designs

The performance of each structural upgrade design was evaluated using the same multiple stripe analysis process used for the original structure but with updated first mode periods when required. Table 5.4 summarizes the obtained Q_θ values for each structural upgrade design and also includes the values of Q_β to demonstrate the validity of approximating Q_β as 1.0 in the MSP method.

Table 5.4: Calculated Q_θ values for Level 2 of MSP method

Upgrade Design	Collapse	Residual Drift	Floor Acceleration	Floor Drift
	$Q_{\theta,C} (Q_\beta)$	$Q_{\theta,NR} (Q_\beta)$	$Q_{\theta,accel.} (Q_\beta)$	$Q_{\theta,drift} (Q_\beta)$
BRB	1.45 (1.03)	1.31 (1.07)	1.45 (1.14)	0.41 (1.07)
1 SCSHJ	1.40 (0.81)	1.39 (0.88)	1.12 (1.02)	1.28 (1.03)
1 & 2 SCSHJ	1.30 (0.80)	1.34 (0.87)	1.20 (1.01)	1.29 (1.03)
1, 2 & 3 SCSHJ	1.51 (0.79)	1.54 (0.90)	1.255 (1.02)	1.31 (1.05)
1 10% VD	1.57 (0.93)	1.40 (1.03)	0.58 (1.00)	0.43 (1.03)
1 & 2 10% VD	1.68 (0.97)	1.56 (0.99)	0.51 (1.02)	0.25 (1.02)
1, 2 & 3 10% VD	1.85 (0.99)	1.64 (0.98)	0.45 (1.03)	0.21 (1.04)
1 25% VD	1.60 (0.92)	1.52 (0.97)	0.58 (0.99)	0.25 (1.05)
1 & 2 25% VD	1.78 (0.90)	1.73 (0.94)	0.52 (0.99)	0.19 (1.01)
1, 2 & 3 25% VD	2.39 (0.95)	1.96 (0.91)	0.43 (1.02)	0.16 (1.01)
Nonstructural Only	1.00 (1.00)	1.00 (1.00)	1.00 (1.00)	1.00 (1.00)

EAL values for all four loss categories are shown in Figure 5.8 for all structural configurations in both scenarios (original and upgraded) as a function of their respective Q_θ values. A function correlating EAL to Q_θ values was fitted for each of the loss categories and shown in Figure 5.8. While the type of function is determined from the nature of the calculation of the annual frequency of occurrence of damage ($\lambda(DS)$), as described in Section 5.3.3, the regression constants of each function are unique to this case study. Furthermore, the cause for the imperfect correlation of the $EAL(Q_\theta)$ functions is the result of the small deviations in lognormal standard deviation from the original to the upgraded curves, as shown in Table 5.4. When considering only net benefit from the structural upgrade designs without the inclusion of the nonstructural options, the results shown in Figure 5.8 indicate that the various viscous damping designs are the only structural upgrades that lower the EAL in all four categories. While all structural upgrade designs provide reductions in losses caused by both collapse and non-repairable residual drifts by increasing the median value of

both curves, the BRB and SCSHJ upgrades increase some of the floor hazard values resulting in increased $EALs$, as shown in Figure 5.8. The BRB upgrade increases the peak floor accelerations, causing the increase in $EALs$ associated with the acceleration-sensitive nonstructural components to outweigh the total decreases in EAL from the other three loss categories, resulting in a net negative change in EAL due to structural changes alone.

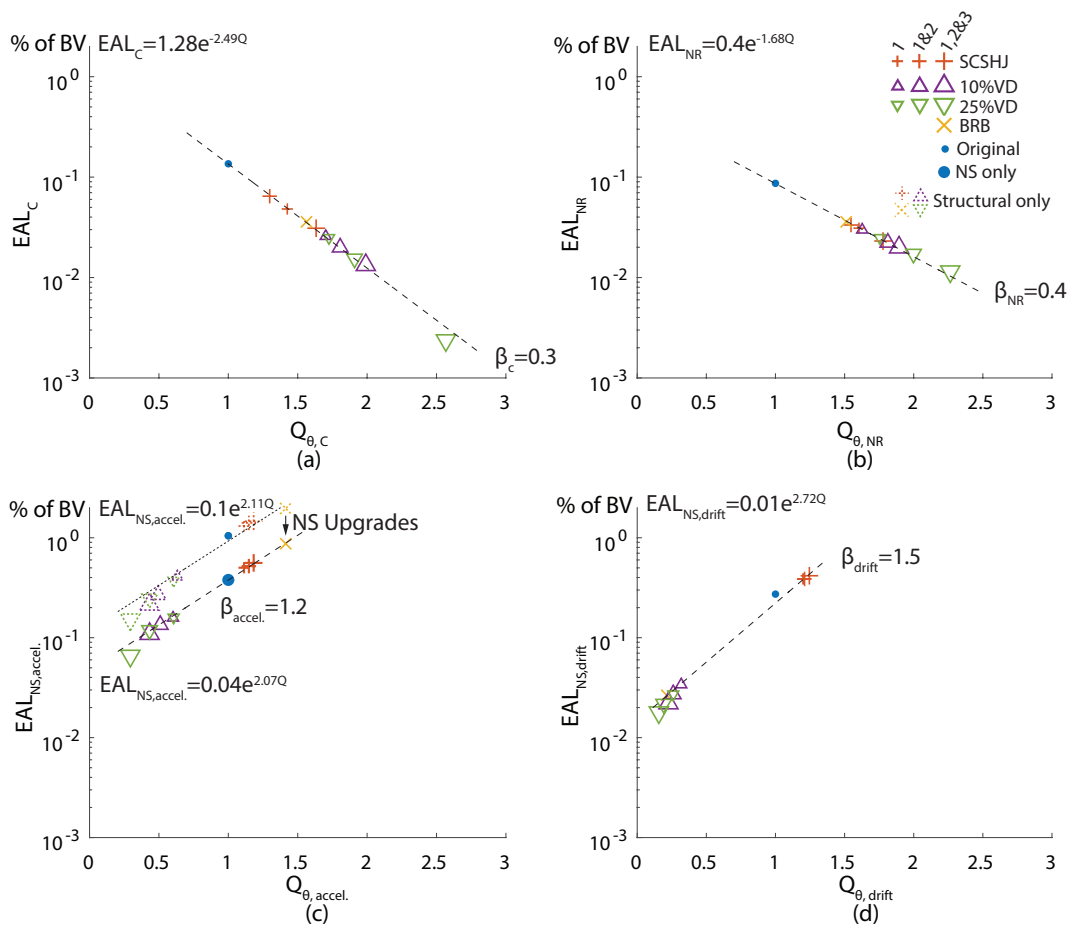


Figure 5.8: EAL values for all four loss categories

Step 4: Non-Structural Upgrades

The selection of nonstructural components for upgrade was identical to Step 4 of Level 1, with the distinguishing feature of using the floor hazard curve

calculated using the results of the multiple stripe analyses, as described in Section 5.3.2. For all upgrade designs, only acceleration-sensitive nonstructural component upgrades had BCR values exceeding one at this amortization value, as will be discussed in Section 5.6.3. Since the BRB and SCSHJ structural upgrades induced the largest floor hazards, these structural upgrades led to the most extensive implementation of nonstructural upgrades as their larger values of $f(EDP)$ increase the BCR value in Equation (5.3.16) for all nonstructural component upgrades. Since the results used in Figure 5.8 do not indicate the viability of each structural upgrade design, the changes in EAL values as well as the upgrade costs are summarized in Table 5.5 for each of the 10 structural upgrade designs. Each row shown in Table 5.5 is the result for that structural upgrade design at the specific amortization value, with each nonstructural upgrade being selected only when it provided a net positive benefit to the NPV for that particular structural upgrade strategy.

Step 5: Evaluation of NPV

The final step in the Level 2 analysis is the evaluation of the NPV of each upgrade design. This consists of the summation of all changes in EAL obtained from the previous step (EAL_T), as well as the summation of all upgrade costs identified in Step 2 and Step 4. Using these values, along with the amortization of the owner profile, the NPV was calculated using Equation (5.2.1) and is presented as a percentage of the building value. These values are shown in Table 5.5 for each upgrade design, along with an overall BCR value which indicates the most efficient upgrade designs. To illustrate the effect of structural and nonstructural upgrades, the change in losses associated with each of the 11 designs (10 structural and 1

nonstructural only) was calculated with and without the inclusion of the nonstructural upgrades.

Table 5.5: Summary of change in EAL for each structural upgrade and net positive nonstructural upgrade

Upgrade Design	$\Delta(EAL_C)$ (% of BV)	$\Delta(EAL_{NR})$ (% of BV)	$\Delta(EAL_{Accel.})$ (% of BV)	$\Delta(EAL_{Drift})$ (% of BV)	$\Delta(EAL_{Total})$ (% of BV)	Cost (% of BV)	BCR (2%/40 years)	NPV with non-structural upgrades	NPV without non-structural upgrades (%) (2%/40 years)
NS Only	0	0	0.67	0	0.67	6.43	2.85	11.90	N/A
BRB	0.08	0.05	0.18	0.26	0.57	12.99	1.20	2.60	-21.97
1 SCSHJ	0.06	0.06	0.56	-0.11	0.57	13.64	1.14	1.95	-13.3
1 & 2 SCSHJ	0.05	0.05	0.52	-0.12	0.50	12.38	0.89	-1.70	-17.51
1, 2 & 3 SCSHJ	0.08	0.06	0.48	-0.14	0.48	16.60	0.79	-3.47	-19.96
1 10% VD	0.09	0.06	0.79	0.25	1.19	12.94	2.52	19.61	10.94
1 & 2 10% VD	0.09	0.06	0.87	0.26	1.28	16.85	2.53	21.17	14.43
1, 2 & 3 10% VD	0.10	0.07	0.90	0.26	1.33	15.46	2.35	20.92	14.90
1 25% VD	0.09	0.06	0.80	0.26	1.21	12.60	2.63	20.50	12.43
1 & 2 25% VD	0.10	0.07	0.87	0.27	1.31	15.28	2.35	20.56	13.43
1, 2 & 3 25% VD	0.11	0.08	0.89	0.27	1.35	15.01	2.46	21.92	17.39

For this case study example, the upgrade design considering only nonstructural components has the highest *BCR* value of all upgrade designs, suggesting that this upgrade design is the most efficient. However, the *NPV* indicates that the largest net benefit is obtained when implementing the viscous damper upgrade with 25% damping in all three stories. The difference in which upgrade strategy seem most desirable according to the *BCR* versus the *NPV* indicates a diminishing return on investment when the *BCR* reduces but is still greater than 1.00. The *NPV* of the scenario considering only structural upgrades highlights the net negative result obtained when implementing the BRB and SCSHJ upgrades discussed earlier. The benefit of including nonstructural upgrades with each structural upgrade design is identified by comparing the two *NPV* value column; where the MSP method identifies nonstructural upgrades with a net benefit of 11.9% when considering the original structure, 24.5% with the BRB upgrade, but only 4.5% for the 25% viscous damping upgrade at all storeys because fewer nonstructural components are susceptible to the reduced demands in this case. However, including nonstructural component upgrades indicates that 9 of the 11 considered structural upgrade designs result in a positive *NPV*, so these would be included as options in a Level 3 analysis.

Potential Adjustment to Step 4: Iteration of *BCR* in MSP Method

To improve the accuracy of a Level 2 analysis, an iterative *BCR* evaluation process was implemented in the Level 2 MSP method to account for the shared upgrade tasks across upgrades, as mentioned in Section 5.5.3. The addition of cost iterations to the MSP method, referred to as MSPIT, determined initial *BCR* values using the same process as the MSP method on the first iteration

but used the information about the selected components' upgrade tasks to reduce the upgrade cost of other components by the value of shared tasks before recalculating their *BCR*. This iteration process was repeated until no new upgrades were identified. However, the shared consequence functions and economies of scale captured in the Level 3 analysis (see section 5.5.3) are still not reflected in this proposed MSPIT method.

5.6.3 Level 3: Optimizing Upgrades Using Genetic Algorithm

The archetype structure and the maximization of the economic NPV in Equation (5.2.1) at the 2% rate of return and 40-year occupancy is identical to the archetype scenario presented in Chapter 4 and that study serves herein as the Level 3 analysis. The GA optimization run was repeated 100 times, and the rate at which components were selected in the optimal solution at each value was recorded. These are summarized in Figure 5.9 and range from values of 100 for components whose upgrade was selected in every analysis, to 0 for components whose upgrade was never selected. Figure 5.9 also lists the results obtained from the MSP method used in the Level 2 analysis and the modified MSPIT method presented in Section 5.6.2.6. All three approaches resulted in the selection of 25% viscous damping as the optimal structural upgrade design, and the identification of various nonstructural mechanical equipment for upgrade. However, while all three approaches have some similarities in component selection, the systemic differences caused by the factors presented in Section 5.5.3 become apparent across the selected components. By taking advantage of the task sharing accounting, the GA

and MSPIT identified several additional nonstructural component upgrades as optimal when compared to the MSP method, such as the piping systems which can be installed using common suspended trapeze restraint systems.

		High Priority			Low Priority			r=2%			r=4%			r=8%			r=12%		
		MSP	MSPIT	GA	MSP	MSPIT	GA	MSP	MSPIT	GA	MSP	MSPIT	GA	MSP	MSPIT	GA	MSP	MSPIT	GA
Category	Component																		
No Structural Upgrades	First Floor Structural							10			70	100	100	100					
	Second Floor Structural							10	100	100	90	100	100	100					
	Third Floor Structural							30	100	100	90	100	100						
Structural SCSHJ	First Floor Structural																		
	Second Floor Structural																		
	Third Floor Structural																		
Structural 10% VD	First Floor Structural																		
	Second Floor Structural																		
	Third Floor Structural																		
Structural 25% VD	First Floor Structural	100	100	100	100	100	90	100	100	30									
	Second Floor Structural	100	100	100	100	100	90			10									
	Third Floor Structural	100	100	100	100	100	70			10									
Structural BRB	First Floor Structural																		
	Second Floor Structural																		
	Third Floor Structural																		
Mech. Equip.	Chiller	100	100	100	100	100	100	100	100	100	100	100	100	100	100	100	100	100	100
	Cooling Tower	100	100	100	100	100	100	100	100	100	100	100	100	100	100	100	100	100	100
	Air Handling Unit	100	100	77	100	100	77												
	Control Panel	100	100	100		100	100		100	60									40
	Motor Controller	100	100	100		100	100		100	100									60
	Low Voltage Transformer		100	75		100	75			40									
	Distribution Panel		100	100		100	100		100	90		100	90		100	90			
Plumbing	Potable Piping		100	65			35												
	Large Diam. Heat Piping	100	100	100			100			35									
	Small Diam. Heat Piping		100	65			35			35									
	Sanitary Piping			45			35			35									
	Sprinkler Piping		100	70			70			70									
	Sprinkler Head		100	70			70			50									
Contents	Lighting	100	100	100			100			35									
	Desktop Equipment																		
	Office Furniture																		
Finishes	Suspended Ceiling																		
	Raised Floor																		
	Curtain Glazing																		
	Wall Partitions																		
	Roof Covering																		
HVAC	Large HVAC Duct																		
	Small HVAC Duct																		
	HVAC Diffuser																		
	Stairs																		
	Elevator																		

Figure 5.9: Comparison of selected upgrades (for occupancy time = 40 years)

5.6.4 Influence of Rates of Return

Figure 5.9 also includes the selection of components and designs for the optimal upgrade selected by the MSP, MSPIT, and GA methods at three other rates of return. The differences in optimal selection between the MSP analysis and the GA analysis noted above for the 2% rate of return become more apparent at the higher rates, where the BCR values obtained by Equation (5.3.16) reduces for all nonstructural components, leading to the de-prioritization of some in the GA and their non-selection in the MSP method. The MSPIT method identifies upgrades to the piping system at the lower rates of return but does not identify as many nonstructural components as candidates for upgrade as the GA at the higher rates. Figure 5.10 summarizes the comparison between the MSP, MSPIT, and GA method by quantifying the total upgrade cost of the optimal solution obtained from all three methods at rates of return ranging from 2 to 16% with an occupancy time of 40 years. For the GA method, the upgrade costs are the mean value of the 100 solutions obtained at each rate. The results of each method are shown fitted with an exponential decay curve. The differences in identified optimal upgrade costs, visualized in Figure 5.10, show that the Level 3 GA method leads to the highest upgrade cost at all rates of return, followed by the MSPIT, which underestimates the optimal upgrade cost by 1% to 3% at all rates of return but mirrors the GA results in both scope and component upgrade selection. Finally, while the MSP curve identifies all of the upgrades with the largest benefit to cost ratio, it only captures approximately two thirds of the total optimal solution obtained by the Level 3 GA method, missing potentially worthwhile upgrades that have a relatively small positive contribution to the upgrade NPV . This indicates

that the MSP method is a viable tool for the Level 1 and Level 2 goals of assessing the viability of seismic upgrades, and can become more accurate with the addition of an iterative approach to determine upgrade costs. However, a Level 3 analysis using a scenario-based optimization approach, such as the GA, still provides further optimization refinement.

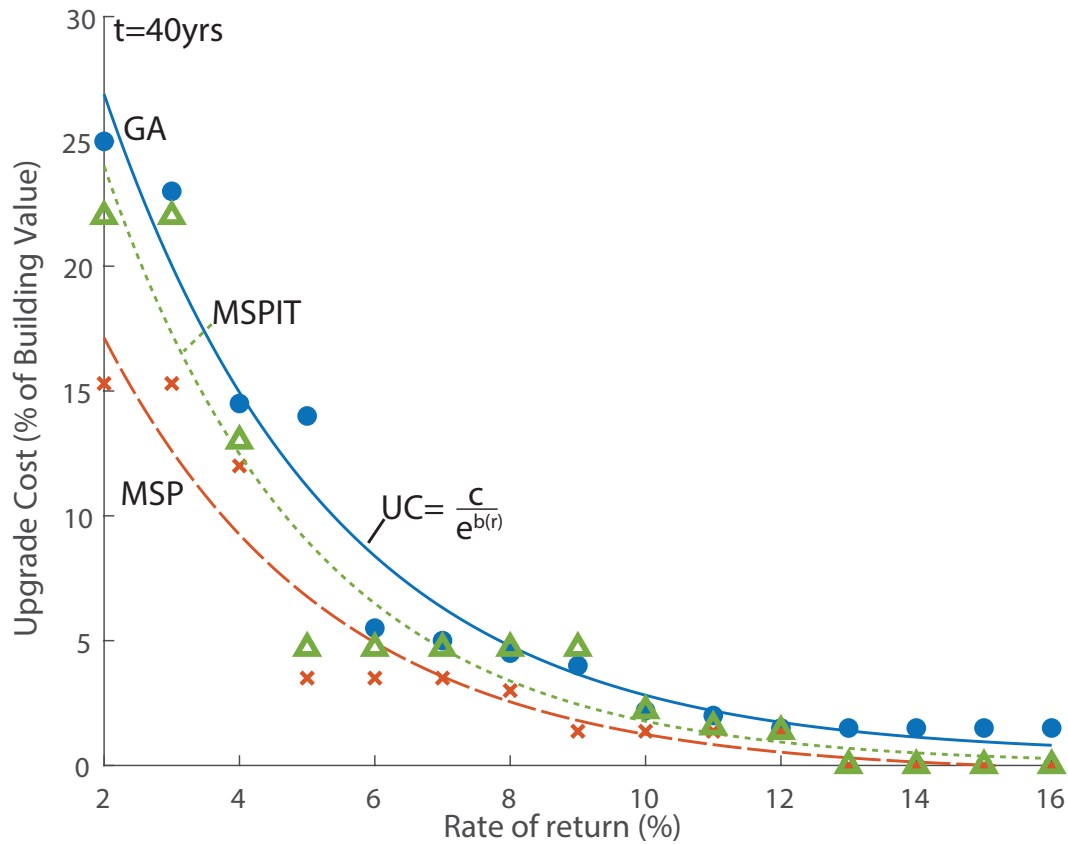


Figure 5.10: Total optimal upgrade cost obtained from each method

5.7 Conclusions

This paper provides a framework to identify and assess the viability of seismic upgrades considering both structural and nonstructural components options. The three-level framework is structured to initially require relatively

low computational resources and provides quantifiable milestones to indicate the continued estimated viability of the seismic upgrades being considered. While the third level of the framework utilizes a previously developed genetic algorithm optimization implementation structured around the Monte Carlo PBEE analysis, the initial two levels of the framework use the median shift probability (MSP) method, a rapid PBEE implementation method introduced in this paper. The MSP method measures the losses caused by different structural and nonstructural damage states while formalizing the relationships between structural and nonstructural component performance through the consideration of probability distributions, which define both structural performance and floor hazards. Each upgrade option is quantified by a shift in the median value of these curves. A case study example of the first two levels of the framework using a three-story steel moment resisting frame archetype structure led to an optimized solution for a upgrade strategy, which was then compared with results from a Level 3 analysis previously published by the authors. These observations indicate that the preliminary analysis provided by the use of the MSP method in the first two levels of the framework provided good indications of the optimal and viable upgrade strategy for a fraction of the computational effort required for the detailed Level 3 optimization. While the case study discussed in this paper focused on time dependent loss analysis by considering expected annual losses, a scenario based loss analysis could also be optimized using the same framework where a target performance is achieved at a specific intensity for a minimization of costs. In this scenario based analysis, the interaction of potential upgrades to both the structural and non-structural components must be considered when weighing the benefits and costs within a holistic

upgrade strategy.

As this framework provides a formal interpretation of the impact of structural modifications on the viability of seismic upgrades, continued research is required to provide guidance on the influence of various structural upgrades applied to different probability distributions of common archetype structures. The assumed shift in performance due to an upgrade (the Q_θ factors in Step 3 of the MSP process in Level 1) is a critical step in determining the viability of a structural upgrade, so developing guidance to estimate the assumed behaviour of an upgrade more accurately during preliminary design would allow for more certainty of a positive result before conducting Level 2 analysis. This would be possible if future studies of seismic structural upgrade approaches included quantification of structural response in terms of a shift in median probability distribution values (Q_θ). Finally, future case studies would also provide examples from which empirical guidelines on future upgrade implementations can be determined.

5.8 References

- AISC(American Institute of Steel Construction). (2016). “Specification for Structural Steel Buildings.” *AISC 360-16*, Chicago, IL, US
- Almufti, I., Willford, M. (2013) “REDi Rating System” *Resilience-Based Earthquake Design Initiative Rating System*
- ASCE(American Society of Civil Engineers). (2017). “Seismic Evaluation and Retrofit of Existing Buildings.” *ASCE 41-17*, Reston, VA, US
- Baker, J. W. (2015). “Efficient Analytical Fragility Function Fitting Using

- Dynamic Structural Analysis.” *Earthquake Spectra*, 31(1) 579–599.
- Baker, J. W., and Lee, C. (2017). “An Improved Algorithm for Selecting Ground Motions to Match a Conditional Spectrum.” *Journal of Earthquake Engineering*, 22 (4), 708-723.
- Behr, R. (2001) “Architectural Glass for Earthquake-resistant Buildings.” *Glass Processing Days*, Vol. 14, 18-21.
- Bradley, B., Dhakal, R., Cubrinovski, M., MacRae, G., and Lee, D. (2009) “Seismic loss estimation for efficient decision making” *Bulletin of the New Zealand Society for Earthquake Engineering*, 42 (2), 96-110.
- Bull, D., (2011) “Stairs and Access Ramps Between Floors in Multi-story Buildings.” *Report to the Royal Commission*, Vol. 1, 1-8.
- Chakravarti, Laha, and Roy, (1967). *Handbook of Methods of Applied Statistics*, Volume I, John Wiley and Sons, pp. 392-394.
- Christopoulos, C., and Filiatrault, A. (2006) Principles of Passive Supplemental Damping and Seismic Isolation, IUSS Press, Pavia, Italy
- Chopra, A., (2012). Dynamics of Structures. Pearson, 4th edition.
- Comerio, Mary C., 2000. “The Economic Benefits of a Disaster Resistant University: Earthquake Loss Estimation for UC Berkeley”, *IURD Working Paper WP-2000-02*, Institute of Urban & Regional Development, Department of Architecture, University of California, Berkeley, CA.
- Cornell, C., and Krawinkler, H., (2000) “Progress and challenges in seismic performance assessment.” *PEER News*, April

DHS/FEMA(2007), "Multi-hazard Loss Estimation Methodology: Earthquake Model, HAZUS-MH MR3 Technical Manual", *National Institute of Building Sciences (NIBS) for the Department of Homeland Security, Emergency Preparedness and Response Directorate*, Federal Emergency Management Agency, Mitigation Division.

DOT(Department of Transportation) (2016) "Guidance on Treatment of the Economic Value of a Statistical Life (VSL) in U.S. Department of Transportation Analyses – 2016 Adjustment." *U.S. Department of Transportation Office of the Secretary of Transportation, Memorandum to Secretarial Officers*, August 8th, 2016, Washington, D.C.

FEMA(2000). "Recommended Seismic Evaluation and Upgrade Criteria for Existing Welded Steel Moment-Frame Buildings" *Report 351 Federal Emergency Management Agency*, Washington, D.C.

FEMA(2009). "Quantification of Building Seismic Performance Factors" *Report P-695 Federal Emergency Management Agency*, Washington, D.C.

FEMA(2011). "Reducing the Risks of Nonstructural Earthquake Damage-A Practical Guide" *Report E-74 Federal Emergency Management Agency*, Washington, D.C.

FEMA(2012). "Seismic Performance Assessment of Buildings - Methodology." *Report P-58 Federal Emergency Management Agency*, Washington, D.C.

Filiatrault, A., Kuan, S., and Tremblay, R. (2004) "Shake Table Testing of Bookcase-partition Wall Systems." *Canadian Journal of Civil Engineering*, 31, 664-676.

- Flores, F., Lopez-Garcia, D., and Charney F., (2015) “Floor Accelerations in Building Having Different Structural Systems” *ASCE Structures Congress*, Portland, Oregon.
- Galanis, P., Sycheva, A., Mimra, W., Stojadinvic, B. (2018) “A Framework to Evaluate the Benefit of Seismic Upgrading” *Earthquake Spectra*, 34, 527-548.
- Günay, S., Mosalam, K., (2013). “PEER Performance-Based Earthquake Engineering Methodology, Revisited” *Journal of Earthquake Engineering*, 17(6), 829-858.
- Gupta, A., and Krawinkler, H. (1999). “Seismic Demands for Performance Evaluation of Steel Moment Resisting Frame Buildings.” *Department of Civil and Environmental Engineering*, Stanford University, Report No. 132.
- Hofer, L., Zanini, M., Faleschini, F., and Pellegrino, C. (2018) “Profitability Analysis for Assessing the Optimal Seismic Retrofit Strategy of Industrial Productive Processes with Business-Interruption Consequences” *Journal of Structural Engineering*, 144 (2)
- Ibarra, L., Medina, R., and Krawinkler, H. (2005). “Hysteretic Models That Incorporate Strength and Stiffness Deterioration” *Earthquake Engineering and Structural Dynamics*, 34, 1489-1511.
- Khoo, H.-H., Clifton, C., Butterworth, J., MacRae, G., Gledhill, S., and Sidwell, G. (2012). “Development of the self-centering Sliding Hinge Joint with friction ring springs.” *Journal of Constructional Steel Research*, 78, 201–211.

- Liel, A., Haselton, C., Deierlein, G., Baker, J., (2009). “Incorporating modeling uncertainties in the assessment of seismic collapse risk of buildings” *Structural Safety*, vol. 31, 197-211.
- Mayes, R., Wetzel, N., Weaver, B., Tam, K., Parker, W., Brown, A., and Pietra, D. (2013) “Performance Based Design of Buildings to Assess Damage and Downtime and Implement a Rating System” *Bulleting of Earthquake Engineering*, 46(1), 40-55.
- McKenna, F., Fenves, G. L., and Scott, M. (2000). Open System for Earthquake Engineering Simulation. University of California Berkeley, CA.
- Merino, R., Perrone, D., Filiatrault, A. (2019). “Consistent Floor Response Spectra for Performance-Bases Seismic Design of Nonstructural Elements” *Earthquake Engineering and Structural Dyanmics*, 49(3), 261-284.
- Miranda, E., and Aslani, H. (2003) “Probabilistic Response Assessment for Building-Specific Loss Estimation” *Pacific Earthquake Engineering Research Center Report No. 2003/03*, University of California Berkeley, California.
- Miranda, E., and Taghavi, S. (2003) “Estimation of seismic demands on acceleration-sensitive Nonstructural components in critical facilities.” *Proceedings of ATC-29-2 Seminar on Seismic Design, Performance, and Retrofit of Nonstructural Components in Critical Facilities*, ATC-29-2 Report, Applied Technology Council, California

Moon, K., Han, S., Lee, T., Seok, S., (2012) “Approximate MPA-based method for performing incremental dynamic analysis” *Nonlinear Dynamic*, Vol. 67, 2865-2888.

O’Reilly, G., Calvi, G., (2020) “Quantifying Seismic Risk in Structures via Simplified Demand-Intensity Models” *Bulletin of Earthquake Engineering*, 18, 2003-2022.

O’Reilly, G., Monteiro, R., (2019) “Probabilistic models for structures with bilinear demand-intensity relationships” *Earthquake Engineering and Structural Dynamics*, 48(2), 253-268.

PEER(Pacific Earthquake Engineering Research Center) (2013) “PEER NGA-West2 Database.” *Pacific Earthquake Engineering Research Center Report No. 2012/03*, Berkeley, California

Perrone, G., Cardone, D., O’Reilly, G., Sullivan, T. (2019) “Developing a Direct Approach for Estimating Expected Annual Losses of Italian Buildings” *Journal of Earthquake Engineering*, DOI: 10.1080/13632469.2019.1657988

Retamales, R., Davies, R., Mosqueda, G., and Filiatrault, A. (2013) “Experimental Seismic Fragility of Cold-Formed Steel Framed Gypsum Partition Walls.” *Journal of Structural Engineering*, 139 (8), 1285-1293.

RSMeans(2018) “Commercial Renovation Cost Data” *Reed Construction Data*, Norwell, MA,

Shilling, J. and Wurtzebach, C. (2012) “Is Value-Added and Opportunistic Real Estate Investing Beneficial? If So, Why?” *Journal of Real Estate*

Research, 34 (4), 429-461.

Soroushian, S., Zaghi, A., Maragakis, M., Echevarria, A., Tian, Y., and Filiatrault, A. (2015) “Analytical Seismic Fragility Analyses of Fire Sprinkler Piping Systems with Threaded Joints.” *Earthquake Spectra*, 31 (2), 1125-1155.

Steneker, P., Wiebe, L., Filiatrault, A., (2019). “Steel Moment Resisting Frames with Sliding Hinge Joint Connections: Seismic Evaluation Using Various Response Indices” *12th Canadian Conference on Earthquake Engineering*, Québec City, Canada

Sullivan, T., Welch, D., Calvi, M. (2014) “Simplified Seismic Performance Assessment and Implications for Seismic Design” *Earthquake Engineering and Engineering Vibration*, 13, 95-122.

USGS(United States Geological Survey) (2014). “Unified Hazard Tool” Version 4.1.9 (Lat: 47.6, Long: -122.3, T: 1.0 Sec)

Vamvatsikos, D., and Cornell, C. (2001). “Incremental Dynamic Analysis”, *Earthquake Engineering and Structural Dynamics*, 31(3), 491-514.

Welch, D., Sullivan, T., Calvi, G. (2014). “Developing Direct Displacement-Based Procedures for Simplified Loss Assessment in Performance-Based Earthquake Engineering” *Journal of Earthquake Engineering*, 18, 290-322.

Yeow, T., Orumiyehi, A., Sullivan, T., MacRae, G., Clifton, G., Elwood, K., (2018) “Seismic performance of steel friction connections considering direct-repair costs.” *Bulletin of Earthquake Engineering*, 16, 5963–5993.

Chapter 6

CONCLUSIONS AND RECOMMENDATIONS

The previous chapters presented the work completed as part of this sandwich thesis, where each manuscript is independent but pertains to the overall theme of seismic resiliency improvement of buildings with steel moment resisting frames (MRF). This chapter begins by providing a summary of the contributions of each of the thesis chapters in attaining the primary goal by answering their respective objective question, presented in Section 6.1. This is followed by Section 6.2 which recommends specific areas of future study centered on the continued optimization of seismic upgrades of buildings with steel moment resisting frames. Finally, Section 6.3 includes some closing remarks on the main contributions of this research and its applications to current industry practice.

6.1 Answers to Driving Research Questions

What global frame performance benefits are provided by replacing either pre-Northridge or pre-qualified connections with low-damage and high-performance connections?

The impact on the global frame performance caused by the replacement of either pre-Northridge or pre-qualified connections with low-damage and

high-performance alternatives was evaluated. The Sliding Hinge Joint (SHJ) and Self-Centering Sliding Hinge Joint (SCSHJ) connections were identified as potential candidates to produce a more resilient seismic design, and the impact of their implementation was determined by comparing the results of numerical models of identical archetype structures with differing connection detailing. Nonlinear numerical component models for both connection types were developed and were validated using prior experimental component test results. The frame performance was compared for three frames with different heights, all located in Seattle, Washington. The proximity of this site to the Cascadia and Puget Sound faults (USGS 2014) allowed the performance of frames to be compared across three different seismic hazard types, and the impact on global performance of the different connections was measured using three different engineering demand parameters (EDP) to account for damage states in addition to collapse. The frames with SCSHJ connections had the highest overall performance, followed by frames with the SHJ connections, frames with pre-qualified Reduced Beam Section (RBS) connections, and finally frames with pre-Northridge (PRENORTH) connections. The relative benefit provided by the use of SCSHJ connections was largest during ground motions with longer duration, during main-shock-after-shock ground motion sequences, in taller frames without soft-story irregularities, and when considering residual inter-story drift and acceleration EDPs. The implementation of the SHJ connection did not provide the same scale of benefit as the SCSHJ connection over the RBS connection as it exceeded the performance of the frame with RBS connection in only a limited number of performance metrics, such as providing slight reductions in peak floor acceleration in taller frames, and improvements in

collapse performance during main-shock-after-shock ground motions.

Can these benefits to the global frame performance be achieved by upgrading only a select subset of the MRF connections?

Following the identification of the global performance benefits provided by implementing low-damage connections described above, an investigation was undertaken to determine if only a limited number of locations with high connection ductility were required to achieve the desired global performance benefit level. The same three frames, each with differing heights and all located in Seattle, Washington, were examined and the global performance of the frames using only a single connection type were used as baseline curves. A criterion was developed to identify critical connections based on a connection's annual frequency of exceeding its strength degradation rotation (SDR). A limit of an annual frequency of exceedance of 4×10^{-5} was identified and the collapse performance of frames using SCSHJ connections placed only at locations exceeding this limit were compared with baseline frames using uniform connection implementation. The performance of frames with SCSHJ connections placed only at the critical connection locations had essentially the same performance as frames using SCSHJ connections at all locations, indicating that the same performance benefit can be achieved with a partial implementation of high-performance MRF connections. A design process for selecting the location of these critical connections at a single floor was developed based on direct displacement based design (DDBD) (Priestley et al. 2007) and the global performance of frames designed with the SCSHJ parameters obtained from this process mirrored the performance of the frame using only SCSHJ connections. Not only could these results encourage

designers to examine the potential of mixing connection types when designing new steel MRFs to achieve more resilient buildings, but the ability to replace only a subset of pre-Northridge MRF connections with high-performance variants while still exceeding the performance of code conforming frames implies a potentially advantageous retrofit strategy for existing sub-standard buildings.

How can a designer determine the optimal upgrade strategy when considering alternative upgrades to both structural and non-structural components?

The potential scope of seismic resiliency upgrade of buildings with steel moment resisting frames was expanded to include both structural strategies beyond just the replacement of MRF connections and the upgrade of non-structural components. This chapter presents an optimization methodology which uses a genetic algorithm to identify the most viable upgrade strategy according to a user-defined target metric. The performance of upgrade strategies was evaluated using a Monte Carlo implementation of Performance Based Earthquake Engineering (PBEE) (Miranda and Aslani 2003), as presented in FEMA P-58 (FEMA 2012). The optimization process identified the hierarchy of upgrade strategies for one of the archetype frames studied in the previous chapter across three different target metrics: economic loss reduction, downtime reduction, and casualty reduction. For all three targets, the most viable of the structural upgrade strategies was the installation of large viscous dampers, but this strategy was limited to implementation in scenarios with owner occupancy times greater than 40 years and rates of return less than 8%. However, for both the economic and

downtime targets, the upgrade of distinct non-structural components had the highest priority across all upgrades, and some were deemed viable even at rates of return exceeding 15% and/or short occupancy times of less than 10 years. For the economic target, the mechanical equipment had the highest upgrade priority, followed by the piping systems and lighting. For the downtime target, the upgrade of the larger mechanical equipment and finishes (such as the glazing and partitions) had the highest priority, followed by the upgrade of the contents and then plumbing. In no case was the structural upgrade of the MRF connections with SCSHJ connection identified as preferable to the addition of viscous dampers. This optimization process, while presented for a limited number of case studies, could easily be applied to other building scenarios and non-structural populations.

How can the relationship between a structure and its non-structural components be delineated to quickly assess and identify viable upgrade strategies?

The interconnected relationships between a structure and its non-structural components exist implicitly in the scenario-based and holistic Monte Carlo implementation of PBEE, limiting the ability to easily identify the optimal upgrade strategy for specific buildings. While the GA optimization methodology proposed in the previous chapter provided a systematic method of obtaining the optimal upgrade strategy, a further understanding of the implicit PBEE relationships allowed for an assessment and comparison of the viability of competing upgrade strategies by utilizing both component level analysis and engineering judgment. In this chapter, modification of the total probability based implementation of the PBEE

methodology provided both an explicit link between a structure and its non-structural components and allowed a deaggregation of loss across various structural and non-structural categories. This modification to the PBEE method, referred to as the median shift probability method (MSP), allows designers to more easily quantify the relative impact of any proposed structural upgrade on both structural and non-structural losses, while also identifying upgrades of non-structural components that would be beneficial. The MSP method is integrated in this chapter into a proposed three-level assessment framework which includes the GA optimization as the final level and provides consideration for the limited initial design time investment. The same case study archetype frame from Chapter 4 was used as an example of this framework and the results obtained from the first two levels of the framework, which use the MSP method to first assess upgrade strategy viability and then verify the viability of the schematic upgrade design, were compared with the results obtained from the GA optimization. The MSP method only identifies a subset of the non-structural component upgrades identified in using the GA optimization due to the GA's inclusion of cost savings provided by common upgrade tasks between components. Finally, the MSP method indicated that the SCSHJ structural upgrade strategy was the least competitive among those investigated as it caused increases in the drift sensitive non-structural component losses, which are relatively expensive components to upgrade, and these losses outweigh the benefits provided by other improvements in structural performance. Conversely, the other strategies, such as increases to the strength and stiffness through installation of buckling restrained braces (BRBs), provided larger increases to the collapse performance and reduced the inter-story drifts, but increased the

floor accelerations, a factor which is mitigated by non-structural component upgrades. Finally, the viscous damping upgrades provide both a benefit in structural performance, and decreases in both inter-story drifts and floor accelerations, justifying their larger capital investment.

6.2 Recommendations for Future Research

6.2.1 Continued SHJ and SCSHJ Connection

Component Testing

Current component testing completed by Khoo et al. (2013) has provided an adequate understanding of the non-linear hysteretic behaviour of the SHJ and SCSHJ connections. This testing verified the energy dissipation and ductile capacity of these connections, both allowing for the creation and validation of detailed analytical models and allowing for their implementation in new construction. However, as these component tests did not exceed the design rotations, they have not provided an indication of the failure mode of these connections. This is a parameter which is critical in understanding the component behaviour when approaching collapse of the structure. This lack of failure mode definition was overcome in this work by specifying that the asymmetrical friction connection would undergo its full non-linear behaviour before the mechanism would lock up and yielding of the adjacent beam section was anticipated, however, this assumption requires experimental validation. Beyond the definition of failure mode, research efforts should continue to examine the friction properties of the asymmetrical friction connection components in order to better control the non-linear

hysteretic behaviour.

6.2.2 Further Investigation of External Factors Influencing the Adoption of Low-Damage and High-Performance Systems

Continued investigation of the impact of building scenario factors on the benefits of implementing low-damage and high-performance systems should be pursued as these would provide a clearer understanding of situations when their implementation may become more viable. Examples of these factors include:

- The type of ground motion expected at the site impacting the use of high-performance systems.
- The influence of the building occupancy, which affects the population of non-structural components, on the structural system identified as most advantageous.
- The concentrated implementation of the high-performance systems at the location with highest benefit.

These investigations should go beyond the SHJ or SCSHJ connections, to include other high-performance systems which have local component implementations as their design scope can be modified locally while still increasing the global performance of the structure.

6.2.3 Tailoring Non-linear Hysteretic Structural Behaviour for Loss Reduction Objective

The majority of energy dissipation used in design codes consists of the yielding of a ductile element(s) identified during the capacity design process. This plastic energy dissipation is typically non-adjustable as both the stiffness and strength are determined by geometric properties of the member in question (e.g. an MRF connection strength is related to the beam (and therefore frame) stiffness, etc.). However, the introduction of innovative high-performance and low-damage energy dissipation methods provides designers with a wider degree of flexibility in perfecting the most seismic resilient system. Similar to research summarized in Christopoulos and Filiatrault (2006), which has demonstrated the advantages of modifying stiffness and strength independently to provide an optimal energy dissipation in hysteretic dampers, the opportunity to tune the non-linear hysteretic behaviour in high-performance systems allows for the optimization of the response of the system at multiple seismic intensities. As an example, the implementation of initial low activation force, high ductility and self-centering capable systems, combined with upgraded drift sensitive non-structural components, could provide excellent resiliency at low and medium intensity ground motions, while still satisfying the original collapse performance design code objective. The loss reduction optimization methods provided in this thesis can provide a framework for the investigation of these highly modifiable systems.

6.2.4 Continued Development of Structural Upgrade Strategy Behaviour (Q_θ Values)

The case study example using in this work considered structural upgrade strategies whose modifications to the behaviour of the original archetype structure was already well understood and documented in literature. However, even with these well documented structural systems, the initial Q_θ values used for each curve in Chapter 5 were difficult to assign in the initial stages of the upgrade assessment framework. As the accuracy of these values helps to indicate the early viability of a structural upgrade by identifying the required scale of the structural upgrade, a relationship between the structural upgrade cost and each of the Q_θ values would provide both a more rapid and a more accurate initial viability assessment of structural upgrades. Therefore, an effort to formalize the assignment of these behaviour values, including upgrades to structure types beyond those considered in this study, is recommended.

6.2.5 Development of Empirical Guidelines for Optimal Seismic Upgrade Strategies

The development of both the formal seismic upgrade assessment framework, and the evaluation methodologies used at each level, provides a means of systematically evaluating the viability of upgrades to individual structures. However, even when implementing the rapid evaluation tools, the viability and priority identification of individual upgrades requires some degree of analysis unique to the specific structure being investigated. The development

of pre-determined guidelines could provide important insight for practitioners seeking an instantaneous and generalized answer to both the viability and priority of upgrades. These guidelines, developed from empirical analysis of large populations of structures, would account for aspects such as different initial building conditions, non-structural component populations, and owner objectives and scenarios.

6.2.6 Expansion of Methods for Building Population Level Optimization

Finally, the identification and prioritization of viable resiliency upgrades should be of interest to owners of large numbers of individual structures as it could help identify common upgrades consistent throughout a typical building population. This is particularly true when utilizing the rapid MSP method, as general guidelines can often be developed using approximate methods which provide an adequate level of precision to determine the most viable upgrades. A proposed process would divide a population of buildings among several groups, typically defined by their dynamic response and distribution of the non-structural components, and then upgrades would be prioritized among the archetype groups using the empirical guidelines mentioned previously.

6.3 Looking Forward

Having developed several tools to help practicing engineers optimize potential seismic upgrade strategies, this work can be viewed as an extension

of the development of resilient design by focusing on the interaction between a structure and its non-structural components. This recognition of the interaction between both structural and non-structural upgrades provides further indication that seismic upgrading and resilient design do not necessarily require extensive structural upgrades. In contrast, many of the most viable upgrades are typically centered on the non-structural components, and default assumptions when beginning the process of resiliency design should begin with the influence of both potential non-structural component upgrades and structural changes on the performance of the non-structural components. This research has also further demonstrated the importance of consistently considering non-structural upgrade options as important contributions to an overall seismic resiliency improvement strategy, as the omission of their performance can contradict the intended improvements provided by proposed structural upgrades.

Several of the conclusions developed through this work could be immediately extended to practice as initial design guidelines. When contemplating enhancing the resiliency of new construction to reduce both financial and downtime consequences, designers should ideally aim to reduce floor accelerations and storey drifts simultaneously by selecting a structural system with efficient and non-damaging energy dissipation methods, such as supplemental viscous damping. A focus on acceleration reduction is important as components vulnerable to this EDP typically encompass a majority of the building value and upgrades to acceleration-sensitive contents (e.g. bookshelves) can be inconvenient to daily occupants, while seismic damage to drift-sensitive components can be mitigated by upgrading these components at relatively low marginal cost increases for new construction. In

retrofit scenarios, the situation becomes less clear, where strategies for minimizing repair costs may not be the same as for minimizing downtime. Like for new construction, the optimal solution identified in this work tended to include structural retrofits with viscous damping to reduce both acceleration and displacement demands. When this was not viable, retrofits to drift-sensitive finishes can be costly, so such non-structural upgrades were generally not recommended for a loss-based analysis. However, damage to these drift-sensitive components should likely be mitigated when seeking reductions in downtime, pointing towards retrofit solutions that reduce floor displacements by increasing the stiffness of the structure. With this increase in stiffness, such an upgrade strategy only increases the need to upgrade acceleration-sensitive non-structural components, which was generally recommended as part of any retrofit strategy.

6.4 References

- Christopoulos, C., and Filiatrault, A. (2006) *Principles of Passive Supplemental Damping and Seismic Isolation*, IUSS Press, Pavia, Italy
- FEMA(2012). “Seismic Performance Assessment of Buildings - Methodology.” *Report P-58 Federal Emergency Management Agency*, Washington, D.C
- Khoo, H. H., Clifton, C., Butterworth, J., and MacRae, G., (2013). “Experimental study of full-scale self-centering sliding hinge joint connections with friction ring springs.” *Journal of Earthquake Engineering*, 17(7), 972–977.
- Priestley, M.J.N., Calvi, G.M. and Kowalsky, M.J. (2007). *Direct*

Displacement-Based Seismic Design of Structures. IUSS Press, Pavia.

USGS(United States Geological Survey). (2014). “Unified Hazard Tool”

(Lat: 47.6, Long: -122.3, T: 1.0 Sec) URL:

<https://earthquake.usgs.gov/hazards/interactive/>.

Appendix A

CALIBRATION OF BEAM HINGE MODELS

A.1 Modeling of Existing MRF connections

A.1.1 Review of Experimental MRF Pre-Qualified Connection Testing

The 1994 Northridge Earthquake highlighted the unacceptable performance of common connection details for moment resisting frames, with fractures in beam-to-column connections occurring at rotation levels lower than had been expected (Bruneau 2011; Biddah and Heidebrecht, 1999, FEMA 2000b). These cracks were often observed at or near the beam bottom flange and they frequently initiated near the steel backup bar at the root pass of the weld (Tremblay et al. 1995; Barsom and Pellegrino 2002). An intensive research program was undertaken following these observations to develop connections that would avoid early fracture (FEMA 2000a). The main outcome of this research effort was the development of connections that have been shown to have reliable component-level ductile performance (FEMA 2000a). In United States standards, these connections have been identified as pre-qualified for use in the construction of MRFs (AISC 2016). Current design procedure consists of selecting a preferred pre-qualified connection, and subsequently using it uniformly throughout the frame (CISC 2014, AISC 2016). Some of these connections are shown in Figure A.1 and include the

reduced beam section (RBS), the welded unreinforced flange (WUF), bolted flange plate (BFP), Kaiser bolted bracket (KBB), bolted stiffened end plate (BSEP) and the bolted unstiffened end plate (BUEP).

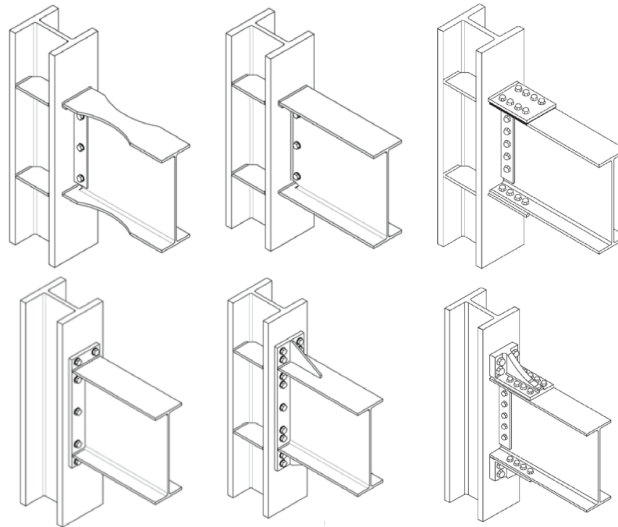
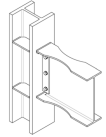
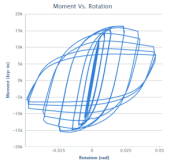
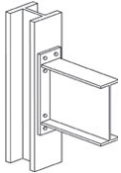
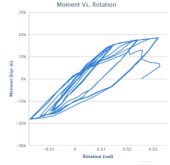
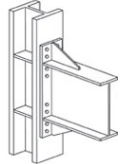
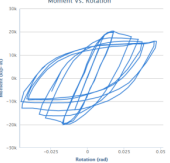


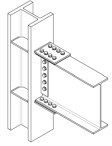
Figure A.1: Isometric view of pre-qualified connections (from top left, clockwise: RBS, WUF, BFP, KBB, WSEP, WUEP)

The ductile performance of each of the prequalified connections has been validated using extensive component testing and design guidelines have been developed according to the component test results. A summary of each of the currently available prequalified connections is presented in Table A.1, including the overall hysteresis shape, construction limitations and particular susceptibilities.

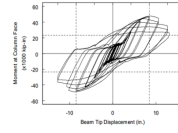
Table A.1: Summary of pre-qualified connections

Prequalified Connection	Location of plastic hinge (from centerline of column)	Hysteresis shape	Construction Limitations	Susceptibility
<p>Reduced Beam Section (RBS)</p> 	<p>Middle of the reduced section $(dc/2+a+b/2)$ Where dc is the column depth, a is the distance from the face of the column to the start of the cut and b is the length of cut.</p>	 <p>(Chi, 2002) Beam: 30x99 Column: 14x176</p>	<p>Prequalified Welds in both top and bottom flange. Backing bar must be removed, CJP must be back gouged and notches fixed. Welds must be inspected. Can use either bolted or welded web connection. Maximum beam depth: W920</p>	<p>Local buckling of section near RBS cuts</p>
<p>Bolted Unstiffened end-plate connection (BUEP)</p> 	<p>One third of the beam depth from the end-plate $(dc/2+tp+db/3)$ Where dc is the column depth, tp is the thickness of the end-plate and db is the depth of the beam</p>	 <p>(Sumner & Murray, 2002) Beam: 30x99 Column: 14x193</p>	<p>End-plate is shop welded to beam. No prequalified welds Maximum beam depth; W1400 (CAN), W760 (OMF, USA), W610 (SMF, USA)</p>	<p>Prying action on bolts causing tension yielding</p>
<p>Bolted Stiffened end-plate connection (BSEP)</p> 	<p>End of the stiffener $(dc/2+tp+Lst)$ Where dc is the column depth, tp is the thickness of the end plate and Lst is the length of the stiffener along the beam</p>	 <p>(Sumner & Murray, 2002) Beam: 30x99 Column: 14x193</p>	<p>End-plate is shop welded to beam. No prequalified welds Maximum beam depth: W920</p>	<p>Bolt slip causing pinching of hysteresis</p>

Bolted flange plate connection (BFP)



End of the flange plate ($d_c/2+L_p$) Where d_c is the column depth, L_p is the length of the flange plate

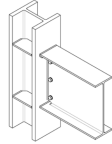


(Sato, Newell, & Uang, 2007) Beam:
35x150 Column:
14x311

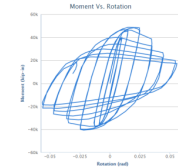
Flange plate is shop welded to column. No prequalified welds Maximum beam depth: W920 (CAN), W920 (OMF, USA), W760 (SMF, USA)

Bolt slip causing pinching of hysteresis

Welded unreinforced flange – welded web (WUF-W)



Half the beam depth from the column face ($d_c/2+d_b/2$) Where d_c is the column depth and d_b is the beam depth

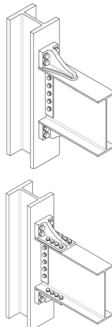


(Ricles, Fisher, & Faufmann, 2002) Beam: 36x150 Column: 27x258

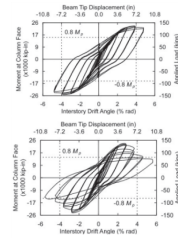
Beam flanges to column flange are prequalified welds. Backing bar must be removed, CJP must be back gouged and notches fixed. Welds must be inspected. Must weld web connection Maximum beam depth: W920 (USA only)

Strain hardening in beam flanges

Kaiser bolted bracket (KBB)



End of brackets ($d_c/2+L_b$) Where d_c is the column depth and L_b is the length of the bracket along the beam



((Shahidi, Nateghi-A, Razzaghi, & Shahidi, 2013)) Beam: 30x108 Column 14x233

Welded bracket connection to beam flange is prequalified. No weld can end within 25 mm of the end of the bracket. Weld notches must be grounded and fixed. Weld must be inspected. Maximum beam depth: W840 (USA only)

Bolt slip causing pinching of hysteresis Brittle weld failure

A schematic of a typical connection component test is shown in Figure A.2 (a) (from Chi and Uang 2002). The quantity of available component tests (Lignos and Al-Shawwa 2013) allows for the calibration of models which replicate the hysteretic (moment-rotation) behaviour of the connections. A replication of a component test using an analytical model is shown in Figure A.2 (b). This analytical model is constructed in OpenSees (McKenna et al. 2000) using a series of finite elements, including elastic beam/columns and non-linear springs.

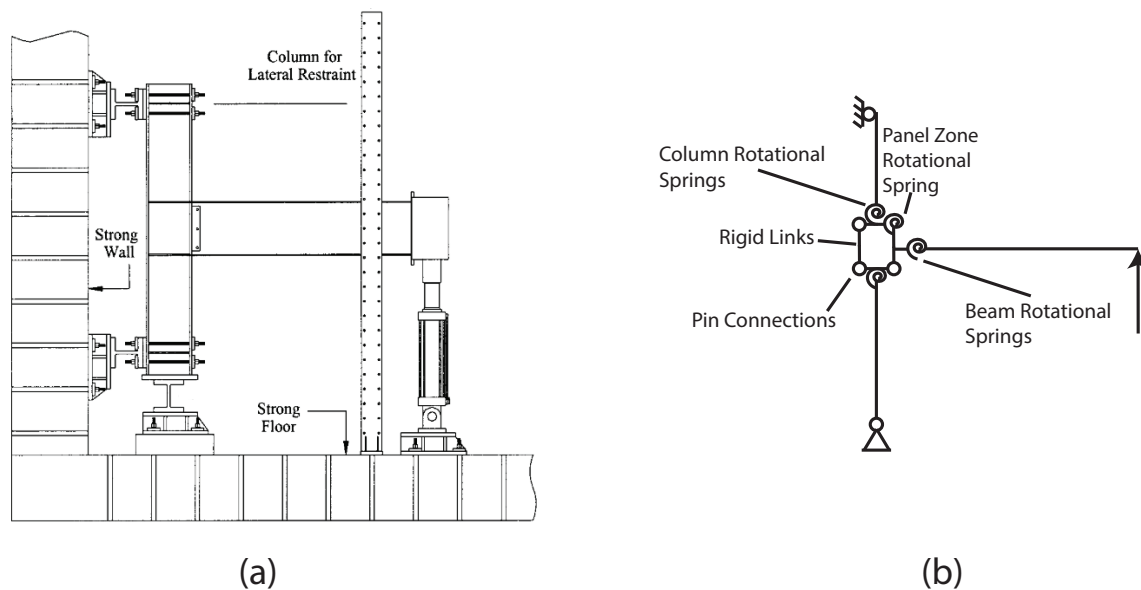


Figure A.2: (a) Typical MRF connection component test (Chi & Uang, 2002), (b) Analytical model of MRF connection component test

In the analytical component model, the effect of panel zone inelasticity was included using the Krawinkler spring box model (Gupta and Krawinkler 1999, Ibarra and Krawinkler 2005). This sub-assembly panel zone model captures the shear yielding of the panel zone using a trilinear hysteresis rotational spring

(Charney et al. 2004) calibrated to the geometric properties of the connecting elements, along with any added stiffener or doubler plates. The single rotational spring allows for the entire hysteretic behaviour of the panel zone to be controlled by one inelastic member, while the perimeter elements consist of rigid links connected by pin connections. However, no non-linear behaviour of either the columns or panel zone were observed during any of the component tests selected for use as benchmark calibrations for the beam spring.

A.1.2 Current Recommended MOdeling Procedure for Pre-Qualified Connections

Extensive research has been conducted on the topic of generating and calibrating reliable nonlinear models which replicated the behaviour of beam hinges in moment resisting connections (Lignos and Al-Shawwa 2013; ATC-72 2010). The current recommended modeling approach (ATC-72, 2010) uses the Ibarra-Medina-Krawinkler (Medina and Krawinkler, 2005) deterioration models to capture hysteretic behaviours such as post-yield strength and stiffness deterioration, cyclic and in-cycle deteriorations, kinematic and isotropic hardening as well as the behaviour at extreme rotations with the onset of fracture. Some guidance has been provided in the literature to determine values for many of the most important parameters of the IMK model. The current most widely used approach is based on regression equations presented in ATC-72 (2010) which identify three of the five critical hysteretic properties as functions of geometric properties of the beam cross section. These three parameters are the pre-capping plastic rotation (θ_p), the post-capping rotation (θ_{pc}), and the cumulative plastic rotation (Λ). No guidance is provided in the literature mentioned above to

determine the strain hardening ratio (α) and ultimate rotation (θ_u), as these parameters are both material and model dependant. The impact of these parameters on a hysteretic IMK model is shown in Figure A.3.

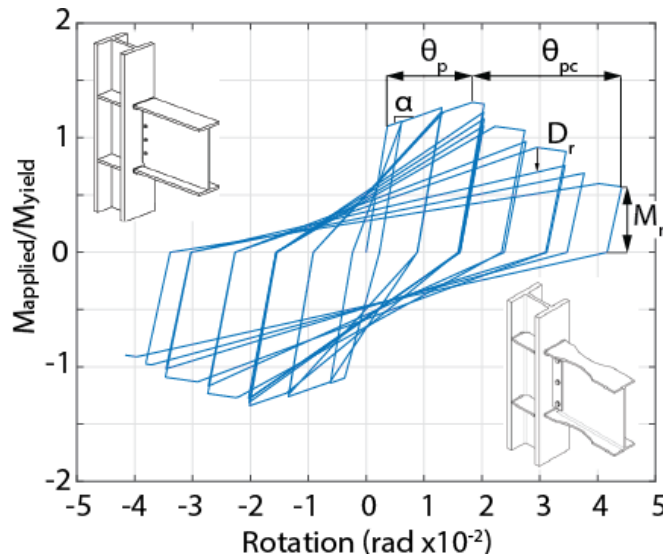


Figure A.3: Influence of major parameters for IMK model

Two sets of regression equations are made available in ATC-72 (ATC 2010) to calculate the pre-capping, post-capping and cumulative plastic rotations parameters: one for RBS connections and another for non-RBS connections. The regression equations for these three parameters are listed below, beginning with the RBS connections and concluding with the non-RBS connections. Plots of the data used to develop each regression equation are also included for each equation.

Pre-capping plastic rotation (θ_p), for beams with RBS connections:

$$\theta_p = 0.19 \left(\frac{h}{t_w}\right)^{-0.314} \left(\frac{b_f}{2t_f}\right)^{-0.1} \left(\frac{L_b}{r_y}\right)^{-0.1185} \left(\frac{d}{C_{unit}^1 21}\right)^{-0.76} \left(\frac{C_{unit}^2 F_y}{50}\right)^{-0.07} \quad (\text{A.1.1})$$

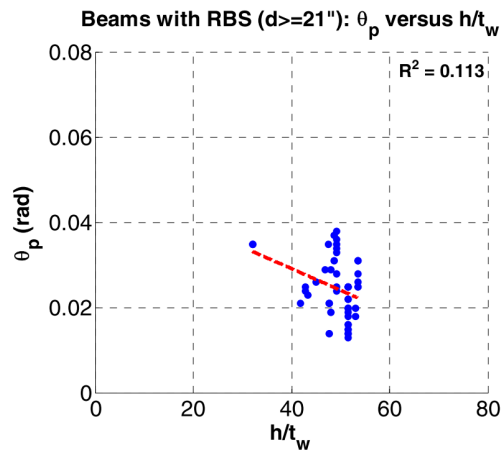


Figure A.4: Plot of regression data for pre-capping plastic rotation for RBS connections (ATC, 2010)

Post-capping plastic rotation (θ_{pc}), for beams with RBS connections:

$$\theta_{pc} = 9.62 \left(\frac{h}{t_w}\right)^{-0.513} \left(\frac{b_f}{2t_f}\right)^{-0.863} \left(\frac{L_b}{r_y}\right)^{-0.108} \left(\frac{C_{unit}^2 F_y}{50}\right)^{-0.36} \quad (\text{A.1.2})$$

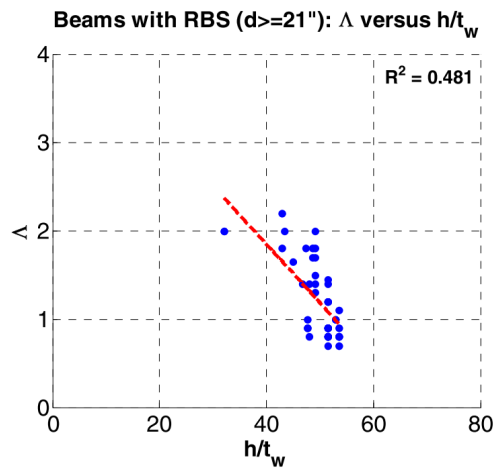


Figure A.5: Plot of regression data for post-capping plastic rotation for RBS connections (ATC, 2010)

Cumulative plastic rotation (Λ), for beams with RBS connections:

$$\Lambda = \frac{E_t}{M_y} = 592 \left(\frac{h}{t_w}\right)^{-1.138} \left(\frac{b_f}{2t_f}\right)^{-0.632} \left(\frac{L_b}{r_y}\right)^{-0.205} \left(\frac{C_{unit}^2 F_y}{50}\right)^{-0.391} \quad (\text{A.1.3})$$

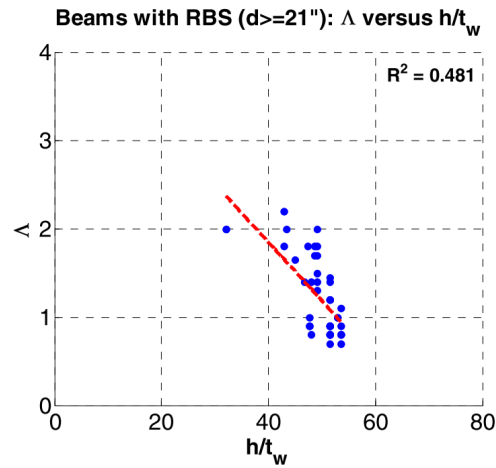


Figure A.6: Plot of regression data for cumulative plastic rotation for RBS connections (ATC, 2010)

Pre-capping plastic rotation (θ_p), for beams with non-RBS connections:

$$\theta_p = 0.087 \left(\frac{h}{t_w}\right)^{-0.365} \left(\frac{b_f}{2t_f}\right)^{-0.14} \left(\frac{L_b}{r_y}\right)^{0.34} \left(\frac{d}{C_{unit}^1 21}\right)^{-0.721} \left(\frac{C_{unit}^2 F_y}{50}\right)^{-0.23} \quad (\text{A.1.4})$$

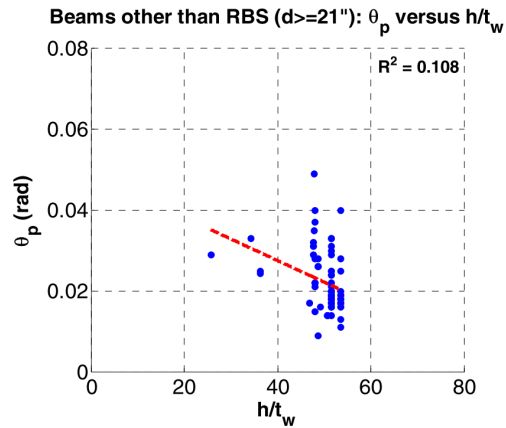


Figure A.7: Plot of regression data for Pre-capping plastic rotation for non-RBS connections (ATC, 2010)

Post-capping plastic rotation (θ_{pc}), for beams with non-RBS connections:

$$\theta_{pc} = 5.7 \left(\frac{h}{t_w}\right)^{-0.565} \left(\frac{b_f}{2t_f}\right)^{-0.8} \left(\frac{L_b}{r_y}\right)^{-0.28} \left(\frac{C_{unit}^2 F_y}{50}\right)^{-0.43} \quad (\text{A.1.5})$$

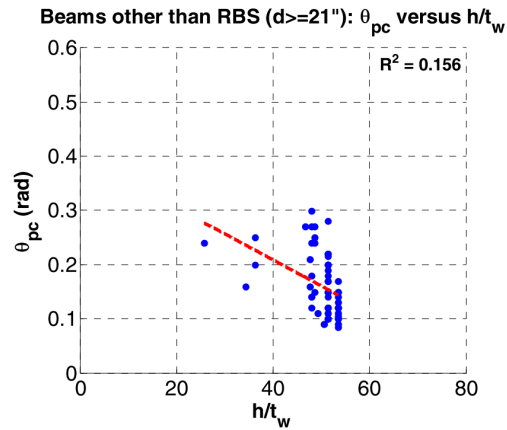


Figure A.8: Plot of regression data for post-capping plastic rotation for non-RBS connections (ATC, 2010)

Cumulative plastic rotation (Λ), for beams with non-RBS connections:

$$\Lambda = \frac{E_t}{M_y} = 500 \left(\frac{h}{t_w} \right)^{-1.34} \left(\frac{b_f}{2t_f} \right)^{-0.595} \left(\frac{C_{unit}^2 F_y}{50} \right)^{-0.36} \quad (\text{A.1.6})$$

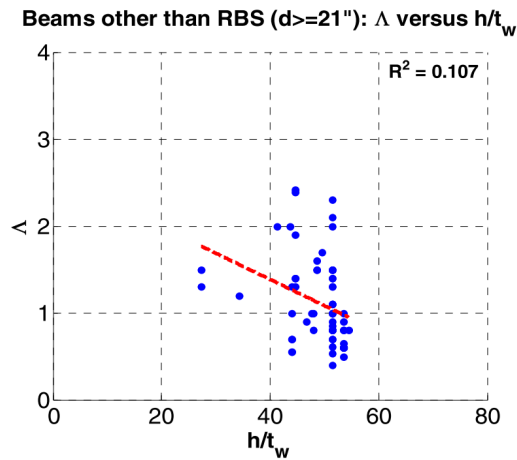


Figure A.9: Plot of regression data for cumulative plastic rotation for non-RBS connections (ATC, 2010)

Where the parameters used in these equations are defined as:

- h/t_w is the ratio of fillet-to-fillet depth to web thickness. The range of the data is from 21 to 55 for RBS connections and 20 to 55 for non-RBS.
- L_b/r_y is the ratio of unbraced length to the radius of gyration about the weak axis of the cross section. The range of the data is from 20 to 65 for RBS connections and 20 to 80 for non-RBS.
- $b_f/2t_f$ is the ratio of flange width to thickness. The range of the data is from 4.5 to 7.5 for RBS connections and 4 to 7 for non-RBS.

- L/d is the ratio of shear span to depth. The range of the data is from 2.3 to 6.3 for RBS connections and from 2.5 to 7 for non-RBS.
- d is the depth of beam using either metric or imperial units. The range of the data is from 18 to 36 for RBS connections and 4 to 36 for non-RBS.
- F_y is the yield strength of the flange in ksi. The range of the data is from 38 to 63 for RBS connections and from 35 to 65 for non-RBS.
- c_{unit} is a coefficient for unit conversion. If using metric, the value is 0.0254 for c_{unit}^1 and 0.145 for c_{unit}^2 . Both values are 1.0 if using imperial units.

While the regression equations presented in ATC-72 and summarized above provide guidance on determining only three of the 26 parameters for the IMK model, no equations are provided for many of the remaining parameters. Furthermore, a majority of the coefficient of determinations (R^2) of the regression equations are between 0.1 and 0.2, as shown in each figure, indicating a very limited statistical correlation between the ratio of fillet-to-fillet depth over web thickness and the three parameters in question. An initial hypothesis of the factors leading to these low R^2 values is other, external properties of the component tests which are not captured by the comparison of only beam cross section geometric properties. An example of this variation can be seen in Figure A.10 (a-f) which shows the moment-rotation relationship for seven component tests conducted using W36 beam sizes varying from W36x135 to W36x194, with four of the tests being conducted on W36x150 (Popov et al 1997, Engelhardt and Sabol 1994, Moore and Engelhardt 2000, Chi and Uang 2002). Even within this single beam size, which would have similar model parameters obtained from the regression equations, large variations can be observed in the skeleton curves shown in Figure A.10 (i). Across

these seven component tests conducted on beams of the same depth, the magnitude of the differences in hysteretic behaviour amounts to some component tests having approximately 25% more energy dissipated than another test with an identical beam section (W36x150 beam with W27x194 column vs W36x150 beam with W14x426 column). Therefore, these variations in hysteretic behaviour, particularly when comparing the four W36x150 beam types, could be attributed to factors ranging from differences in column section size, to variations in the properties of the RBS cut, as well as modifications of the panel zone such as doubler plates and continuity plates. These external differences are not accounted for when using the regression equations proposed in ATC-72 and therefore, the ATC-72 values are used only as preliminary parameters in this study.

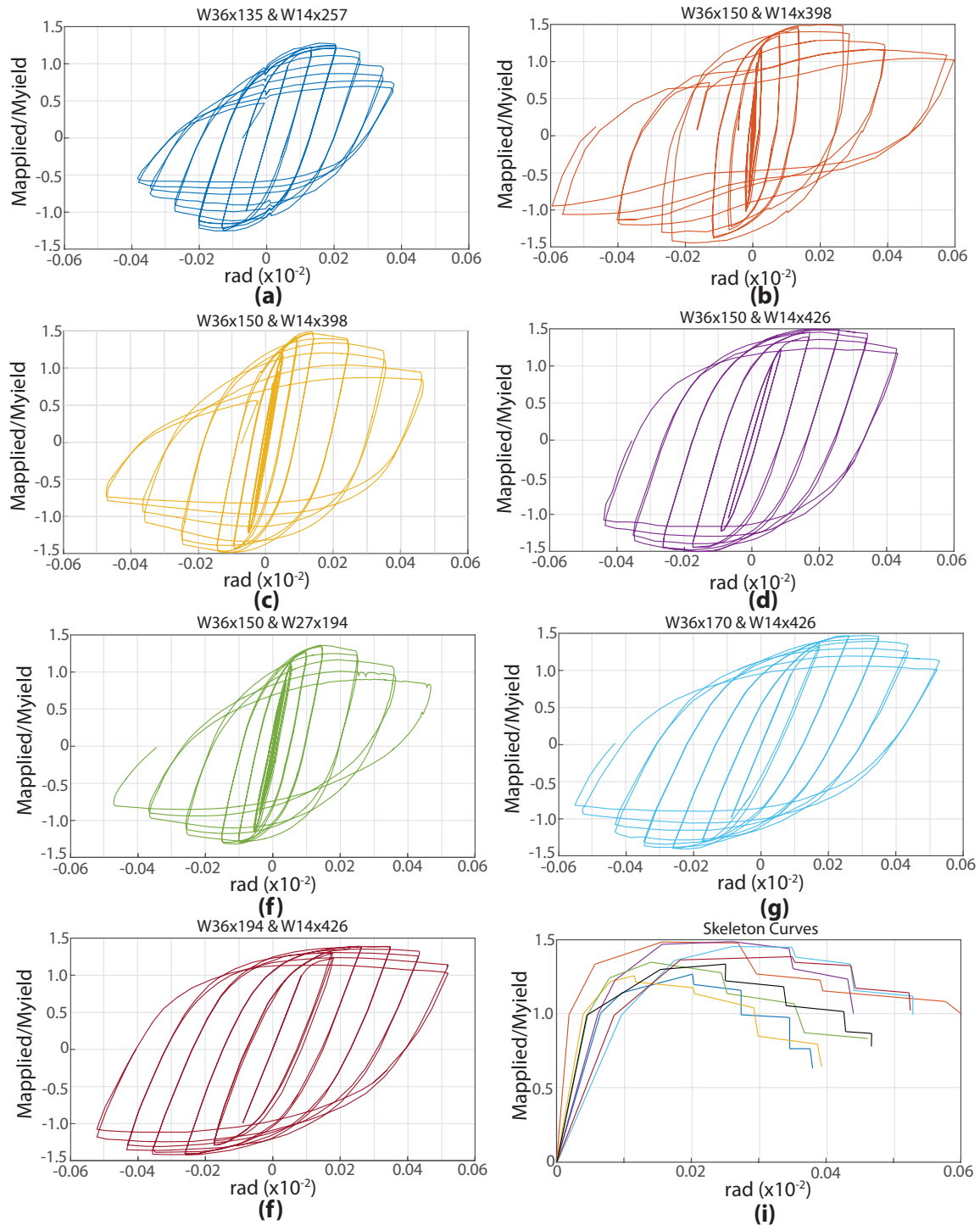


Figure A.10: Moment-rotation relationship for various RBS component tests [a) Popov et al., 1997; b) Moore and Engelhardt, 2000; c) Gilton and Uang, 2002; d) Engelhardt and Sabol, 1994; f) Chi and Uang, 2002; g) Engelhardt and Sabol, 1994; h) Engelhardt and Sabol, 1994], (i) skeleton curve of each component test

With so many variations in possible connection properties, component tests with the exact properties as the connections which were designed for the archetype frames are not currently available. In order to begin calibrating the IMK parameters, component test results of beam and column sections of similar sizes as those used in the three archetype frames were considered. The currently available component test results with sections having sizes which most closely matched the variable sizes of beams in the archetype frames were selected and are shown in Figure A.11. These vary in depth from W24 to W33 with several variations in connection properties, such as doubler and continuity plates, occurring across different connections (Chi and Uang (2002), Engelhardt and Sabol (1994), Moore and Engelhardt (2000), Popov and al (1997)). Similarly, the depth of the beams in the archetype frames varied from W21 to W33 for the three story frame, W24 to W30 for the six story frame and only W24 for the entire twelve story frame. The backbone and skeleton curves for all six of the component tests are shown in Figure A.12 (a) and (b), respectively, and demonstrate a much smaller variability, particularly at rotation values less than 0.035 rad, when compared to the skeleton curves shown in Figure A.10 (i) for the larger beam sizes.

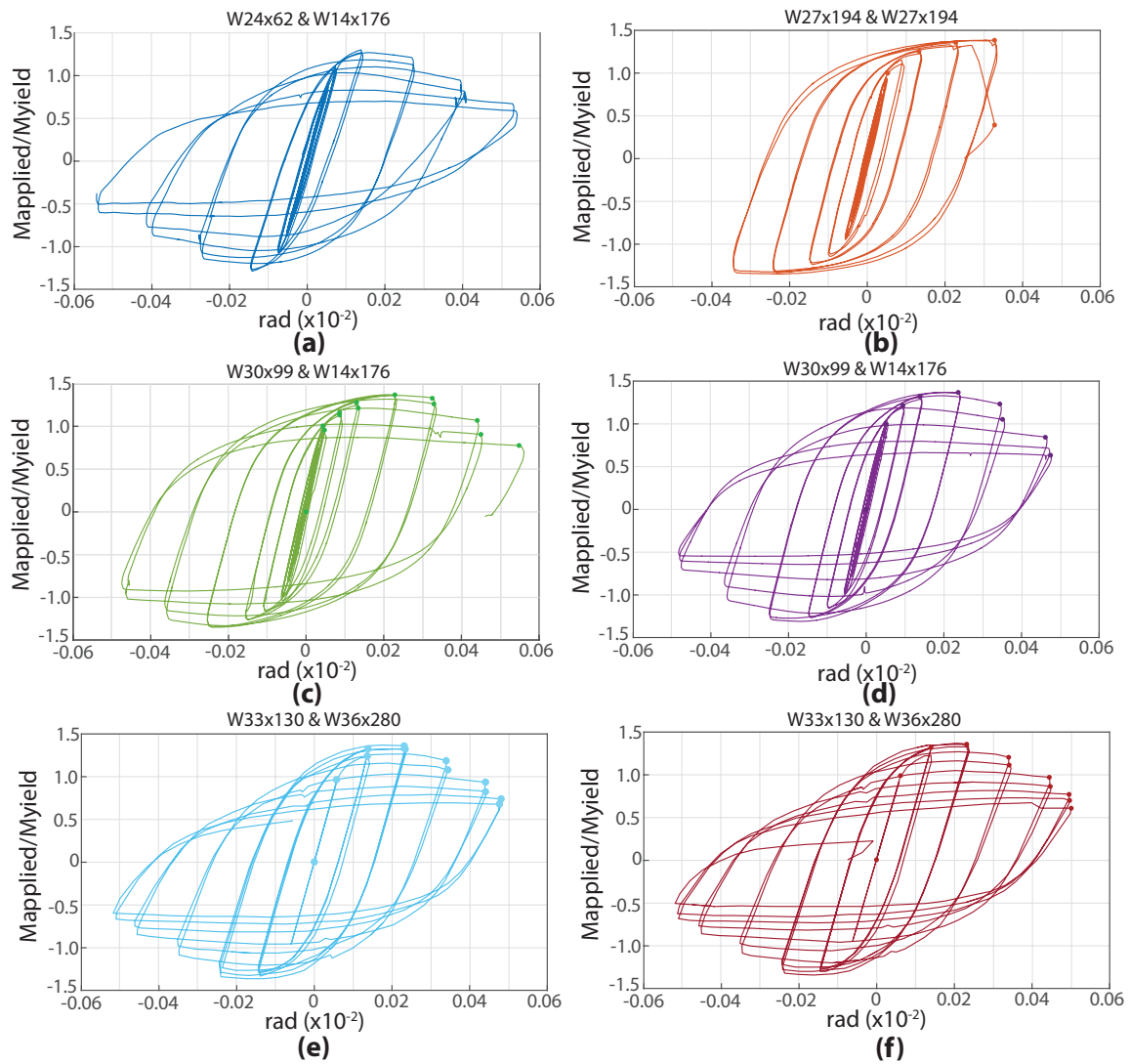


Figure A.11: Moment-Rotation relationships for component tests of beam sections used in archetype frames (Chi and Uang (2002), Engelhardt and Sabol (1994), Moore and Engelhardt (2000), Popov and al (1997))

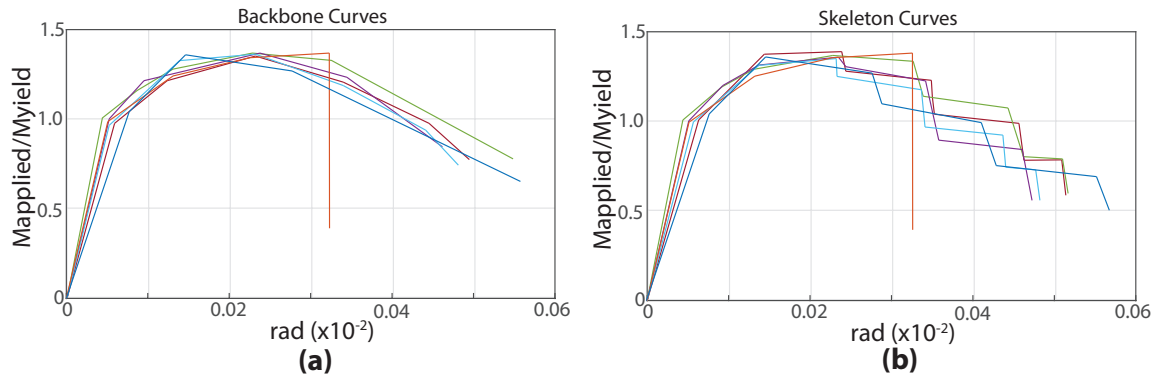


Figure A.12: (a) Backbone curves for component tests of beam sections used in archetype frames

A.1.3 Additional Modeling Procedure for Pre-Qualified Connections

The calibration of all of the IMK parameters was conducted using the component test with section sizes most closely matched to those of the archetype structure. This selection is summarized in Table A.2.

Table A.2: Selection of component test for connection model calibration

Modeled connection	Component test	Location in archetype frames
W33x141 & W14x398	W33x130 & W36x280	1st floor, three-story frame
W21x62 & W14x398	W21x62 & W14x176	2nd floor, three-story frame
W21x62 & W14x159	W21x62 & W14x176	3rd floor, three-story frame
W30x99 & W30x173	W30x99 & W14x176	1st and 2nd floor, six-story frame
W27x94 & W27x146	W27x194 & W27x194	3rd and 4th floor, six-story frame
W24x76 & W24x104	W24x62 & W14x176	5th and 6th floor, six-story frame
W24x162 & W24x162	W24x62 & W14x176	1st and 2nd floor, 12-story frame
W24x146 & W24x131	W24x62 & W14x176	3rd and 4th floor, 12-story frame

Continued on the next page

Continued from previous page

Modeled connection	Component test	Location in archetype frames
W24x131 & W24x103	W24x62 & W14x176	5th and 6th floor, 12-story frame
W24x94 & W24x84	W24x62 & W14x176	7th and 8th floor, 12-story frame
W24x84 & W24x76	W24x62 & W14x176	9th and 10th floor, 12-story frame
W24x76 & W24x76	W24x62 & W14x176	11th and 12th floor, 12-story frame

After the chosen component test result was selected, a multivariable optimization process was developed in Matlab (MATLAB 2015) to determine the optimal values of all 26 IMK parameters of the analytical model. Functions defining the influence of each model parameter on the accuracy of three hysteretic properties were defined using bounding sensitivity analyses. These three properties consisted of the total quantity of energy dissipated (E_{tot}), the quantity of energy dissipated per-cycle (E_{cycle}) and the accuracy of the skeleton curve to the skeleton curve of the component test ($Dev_{skeleton}$). Each of these properties is obtained as a function of each model parameter and are not always linear as they can also vary as a function of the value of other IMK parameters. The three hysteretic properties mentioned were used as objective functions during the calibration process, with a weighted summation ranking the functions into an overall objective to be minimized. This function is shown in equation A.1.7, where X_1 , X_2 and X_3 are weighting multipliers whose values were chosen as 1, 2, and 3 to prioritize the accuracy of the skeleton curve first, followed by the energy dissipated per cycle, and finally, the total energy dissipated. The starting IMK values used in this optimization were those obtained using the regression equation values outlined in ATC-72 (ATC 2010) as well as recommended IMK default values provided by Lingos and Al-Shawwa (2013). The system was then minimized using partial

differential equations of the correlating functions to limit the number of sets of possible IMK values to all minima in the system. Once the results of all sets of possible IMK values leading to minima were analyzed, the global optimal set was selected as the IMK parameters for each beam section size being considered.

$$\begin{aligned}
 \min(F) = & (X_1)|E_{totmodel}(P_1, P_2, \dots, P_{26}) - E_{tottest}| \\
 & + (X_2) \sum |E_{cyclemodel}(P_1, P_2, \dots, P_{26}) - E_{cycletest}| \\
 & + (X_3)Dev_{skeleton}(P_1, P_2, \dots, P_{26}) \quad (\text{A.1.7})
 \end{aligned}$$

The moment-rotation relationship of the final analytical IMK model and the component test results for the W24x61 are shown in Figure A.13 (a), while Figure A.13 (b) shows the backbone curves of the IMK model, component test and the curve obtained from the ATC-72 regression equations. Finally, Figure A.13 (c) shows the skeleton curves of the component tests as well as the skeleton curve of the analytical IMK model. While this model provides a more accurate approximation of the inelastic deterioration of the beam hinge when compared to the values obtained solely from the regression equations, the slight differences in beam and column sizes between the component tests and the corresponding different beam-column connections in the archetype frames combined with the possible variations in behaviour observed in Figure A.11 indicate that the IMK model parameters calibrated for the W24x62 component test will also provide the model with an acceptable level of accuracy for the other W24 beam sizes in the archetype frames. Without perfectly sized and detailed component tests, any further calibration to attempt to adjust the IMK parameters for variations such as

different column sections, beam weight or doubler and continuity plate thickness, seen as important during the observations of the W36 component tests shown in Figure A.10, would likely result in modifications to the IMK parameters which would have a negligible effect on the behaviour of the overall frame as well as further increase the illusion of accuracy.

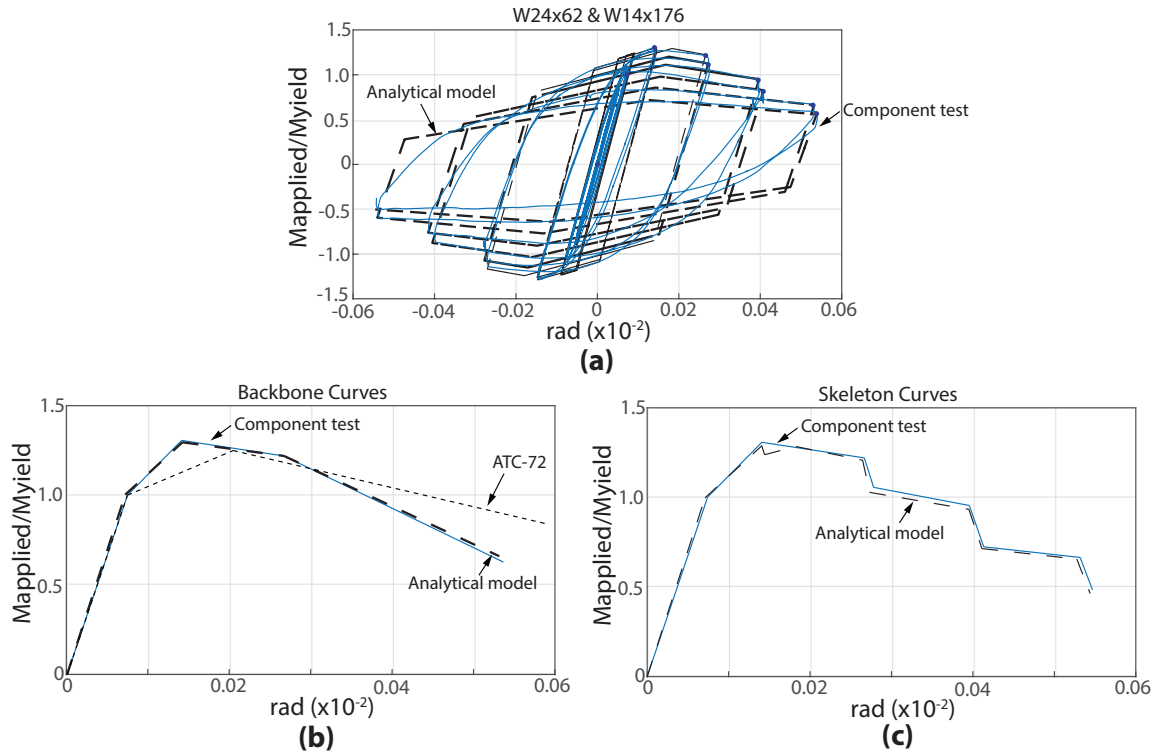


Figure A.13: (a) Comparison of moment-rotation relationship of W24 component test and analytical model, (b) backbone curves of W24 component tests of beam sections used in archetype frames, of ATC-72 regression values and of final IMK model, (c) skeleton curves of component tests of beam sections used in archetype frames and of final IMK model

This calibration process was repeated for the other beam sizes using the component tests whose beam sizes were nearest those of the beams in the frames. The W33, W30 and W24 beams all have component tests with beams having the

same depth and thus can be calibrated with a similar level of accuracy, while modifying some parameters such as yield moment and elastic stiffness for beams with the same depth classification but different section weights. However, the W21x62 beam size in the three story archetype frame was calibrated using the W24 component test as this was the closest available component test found in the literature at the time of calibration. Figure A.14 (a) shows the final analytical IMK model and component test for the W30 beams, while Figure A.15 (a) shows the same information for the W33 beams. Figure A.14 (b) and Figure A.15 (b) show the backbone curves for the component test, analytical model, and ATC-72 regression for the W30 and W33, respectively. Figure A.14 (c) and Figure A.15 (c) show the skeleton curves for the component test, and the analytical model for the W30 and W33, respectively. Table A.3 summarizes the 5 IMK parameter values obtained from the ATC-72 regression equations and their corresponding modified values obtained from the multivariable optimization process for each of the three beam size models. Table A.3 also includes all of the other remaining values for the IMK models and, since the behaviour of the connections are assumed to be symmetrical, the values in Table A.3 are for both the positive and negative directions when applicable.

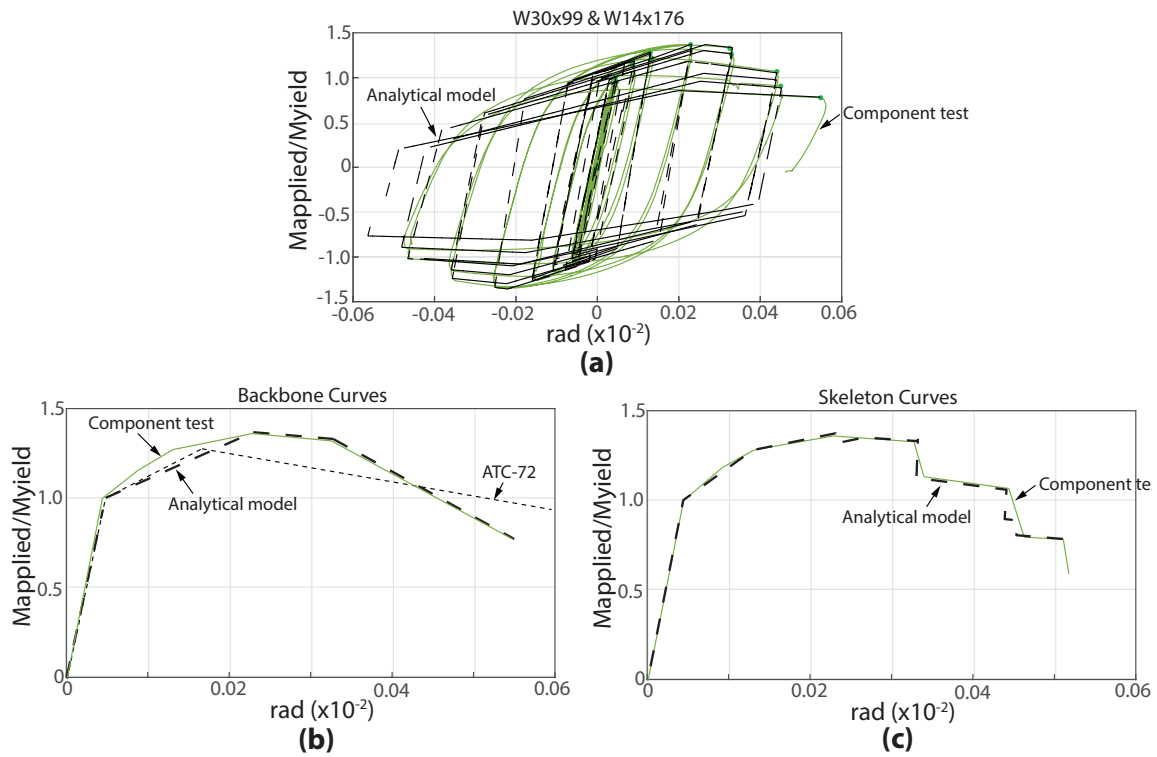


Figure A.14: (a) Comparison of moment-rotation relationship of W24 component test and analytical model, (b) backbone curves of W24 component tests of beam sections used in archetype frames, of ATC-72 regression values and of final IMK model, (c) skeleton curves of component tests of beam sections used in archetype frames and of final IMK model

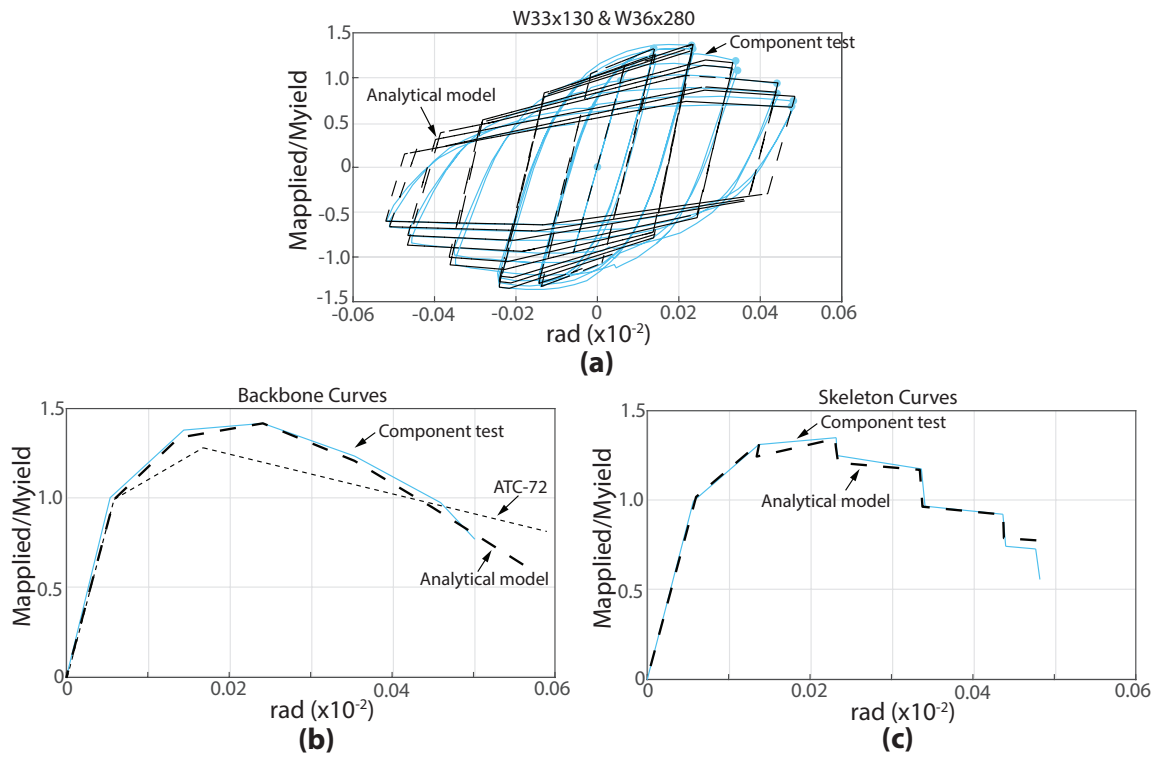


Figure A.15: (a) Comparison of moment-rotation relationship of W24 component test and analytical model, (b) backbone curves of W24 component tests of beam sections used in archetype frames, of ATC-72 regression values and of final IMK model, (c) skeleton curves of component tests of beam sections used in archetype frames and of final IMK model

Table A.3: Comparison of IMK values

IMK PARAMETERS (CRITICAL PARAMETERS)	W24		W30		W33	
	ATC-72	Optimized	ATC-72	Optimized	ATC-72	Optimized
Strain Hardening Ratio (M_c/M_y) (+ and -)	1.1	1.06	1.1	1.06	1.1	1.06
Pre-Capping Rotation (θ_p) (+ and -)	0.020	0.020	0.017	0.020	0.016	0.020
Post-Capping Rotation (θ_{pc}) (+ and -)	0.16	0.20	0.13	0.18	0.15	0.16
Ultimate Rotation (θ_u) (+ and -)	0.10	0.05	0.10	0.05	0.10	0.05

Continued on the next page

Continued from previous page

IMK PARAMETERS (CRITICAL PARAMETERS)	W24		W30		W33	
	ATC-72	Optimized	ATC-72	Optimized	ATC-72	Optimized
Cumulative Rotation (Δ) (+ and -)	0.80	0.50	0.70	0.46	0.80	0.43
Cyclic deterioration parameter for strength deterioration	N/A	0.97	N/A	0.92	N/A	0.96
Cyclic deterioration parameter for post-capping strength deterioration	N/A	0.98	N/A	0.94	N/A	0.97
Cyclic deterioration parameter for acceleration reloading stiffness deterioration	N/A	0	N/A	0	N/A	0
Cyclic deterioration parameter for unloading stiffness deterioration	N/A	0.93	N/A	0.99	N/A	0.96
Rate of strength deterioration	N/A	0.94	N/A	0.92	N/A	0.97
Rate of post-capping strength deterioration	N/A	0.88	N/A	0.94	N/A	0.84
Rate of accelerated reloading deterioration	N/A	0.71	N/A	0.86	N/A	0.78
Rate of unloading stiffness deterioration	N/A	1.0	N/A	0.98	N/A	1.0
Residual strength ratio(+ and -)	N/A	0.3	N/A	0.42	N/A	0.38
Elastic stiffness amplification factor	N/A	10	N/A	10	N/A	10

A.1.4 Stiffness Adjustements for Connections in a Global Model

Following the component calibration of the various connection models and to account for the addition of the concentrated hinges at the ends of the beam-column elements, the stiffness of each original beam-column element (K_{mem}) was increased to a new value (K_{bc}) by a function of a multiplier n , as shown in Equation A.1.8.

Furthermore, the concentrated spring stiffness (K_s) was increased by a function of the same multiplier n , as shown in Equation A.1.10 (Gupta and Krawinkler 1999).

$$K_{mem} = \left[\frac{6EI_e}{L} \right] \quad (\text{A.1.8})$$

$$K_{bc} = \left[\frac{1+n}{n} \right] K_{mem} \quad (\text{A.1.9})$$

$$K_s = (n+1)K_{mem} \quad (\text{A.1.10})$$

Gupta and Krawinkler (1999) recommended using an n value of 10 for beam-column elements with a single non-linear spring placed in series at each end. This value was verified using a parametric study on the analytical component system used to calibrate the beam models, shown in Figure A.2 (b). Beam-column component systems using increasing n values were compared to the component model system without a non-linear spring using the stiffness obtained from a pushover analysis, and verified by comparing the fundamental period obtained using a constant mass applied to the top of the panel zone. This comparison is shown in Figure A.16, where the target with no non-linear spring (dashed black line) represents the true elastic performance of the system, and the solid black line is for the component system with a non-linear spring but no stiffness adjustment. With the introduction of the non-linear spring, a yielding point is identified in the pushover curve corresponding to the yield moment of the beam spring. Increasing values of n adjust both the stiffness and period of the system towards the target values. As recommended by Gupta and Krawinkler (1999), an n value of 10 is the smallest usable value which replicates the elastic behaviour of the system. However, the introduction of extra

non-linear springs in series (used for connection models introduced in section A-2.1) may require larger values of n .

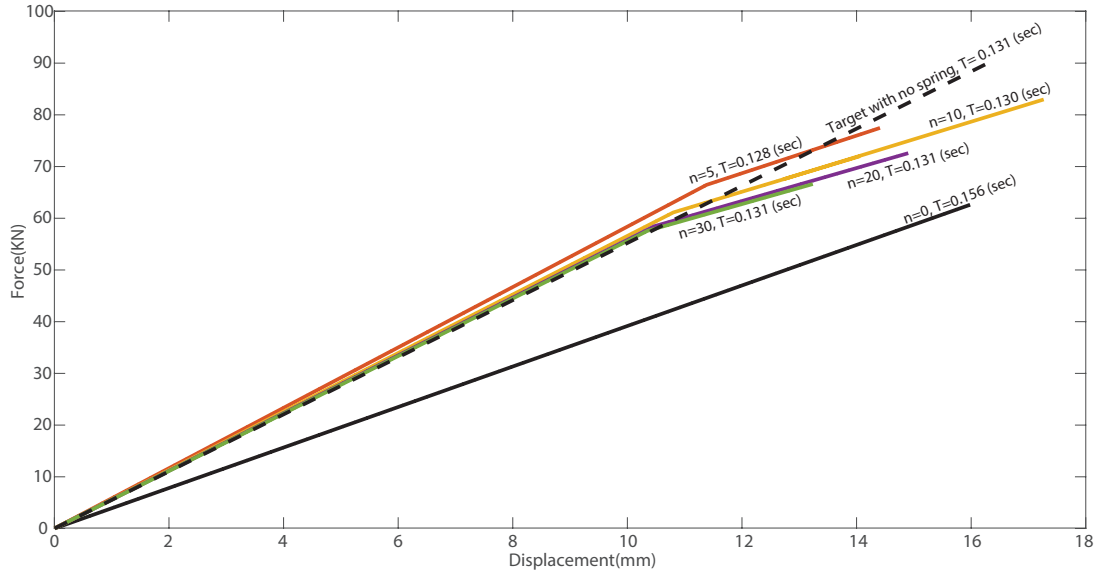


Figure A.16: Impact of n -factor on pushover behaviour and dynamic period of component test model

The adjustment in stiffness was accounted for when determining an equivalent Rayleigh damping value when applied to the global frame, typically in the first and second elastic modes to mirror common modeling practices. The Rayleigh damping is applied using a combination of mass proportional and constant stiffness proportional based on initial conditions. However, to avoid unrealistic and spurious damping forces, the stiffness proportional damping were determined using a proposed approach by Zareian and Medina (2010), in which zero stiffness proportional damping is assigned to the beam-column zero-length springs and the stiffness proportional damping constant (β) applied to the other elastic elements is increased as a function of the same n multiplier previously introduced as shown in

Equation A.2.6:

$$\beta' = \left[\frac{1+n}{n} \right] \beta \quad (\text{A.1.11})$$

No stiffness proportional damping is assigned to the Krawinkler spring box model elements.

A.2 Development of Models for Low-Damage Connections

A.2.1 Review of SHJ Connection Testing

Other research efforts have focused on the development of high performing MRF connections which use friction energy dissipating devices rather than plastic yielding as an energy dissipation method (Khoo et al. 2012). An isometric view of the SHJ connection and its hinging mechanism are shown in Figure A.17. These connections use bolted plates placed at the extremes of the beam flanges to transfer moments to the column and use a sliding friction surface placed at the bottom of the beam to provide energy dissipation, referred to as the asymmetrical friction connection (AFC). The main advantage of such a connection is to provide energy dissipation with very little permanent damage to the beam section, as it does not enter the plastic rotation range, therefore avoiding cyclic deterioration. Control of the strength parameters can be configured independently of the stiffness by specifying the number of shear bolts used to assemble the connection (Khoo et al., 2012).

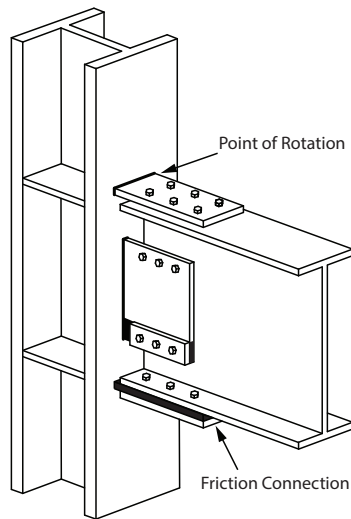


Figure A.17: Isometric view of a SHJ connection

The idealized hysteretic behaviour of the SHJ connection is shown in Figure A.18 (a), and demonstrates a loading moment-rotation relationship with four distinct portions (Khoo et al., 2012). Portion A of the moment-rotation relationship corresponds to the elastic stiffness, as both surfaces remain static, portion B corresponds to the sliding of the first friction surface, portion C corresponds to the transition stiffness as both friction surfaces begin to slip, and portion D corresponds to the moment where slippage of all surfaces has been achieved. Any modeling process used to represent the SHJ connection must therefore capture this trilinear and pinched hysteretic behaviour, particularly as these can be modified by the designers using different sliding surfaces and clamping forces. However, the hysteretic results of a component test of the SHJ connection, conducted in a similar manner as those of prequalified connections presented in section A-1.1, is shown in Figure A.18 (b). The distinct trilinear and pinching behaviour shown in Figure A.18 (a) is not very apparent in cycles less than 0.003 rad, which demonstrates a distinctly bilinear behaviour, but becomes more

pronounced as the cycle amplitudes become larger. This initial bilinear behaviour explained in Clifton (2005) and Khoo et al. (2013), where the SHJ connection component tests resulted in an effective hysteretic behaviour shown in Figure A.18 (c) which has an initial flexural strength capacity larger than the theoretical values obtained from the AFC. This is caused by the contributions of secondary elements, such as prying of flange plates, which lead to the more distinctive initial bilinear behaviour, as highlighted in Figure A.18 (d). More information on this effect is available in MacRae et al. (2010). Figure A.18 (b) demonstrates that the model should also be able to capture this transition from bilinear to trilinear behaviour. Furthermore, the connection demonstrates some stiffness degradation at the large amplitudes which has been attributed by Khoo et al (2012) to a decrease in the clamping force of the bolts due to their plasticity at higher rotations. This stiffness degradation is to be included in the analytical model. A summary of the key features is listed:

- Dominant bilinear moment-rotation behaviour at small cycles (less than 0.003 rad).
- Dominant trilinear and pinched moment-rotation behaviour with larger cycle.
- Dominant stiffness throughout, linked to cycle amplitude and quantity.

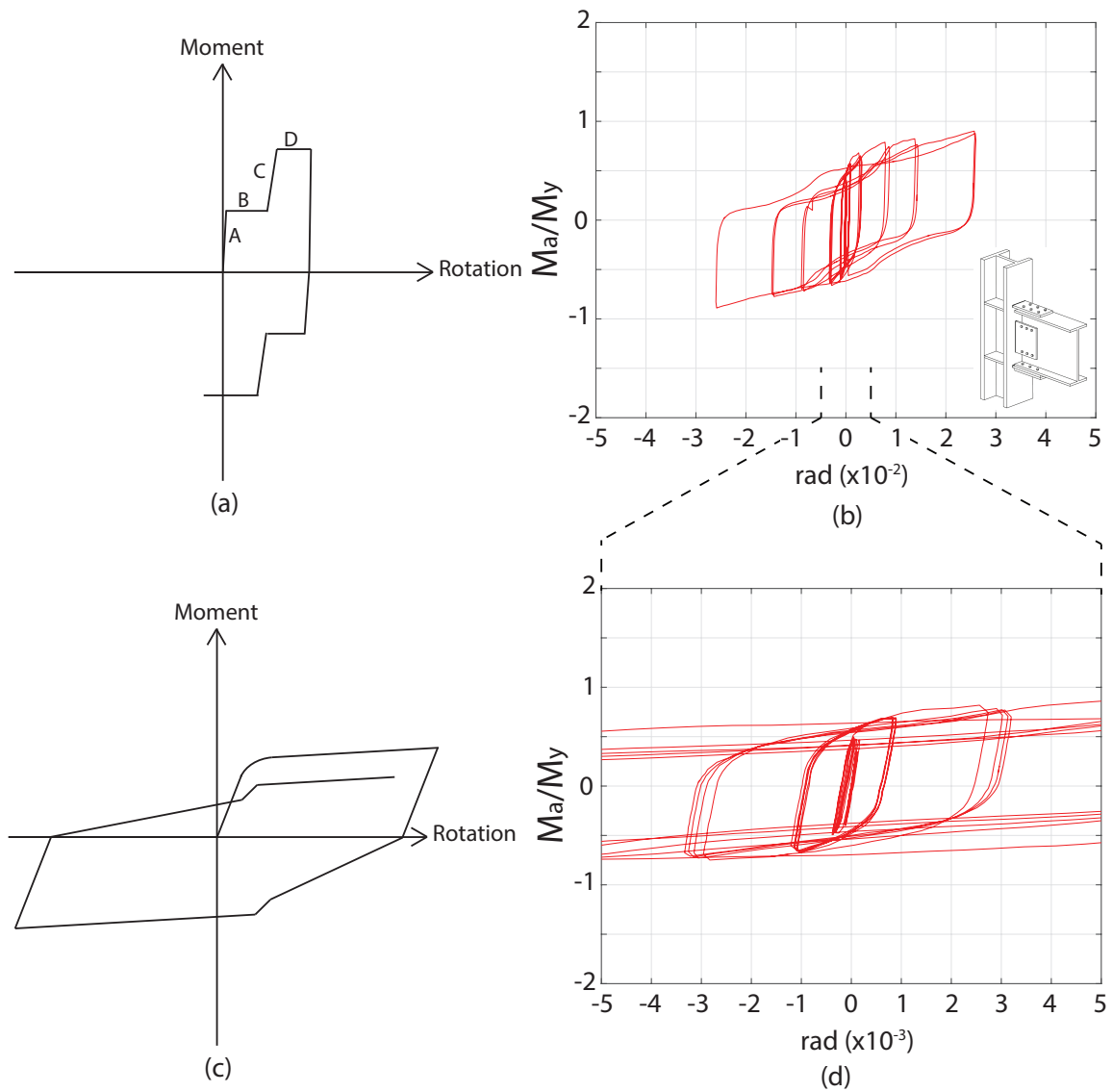


Figure A.18: (a) Idealized AFC only Moment-Rotation behaviour of SHJ connection (after Khoo et al. 2012), (b) Experimental component results for SHJ connection, (c) Effective Moment-Rotation behaviour of SHJ connection (after Khoo et al. 2012), , and (d) Bilinear-dominated moment-rotation behaviour at low rotations

A.2.2 Creation and Calibration of SHJ Model

Each aspect of the hysteretic behaviour of the SHJ connection that was described above is captured using pre-existing materials combined in parallel within the chosen software, OpenSees (McKenna et al. 2000). As discussed in Section A-2.1, the analytical model developed for the SHJ connection captures the initial bilinear behaviour during the initial cycles and the trilinear pinching behaviour at large cycles with two different material models, as shown in Figure A.19 (a), as well as the general stiffness degradation with a third material. Since the design of the SHJ connection allows for the independent selection of the stiffness and activation moments of the connection, these parameters must be specified independently within the analytical model. The Hysteretic material is used to define the trilinear backbone curve behaviour of the AFC by defining stress-strain points, where each point is defined independently. To capture the initial bilinear behaviour of the connection at small cycles, the SHJ model uses the Steel02 material, based on the Giuffré-Menegotto-Pinto model (Menegotto and Pinto 1973). These two materials are combined in parallel with equal weights, and the contribution of the Steel02 model is reduced as the cycle number and amplitude increase by reversing the isotropic hardening mechanism already implemented in this material. Traditionally, a positive value for this parameter activates this hardening mechanism, which is used to increase the strength of the Steel02 material as the cycle number and amplitude increase. However, by using a negative value, the contribution of the Steel02 material decreases as the number and amplitude of cycles increase, leading to the bilinear behaviour being replaced by the trilinear behaviour of the Hysteretic material. This represents the plasticity of the steel bolts and reduction in clamping force mentioned previously. The final parallel material is then wrapped using a

Fatigue material which provides continued stiffness degradation using a cyclic rain flow counting method, increasing the degradation as the number and size of cycle increases. The amount of this degradation can be modified through the Fatigue material parameters. A summary of the values used in the SHJ connection model is shown in Table A.4 and described below.

Figure A.19 (b) shows the idealized combination of each hysteretic material and identifies the key moment and stiffness parameters to replicate the component test from Figure A.18 (b). The activation moment, (M_{AB}), is the design moment of the AFC and is the first stress value of the Hysteretic material, as shown in Equation A.2.1. The Hysteretic material also requires a strain at each stress point, defined in Equation A.2.2. The initial stiffness of the spring is defined using K_s from Equation A.1.10. Khoo et al. (2013) empirically determined that the dependable moment, M_d , is approximately 1.5 times the design moment M_{AB} , and the second stiffness (K_2) is 10% ($\alpha_1=0.1$) of the initial stiffness, shown in Equation A.2.3. The dependable moment is represented by the second stress and strain point of the hysteretic model, defined by Equations A.2.4 and A.2.5. Finally, the stiffness of the third linear segment is determined by finding a further reduction from the initial stiffness, in this case set to an empirical value of 2% of the initial stiffness ($\alpha_2=0.02$) shown in Equation A.2.6, and this stiffness, along with the yield moment of the beam (M_y), is used to determine the third stress-strain point in the Hysteretic model (M_y and ϵ_3), defined in Equations A.2.7 and A.2.8. Pinching values are defined in the Hysteretic model as 0.5 for the deformation and 0.35 for the force during reloading. These factors are based on ratios of the reloading stiffness observed in successive cycles in the component test, although some trial and error was necessary to determine values for these parameters. No damage values were used in the Hysteretic model. All deviations from the trilinear backbone curve defined by the Hysteretic model and

shown in Figure A.19 (b) are a result of either the Steel02 model or the Fatigue model, explained in the next paragraph. A comparison of the behaviour of the component test results obtained from the analytical model and the experimental test are shown in Figure A.19 (d).

$$\sigma_1 = M_{AB} \tag{A.2.1}$$

$$\epsilon_1 = \frac{\sigma_1}{K_s} \tag{A.2.2}$$

$$K_2 = \alpha_1 K_s \tag{A.2.3}$$

$$\sigma_2 = M_d \tag{A.2.4}$$

$$\epsilon_2 = \epsilon_1 + \frac{M_d - M_{AB}}{K_2} \tag{A.2.5}$$

$$K_3 = \alpha_2 K_s \tag{A.2.6}$$

$$\sigma_3 = M_y \tag{A.2.7}$$

$$\epsilon_3 = \epsilon_2 + \frac{M_y - M_d}{K_3} \tag{A.2.8}$$

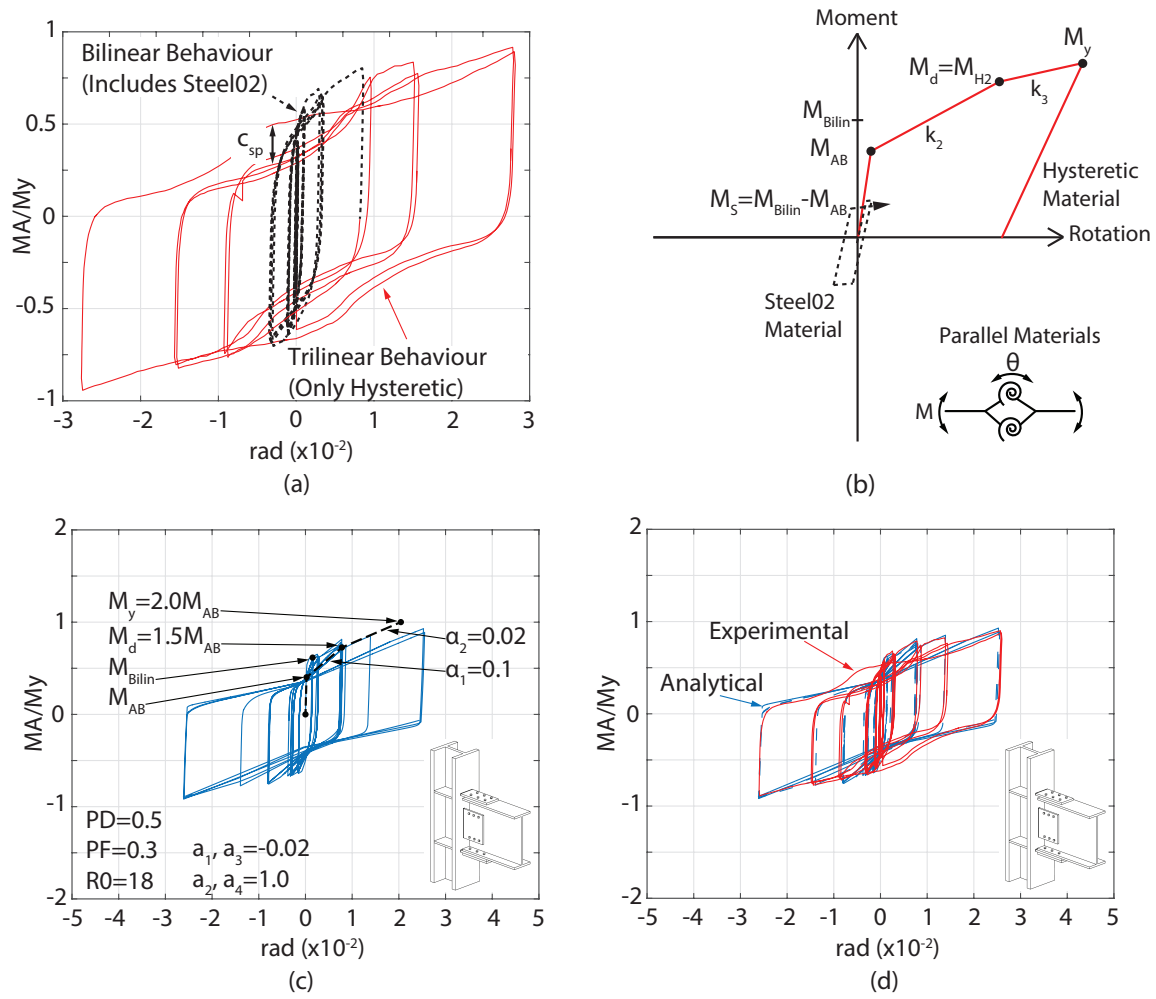


Figure A.19: (a) Division of moment-rotation behaviour, (b) Idealized moment-rotation behaviour of Steel02 and Hysteretic materials, (c) Key SHJ connection model parameters, and (d) Analytical and experimental SHJ component tests

As mentioned, the SHJ component test revealed an overstrength bilinear behaviour observed at small cycles. Therefore, the first onset of inelastic behaviour occurs when both the design moment of the AFC and the strength over moment caused by the initial bilinear behaviour are exceeded (M_{Bilin}). This over strength

has been empirically determined in Clifton (2005) as 1.45 times larger than the design moment ($c_{sp}=1.45$), and this is shown in Equation A.2.9. This initial increased component of the total moment is modeled by the Steel02 material used in parallel with the Hysteretic material and the yield moment of the Steel02 material (M_S) is the difference between the combined initial moment and the design moment, as shown in Equation A.2.10. The initial stiffness of the Steel02 material was identical to that of the Hysteretic material, increasing the initial spring stiffness. In this connection case, the post-yield stiffness of the Steel02 material was selected as 0.02. The transition from elastic to plastic parameters, R_0 , is 30 and the recommended default cR_1 and cR_2 values are used. Both a positive and negative isotropic hardening value of -0.02 was used to reduce the bilinear effect of the Steel02 model as the connection bolts undergo plastic deformations and reduce their clamping force. The final parallel model was wrapped using a fatigue model, as noted above. The default values provided energy dissipation that was within 3% of the amount obtained for the component test results, and thus no modifications to the fatigue parameters were made.

$$M_{Bilin} = c_{sp}M_{AB} \tag{A.2.9}$$

$$M_S = M_{Bilin} - M_{AB} \tag{A.2.10}$$

Table A.4: Parameters for SHJ model

Parameter	SHJ	Material Property
Size of Test Beam/Test Column	W360x45/W310x158 (W14x30/W12x106)	
Analytical Model Used	SHJ	

Continued on the next page

Continued from previous page

Parameter	SHJ	Material Property
Activation Moment (M_{AB})	$0.4 M_y$	First Hysteretic Material Force
Dependable Moment (M_d)	$1.5 M_{AB}$	Second Hysteretic Material Force
First Post-Activation Stiffness (α_1)	0.1	From First Hysteretic Strain
Second Post-Activation Stiffness (α_2)	0.02	From Second Hysteretic Strain
Pinching Displacement (P_D)	0.5	Hysteretic Parameter
Pinching Force (P_F)	0.35	Hysteretic Parameter
Empirical Strength Increase Constant (c_{sp})	1.45	
Initial Bilinear Moment Increase (M_s)	$(c_{sp} - 1)M_{AB}$	Steel02 Moment
Bilinear Post Activation Stiffness (α_B)	0.02	Steel02 Parameter
Curvature Transition (R_0)	30	Steel02 Parameter
cR_1	0.925	Steel02 Parameter
cR_2	0.15	Steel02 Parameter
Isotropic Hardening Stiffness (a_1, a_3)	-0.02	Steel02 Parameter
Isotropic Hardening Activation (a_2, a_4)	1.0	Steel02 Parameter
Single Cycle Failure Strain	0.191	Fatigue Parameter
Coffin-Manson Log-Log Curve Slope	-0.458	Fatigue Parameter
Global Strain min/max	+/- 1e16	Fatigue Parameter

This connection design and corresponding model parameters was used for all of the SHJ connections in each of the archetype structures, as each of the parameters is defined relative to the initial condition of the beam (initial stiffness and yield moment).

A.2.3 Review of SCSHJ Connection Testing

A recent addition to the SHJ connection uses a series of ring springs (Filiatrault et al., 2000) at the bottom flange to allow the connection to become a self centering

SHJ connection (SCSHJ) (Ramhormozian et al. 2014). These springs are placed at the bottom flange of the beam, farthest from the point of rotation, and fixed to the column, providing a restoring force to the component assembly. An isometric view of the SCSHJ connection is shown in Figure A.20.

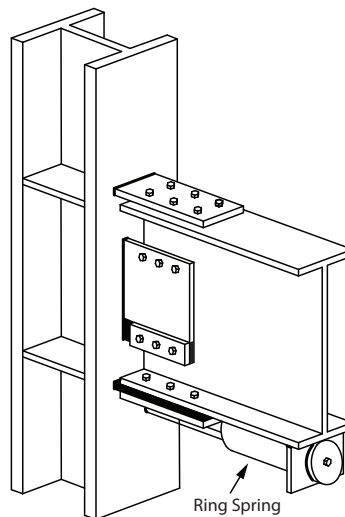


Figure A.20: Isometric view of a SCSHJ connection

The behaviour of the SCSHJ connection deviates from the behaviour of the SHJ connection due to the addition of the ring spring, which adds a self-centering capability to the connection, and eliminates the degradation in connection stiffness since the spring provides additional reliable stiffness to the connection and reduces the quantity of bolts required (Khoo et al., 2012). The idealized behaviour of the ring spring is shown in Figure A.21 (a), demonstrating that the spring has a linear stiffness (portion A) until the activation load is achieved, where a post-activation stiffness is provided (portion B), leading to a flag shaped hysteresis as the spring unloads back to its original position (portion C). None of these stiffnesses are susceptible to degradation during repeated cycles. The proportion of self centering

behaviour can be modified both by the internal design of the ring spring mechanism and by the ratio of the spring strength to the activation load of the friction surface assembly. This adds additional parameters which should be captured by the analytical model. The results of a component test of the SCSHJ connection are shown in Figure A.21 (b). At large displacements past the idealized behavior shown in Figure A.21 (a), the ring spring begins to reach its maximum deformation and provides a third stiffness, as shown in Figure A.21 (b), leading to a quadrilinear behaviour. A summary of the key features of the analytical model includes:

- Overall quadrilinear moment-rotation behaviour.
- Self-centering capability, determined independently from the other properties.
- A post lock-up stiffness.
- No degradation in stiffness.

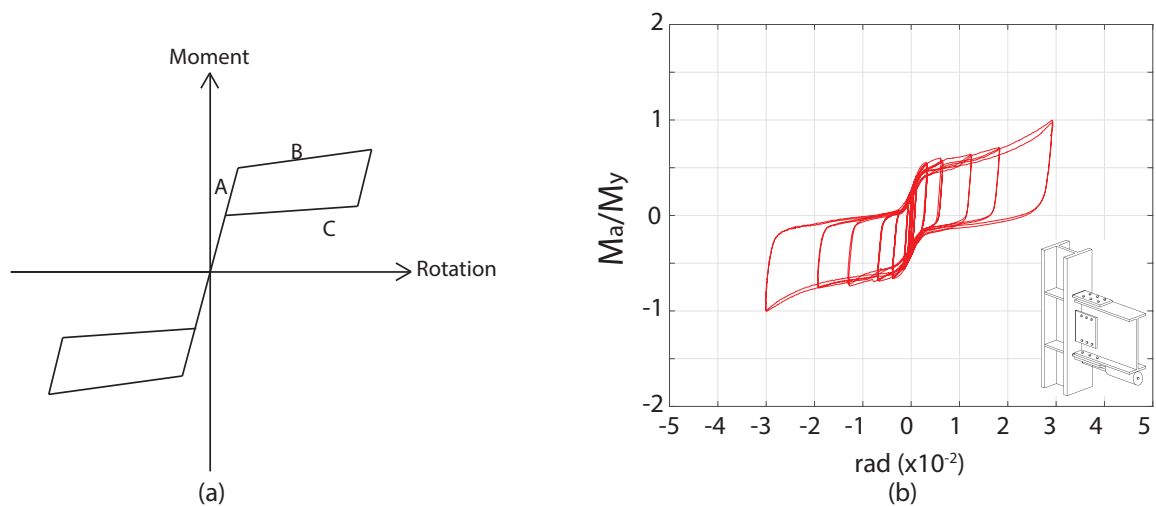


Figure A.21: (a) Idealized moment-rotation contribution of self-centering ring spring, and (b) Experimental component results for SCSHJ connection

A.2.4 Creation and Calibration of SCSHJ Model

As presented in Section A-2.3, the key aspects of the SCSHJ connection consist of 1) the quadrilinear behaviour of the sliding backbone curve, 2) the self centering mechanism and its stiffness, 3) the lock-up increase in stiffness at large rotations, and 4) the lack of any deterioration. The analytical model was constructed using a similar method as was used for the SHJ connection, by assembling several existing materials already made available in the OpenSees software in parallel. The connection model uses both the SelfCentering and Steel02 models as the baseline materials, with the addition of two Elastic-Perfectly-Plastic-Gap materials to provide the fourth stiffness required. The idealized moment-rotation behaviour of the Steel02 and SelfCentering materials is shown in Figure A.22 (a). Using Steel02 as the baseline material for the SCSHJ connection, its stiffness was assigned as 95% of the initial stiffness of the connection, as shown in Equation A.2.11 (K_s from Equation A.1.10), while its yield moment was set to match the first dependable moment of the connection (M_d) less the moment contribution from the SelfCentering material at the yield strain (see Equation A.2.12), and the post yield stiffness (α_2) set to 0.4% of the initial stiffness, described in equation A.2.13. The curvature parameter (R_0) was set to 16, and default values were used for the other two curvature parameters ($cR_1=0.925$ and $cR_2=0.15$). Finally, no isotropic hardening was included in this version of the material. The SelfCentering material was added and adjusted to modify the overall behaviour of the model. As shown in Figure A.22 (b) and described in equation A.2.14, the stiffness assigned to the SelfCentering material was 5% of the initial connection stiffness ($\lambda_{SC}=0.05$), while the yield moment assigned to the SelfCentering material was defined based on the stiffness of the two springs to achieve the desired activation moment, shown in

Equation A.2.15. The post yield stiffness was also 0.4% of the initial stiffness, as shown in Equation A.2.16. These series of different initial and post yield activation stiffnesses in the Steel02 and SelfCentering materials determine the behaviour of the first three stages of the backbone curve. The self centering quantity (β_{SC}) of the SelfCentering material was a negligible value (0.0001) since the Steel02 material provided the energy dissipation. Finally, an ElasticPPGap material was added in both the positive and negative directions, activating at the rotation of a second dependable moment (M_{d2}), a value of 0.02 rad in this case. The stiffness of this material was calibrated to provide the second-dependable stiffness equal to 1% of the initial stiffness when combined with the stiffness of the Steel02 and SelfCentering material. These ElasticPPGap materials represent the “lock-up” of the sliding surfaces, a rotation which can be adjusted in the connection design. The final comparison of the analytical model to the experimental results is shown in Figure A.22 (c) and all values used to model this particular component test are summarized in Table A.5.

$$K_{Steel02} = (1 - \lambda_{SC})K_s = 0.95(K_s) \quad (A.2.11)$$

$$M_{Steel02} = M_d - M_{SC} - \alpha_{SC}K_{SC} \left(\frac{M_d - M_{AB}}{\alpha_{SC}K_{SC} + K_{Steel02}} \right) \quad (A.2.12)$$

$$\alpha_{Steel02} = \alpha_2 = 0.004 \quad (A.2.13)$$

$$K_{SC} = \lambda_{SC}K_s = 0.05(K_s) \quad (A.2.14)$$

$$M_{SC} = M_{AB} \left(1 + \frac{K_{Steel02}}{K_{SC}} \right)^{-1} \quad (A.2.15)$$

$$\alpha_{SC} = \alpha_2 = 0.004 \quad (A.2.16)$$

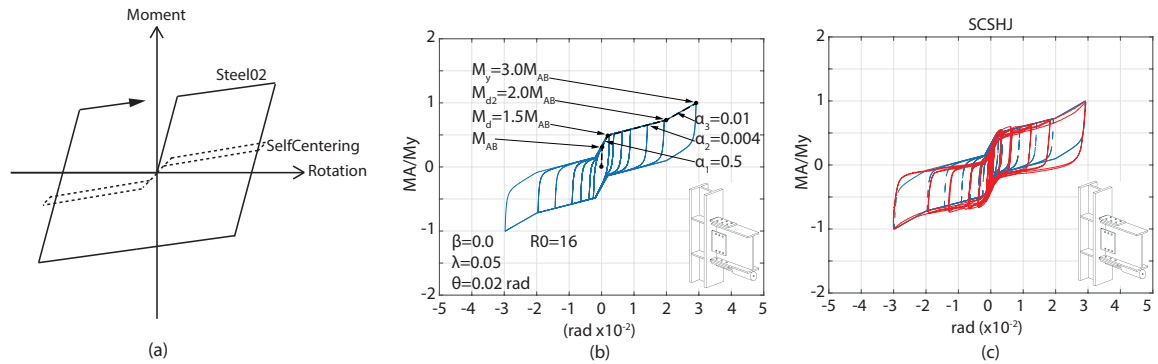


Figure A.22: (a) Idealized moment rotation behaviour of Steel02 and SelfCentering materials, (b) Key SCSHJ connection model parameters, and (c) Comparison of analytical and experimental SCSHJ component test

Table A.5: Parameters for SCSHJ model

Parameter	SCSHJ	Material Property
Size of Test Beam/Test Column	W360x57/W460x74 (W14x38/W18x50)	
Analytical Model Used	SCSHJ	
Activation Moment (M_{AB})	$0.3 \times M_y$	SelfCentering Moment
Dependable Moment (M_d)	$2.0 \times M_{AB}$	Steel02 Moment
Second Dependable Moment (M_{d2})	$3.0 \times M_{AB}$	ElasticPPGap Displacement
First Post-Activation Stiffness (α_1)	0.5	Initial Stiffness of SelfCentering and Steel02
Second Post-Activation Stiffness (α_2)	0.004	Post-Yield Stiffness of SelfCentering and Steel02
Third Post-Activation Stiffness (α_3)	0.01	Stiffness of ElasticPPGap

Continued on the next page

Continued from previous page

Parameter	SCSHJ	Material Property
Curvature Transition (R_0)	16	Steel02 Parameter
cR_1	0.925	Steel02 Parameter
cR_2	0.15	Steel02 Parameter
Self-Centering Ratio (λ_{SC})	0.05	SelfCentering Parameter
Forward-Reverse Activation Ratio (β_{SC})	0.0001	SelfCentering Parameter
Deformation at Final Stiffness (θ_{SC})	0.02	ElasticPPGap Parameter

A.2.5 Additional Modeling Considerations for SHJ and SCSHJ connection models

The bank of available component test results on which to base the SHJ and SCSHJ connection models is more limited when compared to the library of component tests of pre-qualified connections discussed in section A-1.1. Particularly, at the time of this model calibration, no component test capturing rotations past 0.03 rad was available. Since the SHJ and SCSHJ connections were designed not to undergo fracture at rotations less than 0.03 rad, no fracture mechanisms are known. The assumption used in the SHJ and SCSHJ connection model is that the final stiffness of the connections will remain constant past the 0.03 rad rotation. However, a second connection model, representing the steel beam section used, is placed in series with the SHJ or SCSHJ connection model. This second non-linear spring model has a hysteretic behaviour calibrated to the WFP connection, a prequalified connection presented in section A-1.1. Since this connection represents a beam-column connection with no change in beam stiffness (such as with the RBS or WSEP connection), it is used to represent

a typical steel beam, decoupled from the energy dissipation mechanisms provided by the friction surfaces and/or ring springs. This connection combination is shown in Figure A.23 for a typical beam-column connection in the analytical model. A larger value of n , presented in section A-1.4, is required for both the SHJ and SCSHJ connection models when these models include two more non-linear spring elements placed in series. In these studies, a value of n equal to 20 was used, following a similar sensitivity analysis presented in Figure A.16.

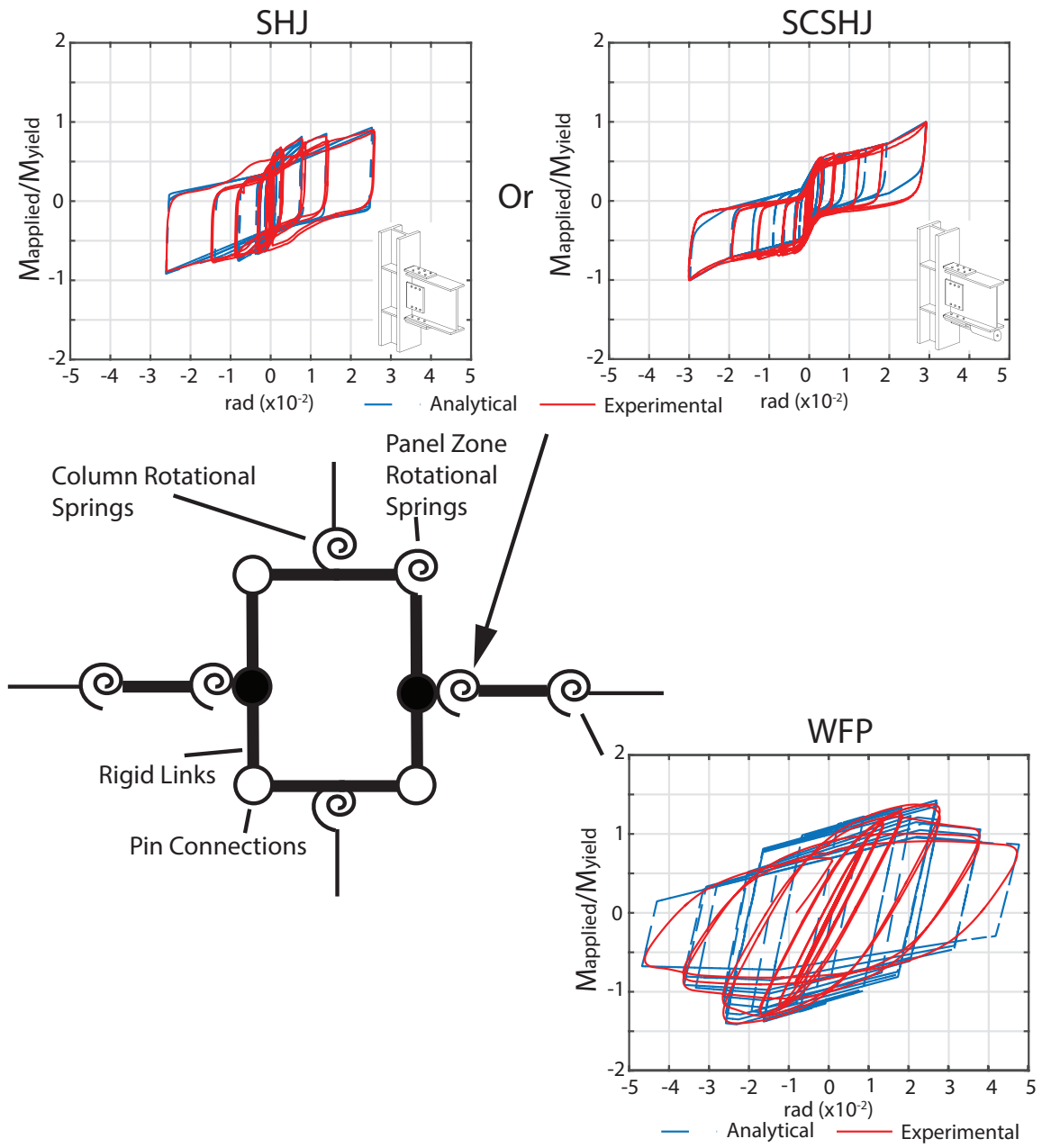


Figure A.23: Connection model for SHJ and SCSHJ connection

A.3 References

- AISC, (2016). “Prequalified Connections for Special and Intermediate Steel Moment Frames for Seismic Applications.” *American Institute of Steel Construction 358-16*, Chicago, IL, US.
- ASCE, (2016). “Minimum Design Loads and Associated Criteria for Buildings and Other Buildings.” *American Society of Civil Engineers 7-16*, Reston, VA, US.
- ATC-72, (2010). “ATC-72-1: Modeling and acceptance criteria for seismic design and analysis of tall buildings” *Applied Technology Council*
- Bruneau, M., Uang, C.-M. and Sabelli, R., (2011) “Ductile Design of Steel Structures.” Second Edition.
- Biddah, A., and Heidebrecht, A. C., (1999) “Evaluation of the seismic level of protection afforded to steel moment resisting frame structures designed for different design philosophies,” *Canadian Journal of Civil Engineering*, vol. 26, no. 1, pp. 35–54.
- Barsom, J. M. and Pellegrino, J. V., (2002) “Failure Analysis of Welded Steel Moment-Resisting Frame Connections,” *Journal of Materials in Civil Engineering*, vol. 14, no. 1, pp. 24–34,
- Charney, F., and Downs, W., (2004). “Modeling Procedures for Panel Zone Deformations in Moment Resisting Frames” *Connections in Steel Structures*, Amsterdam, NL.
- Chi, B. and Uang, C.-M., (2002). “Cyclic Response and Design Recommendations

- of Reduced Beam Section Moment Connections with Deep Columns” *Journal of Structural Engineering*, 128(4), 464–473.
- CISC, (2014). Moment Connections for Seismic Applications, Second Edition. 19-26.
- Clifton, G.C., (2005). “Semi-Rigid Joints For Moment-Resisting Steel Framed Seismic-Resisting Systems.” *Doctoral Dissertation, Department of Civil and Environmental Engineering*, University of Auckland, New Zealand.
- Engelhardt, M. D. and Sabol, T. A., (1994). “Testing of welded steel moment connections in response to the Northridge earthquake.” *AISC Northridge Steel Update*, (1).
- FEMA, (2000a) “State of the art report on connection performance,” *FEMA-355D*, 2000.
- FEMA, (2000b) “State of the Art Report on Past Performance of Steel Moment-Frame Buildings in Earthquakes,” *Fema-355*, 2000
- Filiatrault, A., Tremblay, R. and Kar, R., (2000) “Performance Evaluation of Friction Spring Seismic Damper,” *Journal of Structural Engineering*, 126(4), 491-499.
- Gilton, C. and Uang, C.-M., (2002). “Cyclic Response and Design Recommendations of Reduced Beam Section Moment Connections with Deep Columns” *Journal of Structural Engineering*, 128(4), 452–463.
- Gupta, A. and Krawinkler, H., (1999). “Seismic Demands for Performance Evaluation of Steel Moment Resisting Frame Structures.” *Stanford University Department of Civil and Environmental Engineering Report No. 132*, 1–379.

- Ibarra, L., and Krawinkler, H., (2005). “Global Collapse of Frame Structures under Seismic Excitations” *Pacific Earthquake Engineering Research Report No. 2005/06*, University of California, Berkeley, CA, US.
- Ibarra, L., Medina, R., and Krawinkler, H., (2005). “Hysteretic Models That Incorporate Strength and Stiffness Deterioration” *Earthquake Engineering and Structural Dynamics*, 34, 1489-1511.
- Khoo, H.-H., Clifton, C., Butterworth, J., MacRae, G., Gledhill, S., and Sidwell, G., (2012). “Development of the self-centering Sliding Hinge Joint with friction ring springs.” *Journal of Constructional Steel Research*, 78, 201–211.
- Khoo, H.-H., Clifton, C., Butterworth, J., MacRae, G., (2013). “Experimental study of full-scale self-centering sliding hinge joint connections with friction ring springs” *Journal of Earthquake Engineering*, 17, 972-977.
- Lignos, D. and Al-Shawwa, N., (2013). “Web-Based Interactive Tools for Performance-Based Earthquake Engineering”. <http://resslabtools.epfl.ch/steel/>, accessed in October 2015.
- MATLAB 2015b, The MathWorks, Natick, 2015
- MacRae, G. A., Clifton, G. C., Mackinven, H., Mago, N., Butterworth, J., and Pampanin, S., (2010). “The sliding hinge joint moment connection.” *Bulletin of the New Zealand Society for Earthquake Engineering*, 43(3), 202-212.
- McKenna, F., Fenves, G. L., and Scott, M., (2000). Open System for Earthquake Engineering Simulation. University of California Berkeley, CA

- Menegotto, M., and Pinto, P.E., (1973). “Method of analysis of cyclically loaded RC plane frames including changes in geometry and non-elastic behaviour of elements under normal force and bending.” *Preliminary Report IABSE*, vol 13.
- Moore, K. and Engelhardt, M., (2000). “Behaviour and design of radius cut reduced beam section connections” *SAC Joint Venture BD-00/17*, Sacramento, CA.
- Popov, E., Blondet, P., Marcial, J. and Stepanov, L., (1997). “Cyclic Testing of Four Full-Scale Steel Beam-Column Connections with ”Dogbones”” *Dept. of Civil and Environmental Engineering*, University of California, Berkeley, CA.
- Ramhormozian, S., Clifton, G. C., and Macrae, G. A., (2014) “The Asymmetric Friction Connection with Belleville springs in the Sliding Hinge Joint,” NZSEE Conference, February 2014.
- Ricles, J., Fisher, J., and Faufmann, E., (2002). “Development of Improved Welded Moment Connections for Earthquake-Resistant Design.” *Journal of Construction Steel Research*, 58(5), 565-604.
- Sato, A., Newell, J., and Uang, C.-M., (2007). “Cyclic testing of bolted flange plate steel moment connections for special moment frames.” *Structural systems research project for AISC Report No. SSRP-07/10*, University of California, San Diego, CA.
- Shahidi, F., Nateghi-A, F., Razzaghi, M., and Shahidi, F., (2013). “Influential Factor in Improving the Seismic Performance of the Kaiser Bolted Bracket Moment Connection.” *International Journal of Engineering*, Vol. 26(2), 163-176.
- Sumner, E., and Murray, T., (2002). “Behavior of Extended End-Plate Moment Connections Subject to Cyclic Loading.” *Journal of Structural Engineering*,

128(4), 501-508.

Tremblay, R., Timler, P., Bruneau, M. and Filiatrault, A., (1995) “Performance of steel structures during the 1994 Northridge earthquake,” *Canadian Journal of Civil Engineering*, 22(2), 438–451,.

Zareian, F., and Medina, R., (2010). “A practical method for proper modeling of structural damping in inelastic plane structural systems.” *Computers and Structures*, 88(1), 45-53.

Appendix B

GROUND MOTION SELECTION

B.1 Selection of Ground Motions for Different Hazard Types

The selection of the ground motions used for the analysis of the archetype frames was varied to account for the three different site hazard types being analyzed. The site hazards were identified using the USGS data for the particular location in Seattle. The deaggregation plots demonstrated varying magnitude of hazard sources which depended on the period, as shown in Figure B.1. The seismic hazard at the PGA were dominated by ground motions occurring very close to the site (0-50km) with magnitudes varying from 6 to 7 (USGS, 2008), attributed to the various shallow crustal and intraslab Puget Sound faults. At periods above 1.0 seconds, a second hazard source begins to increase in relative contributions, located between 85 and 150 km and having magnitudes larger than 8.5; this hazard corresponds to the Cascadia subduction fault located off the Pacific coast of Seattle. Finally, the last deaggregation plot shows the hazards at a 2 second period. At the larger period, the subduction contributes much more to the seismic hazard at the selected Seattle location. The percentage contribution of each earthquake type to mean site hazard is provided by the detailed deaggregation information on the USGS tool when specifying individual return periods (USGS, 2008). These

percentages are used to determine the intensity of annual frequency of exceedance curves at different periods, which lead to the annual frequency of exceedance curves shown in Figure 2.5 (g), (h), and (i) for the first mode period of the three-, six-, and 12-story archetype structures.

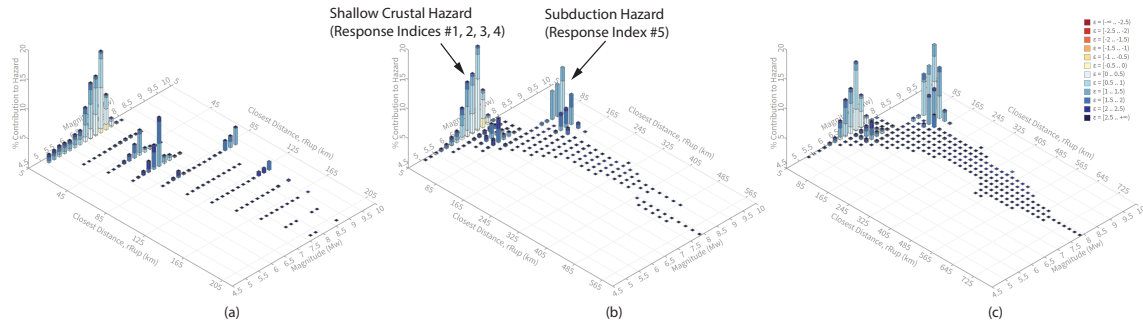


Figure B.1: Deaggregation plots at 2% in 50 year hazard level for (a) PGA, (b) 1 second period and (c) 2 second period (USGS, 2008)

Due to this difference in source hazard, two types of earthquake stripes are selected and scaled at the desired frequencies of occurrences. Each type of hazard will have unique rupture properties such as magnitude and rupture distance. These earthquakes are selected and scaled to match conditional mean spectra (Baker and Cornell 2005, Baker and Lee 2017) by minimizing the deviation of lognormal spectral accelerations while also selecting ground motions which match particular rupture properties expected at the chosen site and intensity, defined as a range of desired magnitude and distance. To conduct a multiple stripe analysis on the frames (Baker, 2015), seven conditional mean spectra of varying intensities (0.5 MCE, 0.75 MCE, 1.0 MCE, 1.25 MCE, 1.5 MCE, 2.0 MCE and 3.0 MCE) are identified and 20 to 40 ground motions are selected and scaled at each intensity and hazard type. For each archetype frame, two sets of conditional mean spectra are generated for each of the seven frequencies of occurrence, one for shallow crustal

earthquakes, shown in Figure B.2; and the other for subduction earthquakes, shown in Figure B.3. Both sets of conditional mean spectra are determined using the corresponding source characteristics (magnitude, rupture distance), then each is scaled within the set to match the desired target spectral acceleration. For the strike slip set, the source characteristics were a magnitude varying from 6 to 7 and a rupture distance from 0 to 50 km (USGS, 2008). The source characteristics used for the subduction source set were a magnitude varying from 8.5 to 9.5 and a rupture distance of 85 to 150 km (USGS, 2008). This difference in source characteristics corresponds to the change in source hazard mentioned previously. The ground motion database used for the scaling and selection of the shallow crustal earthquakes is the PEER NGA-West 2 (Chiou et al. 2008) database while the subduction earthquakes were selected and scaled from the K-NET database due to a greater availability of subduction type motions in the latter option (Fujiwara et al, 2004). The average 90% Arias intensity duration (Arias, 1970) of the shallow crustal earthquake is 45 seconds, while all of the ground motions selected for the subduction hazard had an Arias intensity duration of longer than 120 seconds, as desired, to highlight the difference in earthquake duration between each type of ground motion. A table summarizing the spectra and ground motion information for both the subduction motions and strike slip rupture properties (Magnitude, Distance and shear wave velocity (V_{s30})) are included at the end of this appendix. While the matching of the rupture characteristics were targeted, some deviation was required in order to maintain record to record variability.

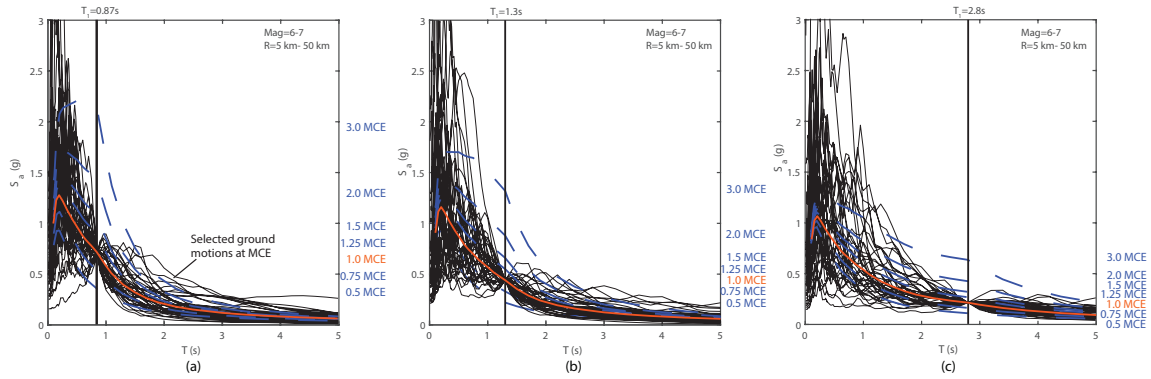


Figure B.2: Conditional mean spectra for shallow crustal hazard for (a) three story frame, (b) six story frame and (c) 12 story frame

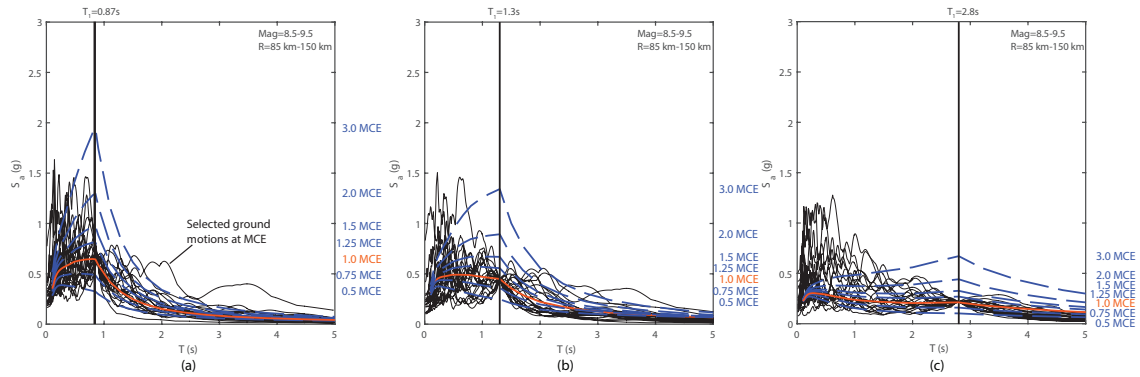


Figure B.3: Conditional mean spectra for subduction hazard for (a) three story frame, (b) six story frame and (c) 12 story frame

B.2 Creating Sets of Main-Shock-After-Shock Hazard Scenarios

Several options for the selection and scaling of main-shock after-shock scenarios were proposed in past literature. Shokrabadi et al (2018) summarized and validated four main categories of sequences for this loading scenario, all of which are listed in Table

B.1. A brief description of each sequence type is included, presenting some of the initial logistical advantages and disadvantages to each sequence.

Table B.1: Proposed MS-AS sequence type (summarized from Shokrabadi et al (2018))

Sequence type	Description
Main-shock- Main-shock (MS-MS)	Selects ground motions for both events from earthquakes classified as main-shocks where the second ground motion can be a scaled or unscaled version of the first or of another main-shock motion selected from the same database. Many potential records are available for this sequence type since several extensive databases of recorded main-shock ground motions exist which cover almost all potential rupture types.
Targeted Main-shock- Main-shock (TG-MS- MS)	Selects second motion from a database of main-shock motions but matches the desired rupture properties of a potential after-shock relating to the main-shock. This consists of a reduction of approximately 1.0 in magnitude and an opposing rupture distance. Since this sequence can take advantage of the same library of main-shock records as those used in the MS-MS sequence, with only minor rupture fault filtering needed, this sequence also has an extensive amount of combinations available.

Same-Sequence Main-shock-After-shock (SS-MS-AS)	These are true, as recorded, main-shock-after-shock pairs which were linked together. While this is the most realistic option, there is a limited number of these pairs and a wide distribution of location and rupture parameters, leading to their adaptation being difficult for specific locations.
Different-Sequence Main-shock-After-shock (DS-MS-AS)	Selects the after-shock from a database of only after-shocks, leading to a limited number of sequences when compared to the TG-MS-MS option but more options than the SS-MS-AS sequences.

Previous studies have commonly used the MS-MS approach. However, the recent analytical work by Shokrabadi et al. (2018) revealed that this procedure provided collapse levels which were unconservative when compared to the performance of structures undergoing real same-sequence main-shock-after-shock events (SS-MS-AS), as shown in an example fragility curve in Figure B.4. Therefore, they recommended the use of any of the other three sequence types, with preference being given to the SS-MS-AS sequence when possible. However, not enough Same-Sequence Main-shock-After-shock events which met the deaggregation information obtained for the Seattle site were available. Therefore, the Targeted main-shock-main-shock (TG-MS-MS) sequence was used because it allowed a large available library of ground motions to be used while maintaining

results which are reasonably similar to those obtained from the SS-MS-AS sequence.

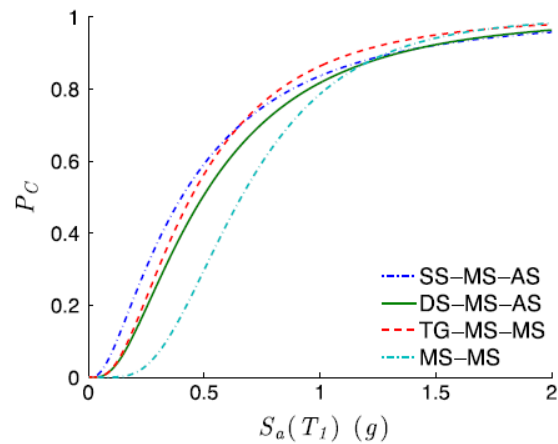


Figure B.4: Comparison of collapse fragility of an 8 story structure using four MS-AS sequence types (from Shokrabadi et al (2018))

Traditional single motion collapse analysis consists of scaling sets of ground motions (generally using increasing spectral accelerations) to determine the damage state at each intensity (generally measured using maximum inter-storey drifts as the EDP), forming a probabilistic relationship between the ground motion intensity and the EDP. To consider collapse due to two different motions in the same sequence, Shokrabadi et al. (2018) used a Markov transition matrix, shown in equations B.2.1 and B.2.2 (Yeo and Cornell 2005), to link the probabilistic relationship of the building transitioning from the damage state resulting from the

main-shock to the final damage state following the after-shock.

$$\Pi = \begin{bmatrix} 0 & P_{1,2} & \dots & P_{1,n} \\ \vdots & 0 & \ddots & \vdots \\ \vdots & \ddots & 0 & P_{m,n} \\ 0 & \dots & \dots & 0 \end{bmatrix} \quad (\text{B.2.1})$$

$$\Pi_{ij} = 0, i \geq j \quad (\text{B.2.2})$$

where i is the damage state resulting from the main-shock, varying from 1 to n (collapse); j is the damage state following the after-shock, varying from 1 to m ; and P_{ij} is defined as:

$$P_{ij} = \int (P_{ij}^{DS}[EDP > edp_j|IM] - P_{ij}^{DS}[EDP > edp_{j+1}|IM])d\lambda_{IM}(im) \quad (\text{B.2.3})$$

where the integral is the probability of the structure being in damage state j given that it has already experienced damage state i when subjected to the previous event, and λ_{IM} is the mean rate of exceedance of the intensity measure (IM) of the seismic hazard at the building's location. Equation B.2.2 limits the possible transitions to only increasing damage states between pairs of ground motions. The total collapse probability caused by after-shock motions following a main-shock motion of any intensity is defined by the sum of the last column vector of the matrix in equation B.2.1. The use of equations B.2.1, B.2.2, and B.2.3 results in case limitation when defining the probability of collapse using a lognormally fitted curve to increasing after-shock intensities following specific main-shock damage. As an example in Shokrabadi et al. (2018), Figure B.4

demonstrate only the fragility curves defining the probability of collapse during the after-shock for the case of an 8-storey building with a previously intact damage state under the main-shock motion.

However, if collapse is the only damage state of interest, a reorganization of the transition matrix can be conducted to define the probability of collapse linking the relative ground motion intensities given n intensity of the main-shock and m intensity of the after-shock motions. This collapse C matrix is shown in equation B.2.4 and B.2.5.

$$C = \begin{bmatrix} PC_{1,1} & \dots & PC_{1,n} \\ \vdots & \ddots & \vdots \\ 0 & \dots & PC_{m,n} \end{bmatrix} \quad (\text{B.2.4})$$

$$C_{ij} = 0, i > j \quad (\text{B.2.5})$$

where PC_{ij} is the combined probability of collapse of the structure given a main-shock ground motion at intensity i , and an after-shock ground motions at intensity j . Equation B.2.5 limits the intensity of the after-shock motions to smaller values than the intensity of the main-shock motions, maintaining the definition of “after-shock”. To develop cumulative probability distribution curves for this matrix of loading scenarios, increasing intensities of main-shock after-shock sequences were needed. The main-shock motions were selected and scaled to the same conditional mean spectra presented in Section B.1, while the after-shock motions were scaled to an intensity level which corresponds to their corresponding main-shock motions. A deaggregation of the lower intensity hazard levels (defined based on the probability of occurrence in 50 years), shown in Figure B.5, determined that the hazard source which corresponds to the shallow crustal ground motions maintains similar rupture

parameters across the three hazards levels. As discussed in Section B.1 for the shallow crustal motions, these parameters have magnitudes concentrated mostly between 6 and 7 and rupture distances which are less than 50 km. Following the guidelines of the TG-MS-MS from Shokrabadi et al. (2018) and Omori’s law (Utsu and Ogata 1995), the after-shock with the highest intensity has a magnitude which is approximately 1 lower than the main shock and has an opposing rupture distance. Two visual examples of these sequences are shown in Figure B.6, where the first sequence has a main-shock magnitude of 6.5 and rupture distance of 10.2 km and its corresponding after-shock has a magnitude of 5.5 and a rupture distance of 39.8 km. The second sequence has a main-shock magnitude of 6.8 and a rupture distance of 42 km while its corresponding after-shock has a magnitude of 5.8 and a rupture distance of 8 km.

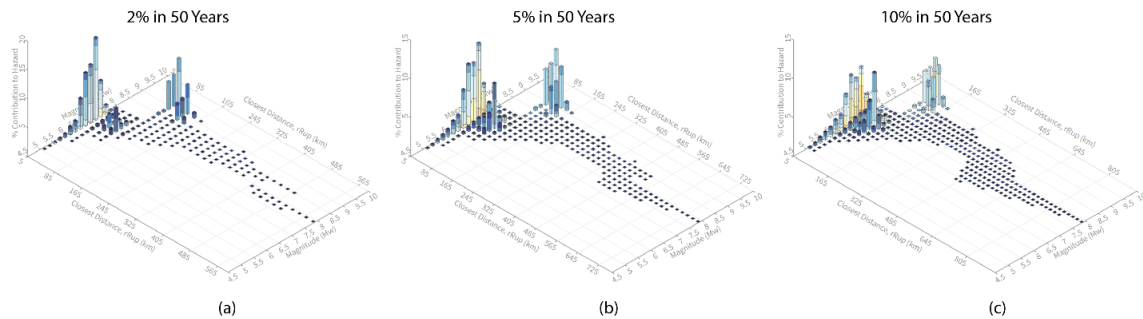


Figure B.5: Deaggregation plots for varying hazard levels

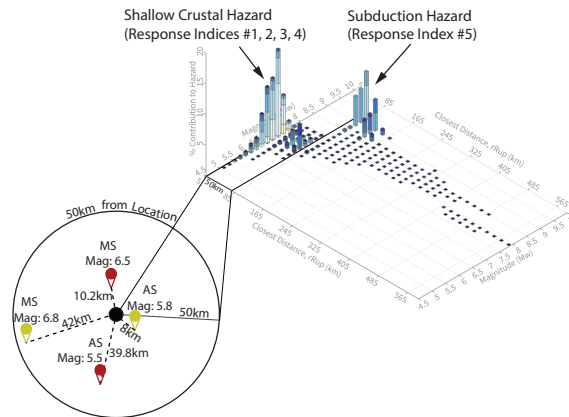


Figure B.6: Demonstration of MS-AS linking on deaggregation

While main-shock motions can be selected and scaled to the desired spectral acceleration at each intensity using developed conditional mean selection methods, the only available guidance for the selection of after-shock motions is based on their rupture parameters as each of the main-shock motions is paired with an after-shock motion with opposing rupture distance, and a reduction of a value of one magnitude. Since this does not provide information regarding the spectral acceleration scaling factor needed for the application of non-linear time history analysis, the after-shock motions were selected and scaled to match a conditional mean spectrum with a first mode spectral acceleration corresponding to the reduction in magnitude of the motions selected as the main-shock, as determined by the attenuation model developed by Boore and Atkinson (2008). This attenuation model was selected as it can be adjusted for the other record parameters such as V_{s30} and rupture distance. The summary of the equation of the attenuation model is shown in equation B.2.6, with a full explanation available in Atkinson & Boore (2008). Figure B.7 demonstrates the relationship between PGA

and magnitude at different rupture distances.

$$\ln(SA_1) = F_M(M) + F_D(R_{JB}, M) + F_S(V_{S30}, R_{JB}, M) + \epsilon\sigma_T \quad (\text{B.2.6})$$

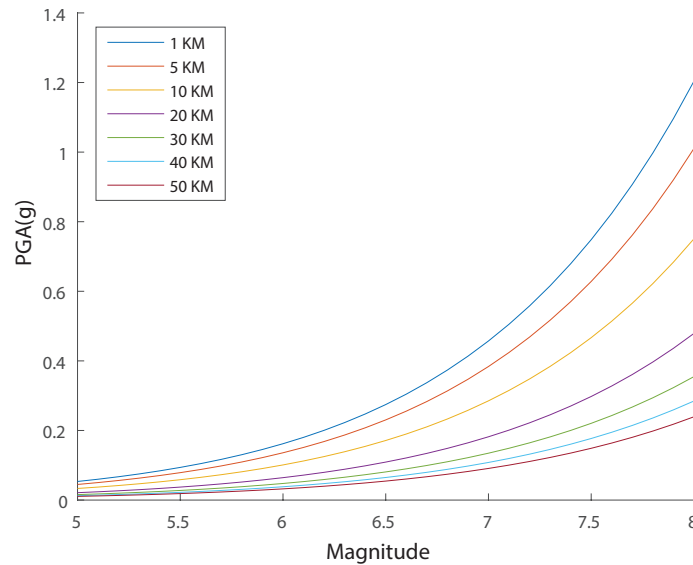


Figure B.7: Boore & Atkinson attenuation model relating PGA to Magnitude for varying rupture distances

An example of this process is conducted for a main shock selected and scaled to match a 0.5 MCE conditional mean spectrum, for which a corresponding after shock is required. For this example, the main-shock motion is initially selected and scaled to match a conditional mean spectrum for the desired intensity, shown in Figure B.8 (a), using a scaling factor of 4.71 as summarized in Table B-2. For that specific ground motion, an attenuation relationship was developed for a V_{s30} of 316.76m/s and a rupture distance of 49.82 km, shown in Figure B.8 (b). At the original scale factor of 4.71 and motion magnitude of 6.61, the PGA had a value of 0.66g. A reduction of magnitude to 5.61 relates to a new scaled PGA of 0.18g, a reduction

factor of 3.67. A new first mode spectral acceleration is then determined from the magnitude reduced ground motion spectrum and a new conditional mean spectrum is drawn with updated rupture distances and magnitudes, as shown in Figure B.8 (c). Finally, as shown in Figure B-8 (d), a new ground motion is selected and scaled as a best fit to match the after-shock ground motion conditional mean spectrum. The selection process considers mostly the standard deviation of the spectral values to the target conditional spectrum, while limiting the scale factor and targeting desired distance, magnitude characteristics. This process is conducted for all main-shocks at all intensity stripes, leading to 40 pairs of ground motions for each of the stripes for each archetype building. Each combination of stripes is included in Tables at the end of this Appendix, including for stripe intensities which were not used in the collapse performance determination but were used in the loss optimization framework of chapters 4 and 5.

Table B.2: Example of MS-AS scaling process

Mainshock Name	RSN	Direction	Scale	Mainshock Station	Mag	Rjb	Vs30
Aftershock Name	RSN	Direction	Scale	Aftershock Station	Adj. Mag	Rjb	Vs30
Tottori Japan 10/6/2000	3921	EW	4.71	OKYH03	6.61	49.82	316.76
Northridge-03 1/17/1994	1672	NS	6.39	Sandberg Bald Mtn	5.2	44.6	421

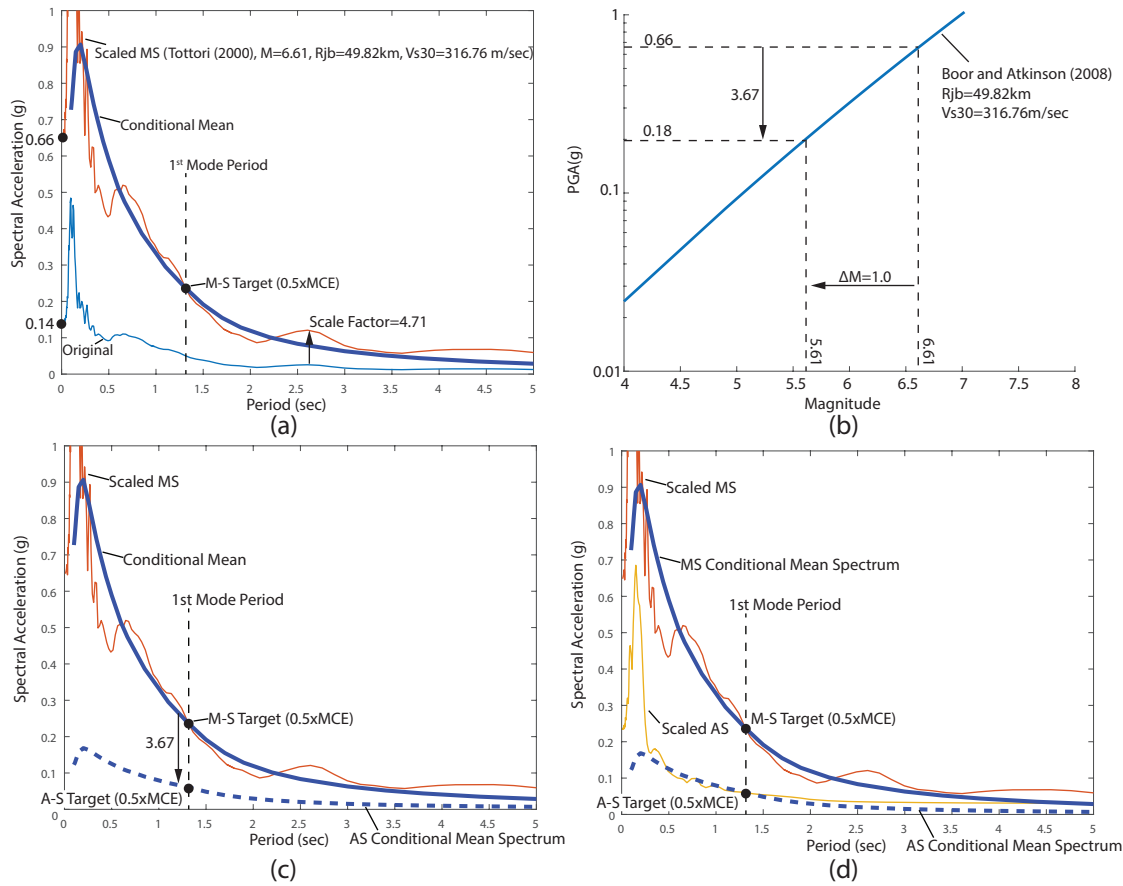


Figure B.8: Process for the selection and scaling of MS-AS intensity stripes

The frequency of exceedance, or alternatively, the return period of the combined main shock and after-shock sequence can be computed using a combination of Omori’s Law and Båth’s Law. Omori’s law dictates the frequency of exceedance of a ground motion exceeding a specific magnitude and is summarized from Reasenber and Jones (1989) as:

$$\lambda(t, M) = \frac{10^{a+b(M_m-M)}}{(t+c)^p} \tag{B.2.7}$$

Where M_m is the magnitude of the mainshock motion, t is the window of time considered for after-shocks, and a, b, c, p are site specific constants, obtained from Reasenberg and Jones (1989). Once the frequency of exceedance of the after-shock is determined, the probability of one or more earthquakes occurring within the desired magnitude range is determined from Bâth's Law:

$$P = 1 - e^{[- \int_{M_1}^{M_2} \int_S^T \lambda(t,M) dt dM]} \quad (\text{B.2.8})$$

Where P is the probability of 1 or more earthquakes occurring in magnitude range M_1 to M_2 and time range S to T , and $\lambda(t,M)$ is as above. The time horizon used for after-shock consideration is one year, which was assumed as the maximum amount of time needed to ensure damage from the main shock was identified and repaired. A value of P can therefore be determined for the magnitudes corresponding to the after-shock magnitudes, based on those of the main-shocks. The resulting probability of after-shock occurrence can be combined in a conditional probability with the frequency of the main-shock occurrence, obtained from the site hazard curve, to determine the total annual frequency of occurrence of the combined main-shock after-shock sequence. This is shown in Figure B.9 (a) for the one second spectral acceleration hazard curve at the Seattle site used throughout this document.

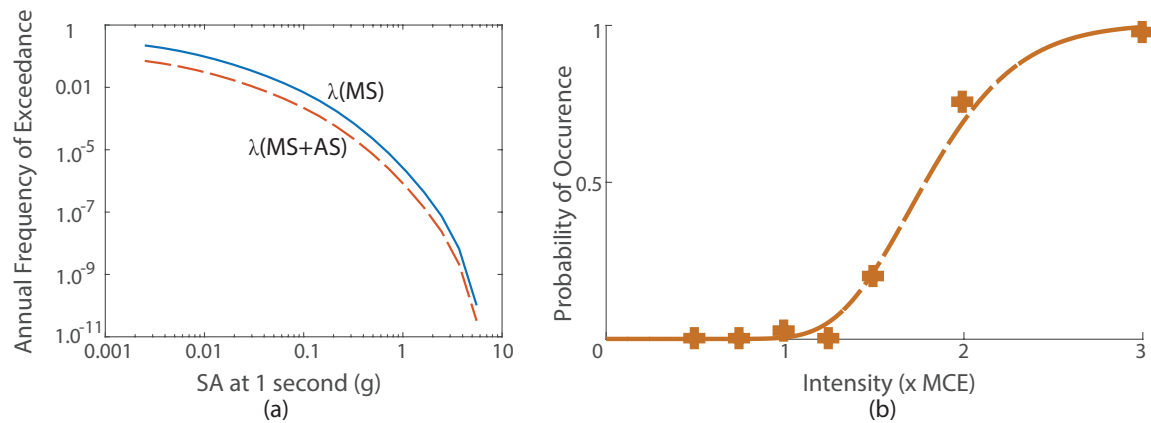


Figure B.9: (a) Site hazard curve, (b) Collapse performance of six-story frame under main-shock only

If the traditional single motion collapse analysis can be represented by a lognormally fitted curve on a 2 dimensional plot, as shown for the six-story frame in Figure B.9 (b), the resulting matrix C of combined collapse performances of a structure under any two sequential ground motions, given a range of intensities of both the main-shock and after-shock motions, is represented by a 3 dimensional surface. As a traditional multiple stripe analysis collapse analysis requires the probability of collapse to be determined at specific stripe intensities, typically defined as a multiple of the first mode spectral acceleration of the maximum considered earthquake (MCE), the same principle of intensity stripe is used for a main-shock-after-shock collapse analysis, where main-shock intensity stripes are identified as multiple of MCE and each have after-shocks selected for the specific main-shock intensity stripe. To maintain simplicity in the matrix of motions, when the intensities of the main-shock and after-shock are not identical, the after-shock is chosen to best match the targeted rupture properties from the bank of ground motions selected for the lower desired stripe intensity. For example, an after-shock described as having an intensity of 1xMCE does not match the MCE target

spectrum for main-shocks, but rather is selected from the bank of ground motions associated with main-shocks with an intensity of 1xMCE. The results of the collapse analysis on the 6-story frame throughout the work are shown in Figure B.10 (a), and the collapses during either the main shock, or the after-shock, are shown in Figure B.10 (b) and (c), respectively. The annual frequency of collapse, consisting simply of the multiplication of the probability of collapse at an intensity and the frequency of occurrence of the intensity is shown in Figure B.10 (e) and (f) for the main-shock and after-shock, respectively, and the total value of the contribution of annual frequency of collapse of the two motions is shown in Figure B.10 (d).

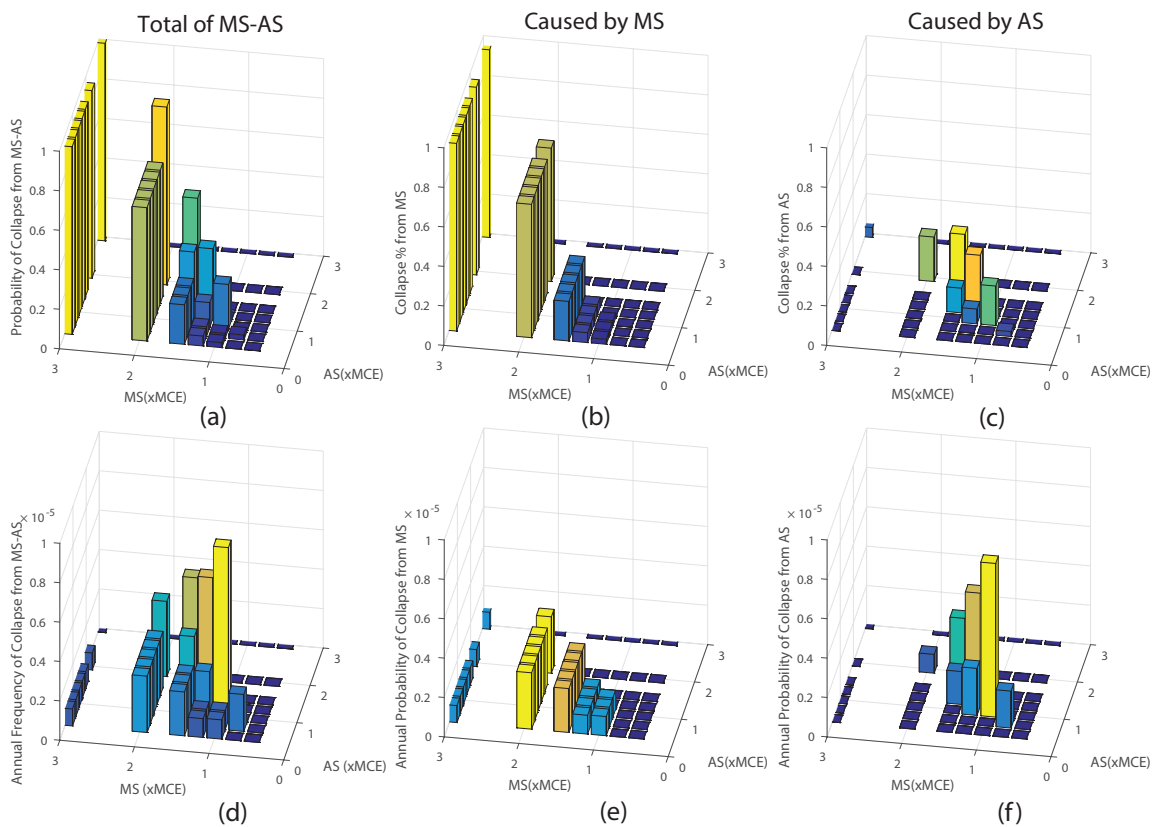


Figure B.10: Collapse of main-shock after-shock combinations of six-story frame

From Figure B-10, several observations can be made. The main-shock ground motions cause a majority of the annual probability of collapse at the intensity of 1.5xMCE and beyond, as seen in Figure B.10 (b). This is expected as the main-shock is the larger of the two ground motions. However, at intensities of MCE and 1.25xMCE, the after-shock motions cause a majority of the collapses as they increase the probability of collapse by approximately 20%, resulting in non-negligible collapse probabilities at these hazard levels. This increase in lower intensity collapse probability is accentuated when comparing the annual probability of collapse, as the lower intensity ground motions occur more frequently than their larger intensity counterparts. Figure B.10 (f) indicates that the majority of the overall annual probability of collapse is observed at the 1xMCE main-shock and 1xMCE after-shock sequence, followed by the 1.25xMCE main-shock and 1.25xMCE after-shock and finally by the 1.5xMCE main-shock and 1.5xMCE after-shock sequences. These three combinations of intensity stripes account for more than 75% of the total annual expected frequency of collapse. Such a result is expected as the intensities along the diagonal of the C matrix in Equation B.2.4 have the largest combined intensities. In fact, the combinations of intensity stripes along the diagonal represent 83% of the total annual frequency of collapse of the structure across all main-shock after-shock sequences, as shown in Figure B.11. Therefore, for the purpose of this analysis, only the diagonal vector of linked intensities was evaluated since the after-shocks used in these scenarios were of the highest possible intensities given each main-shock intensities (Yeo and Cornell 2005, Yeo and Cornell 2009, Shokrabadi et al. 2018). This vector links the intensity of the after-shock ground motions to the intensity of the main-shock ground motions at each main-shock stripe and envelopes the performance of the frame to the most intense loading case for each main-shock intensity. The vector replacing

the matrix in Equation B.2.4 is as follows:

$$C = \begin{bmatrix} PC_{11} \\ \vdots \\ PC_{m,n} \end{bmatrix} \tag{B.2.9}$$

		Main Shock Intensity (x MCE)						
		0.5	0.75	1.0	1.25	1.5	2.0	3.0
After Shock Intensity (x MCE)	0.5							
	0.75		7.7%					
	1.0			32%	10%			
	1.25				23%	7.0%		
	1.5					16%		
	2.0						4%	
	3.0							0.3%

Figure B.11: Contribution of added collapse frequency from After-Shocks

B.3 Conclusion

The selection and scaling of proper ground motions for the collapse evaluation of different buildings under several different hazard sources is presented in this appendix. In Section B-1, the first sets of ground motions which were selected were for two different hazard sources shown in the deaggregation of the selected site. These represented a shallow crustal hazard source within 50 km of the site, and a subduction hazard source which was over 80 km from the site. Conditional mean spectra were developed for these two different sources, each having unique rupture characteristics, and multiple stripes consisting of 40 ground motions in each stripe were developed for both hazard sources. In Section B-2, another collapse scenario

consisted of evaluating the performance of structures in a main-shock-after-shock combination of shallow crustal ground motions. A review of recent literature on the selection and collapse evaluation of this scenario was conducted, and a reduced version of this process was formulated and presented in this appendix. While this process is not as thorough as the current state-of-the-art when considering main-shock-after-shock combinations, the reduced process was considered to envelope the most critical cases of this combination and uses considerably less computational resources than the current state-of-the-art.

B.4 References

- Arias, A. (1970). “A measure of earthquake intensity.” *In: Hansen RJ (1st edition) Seismic design for nuclear power plants*, MIT Press, Cambridge MA, 438-483
- Baker, J. W. (2015). “Efficient analytical fragility function fitting using dynamic structural analysis.” *Earthquake Spectra*, 31(1), 579–599.
- Baker, J. W. and Cornell, C. A. (2005). “A Vector-Valued Ground Motion Intensity Measure Consisting of Spectral Acceleration and Epsilon.” *Earthquake Engineering & Structural Dynamics*, 34 (10), 1193-1217.
- Baker, J. W. and Lee, C. (2017). “An Improved Algorithm for Selecting Ground Motions to Match a Conditional Spectrum.” *Journal of Earthquake Engineering*, 1–16.
- Boore, D. and Atkinson, G. (2008) “Ground-motion prediction equations for the average horizontal component of PGA, PGV, and 5%-damped PSA at spectral periods between 0.01s and 10.0s” *Earthquake Spectra*, 24 (1), 99-138.
- Chiou, B., Darragh, R., Gregor, N., and Silva, W. (2008). “NGA Project Strong-Motion Database.” *Earthquake Spectra*, 24(1), 23–44.

Fujiwara, H., S. Aoi, T. Kunugi, and S. Adachi (2004). “Strong-motion observation networks of NIED: K-NET and KIK-net,” *Cosmos Report*, National Research Institute for Earth Science and Disaster Prevention, Japan.

Hatzigeorgiou, G. and Beskos, D. (2009) “Inelastic displacement ratios for SDOF structures subjected to repeated earthquakes” *Engineering Structures*, 31(11), 2744-2755

Goda, K. (2012). “Nonlinear response potential of Main-shock-After-shock sequences from Japanese earthquakes” *Bulletin of the Seismological Society of America*, 102 (5), 2139-2156

Reasenber, P., Jones, L. (1989) “Earthquake Hazard After a Mainshock in California” *Science*, 243(4895), 1173-1176.

Shokrabadi, M., Burton, H., Stewart, J. (2018) “Impact of Sequential Ground Motion Pairing on Main-shock-After-shock Structural Response and Collapse Performance Assessment” *Journal of Structural Engineering*, 144(10), 1-13.

United States Geological Survey (2008). “Unified Hazard Tool” (Lat: 47.6, Long: -122.3, T: 1.0 Sec).

Utsu, T., and Ogata, Y. (1995) “The centenary of the Omori formula for a decay law of after-shock activity” *Physics of the Earth*, 43 (1): 1–33

Yeo, G. L. and Cornell C. A. (2009). “A probabilistic framework for quantification of after-shock ground-motion hazard in California: Methodology and parametric study” *Earthquake Engineering and Structural Dynamics*, 38, 45-60

Yeo, G. L. and Cornell C. A. (2005). “Stochastic Characterization and Decision Bases Under Time-Dependent After-shock Risk in Performance-Based Earthquake Engineering” *Department of Civil and Environmental Engineering*, Stanford University Reprot No. 149

Table B.5: Spectra for Period 0.87, Amp 0.1

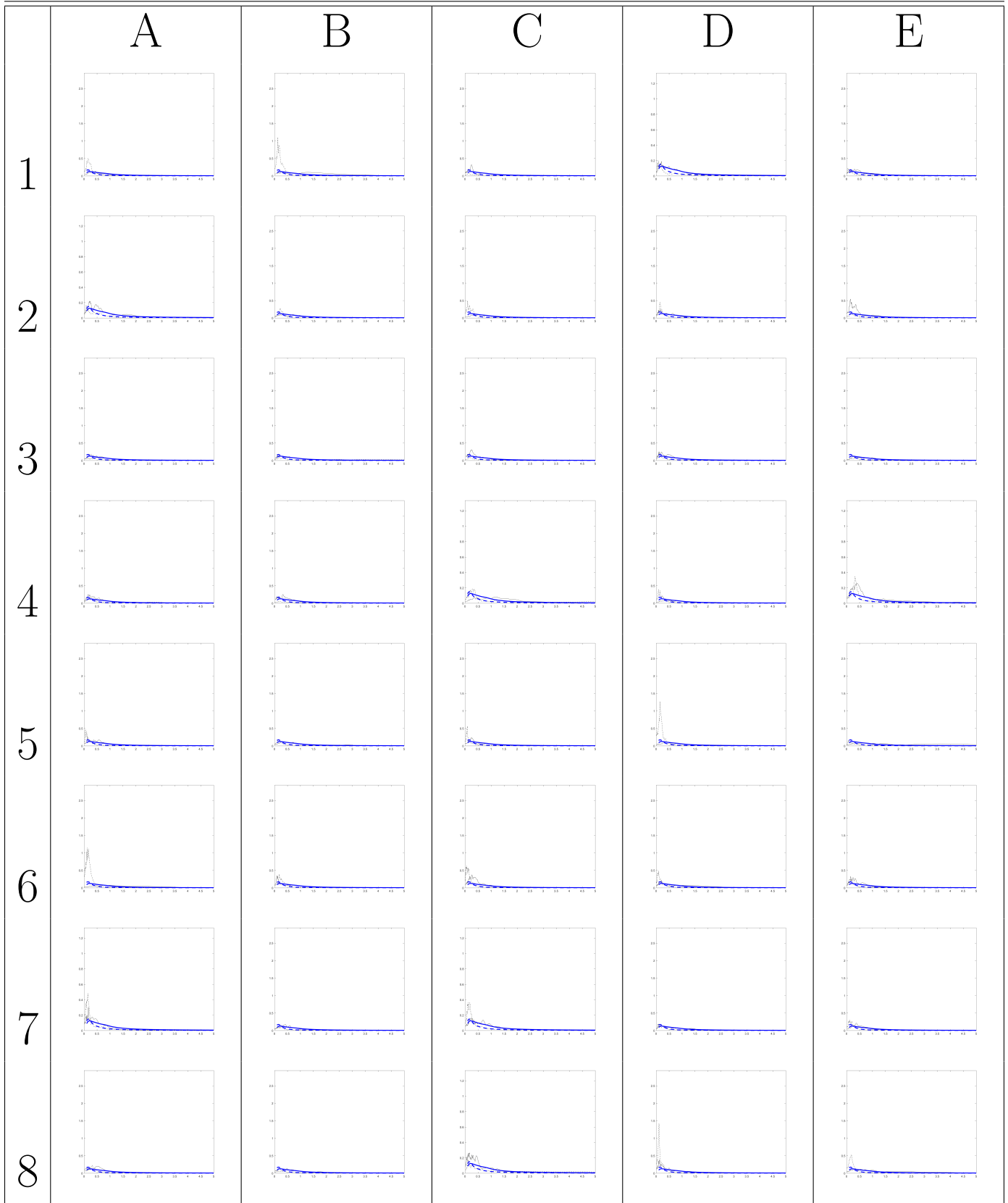


Table B.6: Details for Period 0.87, Amp 0.1

Mainshock Name Aftershock Name	RSN RSN	Direction Direction	Scale Scale	Mainshock Station Aftershock Station	Mag Adj. Mag	Rjb Rjb	Vs30 Vs30	Spec
Kern County 7/21/1952	15	EW	0.23	Taft Lincoln School	7.36	38.89	385.43	A-1
Lytle Creek 9/12/1970	45	EW	0.79	Devil's Canyon	5.33	20.24	667.13	
Borrego Mtn 4/9/1968	36	NS	0.42	El Centro Array 9	6.63	45.66	213.44	B-1
Oroville-01 8/1/1975	106	EW	2.99	Oroville Seismograph Station	5.89	7.99	680.37	
San Fernando 2/9/1971	63	NS	0.99	Fairmont Dam	6.61	30.19	634.33	C-1
N. Palm Springs 7/8/1986	522	NS	0.28	Indio	6.06	35.57	307.54	
Irpinia Italy-01 11/23/1980	291	NS	0.49	Rionero In Vulture	6.9	30.07	574.88	D-1
N. Palm Springs 7/8/1986	525	NS	1.76	Lake Mathews Dike Toe	6.06	66.71	592.42	
Spitak Armenia 12/7/1988	730	EW	0.35	Gukasian	6.77	23.99	343.53	E-1
Chalfant Valley-02 7/21/1986	550	NS	0.51	Bishop - Paradise Lodge	6.19	18.31	585.12	
Loma Prieta 10/18/1989	739	NS	0.25	Anderson Dam (Downstream)	6.93	20.26	488.77	A-2
Whittier Narrows-01 10/1/1987	625	NS	0.2	Inglewood - Union Oil	5.99	25.86	316.02	
Loma Prieta 10/18/1989	775	NS	0.78	Hollister - SAGO Vault	6.93	30.24	621.2	B-2
Northridge-04 1/17/1994	1680	NS	2	Los Angeles - 7-story Univ Hospital (FF)	5.93	51.29	332.28	
Loma Prieta 10/18/1989	778	EW	0.1	Hollister Differential Array	6.93	24.82	215.54	C-2
Little Skull MtnNV 6/29/1992	1742	EW	2.09	Station 3-Beaty	5.65	45.59	404.23	
Loma Prieta 10/18/1989	801	NS	0.22	San Jose - Santa Teresa Hills	6.93	14.69	671.77	D-2
Chi-Chi Taiwan-03 9/20/1999	2622	NS	0.22	TCU071	6.2	16.46	624.85	
Loma Prieta 10/18/1989	810	NS	0.28	UCSC Lick Observatory	6.93	18.41	713.59	E-2
Chi-Chi Taiwan-03 9/20/1999	2658	NS	0.11	TCU129	6.2	12.83	511.18	
Cape Mendocino 4/25/1992	828	EW	0.06	Petrolia	7.01	8.18	422.17	A-3
Chi-Chi Taiwan-03 9/20/1999	2686	EW	2.74	TTN041	6.2	73.85	418.24	
Northridge-01 1/17/1994	987	EW	0.16	LA - Centinela St	6.69	28.3	321.91	B-3
Chi-Chi Taiwan-04 9/20/1999	2710	NS	0.28	CHY036	6.2	30.85	233.14	
Northridge-01 1/17/1994	999	EW	0.19	LA - Obregon Park	6.69	37.36	349.43	C-3
Chi-Chi Taiwan-04 9/20/1999	2725	NS	1.1	CHY061	6.2	60.42	538.69	
Northridge-01 1/17/1994	1016	EW	0.52	La Crescenta - New York	6.69	18.5	411.55	D-3
Chi-Chi Taiwan-04 9/20/1999	2820	NS	0.69	KAU050	6.2	39.73	665.2	
Northridge-01 1/17/1994	1019	NS	0.35	Lake Hughes 1	6.69	35.81	423.34	E-3
Chi-Chi Taiwan-05 9/22/1999	3028	EW	0.44	HWA043	6.2	44.98	543.06	
Northridge-01 1/17/1994	1078	NS	0.27	Santa Susana Ground	6.69	16.74	715.12	A-4
Chi-Chi Taiwan-06 9/25/1999	3320	EW	0.39	CHY111	6.3	68.97	276.34	
Northridge-01 1/17/1994	1087	NS	0.05	Tarzana - Cedar Hill A	6.69	15.6	257.21	B-4
Chi-Chi Taiwan-06 9/25/1999	3471	EW	0.17	TCU075	6.3	26.31	573.02	
Kocaeli Turkey 8/17/1999	1166	EW	0.2	Iznik	7.51	30.73	476.62	C-4
Chi-Chi Taiwan-06 9/25/1999	3512	EW	0.23	TCU141	6.3	45.72	223.04	
Chi-Chi Taiwan 9/20/1999	1211	EW	0.37	CHY052	7.62	39.02	573.04	D-4
Tottori Japan 10/6/2000	3872	EW	0.86	HRS003	6.61	65.81	335.55	
Chi-Chi Taiwan 9/20/1999	1259	NS	0.48	HWA006	7.62	47.86	559.11	E-4
Tottori Japan 10/6/2000	3879	NS	1.25	HRS011	6.61	65.64	549.66	
Chi-Chi Taiwan 9/20/1999	1350	NS	0.32	ILA067	7.62	38.82	665.2	A-5
Tottori Japan 10/6/2000	3891	EW	1.65	HRSH09	6.61	65.98	495.15	
Chi-Chi Taiwan 9/20/1999	1351	EW	0.95	KAU001	7.62	44.93	573.04	B-5
Parkfield-02 CA 9/28/2004	4085	NS	0.27	Shandon-1-story High School Bldg	6	12.97	357.35	
Chi-Chi Taiwan 9/20/1999	1507	EW	0.09	TCU071	7.62	5.8	624.85	C-5
Parkfield-02 CA 9/28/2004	4123	EW	0.33	Parkfield - Gold Hill 4W	6	8.27	421.2	
Chi-Chi Taiwan 9/20/1999	1511	EW	0.08	TCU076	7.62	2.74	614.98	D-5
Umbria-03 Italy 4/29/1984	4313	NS	1.34	Nocera Umbra	5.6	16.76	428	
Chi-Chi Taiwan 9/20/1999	1519	EW	0.27	TCU087	7.62	6.98	538.69	E-5
Umbria-03 Italy 4/29/1984	4317	NS	1.06	Umbertide	5.6	26.98	574.32	
Denali Alaska 11/3/2002	2114	NS	0.07	TAPS Pump Station 10	7.9	2.74	329.4	A-6
Lazio Abruzzo (aftershock 1) Italy 5/11/1984	4321	EW	1.76	Villetta Barrea	5.5	7.95	519	
Tottori Japan 10/6/2000	3921	EW	0.72	OKYH03	6.61	49.82	316.76	B-6
Umbria Marche Italy 9/26/1997	4345	EW	0.44	Assisi-Stallone	6	16.55	376.6	
San Simeon CA 12/22/2003	3979	NS	0.49	Cambria - Hwy 1 Caltrans Bridge	6.52	7.25	362.42	C-6
Umbria Marche (aftershock 3) Italy 10/3/1997	4357	NS	1.04	Nocera Umbra-Biscontini	5.3	7.13	442	
Bam Iran 12/26/2003	4040	NS	0.07	Bam	6.6	1.7	487.4	D-6
Umbria Marche (aftershock 8) Italy 10/12/1997	4377	NS	0.81	Borgo-Cerreto Torre	5.2	10.15	519	
Niigata Japan 10/23/2004	4212	NS	0.28	NIG022	6.63	18.03	193.2	E-6
Umbria Marche (aftershock 2) Italy 10/14/1997	4386	EW	0.93	Colfiorito-Casermette	5.6	10.31	405	
Niigata Japan 10/23/2004	4227	NS	0.4	NIGH10	6.63	39.37	653.28	A-7
Umbria Marche (aftershock 2) Italy 10/14/1997	4389	EW	2.7	Nocera Umbra-Biscontini	5.6	19.72	442	
Chuetsu-oki 7/16/2007	4864	EW	0.14	Yoitamachi Yoita Nagaoka	6.8	16.1	655.45	B-7
L'Aquila Italy 4/6/2009	4472	NS	0.51	Celano	6.3	21.4	612.78	
Chuetsu-oki 7/16/2007	4866	NS	0.15	Kawanishi Izumozaki	6.8	11.75	338.32	C-7
L'Aquila (aftershock 2) Italy 4/9/2009	4556	EW	1.49	Chieti	5.4	64.45	356.39	
Chuetsu-oki 7/16/2007	4869	EW	0.29	Kawaguchi	6.8	29.25	640.14	D-7
Chuetsu-oki 7/16/2007	5018	NS	0.59	FKSH21	6.8	56.06	364.91	
Chuetsu-oki 7/16/2007	4887	EW	0.41	Joetsu Nakanomata	6.8	36.79	561.59	E-7
Iwate 6/13/2008	5480	NS	1.11	AKTH02	6.9	59.62	620.4	
Chuetsu-oki 7/16/2007	4889	EW	0.22	Joetsu Otemachi	6.8	32.94	314.57	A-8
Iwate 6/13/2008	5482	EW	0.04	AKTH04	6.9	17.94	458.73	
Chuetsu-oki 7/16/2007	5268	NS	0.39	NIG022	6.8	41.54	193.2	B-8
Joshua Tree CA 4/23/1992	6876	NS	0.1	Whitewater Trout Farm	6.1	29.4	425.02	
Iwate 6/13/2008	5622	EW	0.69	IWT014	6.9	37.58	314.6	C-8
40204628 10/31/2007	8671	EW	0.8	Calaveras Reservoir 2	5.45	4.29	519	
Iwate 6/13/2008	5657	EW	0.07	IWTH25	6.9	4.8	506.44	D-8
14383980 7/29/2008	8842	NS	2.87	Riverside	5.39	36.83	355.87	
Darfield New Zealand 9/3/2010	6890	NS	0.17	Christchurch Cashmere High School	7	17.64	204	E-8
14383980 7/29/2008	8885	NS	0.57	La Habra - La Habra Monte Vista	5.39	19.37	331.73	

Table B.5: Spectra for Period 0.87, Amp 0.5

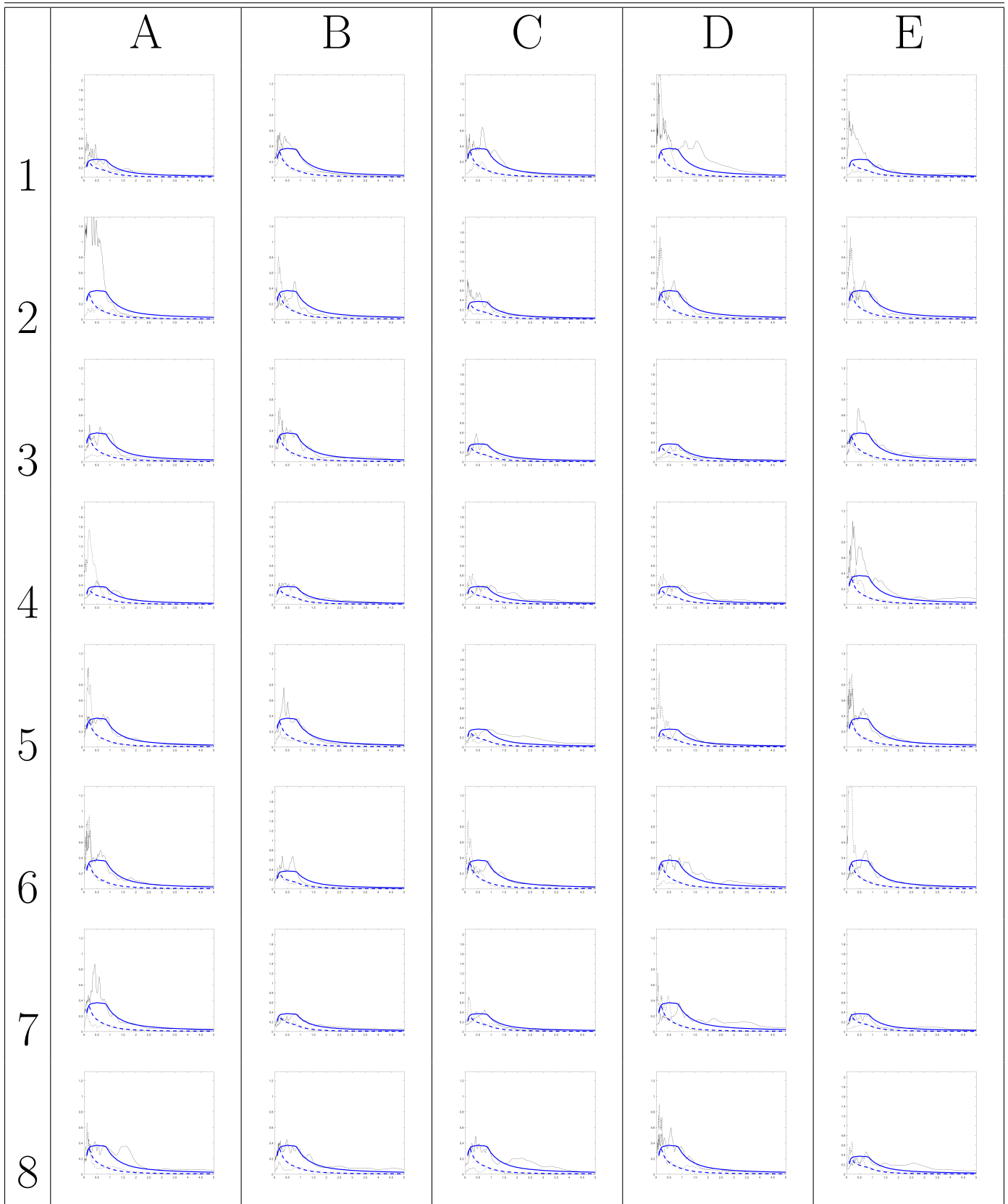


Table B.6: Details for Period 0.87, Amp 0.5

Mainshock Name Aftershock Name	RSN RSN	Direction Direction	Scale Scale	Mainshock Station Aftershock Station	Mag Adj. Mag	Rjb Rjb	Vs30 Vs30	Spec
Kern County 7/21/1952	15	NS	1.19	Taft Lincoln School	7.36	38.89	385.43	A-1
Imperial Valley-08 10/16/1979	209	NS	0.56	Westmorland Fire Sta	5.62	9.76	193.67	
San Fernando 2/9/1971	57	EW	0.82	Castaic - Old Ridge Route	6.61	22.63	450.28	B-1
Livermore-01 1/24/1980	212	EW	0.59	Del Valle Dam (Toe)	5.8	24.95	403.37	
San Fernando 2/9/1971	70	EW	1.76	Lake Hughes 1	6.61	27.4	425.34	C-1
Coalinga-01 5/2/1983	332	EW	0.47	Parkfield - Cholame 6W	6.36	50.2	251.57	
Imperial Valley-06 10/15/1979	158	NS	0.94	Aeropuerto Mexicali	6.53	0.34	259.86	D-1
Coalinga-02 5/9/1983	382	NS	2.5	Palmer Ave	5.09	11.41	458.09	
Imperial Valley-06 10/15/1979	167	NS	2.34	Compuertas	6.53	15.3	259.86	E-1
Coalinga-05 7/22/1983	412	EW	1.28	Pleasant Valley P.P. - yard	5.77	16.05	257.38	
Superstition Hills-02 11/24/1987	727	NS	1.19	Superstition Mtn Camera	6.54	5.61	362.38	A-2
Morgan Hill 4/24/1984	462	NS	0.71	Hollister City Hall	6.19	30.76	198.77	
Loma Prieta 10/18/1989	772	NS	0.95	Halls Valley	6.93	30.49	281.61	B-2
Taiwan SMART1(33) 6/12/1985	487	NS	1.91	SMART1 I01	5.8	41.74	275.82	
Loma Prieta 10/18/1989	801	EW	0.95	San Jose - Santa Teresa Hills	6.93	14.69	671.77	C-2
N. Palm Springs 7/8/1986	518	NS	0.56	Fun Valley	6.06	14.24	388.63	
Northridge-01 1/17/1994	1019	NS	1.73	Lake Hughes 1	6.69	35.81	425.34	D-2
N. Palm Springs 7/8/1986	519	NS	0.86	Hemet Fire Station	6.06	34.71	328.09	
Northridge-01 1/17/1994	1019	EW	1.88	Lake Hughes 1	6.69	35.81	425.34	E-2
Whittier Narrows-01 10/1/1987	598	EW	1.94	Big Tujunga Angeles Nat F	5.99	28.5	550.11	
Northridge-01 1/17/1994	1031	NS	1.01	Leona Valley 5 - Ritter	6.69	37.8	375.22	A-3
Erzican Turkey 3/13/1992	821	NS	0.11	Erzincan	6.69	4.38	352.05	
Northridge-01 1/17/1994	1052	NS	0.51	Pacoima Kagel Canyon	6.69	7.26	508.08	B-3
Northridge-01 1/17/1994	943	NS	2.53	Anacapa Island	6.69	68.93	501.75	
Northridge-01 1/17/1994	1074	NS	1.41	Sandberg - Bald Mtn	6.69	41.56	421	C-3
Northridge-01 1/17/1994	1020	EW	1.39	Lake Hughes 12A	6.69	21.36	602.1	
Kobe Japan 1/16/1995	1121	NS	0.49	Yae	6.9	27.77	256	D-3
Chi-Chi Taiwan-02 9/20/1999	2388	EW	1.78	TCU075	5.9	30.75	573.02	
Chi-Chi Taiwan 9/20/1999	1198	NS	0.77	CHY029	7.62	10.96	544.74	E-3
Chi-Chi Taiwan-03 9/20/1999	2629	EW	0.23	TCU079	6.2	8.48	363.99	
Chi-Chi Taiwan 9/20/1999	1234	EW	0.59	CHY086	7.62	28.42	665.2	A-4
Chi-Chi Taiwan-04 9/20/1999	2820	EW	1.9	KAU050	6.2	39.73	665.2	
Chi-Chi Taiwan 9/20/1999	1236	NS	1.03	CHY088	7.62	37.48	318.52	B-4
Chi-Chi Taiwan-04 9/20/1999	2821	EW	1.77	KAU054	6.2	30.16	497.22	
Chi-Chi Taiwan 9/20/1999	1300	EW	1.13	HWA055	7.62	47.46	369.75	C-4
Chi-Chi Taiwan-04 9/20/1999	2930	NS	1.14	TTN044	6.2	62.37	419.63	
Chi-Chi Taiwan 9/20/1999	1300	NS	1.25	HWA055	7.62	47.46	369.75	D-4
Chi-Chi Taiwan-04 9/20/1999	2935	EW	1.47	TTN051	6.2	37.57	665.2	
Chi-Chi Taiwan 9/20/1999	1380	NS	3.95	KAU054	7.62	30.85	497.22	E-4
Chi-Chi Taiwan-05 9/22/1999	3028	NS	2.88	HWA043	6.2	44.98	543.06	
Chi-Chi Taiwan 9/20/1999	1508	EW	0.34	TCU072	7.62	7.08	468.14	A-5
Chi-Chi Taiwan-05 9/22/1999	3217	NS	0.83	TCU129	6.2	38.91	511.18	
Hector Mine 10/16/1999	1794	EW	0.94	Joshua Tree	7.13	31.06	379.32	B-5
Chi-Chi Taiwan-06 9/25/1999	3264	EW	0.38	CHY024	6.3	31.14	427.73	
Denali Alaska 11/3/2002	2114	NS	0.37	TAPS Pump Station 10	7.9	2.74	329.4	C-5
Chi-Chi Taiwan-06 9/25/1999	3274	EW	0.26	CHY035	6.3	41.58	573.04	
Cape Mendocino 4/25/1992	3748	EW	0.44	Ferndale Fire Station	7.01	19.32	387.95	D-5
Chi-Chi Taiwan-06 9/25/1999	3327	NS	1.08	HWA009	6.3	57.16	373.23	
Landers 6/28/1992	3752	NS	1.97	Forest Falls Post Office	7.28	45.34	436.14	E-5
Chi-Chi Taiwan-06 9/25/1999	3461	EW	0.66	TCU056	6.3	36.11	403.2	
Landers 6/28/1992	3752	EW	2.33	Forest Falls Post Office	7.28	45.34	436.14	A-6
Frulli Italy-03 9/11/1976	3553	EW	2.71	Tarcento	5.5	6.3	629.08	
Landers 6/28/1992	3753	EW	1.07	Fun Valley	7.28	25.02	388.63	B-6
Taiwan SMART1(33) 6/12/1985	3615	EW	2.78	SMART1 I11	5.8	41.88	309.41	
San Simeon CA 12/22/2003	4013	NS	1.39	San Antonio Dam - Toe	6.52	19.01	509.04	C-6
Northridge-06 3/20/1994	3772	NS	2.15	LA - Wadsworth VA Hospital South	5.28	20.15	413.81	
Niigata Japan 10/23/2004	4204	EW	1.21	NIG014	6.63	28.42	128.12	D-6
Chi-Chi (aftershock 2) Taiwan 9/20/1999	3847	EW	0.5	CHY010	6.2	41.72	538.69	
Chuetsu-oki 7/16/2007	4863	NS	0.42	Nagaoka	6.8	16.27	514.3	E-6
Tottori Japan 10/6/2000	3939	NS	2.37	SMN007	6.61	70.49	383.13	
Chuetsu-oki 7/16/2007	4864	EW	0.72	Yoitamachi Yoita Nagaoka	6.8	16.1	655.45	A-7
Parkfield-02 CA 9/28/2004	4065	EW	0.17	PARKFIELD - EADES	6	2.85	383.9	
Chuetsu-oki 7/16/2007	5260	NS	0.94	NIG014	6.8	27.09	128.12	B-7
Parkfield-02 CA 9/28/2004	4066	EW	0.82	PARKFIELD - FROELICH	6	3.19	226.63	
Iwate 6/13/2008	5778	NS	0.64	Matsuyama City	6.9	40.98	436.34	C-7
Parkfield-02 CA 9/28/2004	4067	EW	2.69	PARKFIELD - GOLD HILL	6	3.43	558.33	
Iwate 6/13/2008	5786	NS	0.5	Minamikatamachi Tore City	6.9	34.52	300.21	D-7
Parkfield-02 CA 9/28/2004	4119	NS	1.14	Parkfield - Gold Hill 2E	6	3.84	360.92	
Iwate 6/13/2008	5798	NS	1.04	Takanashi Daisen	6.9	46.41	217.1	E-7
Parkfield-02 CA 9/28/2004	4121	NS	0.84	Parkfield - Gold Hill 3E	6	6.3	450.61	
Iwate 6/13/2008	5816	EW	1.02	Shinmachi Wakayu	6.9	42.02	359.13	A-8
Parkfield-02 CA 9/28/2004	4128	NS	0.79	Parkfield - Stone Corral 3E	6	8.08	565.08	
El Mayor-Cucapah 4/4/2010	5823	NS	0.67	Chihuahua	7.2	19.47	242.05	B-8
Parkfield-02 CA 9/28/2004	4131	NS	0.27	Parkfield - Vineyard Cany 1W	6	2.75	284.21	
Darfield New Zealand 9/3/2010	6912	NS	0.85	Hulverstone Drive Pumping Station	7	25.4	206	C-8
Umbria Marche (aftershock 2) Italy 10/14/1997	4385	EW	0.43	Colfiorito	5.6	11.11	317	
Darfield New Zealand 9/3/2010	6948	NS	1.59	OXZ	7	30.63	481.62	D-8
Chuetsu-oki 7/16/2007	5266	NS	1.62	NIG020	6.8	37.16	331.63	
Darfield New Zealand 9/3/2010	6952	NS	0.63	Papanui High School	7	18.73	263.2	E-8
Iwate 6/13/2008	5469	NS	2.31	AKT014	6.9	54.55	452.15	

Table B.6: Spectra for Period 0.87, Amp 0.75

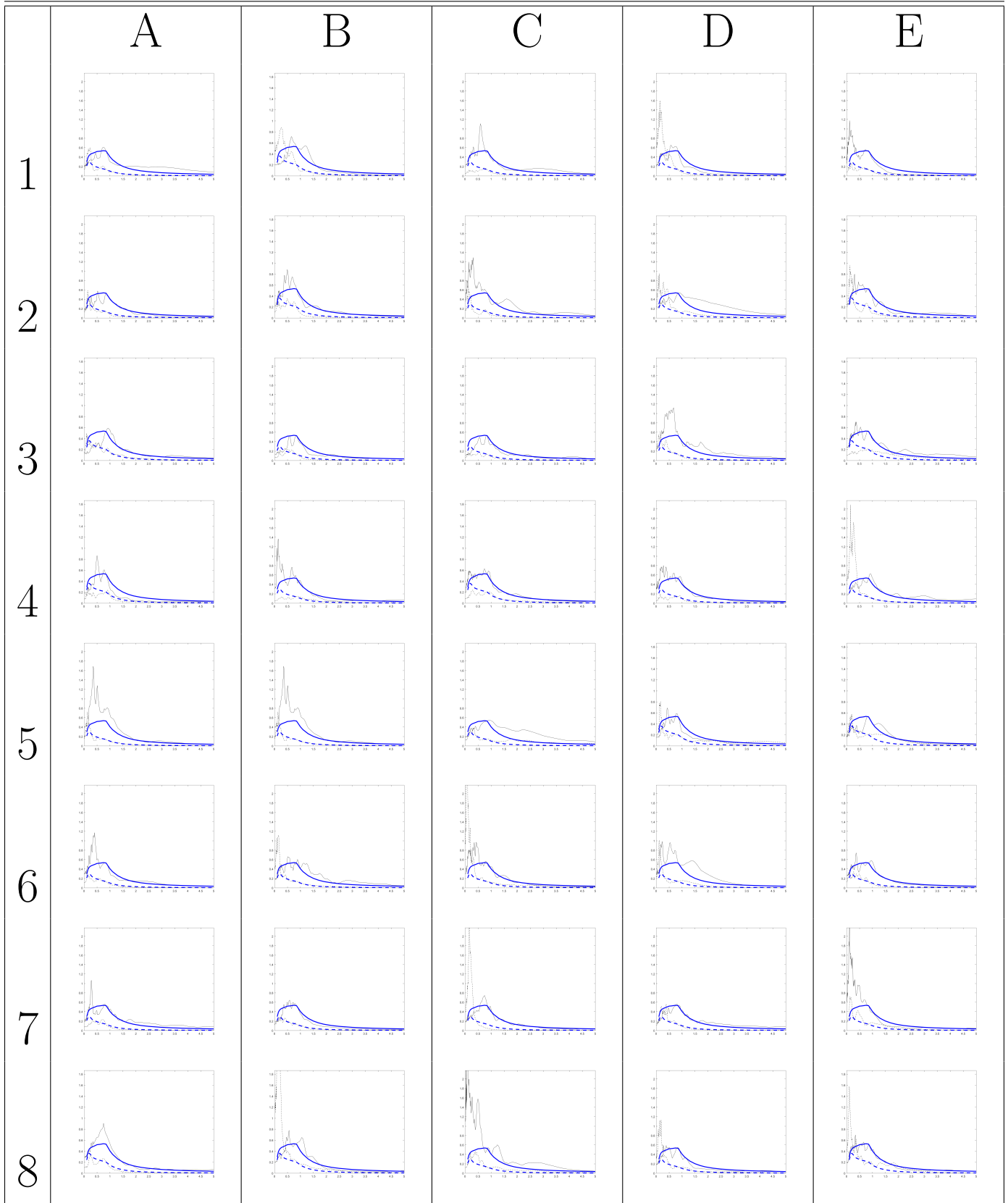


Table B.7: Details for Period 0.87, Amp 0.75

Mainshock Name Aftershock Name	RSN RSN	Direction Direction	Scale Scale	Mainshock Station Aftershock Station	Mag Adj. Mag	Rjb Rjb	Vs30 Vs30	Spec
Imperial Valley-06 10/15/1979 Morgan Hill 4/24/1984	182 459	EW NS	0.45 0.62	El Centro Array 7 Gilroy Array 6	6.53 6.19	0.56 9.87	210.51 663.31	A-1
Loma Prieta 10/18/1989 Chalfant Valley-01 7/20/1986	732 545	EW EW	0.9 1.5	APEEL 2 - Redwood City Bishop - Paradise Lodge	6.93 5.77	43.23 15.13	133.11 585.12	B-1
Loma Prieta 10/18/1989 Chalfant Valley-02 7/21/1986	748 558	NS EW	2.07 0.12	Belmont - Envirotech Zack Brothers Ranch	6.93 6.19	44.11 7.58	627.59 316.19	C-1
Loma Prieta 10/18/1989 Whittier Narrows-01 10/1/1987	753 598	EW EW	0.46 2.92	Corralitos Big Tujunga Angeles Nat F	6.93 5.99	3.85 28.5	462.24 550.11	D-1
Loma Prieta 10/18/1989 Whittier Narrows-01 10/1/1987	811 625	NS EW	0.67 0.37	WAHO Inglewood - Union Oil	6.93 5.99	17.47 25.86	388.33 316.02	E-1
Northridge-01 1/17/1994 Whittier Narrows-01 10/1/1987	953 636	NS NS	0.38 2.64	Beverly Hills - 14145 Mulhol LA - N Faring Rd	6.69 5.99	17.15 31.48	355.81 255	A-2
Northridge-01 1/17/1994 Whittier Narrows-01 10/1/1987	986 655	EW EW	1.37 2.65	LA - Brentwood VA Hospital Leona Valley 5 - Ritter	6.69 5.99	22.5 59.13	416.58 375.22	B-2
Northridge-01 1/17/1994 Whittier Narrows-01 10/1/1987	1005 678	NS NS	2.75 0.68	LA - Temple Hope Pasadena - CIT Indust. Rel	6.69 5.99	31.48 17.3	452.15 341.14	C-2
Northridge-01 1/17/1994 Whittier Narrows-01 10/1/1987	1045 706	NS NS	0.54 1.03	Newhall - W Pico Canyon Rd. Whittier Narrows Dam upstream	6.69 5.99	5.48 14.73	285.93 298.68	D-2
Northridge-01 1/17/1994 Superstition Hills-02 11/24/1987	1052 727	NS EW	0.76 0.22	Pacoima Kagel Canyon Superstition Mtn Camera	6.69 6.54	7.26 5.61	508.08 362.38	E-2
Kobe Japan 1/16/1995 Loma Prieta 10/18/1989	1104 803	NS EW	0.63 0.21	Fukushima Saratoga - W Valley Coll.	6.9 6.93	17.85 9.31	256 347.9	A-3
Kobe Japan 1/16/1995 Griva Greece 12/21/1990	1110 814	NS EW	0.57 0.64	Morigawachi Edessa (bsmt)	6.9 6.1	24.78 33.29	256 551.3	B-3
Kobe Japan 1/16/1995 Griva Greece 12/21/1990	1121 815	NS NS	0.74 1.28	Yae Kilkis	6.9 6.1	27.77 29.2	256 454.56	C-3
Chi-Chi Taiwan 9/20/1999 Northridge-06 3/20/1994	1187 1728	EW EW	1.75 0.48	CHY015 Rinaldi Receiving Sta	7.62 5.28	38.13 12.96	228.66 282.25	D-3
Chi-Chi Taiwan 9/20/1999 Chi-Chi Taiwan-02 9/20/1999	1211 2386	NS NS	2.76 1.46	CHY052 TCU073	7.62 5.9	39.02 10.68	573.04 473.65	E-3
Chi-Chi Taiwan 9/20/1999 Chi-Chi Taiwan-03 9/20/1999	1234 2627	EW NS	0.88 0.61	CHY086 TCU076	7.62 6.2	28.42 14.66	665.2 614.98	A-4
Chi-Chi Taiwan 9/20/1999 Chi-Chi Taiwan-03 9/20/1999	1350 2644	EW EW	1.81 0.77	ILA067 TCU106	7.62 6.2	38.82 35.93	665.2 451.37	B-4
Chi-Chi Taiwan 9/20/1999 Chi-Chi Taiwan-03 9/20/1999	1508 2654	NS NS	0.38 1.03	TCU072 TCU120	7.62 6.2	7.08 23.85	468.14 459.34	C-4
Chi-Chi Taiwan 9/20/1999 Chi-Chi Taiwan-04 9/20/1999	1513 2739	EW EW	0.7 0.39	TCU079 CHY080	7.62 6.2	10.97 12.53	363.99 496.21	D-4
Chi-Chi Taiwan 9/20/1999 Chi-Chi Taiwan-05 9/22/1999	1550 2942	EW NS	1.04 1.81	TCU136 CHY024	7.62 6.2	8.27 48.65	462.1 427.73	E-4
Hector Mine 10/16/1999 Chi-Chi Taiwan-05 9/22/1999	1794 3220	EW EW	1.41 0.87	Joshua Tree TCU138	7.13 6.2	31.06 47.51	379.32 652.85	A-5
Hector Mine 10/16/1999 Chi-Chi Taiwan-06 9/25/1999	1794 3475	NS NS	2.08 0.28	Joshua Tree TCU080	7.13 6.3	31.06 10.2	379.32 489.32	B-5
Denali Alaska 11/3/2002 Cape Mendocino 4/25/1992	2114 3750	NS NS	0.56 0.46	TAPS Pump Station 10 Loleta Fire Station	7.9 7.01	2.74 25.91	329.4 515.65	C-5
Cape Mendocino 4/25/1992 Northridge-06 3/20/1994	3745 3772	EW EW	1.03 2.31	Butler Valley Station 2 LA - Wadsworth VA Hospital South	7.01 5.28	45.43 20.15	525.26 413.81	D-5
Cape Mendocino 4/25/1992 Chi-Chi (aftershock 4) Taiwan 9/22/1999	3748 3857	EW NS	0.66 1.27	Ferndale Fire Station CHY002	7.01 6.2	19.32 67.58	387.95 253.13	E-5
Cape Mendocino 4/25/1992 Parkfield-02 CA 9/28/2004	3749 4081	EW EW	1.02 0.48	Fortuna Fire Station Parkfield - Cholame 5W	7.01 6	20.41 6.87	355.18 236.59	A-6
Nigata Japan 10/23/2004 Parkfield-02 CA 9/28/2004	4204 4122	EW EW	1.81 0.95	NIG014 Parkfield - Gold Hill 3W	6.63 6	28.42 5.41	128.12 510.92	B-6
Nigata Japan 10/23/2004 Parkfield-02 CA 9/28/2004	4219 4123	EW EW	0.44 2.48	NIGH01 Parkfield - Gold Hill 4W	6.63 6	9.46 8.27	480.4 421.2	C-6
Montenegro Yugo. 4/15/1979 Parkfield-02 CA 9/28/2004	4451 4128	EW NS	0.76 1.21	Bar-Skupstina Opstine Parkfield - Stone Corral 3E	7.1 6	6.98 8.08	462.23 565.08	D-6
Chuetsu-oki 7/16/2007 Parkfield-02 CA 9/28/2004	4850 4143	EW NS	0.56 0.38	Yoshikawaku Joetsu City PARKFIELD - UPSAR 07	6.8 6	16.86 9.61	561.59 440.59	E-6
Chuetsu-oki 7/16/2007 Parkfield-02 CA 9/28/2004	4855 4145	NS NS	1.48 0.27	Sanjo PARKFIELD - UPSAR 09	6.8 6	27.15 9.34	245.45 466.12	A-7
Chuetsu-oki 7/16/2007 Parkfield-02 CA 9/28/2004	4862 4146	NS EW	0.84 0.41	Shiura Nagaoka PARKFIELD - UPSAR 10	6.8 6	20.17 9.14	336.93 341.7	B-7
Chuetsu-oki 7/16/2007 Umbria Marche (foreshock) Italy 9/26/1997	4863 4339	NS EW	0.62 1.5	Nagaoka Nocera Umbra	6.8 5.7	16.27 12.32	514.3 428	C-7
Chuetsu-oki 7/16/2007 Umbria Marche Italy 9/26/1997	5260 4352	NS EW	1.4 0.3	NIG014 Nocera Umbra	6.8 6	27.09 8.92	128.12 428	D-7
Iwate 6/13/2008 Umbria Marche (aftershock 2) Italy 10/14/1997	5666 4391	NS EW	4.76 1.46	MYG007 Norcia-Altavilla	6.9 5.6	45.55 18.35	166.75 218	E-7
Iwate 6/13/2008 L'Aquila Italy 4/6/2009	5778 4491	EW NS	0.71 0.98	Matsuyama City Ortucchio	6.9 6.3	40.98 37.16	436.34 388.01	A-8
Iwate 6/13/2008 Darfield New Zealand 9/3/2010	5782 6915	NS EW	1.14 0.98	Misato Miyagi Kitaura - B Heathcote Valley Primary School	6.9 7	47.02 24.47	291.76 422	B-8
Iwate 6/13/2008 Christchurch New Zealand 2/21/2011	5807 8124	NS EW	3.45 0.48	Yuzama Yokobori Riccarton High School	6.9 6.2	29.75 9.44	570.62 293	C-8
El Mayor-Cucapah 4/4/2010 Christchurch New Zealand 2/21/2011	5991 8158	EW EW	0.47 0.31	El Centro Array 10 LPCC	7.2 6.2	20.05 6.12	202.85 649.67	D-8
Darfield New Zealand 9/3/2010 40204628 10/31/2007	6971 8732	NS NS	1.29 1.86	SPFS Pacheco Peak CA USA	7 5.45	29.86 61.45	389.54 686.73	E-8

Table B.7: Spectra for Period 0.87, Amp 1.0

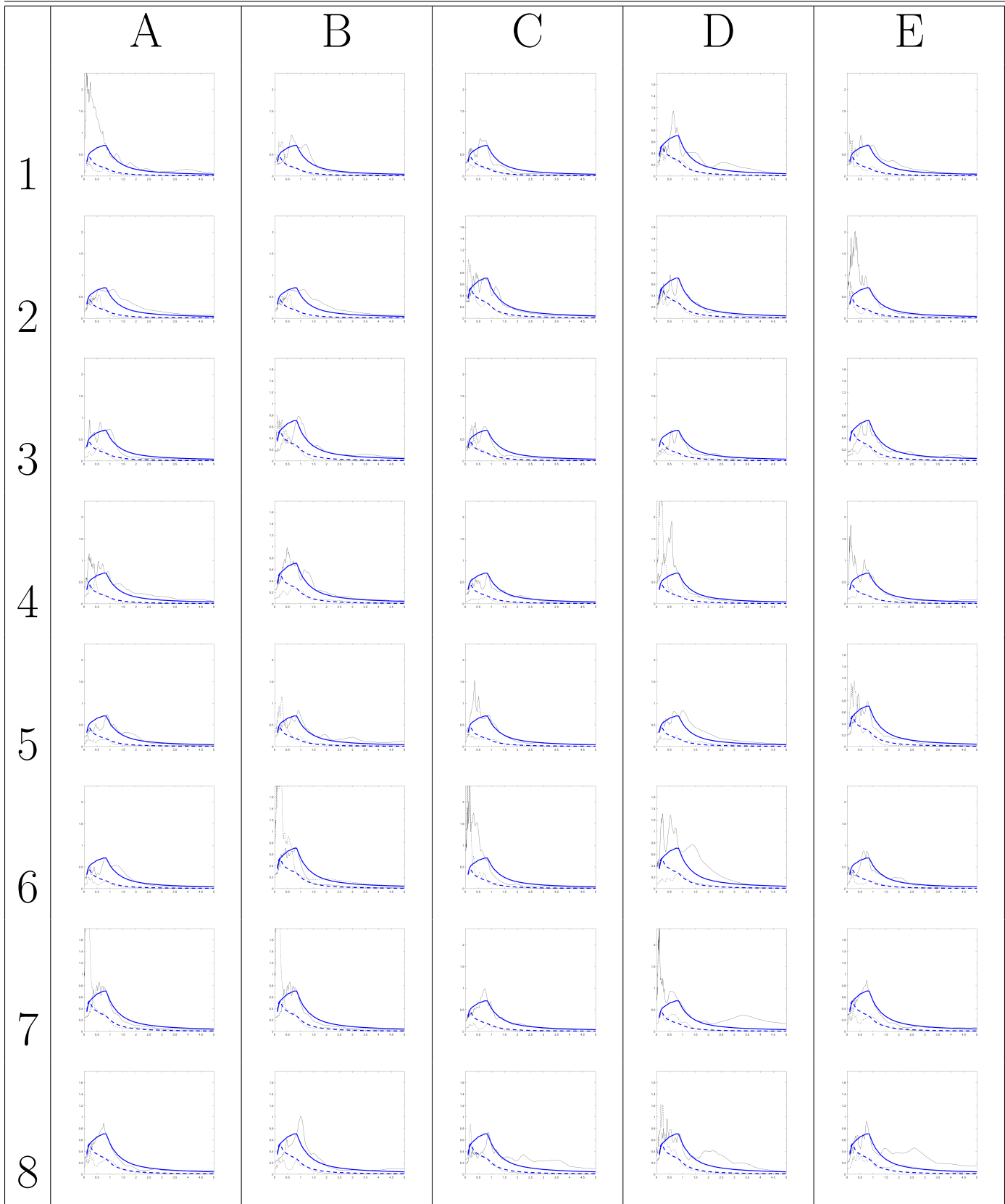


Table B.8: Details for Period 0.87, Amp 1.0

Mainshock Name Aftershock Name	RSN RSN	Direction Direction	Scale Scale	Mainshock Station Aftershock Station	Mag Adj. Mag	Rjb Rjb	Vs30 Vs30	Spec
Imperial Valley-06 10/15/1979	167	NS	4.67	Compuertas	6.53	15.3	259.86	A-1
Mammoth Lakes-06 5/27/1980	246	NS	0.86	Benton	5.94	44.21	370.94	
Loma Prieta 10/18/1989	732	EW	1.2	APEEL 2 - Redwood City	6.93	43.23	133.11	B-1
Coalinga-05 7/22/1983	413	NS	0.78	Skunk Hollow	5.77	11.71	480.32	
Loma Prieta 10/18/1989	753	EW	0.61	Corralitos	6.93	3.85	462.24	C-1
Morgan Hill 4/24/1984	450	EW	0.98	Corralitos	6.19	23.24	462.24	
Loma Prieta 10/18/1989	759	EW	0.85	Foster City - APEEL 1	6.93	43.94	116.35	D-1
Hollister-04 1/26/1986	501	EW	1.19	SAGO South - Surface	5.45	12.32	608.67	
Loma Prieta 10/18/1989	776	NS	0.71	Hollister - South Pine	6.93	27.93	282.14	E-1
N. Palm Springs 7/8/1986	519	NS	1.75	Hemet Fire Station	6.06	34.71	328.09	
Loma Prieta 10/18/1989	777	EW	1.1	Hollister City Hall	6.93	27.6	198.77	A-2
N. Palm Springs 7/8/1986	521	NS	2.31	Hurkey Creek Park	6.06	29.83	407.61	
Loma Prieta 10/18/1989	777	NS	0.96	Hollister City Hall	6.93	27.6	198.77	B-2
Whittier Narrows-01 10/1/1987	610	EW	2.31	Castaic - Old Ridge Route	5.99	72.2	450.28	
Landers 6/28/1992	864	NS	1.02	Joshua Tree	7.28	11.03	379.32	C-2
Whittier Narrows-01 10/1/1987	611	EW	0.63	Compton - Castlegate St	5.99	23.37	266.9	
Northridge-01 1/17/1994	953	NS	0.5	Beverly Hills - 14145 Mulhol	6.69	17.15	355.81	D-2
Whittier Narrows-01 10/1/1987	620	EW	1.71	Glendale - Las Palmas	5.99	22.82	371.07	
Northridge-01 1/17/1994	1012	EW	1.8	LA 00	6.69	19.07	706.22	E-2
Whittier Narrows-01 10/1/1987	678	NS	0.9	Pasadena - CIT Indust. Rel	5.99	17.3	341.14	
Northridge-01 1/17/1994	1031	NS	2.02	Leona Valley 5 - Ritter	6.69	37.8	375.22	A-3
Griva Greece 12/21/1990	814	EW	0.85	Edessa (bsmt)	6.1	33.29	551.3	
Kobe Japan 1/16/1995	1104	NS	0.84	Fukushima	6.9	17.85	256	B-3
Griva Greece 12/21/1990	815	NS	1.74	Kilkis	6.1	29.2	454.56	
Kobe Japan 1/16/1995	1106	EW	0.38	KJMA	6.9	0.96	312	C-3
Northridge-01 1/17/1994	999	EW	0.5	LA - Obregon Park	6.69	37.36	349.43	
Kobe Japan 1/16/1995	1110	NS	0.76	Morigawachi	6.9	24.78	256	D-3
Northridge-01 1/17/1994	1085	NS	0.12	Sylmar - Converter Sta East	6.69	5.19	370.52	
Kobe Japan 1/16/1995	1121	NS	0.99	Yae	6.9	27.77	256	E-3
Northridge-02 1/17/1994	1658	NS	2.84	LA - Century City CC North	6.05	20.47	277.98	
Chi-Chi Taiwan 9/20/1999	1208	EW	1.97	CHY046	7.62	24.1	442.15	A-4
Northridge-04 1/17/1994	1676	NS	1.22	Castaic - Old Ridge Route	5.93	25.17	450.28	
Chi-Chi Taiwan 9/20/1999	1234	EW	1.17	CHY086	7.62	28.42	665.2	B-4
Northridge-06 3/20/1994	1737	NS	1.02	Sylmar - Converter Sta East	5.28	14.87	370.52	
Chi-Chi Taiwan 9/20/1999	1258	NS	1.59	HWA005	7.62	47.58	459.32	C-4
Chi-Chi Taiwan-03 9/20/1999	2490	EW	0.8	CHY074	6.2	28.69	553.43	
Chi-Chi Taiwan 9/20/1999	1283	NS	3.34	HWA034	7.62	44.32	379.18	D-4
Chi-Chi Taiwan-03 9/20/1999	2622	NS	2.23	TCU071	6.2	16.46	624.85	
Chi-Chi Taiwan 9/20/1999	1350	EW	2.41	ILA067	7.62	38.82	665.2	E-4
Chi-Chi Taiwan-03 9/20/1999	2627	EW	0.21	TCU076	6.2	14.66	614.98	
Chi-Chi Taiwan 9/20/1999	1517	NS	0.21	TCU084	7.62	11.48	665.2	A-5
Chi-Chi Taiwan-04 9/20/1999	2739	EW	0.5	CHY080	6.2	12.53	496.21	
Chi-Chi Taiwan 9/20/1999	1550	EW	1.39	TCU136	7.62	8.27	462.1	B-5
Chi-Chi Taiwan-05 9/22/1999	2954	NS	2.7	CHY046	6.2	70.58	442.15	
Hector Mine 10/16/1999	1794	EW	1.87	Joshua Tree	7.13	31.06	379.32	C-5
Chi-Chi Taiwan-05 9/22/1999	3211	EW	0.93	TCU115	6.2	60.01	215.34	
Loma Prieta 10/18/1989	3548	EW	0.76	Los Gatos - Lexington Dam	6.93	5.02	1070.34	D-5
Chi-Chi Taiwan-06 9/25/1999	3502	EW	1.43	TCU120	6.3	32.46	459.34	
Cape Mendocino 4/25/1992	3745	EW	1.37	Butler Valley Station 2	7.01	45.43	525.26	E-5
Chi-Chi Taiwan-06 9/25/1999	3505	EW	0.26	TCU125	6.3	25.66	397.57	
Cape Mendocino 4/25/1992	3748	EW	0.88	Ferndale Fire Station	7.01	19.32	387.95	A-6
Lazio Abruzzo Italy 5/7/1984	3605	NS	0.61	Cassino-Sant' Elia	5.8	24.4	436.79	
Tottori Japan 10/6/2000	3968	EW	0.3	TTRH02	6.61	0.97	310.21	B-6
Northridge-06 3/20/1994	3767	EW	1.36	Sylmar - Olive View Med FF	5.28	16.63	440.54	
Niigata Japan 10/23/2004	4227	NS	3.94	NIGH10	6.63	39.37	653.28	C-6
Parkfield-02 CA 9/28/2004	4075	NS	2.85	PARKFIELD - WORK RANCH	6	10.76	446.5	
Montenegro Yugo. 4/15/1979	4451	EW	1.01	Bar-Skupstina Opstine	7.1	6.98	462.23	D-6
Parkfield-02 CA 9/28/2004	4119	EW	2.48	Parkfield - Gold Hill 2E	6	3.84	360.92	
Chuetsu-oki 7/16/2007	4861	NS	0.9	Nakanoshima Nagaoka	6.8	19.89	319	E-6
Parkfield-02 CA 9/28/2004	4131	NS	0.56	Parkfield - Vineyard Cany 1W	6	2.75	284.21	
Chuetsu-oki 7/16/2007	4862	NS	1.11	Shiura Nagaoka	6.8	20.17	336.93	A-7
Umbria Marche Italy 9/26/1997	4352	EW	0.4	Nocera Umbra	6	8.92	428	
Chuetsu-oki 7/16/2007	4862	EW	1.31	Shiura Nagaoka	6.8	20.17	336.93	B-7
Umbria Marche (aftershock 1) Italy 10/6/1997	4368	NS	1.56	Nocera Umbra-Biscontini	5.5	7.87	442	
Chuetsu-oki 7/16/2007	4863	NS	0.83	Nagaoka	6.8	16.27	514.3	C-7
Umbria Marche (aftershock 2) Italy 10/14/1997	4385	EW	0.86	Colfiorito	5.6	11.11	317	
Iwate 6/13/2008	5775	EW	2.73	Tamati Ono	6.9	28.91	561.59	D-7
Umbria Marche (aftershock 2) Italy 10/14/1997	4390	EW	1.36	Nocera	5.6	19.06	678	
Iwate 6/13/2008	5778	NS	1.28	Matsuyama City	6.9	40.98	436.34	E-7
L'Aquila Italy 4/6/2009	4491	NS	1.37	Ortucchio	6.3	37.16	388.01	
Iwate 6/13/2008	5778	EW	0.95	Matsuyama City	6.9	40.98	436.34	A-8
Iwate 6/13/2008	5778	NS	0.34	Matsuyama City	6.9	40.98	436.34	
Iwate 6/13/2008	5782	NS	1.52	Misato Miyagi Kitaura - B	6.9	47.02	291.76	B-8
Iwate 6/13/2008	5792	EW	0.72	Rifu Town	6.9	57.78	520.7	
Iwate 6/13/2008	5786	NS	1.01	Minamikatamachi Tore City	6.9	34.52	300.21	C-8
Christchurch New Zealand 2/21/2011	8060	NS	1.75	ASHS	6.2	30.46	295.74	
Darfield New Zealand 9/3/2010	6912	NS	1.71	Hulverstone Drive Pumping Station	7	25.4	206	D-8
Christchurch New Zealand 2/21/2011	8158	NS	0.69	LPCC	6.2	6.12	649.67	
Darfield New Zealand 9/3/2010	6952	NS	1.26	Papanui High School	7	18.73	263.2	E-8
14383980 7/29/2008	8795	EW	1.01	Fullerton	5.39	19.04	351.22	

Table B.8: Spectra for Period 0.87, Amp 1.25

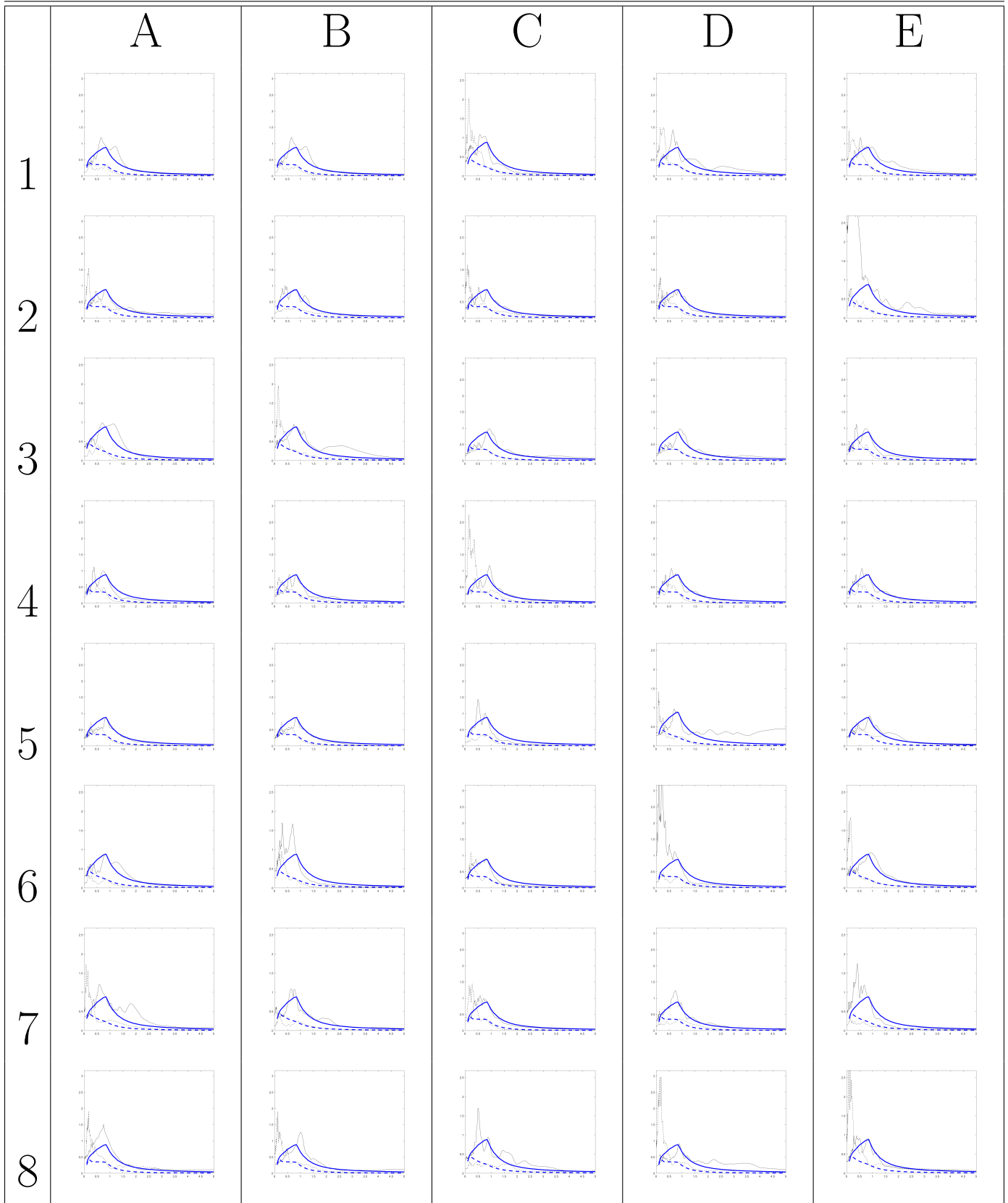


Table B.9: Details for Period 0.87, Amp 1.25

Mainshock Name Aftershock Name	RSN RSN	Direction Direction	Scale Scale	Mainshock Station Aftershock Station	Mag Adj. Mag	Rjb Rjb	Vs30 Vs30	Spec
Loma Prieta 10/18/1989 Livermore-01 1/24/1980	732 212	NS NS	1.28 1.69	APEEL 2 - Redwood City Del Valle Dam (Toe)	6.93 5.8	43.23 24.95	133.11 403.37	A-1
Loma Prieta 10/18/1989 Westmorland 4/26/1981	732 316	EW EW	1.49 0.47	APEEL 2 - Redwood City Parachute Test Site	6.93 5.9	43.23 16.66	133.11 348.69	B-1
Loma Prieta 10/18/1989 Coalinga-05 7/22/1983	753 406	EW NS	0.76 1.61	Corralitos Coalinga-14th Elm (Old CHP)	6.93 5.77	3.85 10.78	462.24 286.41	C-1
Loma Prieta 10/18/1989 Coalinga-05 7/22/1983	759 413	EW NS	1.07 0.97	Foster City - APEEL 1 Skunk Hollow	6.93 5.77	43.94 11.71	116.35 480.32	D-1
Loma Prieta 10/18/1989 Whittier Narrows-01 10/1/1987	776 610	NS EW	0.89 2.88	Hollister - South Pine Castaic - Old Ridge Route	6.93 5.99	27.93 72.2	282.14 450.28	E-1
Loma Prieta 10/18/1989 Whittier Narrows-01 10/1/1987	777 611	NS EW	1.2 0.79	Hollister City Hall Compton - Castlegate St	6.93 5.99	27.6 23.37	198.77 266.9	A-2
Landers 6/28/1992 Whittier Narrows-01 10/1/1987	864 615	NS EW	1.28 0.72	Joshua Tree Downey - Co Maint Bldg	7.28 5.99	11.03 20.82	379.32 271.9	B-2
Northridge-01 1/17/1994 Whittier Narrows-01 10/1/1987	953 642	NS NS	0.63 0.55	Beverly Hills - 14145 Mulhol LA - W 70th St	6.69 5.99	17.15 22.17	355.81 241.41	C-2
Northridge-01 1/17/1994 Whittier Narrows-01 10/1/1987	978 648	EW EW	1.14 0.79	Hollywood - Willoughby Ave La Crescenta - New York	6.69 5.99	23.07 26.04	347.7 411.55	D-2
Northridge-01 1/17/1994 Loma Prieta 10/18/1989	987 801	NS NS	4.84 0.73	LA - Centinela St San Jose - Santa Teresa Hills	6.69 6.93	28.3 14.69	321.91 671.77	E-2
Northridge-01 1/17/1994 Griva Greece 12/21/1990	1054 814	NS EW	0.63 1.07	Pardee - SCE Edessa (bsmt)	6.69 6.1	7.46 33.29	325.67 551.3	A-3
Northridge-01 1/17/1994 Northridge-01 1/17/1994	1084 987	NS NS	0.53 1.28	Sylmar - Converter Sta LA - Centinela St	6.69 6.69	5.35 28.3	251.24 321.91	B-3
Kobe Japan 1/16/1995 Northridge-04 1/17/1994	1104 1676	NS NS	1.05 1.52	Fukushima Castaic - Old Ridge Route	6.9 5.93	17.85 25.17	256 450.28	C-3
Kobe Japan 1/16/1995 Northridge-06 3/20/1994	1104 1728	EW EW	1.45 0.81	Fukushima Rinaldi Receiving Sta	6.9 5.28	17.85 12.96	256 282.25	D-3
Kobe Japan 1/16/1995 Northridge-06 3/20/1994	1106 1737	EW NS	0.47 1.28	KJMA Sylmar - Converter Sta East	6.9 5.28	0.96 14.87	312 370.52	E-3
Kobe Japan 1/16/1995 Chi-Chi Taiwan-02 9/20/1999	1106 2382	NS NS	0.46 0.58	KJMA TCU065	6.9 5.9	0.96 33.48	312 305.85	A-4
Kobe Japan 1/16/1995 Chi-Chi Taiwan-02 9/20/1999	1110 2387	NS EW	0.95 0.49	Morigawachi TCU074	6.9 5.9	24.78 7.68	256 549.43	B-4
Chi-Chi Taiwan 9/20/1999 Chi-Chi Taiwan-03 9/20/1999	1201 2466	NS NS	0.88 1.39	CHY034 CHY035	7.62 6.2	14.82 34.52	378.75 573.04	C-4
Chi-Chi Taiwan 9/20/1999 Chi-Chi Taiwan-03 9/20/1999	1202 2622	EW EW	1.07 1.39	CHY035 TCU071	7.62 6.2	12.65 16.46	573.04 624.85	D-4
Chi-Chi Taiwan 9/20/1999 Chi-Chi Taiwan-04 9/20/1999	1202 2709	NS NS	1.03 1.11	CHY035 CHY035	7.62 6.2	12.65 25.06	573.04 573.04	E-4
Chi-Chi Taiwan 9/20/1999 Chi-Chi Taiwan-04 9/20/1999	1231 2715	NS NS	0.29 1.28	CHY080 CHY047	7.62 6.2	2.69 38.62	496.21 169.52	A-5
Chi-Chi Taiwan 9/20/1999 Chi-Chi Taiwan-04 9/20/1999	1231 2739	EW EW	0.34 0.63	CHY080 CHY080	7.62 6.2	2.69 12.53	496.21 496.21	B-5
Chi-Chi Taiwan 9/20/1999 Chi-Chi Taiwan-05 9/22/1999	1234 3217	EW EW	1.47 1.65	CHY086 TCU129	7.62 6.2	28.42 38.91	665.2 511.18	C-5
Chi-Chi Taiwan 9/20/1999 Chi-Chi Taiwan-05 9/22/1999	1246 3220	NS EW	1.45 1.45	CHY104 TCU138	7.62 6.2	18.02 47.51	223.24 652.85	D-5
Chi-Chi Taiwan 9/20/1999 Chi-Chi Taiwan-06 9/25/1999	1517 3302	NS NS	0.26 1.36	TCU084 CHY076	7.62 6.3	11.48 70.37	665.2 169.84	E-5
Cape Mendocino 4/25/1992 Lazio Abruzzo Italy 5/7/1984	3748 3605	EW NS	1.1 0.76	Ferndale Fire Station Cassino-Sant' Elia	7.01 5.8	19.32 24.4	387.95 436.79	A-6
Landers 6/28/1992 Northridge-06 3/20/1994	3753 3767	NS EW	2.02 1.71	Fun Valley Sylmar - Olive View Med FF	7.28 5.28	25.02 16.63	388.63 440.54	B-6
Tottori Japan 10/6/2000 Tottori Japan 10/6/2000	3968 3937	EW NS	0.38 2.31	TTRH02 SMN005	6.61 6.61	0.97 45.73	310.21 182.3	C-6
Niigata Japan 10/23/2004 Parkfield-02 CA 9/28/2004	4229 4081	NS EW	2.37 0.82	NIGHT Parkfield - Cholame 5W	6.63 6	10.72 6.87	564.25 236.59	D-6
Montenegro Yugo. 4/15/1979 Parkfield-02 CA 9/28/2004	4451 4122	NS EW	0.88 1.56	Bar-Skupstina Opstine Parkfield - Gold Hill 3W	7.1 6	6.98 5.41	462.23 510.92	E-6
Chuetsu-oki 7/16/2007 Parkfield-02 CA 9/28/2004	4849 4128	EW EW	1.68 2.33	Kubikiku Hyakken Joetsu City Parkfield - Stone Corral 3E	6.8 6	22.18 8.08	342.74 565.08	A-7
Chuetsu-oki 7/16/2007 Parkfield-02 CA 9/28/2004	4861 4131	NS NS	1.13 0.71	Nakanoshima Nagaoka Parkfield - Vineyard Cany 1W	6.8 6	19.89 2.75	319 284.21	B-7
Chuetsu-oki 7/16/2007 Sicilia-Orientale Italy 12/13/1990	4862 4331	NS EW	1.39 2.28	Shiura Nagaoka Sortino	6.8 5.6	20.17 26.93	336.93 412.59	C-7
Chuetsu-oki 7/16/2007 Umbria Marche (foreshock) Italy 9/26/1997	4863 4339	NS EW	1.04 2.47	Nagaoka Nocera Umbra	6.8 5.7	16.27 12.32	514.3 428	D-7
Chuetsu-oki 7/16/2007 Umbria Marche Italy 9/26/1997	4886 4351	NS NS	0.72 1.18	Tamati Yone Izumozaki Matelica	6.8 6	11.48 25.24	338.32 437	E-7
Iwate 6/13/2008 Umbria Marche (aftershock 2) Italy 10/14/1997	5778 4385	EW EW	1.18 1.08	Matsuyama City Colforito	6.9 5.6	40.98 11.11	436.34 317	A-8
Iwate 6/13/2008 Iwate 6/13/2008	5782 5782	NS NS	1.9 0.5	Misato Miyagi Kitaura - B Misato Miyagi Kitaura - B	6.9 6.9	47.02 47.02	291.76 291.76	B-8
Iwate 6/13/2008 Iwate 6/13/2008	5785 5816	EW EW	2.24 0.68	Yoneyamacho Tome City Shinmachi Wakayu	6.9 6.9	38.96 42.02	274.23 359.13	C-8
Iwate 6/13/2008 Christchurch New Zealand 2/21/2011	5786 8123	NS NS	1.26 0.21	Minamikatamachi Tore City Christchurch Resthaven	6.9 6.2	34.52 5.13	300.21 141	D-8
El Mayor-Cucapah 4/4/2010 Christchurch New Zealand 2/21/2011	5991 8158	EW NS	0.79 0.9	El Centro Array 10 LPCC	7.2 6.2	20.05 6.12	202.85 649.67	E-8

Table B.9: Spectra for Period 0.87, Amp 1.5

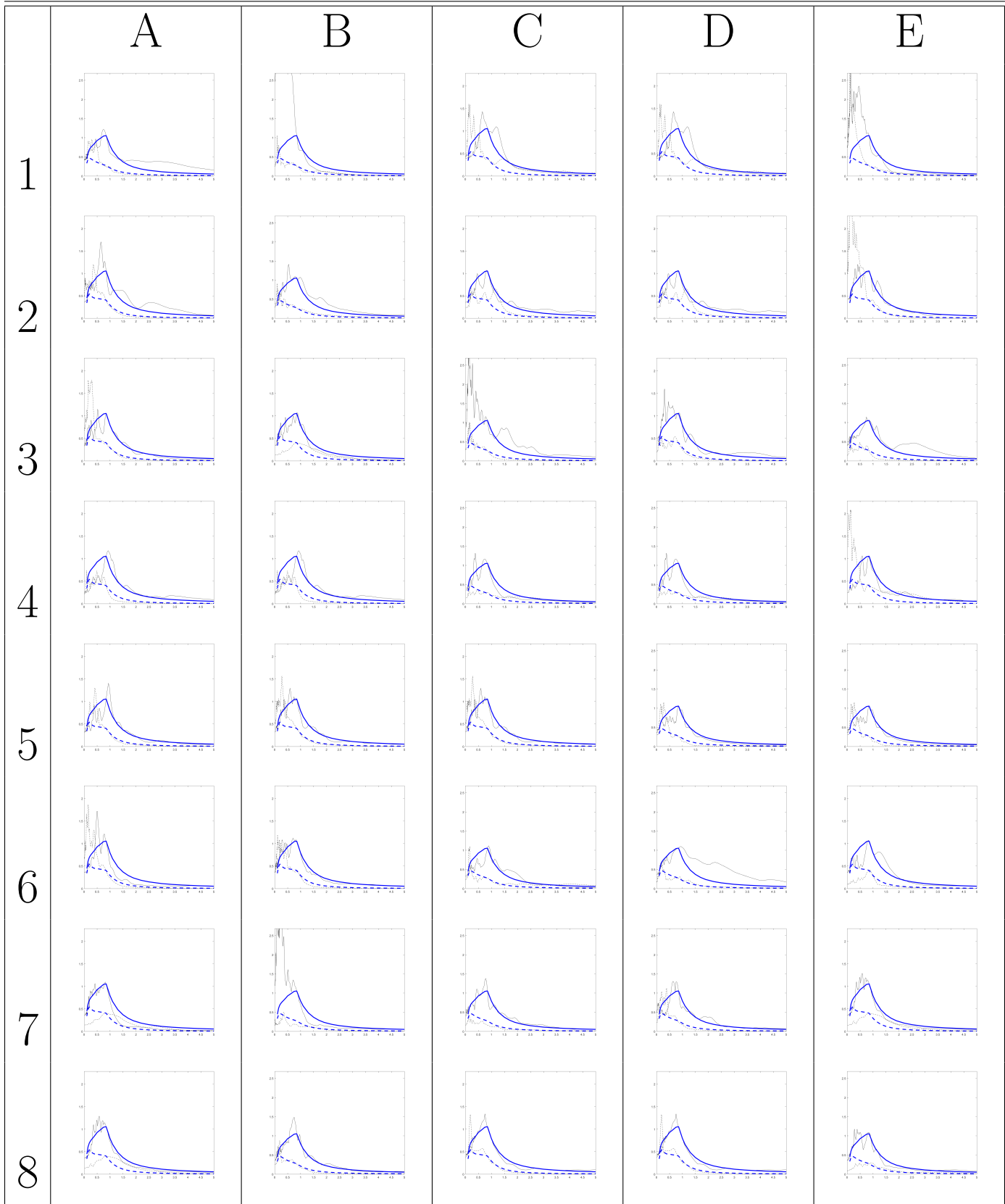


Table B.10: Details for Period 0.87, Amp 1.5

Mainshock Name Aftershock Name	RSN RSN	Direction Direction	Scale Scale	Mainshock Station Aftershock Station	Mag Adj. Mag	Rjb Rjb	Vs30 Vs30	Spec
Imperial Valley-06 10/15/1979	182	EW	0.89	El Centro Array 7	6.53	0.56	210.51	A-1
Northwest Calif-01 9/12/1938	5	NS	2.78	Ferndale City Hall	5.5	53.58	219.31	
Superstition Hills-02 11/24/1987	727	NS	3.56	Superstition Mtn Camera	6.54	5.61	362.38	B-1
Imperial Valley-08 10/16/1979	209	NS	1.66	Westmorland Fire Sta	5.62	9.76	193.67	
Loma Prieta 10/18/1989	732	NS	1.54	APEEL 2 - Redwood City	6.93	43.23	133.11	C-1
Westmorland 4/26/1981	316	EW	0.57	Parachute Test Site	5.9	16.66	348.69	
Loma Prieta 10/18/1989	732	EW	1.79	APEEL 2 - Redwood City	6.93	43.23	133.11	D-1
Westmorland 4/26/1981	319	NS	0.36	Westmorland Fire Sta	5.9	6.5	193.67	
Loma Prieta 10/18/1989	741	EW	1.49	BRAN	6.93	10.72	476.54	E-1
Coalinga-05 7/22/1983	406	EW	1.7	Coalinga-14th Elm (Old CHP)	5.77	10.78	286.41	
Loma Prieta 10/18/1989	759	EW	1.28	Foster City - APEEL 1	6.93	43.94	116.35	A-2
Coalinga-05 7/22/1983	407	EW	0.96	Oil City	5.77	8.46	398.49	
Loma Prieta 10/18/1989	776	NS	1.06	Hollister - South Pine	6.93	27.93	282.14	B-2
Coalinga-05 7/22/1983	408	EW	1.51	Oil Fields Fire Station - FF	5.77	11.1	474.15	
Loma Prieta 10/18/1989	777	NS	1.44	Hollister City Hall	6.93	27.6	198.77	C-2
Coalinga-05 7/22/1983	413	NS	1.17	Skunk Hollow	5.77	11.71	480.32	
Loma Prieta 10/18/1989	777	EW	1.65	Hollister City Hall	6.93	27.6	198.77	D-2
Morgan Hill 4/24/1984	464	NS	1.55	Hollister Differential Array 3	6.19	26.43	215.54	
Landers 6/28/1992	864	NS	1.53	Joshua Tree	7.28	11.03	379.32	E-2
N. Palm Springs 7/8/1986	512	EW	2.23	Anza - Tule Canyon	6.06	52.06	530.89	
Northridge-01 1/17/1994	953	NS	0.75	Beverly Hills - 14145 Mulhol	6.69	17.15	355.81	A-3
N. Palm Springs 7/8/1986	519	NS	2.55	Hemet Fire Station	6.06	34.71	328.09	
Northridge-01 1/17/1994	978	EW	1.37	Hollywood - Willoughby Ave	6.69	23.07	347.7	B-3
N. Palm Springs 7/8/1986	529	NS	0.3	North Palm Springs	6.06	4.04	344.67	
Northridge-01 1/17/1994	985	EW	4.27	LA - Baldwin Hills	6.69	29.88	297.07	C-3
Whittier Narrows-01 10/1/1987	611	EW	0.96	Compton - Castlegate St	5.99	23.37	266.9	
Northridge-01 1/17/1994	1052	NS	1.51	Pacoima Kagel Canyon	6.69	7.26	508.08	D-3
Whittier Narrows-01 10/1/1987	620	EW	2.57	Glendale - Las Palmas	5.99	22.82	371.07	
Northridge-01 1/17/1994	1084	NS	0.64	Sylmar - Converter Sta	6.69	5.35	251.24	E-3
Whittier Narrows-01 10/1/1987	648	EW	0.97	La Crescenta - New York	5.99	26.04	411.55	
Kobe Japan 1/16/1995	1104	NS	1.26	Fukushima	6.9	17.85	256	A-4
Whittier Narrows-01 10/1/1987	678	NS	1.35	Pasadena - CIT Indust. Rel	5.99	17.3	341.14	
Kobe Japan 1/16/1995	1104	EW	1.74	Fukushima	6.9	17.85	256	B-4
Whittier Narrows-01 10/1/1987	706	NS	2.04	Whittier Narrows Dam upstream	5.99	14.73	298.68	
Kobe Japan 1/16/1995	1106	EW	0.57	KJMA	6.9	0.96	312	C-4
Griva Greece 12/21/1990	814	EW	1.29	Edessa (bsmt)	6.1	33.29	551.3	
Kobe Japan 1/16/1995	1106	NS	0.56	KJMA	6.9	0.96	312	D-4
Cape Mendocino 4/25/1992	827	NS	1.18	Fortuna - Fortuna Blvd	7.01	19.95	457.06	
Kobe Japan 1/16/1995	1110	NS	1.15	Morigawachi	6.9	24.78	256	E-4
Northridge-01 1/17/1994	974	NS	2.14	Glendale - Las Palmas	6.69	22.21	371.07	
Chi-Chi Taiwan 9/20/1999	1201	NS	1.06	CHY034	7.62	14.82	378.75	A-5
Dinar Turkey 10/1/1995	1141	EW	0.35	Dinar	6.4	3.36	219.75	
Chi-Chi Taiwan 9/20/1999	1202	EW	1.29	CHY035	7.62	12.65	573.04	B-5
Northridge-06 3/20/1994	1728	EW	0.97	Rinaldi Receiving Sta	5.28	12.96	282.25	
Chi-Chi Taiwan 9/20/1999	1202	NS	1.23	CHY035	7.62	12.65	573.04	C-5
Chi-Chi Taiwan-05 9/22/1999	3217	EW	1.98	TCU129	6.2	38.91	511.18	
Chi-Chi Taiwan 9/20/1999	1231	NS	0.34	CHY080	7.62	2.69	496.21	D-5
Chi-Chi Taiwan-06 9/25/1999	3265	EW	0.81	CHY025	6.3	40.33	277.5	
Chi-Chi Taiwan 9/20/1999	1231	EW	0.41	CHY080	7.62	2.69	496.21	E-5
Northridge-06 3/20/1994	3767	EW	2.06	Sylmar - Olive View Med FF	5.28	16.63	440.54	
Chi-Chi Taiwan 9/20/1999	1234	EW	1.76	CHY086	7.62	28.42	665.2	A-6
Tottori Japan 10/6/2000	3908	EW	1.48	OKY005	6.61	28.82	293.37	
Chi-Chi Taiwan 9/20/1999	1508	NS	0.76	TCU072	7.62	7.08	468.14	B-6
Tottori Japan 10/6/2000	3921	EW	2.83	OKYH03	6.61	49.82	316.76	
Chi-Chi Taiwan 9/20/1999	1517	NS	0.32	TCU084	7.62	11.48	665.2	C-6
San Simeon CA 12/22/2003	3994	NS	1.76	San Luis Obispo - Lopez Lake Grounds	6.52	48.11	365.15	
Denali Alaska 11/3/2002	2114	NS	1.11	TAPS Pump Station 10	7.9	2.74	329.4	D-6
Parkfield-02 CA 9/28/2004	4131	EW	1.25	Parkfield - Vineyard Cany 1W	6	2.75	284.21	
Cape Mendocino 4/25/1992	3748	EW	1.32	Ferndale Fire Station	7.01	19.32	387.95	E-6
Niigata Japan 10/23/2004	4171	NS	2.03	GNM003	6.63	63.69	373.23	
Tottori Japan 10/6/2000	3968	EW	0.45	TTRH02	6.61	0.97	310.21	A-7
Sicilia-Orientale Italy 12/13/1990	4331	EW	2.71	Sortino	5.6	26.93	412.59	
Niigata Japan 10/23/2004	4229	NS	2.84	NIGH12	6.63	10.72	564.25	B-7
Umbria Marche (foreshock) Italy 9/26/1997	4337	EW	0.48	Colfiorito	5.7	4.02	317	
Chuetsu-oki 7/16/2007	4853	NS	1.88	Joetsu City	6.8	27.9	294.71	C-7
Umbria Marche Italy 9/26/1997	4351	NS	1.42	Matelica	6	25.24	437	
Chuetsu-oki 7/16/2007	4861	NS	1.35	Nakanoshima Nagaoka	6.8	19.89	319	D-7
Umbria Marche Italy 9/26/1997	4352	EW	0.6	Nocera Umbra	6	8.92	428	
Chuetsu-oki 7/16/2007	4862	NS	1.67	Shiura Nagaoka	6.8	20.17	336.93	E-7
Umbria Marche (aftershock 1) Italy 10/6/1997	4367	EW	2.02	Nocera Umbra	5.5	9.33	428	
Chuetsu-oki 7/16/2007	4862	EW	1.96	Shiura Nagaoka	6.8	20.17	336.93	A-8
Umbria Marche (aftershock 2) Italy 10/14/1997	4385	EW	1.27	Colfiorito	5.6	11.11	317	
Chuetsu-oki 7/16/2007	4863	NS	1.24	Nagaoka	6.8	16.27	514.3	B-8
Umbria Marche (aftershock 2) Italy 10/14/1997	4391	NS	1.1	Norcia-Altavilla	5.6	18.35	218	
Iwate 6/13/2008	5778	EW	1.42	Matsuyama City	6.9	40.98	436.34	C-8
Chuetsu-oki 7/16/2007	4881	NS	2.92	Nagaoka Kouiti Town	6.8	20.77	294.38	
Iwate 6/13/2008	5778	NS	1.92	Matsuyama City	6.9	40.98	436.34	D-8
Iwate 6/13/2008	5472	NS	2.21	AKT017	6.9	33.76	643.62	
El Mayor-Cucapah 4/4/2010	5991	EW	0.95	El Centro Array 10	7.2	20.05	202.85	E-8
Christchurch New Zealand 2/21/2011	8123	NS	0.24	Christchurch Resthaven	6.2	5.13	141	

Table B.10: Spectra for Period 0.87, Amp 2.0

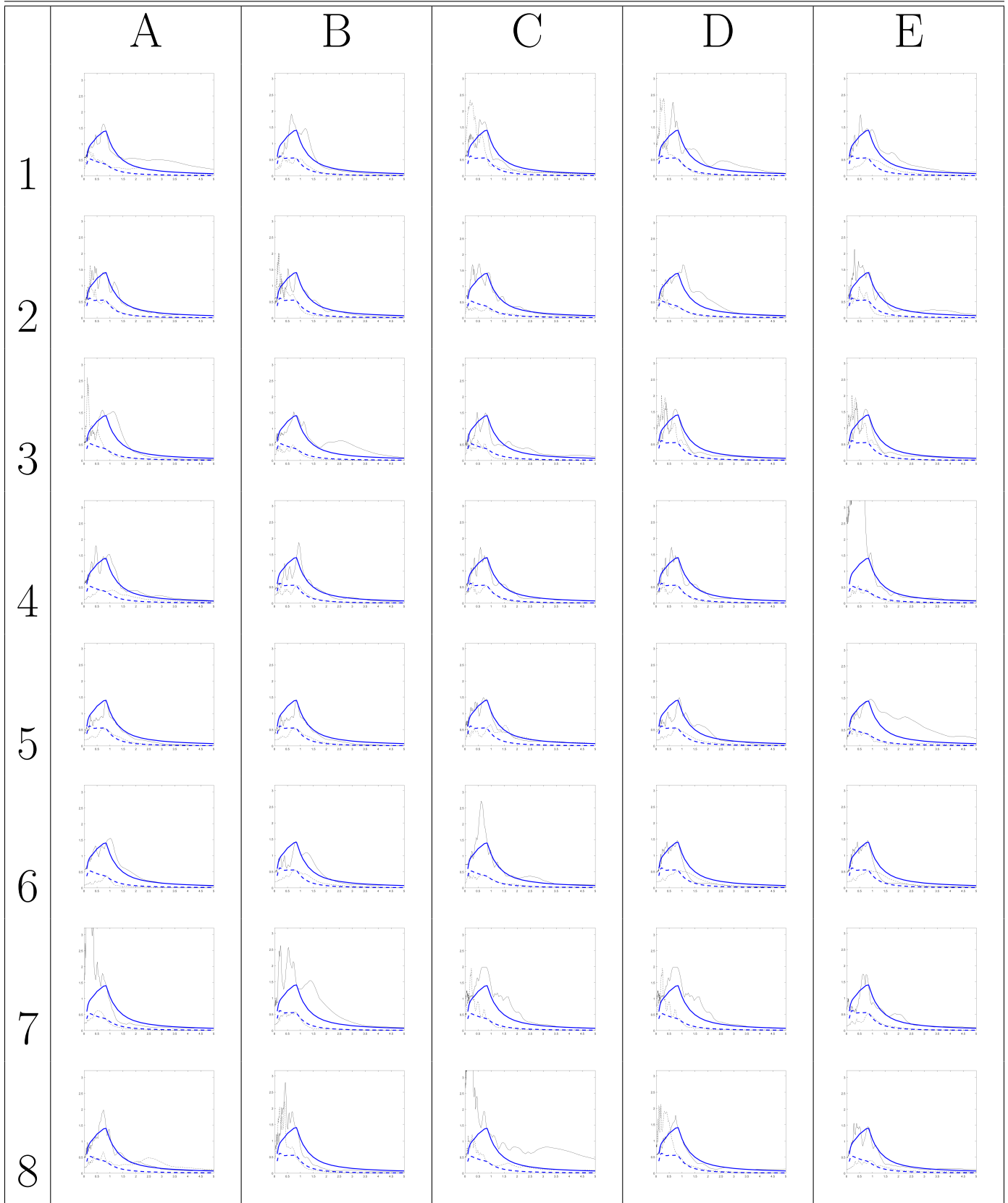


Table B.11: Details for Period 0.87, Amp 2.0

Mainshock Name Aftershock Name	RSN RSN	Direction Direction	Scale Scale	Mainshock Station Aftershock Station	Mag Adj. Mag	Rjb Rjb	Vs30 Vs30	Spec
Imperial Valley-06 10/15/1979	182	EW	1.19	El Centro Array 7	6.53	0.56	210.51	A-1
Imperial Valley-06 10/15/1979	178	NS	0.88	El Centro Array 3	6.53	12.85	162.94	
Loma Prieta 10/18/1989	732	NS	2.05	APEEL 2 - Redwood City	6.93	43.23	133.11	B-1
Mammoth Lakes-01 5/25/1980	232	EW	2.84	Mammoth Lakes H. S.	6.06	4.67	346.82	
Loma Prieta 10/18/1989	753	EW	1.22	Corralitos	6.93	3.85	462.24	C-1
Mammoth Lakes-04 5/25/1980	243	NS	1.42	Long Valley Dam (Upr L Abut)	5.7	14.38	537.16	
Loma Prieta 10/18/1989	759	EW	1.71	Foster City - APEEL 1	6.93	43.94	116.35	D-1
Coalinga-05 7/22/1983	406	EW	2.23	Coalinga-14th Elm (Old CHP)	5.77	10.78	286.41	
Loma Prieta 10/18/1989	776	NS	1.42	Hollister - South Pine	6.93	27.93	282.14	E-1
Coalinga-05 7/22/1983	408	EW	2.02	Oil Fields Fire Station - FF	5.77	11.1	474.15	
Landers 6/28/1992	864	NS	2.04	Joshua Tree	7.28	11.03	379.32	A-2
Coalinga-05 7/22/1983	413	NS	1.57	Skunk Hollow	5.77	11.71	480.32	
Northridge-01 1/17/1994	953	NS	1.01	Beverly Hills - 14145 Mulhol	6.69	17.15	355.81	B-2
Morgan Hill 4/24/1984	450	EW	1.93	Corralitos	6.19	23.24	462.24	
Northridge-01 1/17/1994	963	EW	1.2	Castaic - Old Ridge Route	6.69	20.72	450.28	C-2
N. Palm Springs 7/8/1986	523	NS	2.75	Indio - Coachella Canal	6.06	41.93	339.02	
Northridge-01 1/17/1994	982	EW	0.88	Jensen Filter Plant	6.69	5.43	373.07	D-2
Whittier Narrows-01 10/1/1987	589	NS	0.8	Alhambra - Fremont School	5.99	14.66	549.75	
Northridge-01 1/17/1994	1052	NS	2.02	Pacoima Kagel Canyon	6.69	7.26	508.08	E-2
Whittier Narrows-01 10/1/1987	611	EW	1.25	Compton - Castlegate St	5.99	23.37	266.9	
Northridge-01 1/17/1994	1054	NS	1.01	Pardee - SCE	6.69	7.46	325.67	A-3
Whittier Narrows-01 10/1/1987	614	NS	2.31	Downey - Birchdale	5.99	20.79	245.06	
Northridge-01 1/17/1994	1084	NS	0.85	Sylmar - Converter Sta	6.69	5.35	251.24	B-3
Whittier Narrows-01 10/1/1987	615	EW	1.16	Downey - Co Maint Bldg	5.99	20.82	271.9	
Kobe Japan 1/16/1995	1101	EW	1.23	Amagasaki	6.9	11.34	256	C-3
Whittier Narrows-01 10/1/1987	648	EW	1.28	La Crescenta - New York	5.99	26.04	411.55	
Kobe Japan 1/16/1995	1106	NS	0.74	KJMA	6.9	0.96	312	D-3
Whittier Narrows-01 10/1/1987	649	NS	2.36	La Habra - Briarcliff	5.99	20.28	338.27	
Kobe Japan 1/16/1995	1106	EW	0.76	KJMA	6.9	0.96	312	E-3
Loma Prieta 10/18/1989	772	NS	1	Halls Valley	6.93	30.49	281.61	
Chi-Chi Taiwan 9/20/1999	1182	NS	1.69	CHY006	7.62	9.76	438.19	A-4
Loma Prieta 10/18/1989	777	EW	0.58	Hollister City Hall	6.93	27.6	198.77	
Chi-Chi Taiwan 9/20/1999	1201	NS	1.42	CHY034	7.62	14.82	378.75	B-4
Erzican Turkey 3/13/1992	821	NS	0.43	Erzincan	6.69	4.38	352.05	
Chi-Chi Taiwan 9/20/1999	1202	EW	1.71	CHY035	7.62	12.65	573.04	C-4
Northridge-01 1/17/1994	953	NS	0.27	Beverly Hills - 14145 Mulhol	6.69	17.15	355.81	
Chi-Chi Taiwan 9/20/1999	1202	NS	1.64	CHY035	7.62	12.65	573.04	D-4
Northridge-01 1/17/1994	974	NS	2.85	Glendale - Las Palmas	6.69	22.21	371.07	
Chi-Chi Taiwan 9/20/1999	1205	EW	3.94	CHY041	7.62	19.83	492.26	E-4
Northridge-04 1/17/1994	1676	EW	1.54	Castaic - Old Ridge Route	5.93	25.17	450.28	
Chi-Chi Taiwan 9/20/1999	1231	EW	0.55	CHY080	7.62	2.69	496.21	A-5
Northridge-06 3/20/1994	1728	EW	1.29	Rinaldi Receiving Sta	5.28	12.96	282.25	
Chi-Chi Taiwan 9/20/1999	1231	NS	0.46	CHY080	7.62	2.69	496.21	B-5
Chi-Chi Taiwan-02 9/20/1999	2382	NS	0.93	TCU065	5.9	33.48	305.85	
Chi-Chi Taiwan 9/20/1999	1508	NS	1.01	TCU072	7.62	7.08	468.14	C-5
Chi-Chi Taiwan-04 9/20/1999	2739	NS	1.08	CHY080	6.2	12.53	496.21	
Chi-Chi Taiwan 9/20/1999	1517	NS	0.42	TCU084	7.62	11.48	665.2	D-5
Chi-Chi Taiwan-05 9/22/1999	3220	EW	2.21	TCU138	6.2	47.51	652.85	
Denali Alaska 11/3/2002	2114	NS	1.48	TAPS Pump Station 10	7.9	2.74	329.4	E-5
Chi-Chi Taiwan-06 9/25/1999	3472	EW	1.63	TCU076	6.3	25.85	614.98	
Loma Prieta 10/18/1989	3548	NS	1.27	Los Gatos - Lexington Dam	6.93	5.02	1070.34	A-6
Chi-Chi Taiwan-06 9/25/1999	3505	EW	0.54	TCU125	6.3	25.66	397.57	
Cape Mendocino 4/25/1992	3748	EW	1.76	Ferndale Fire Station	7.01	19.32	387.95	B-6
Lazio Abruzzo Italy 5/7/1984	3605	NS	1.21	Cassino-Sant' Elia	5.8	24.4	436.79	
Landers 6/28/1992	3754	NS	2.36	Indio - Jackson Road	7.28	48.84	292.12	C-6
Parkfield-02 CA 9/28/2004	4113	EW	1.55	Parkfield - Fault Zone 9	6	2.85	372.26	
Tottori Japan 10/6/2000	3968	EW	0.61	TTRH02	6.61	0.97	310.21	D-6
Parkfield-02 CA 9/28/2004	4114	EW	1.98	Parkfield - Fault Zone 11	6	4	541.73	
Tottori Japan 10/6/2000	3968	NS	0.63	TTRH02	6.61	0.97	310.21	E-6
Parkfield-02 CA 9/28/2004	4115	NS	0.36	Parkfield - Fault Zone 12	6	2.65	265.21	
Niigata Japan 10/23/2004	4229	NS	3.79	NIGHT	6.63	10.72	564.25	A-7
Friuli (aftershock 9) Italy 9/11/1976	4276	NS	0.97	Buia	5.5	12.39	310.68	
Montenegro Yugo. 4/15/1979	4451	NS	1.4	Bar-Skupstina Opstine	7.1	6.98	462.23	B-7
Umbria Marche Italy 9/26/1997	4352	NS	0.93	Nocera Umbra	6	8.92	428	
Chuetsu-oki 7/16/2007	4853	EW	1.81	Joetsu City	6.8	27.9	294.71	C-7
Umbria Marche (aftershock 1) Italy 10/6/1997	4367	EW	2.65	Nocera Umbra	5.5	9.33	428	
Chuetsu-oki 7/16/2007	4853	NS	2.51	Joetsu City	6.8	27.9	294.71	D-7
Iwate 6/13/2008	5620	EW	1.82	IWT012	6.9	20.64	264.48	
Chuetsu-oki 7/16/2007	4861	NS	1.8	Nakanoshima Nagaoka	6.8	19.89	319	E-7
Iwate 6/13/2008	5658	EW	0.58	IWTH26	6.9	6.02	371.06	
Chuetsu-oki 7/16/2007	4863	NS	1.66	Nagaoka	6.8	16.27	514.3	A-8
Darfield New Zealand 9/3/2010	6888	NS	0.91	Christchurch Cathedral College	7	19.89	198	
Chuetsu-oki 7/16/2007	4886	NS	1.16	Tamati Yone Izumozaki	6.8	11.48	338.32	B-8
Darfield New Zealand 9/3/2010	6952	EW	0.62	Papanui High School	7	18.73	263.2	
Iwate 6/13/2008	5663	NS	3.48	MYG004	6.9	20.18	479.37	C-8
Darfield New Zealand 9/3/2010	6961	EW	2.64	RKAC	7	16.47	295.74	
Iwate 6/13/2008	5778	EW	1.89	Matsuyama City	6.9	40.98	436.34	D-8
Christchurch New Zealand 2/21/2011	8118	NS	0.66	Papanui High School	6.2	9.06	263.2	
El Mayor-Cucapah 4/4/2010	5991	EW	1.26	El Centro Array 10	7.2	20.05	202.85	E-8
Christchurch New Zealand 2/21/2011	8123	NS	0.33	Christchurch Resthaven	6.2	5.13	141	

Table B.11: Spectra for Period 0.87, Amp 3.0

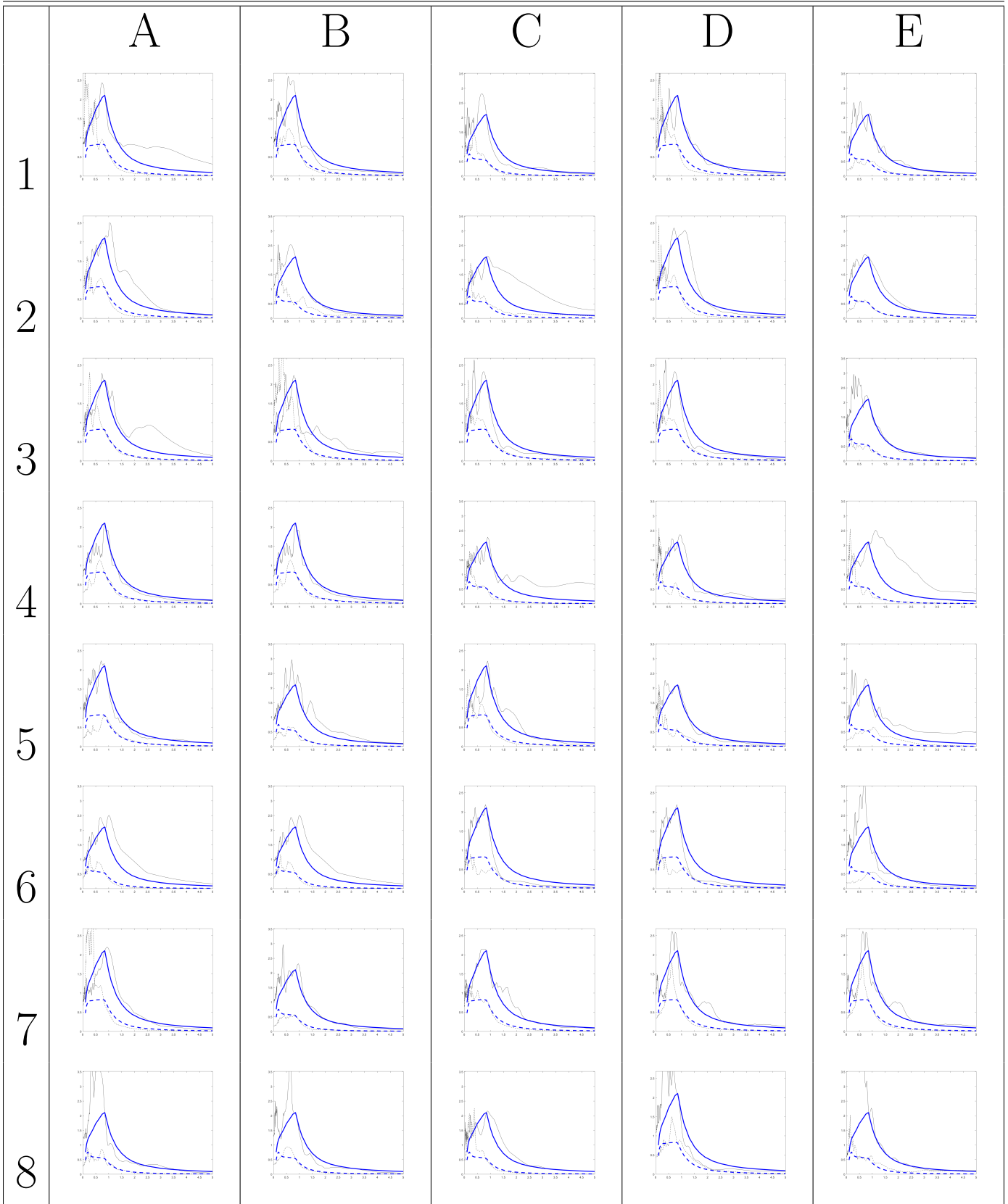


Table B.15: Spectra for Period 1.3, Amp 0.1

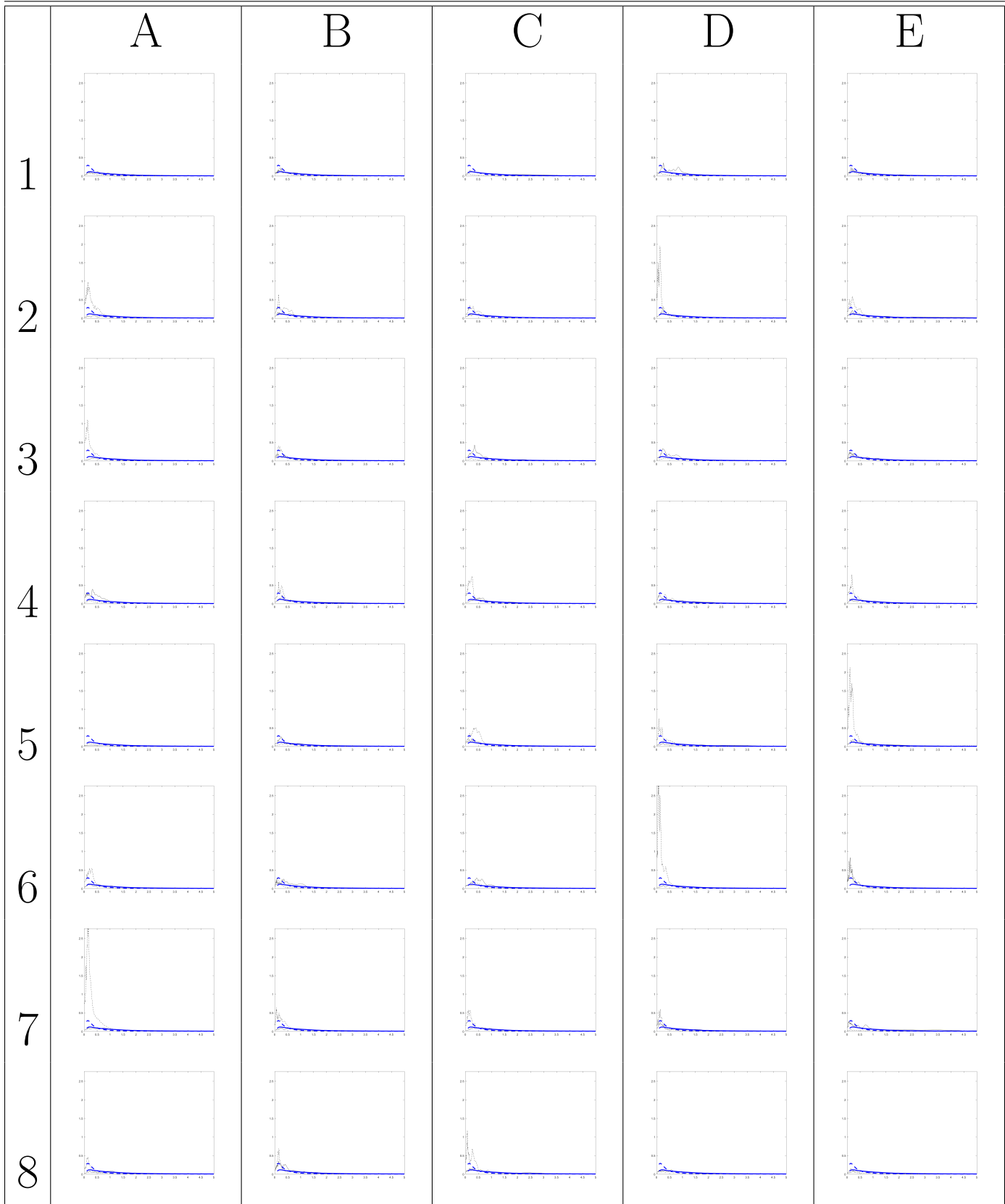


Table B.15: Spectra for Period 1.3, Amp 0.25

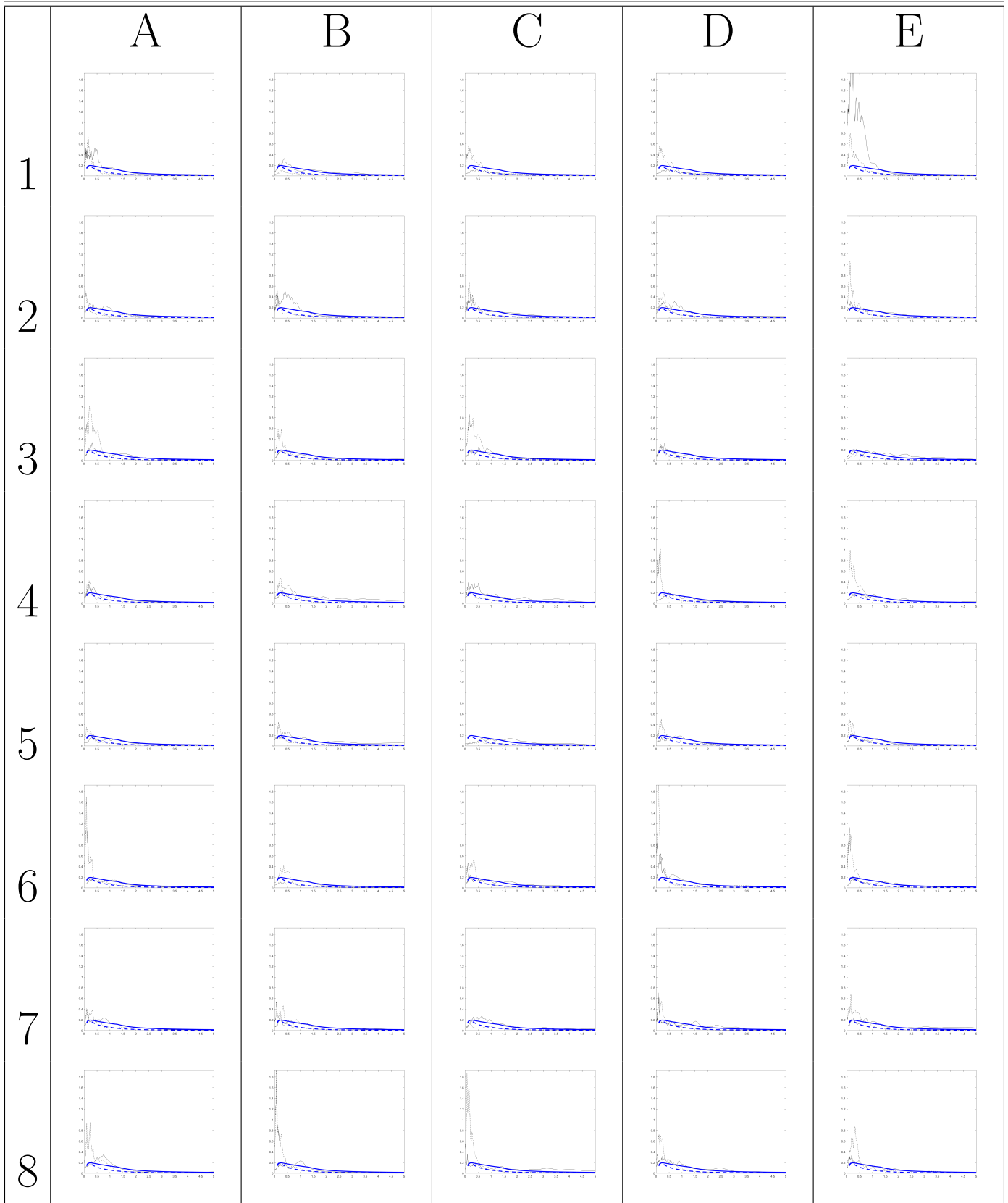


Table B.12: Spectra for Period 1.3, Amp 0.5

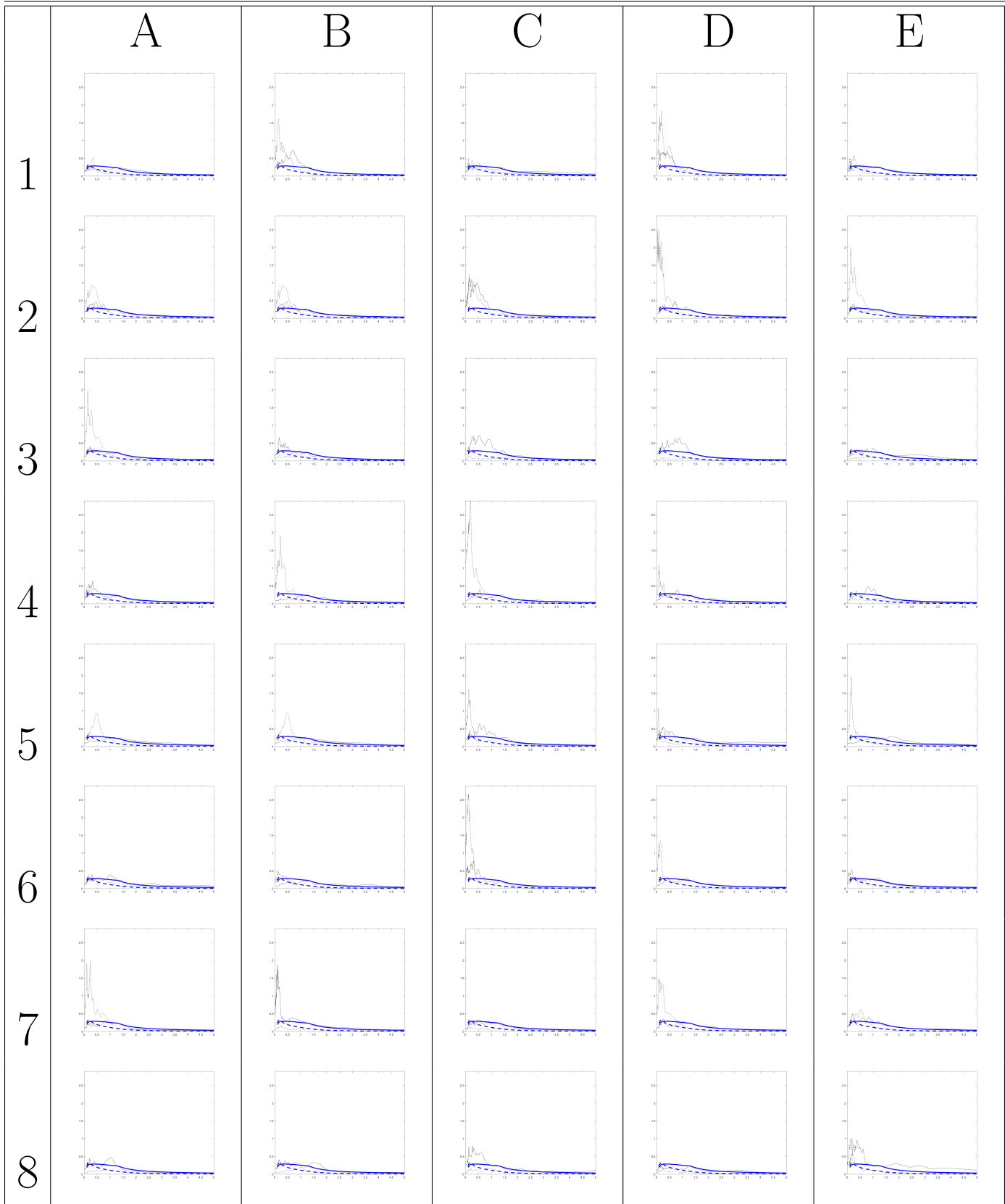


Table B.13: Spectra for Period 1.3, Amp 0.75

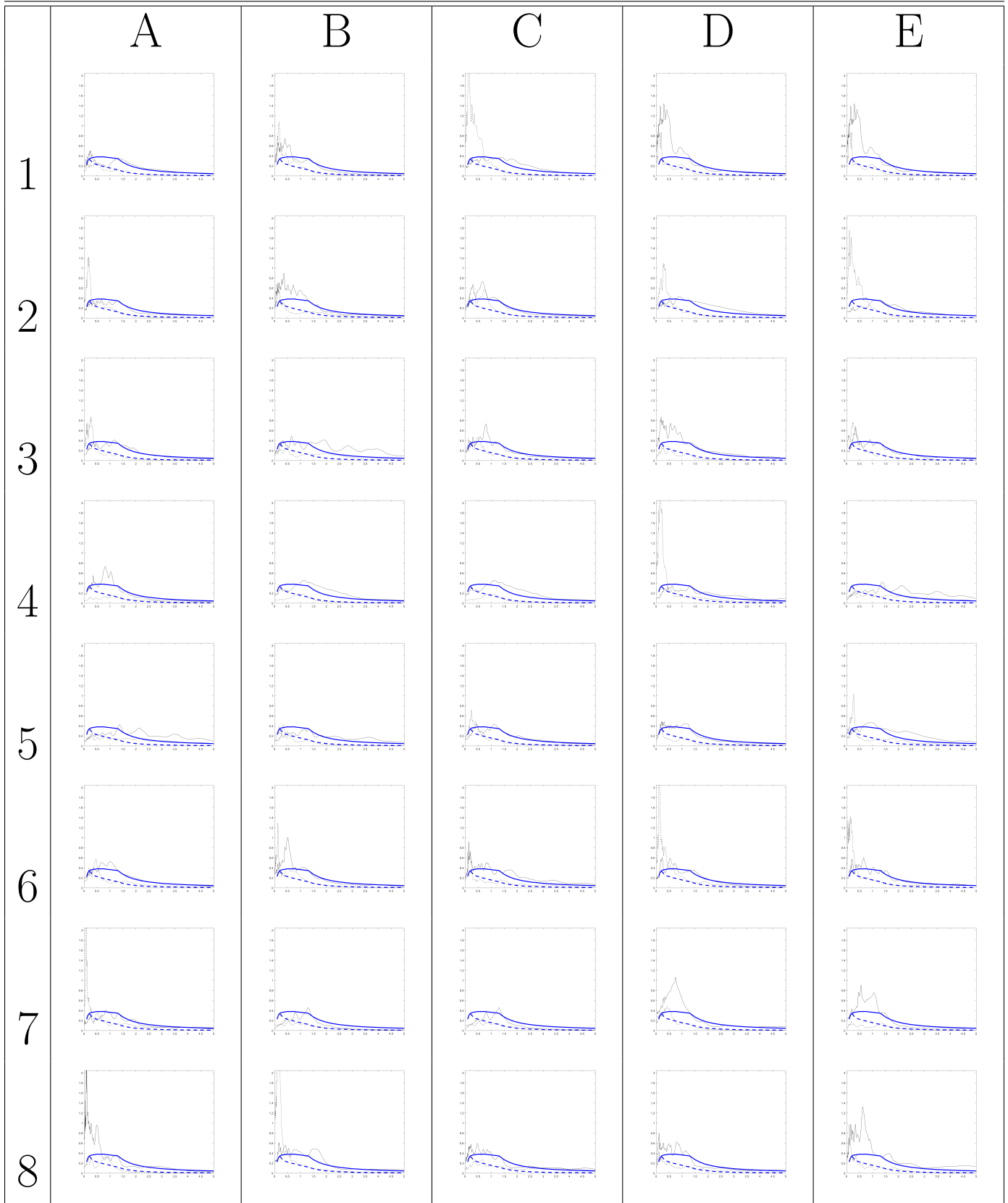


Table B.14: Spectra for Period 1.3, Amp 1.0

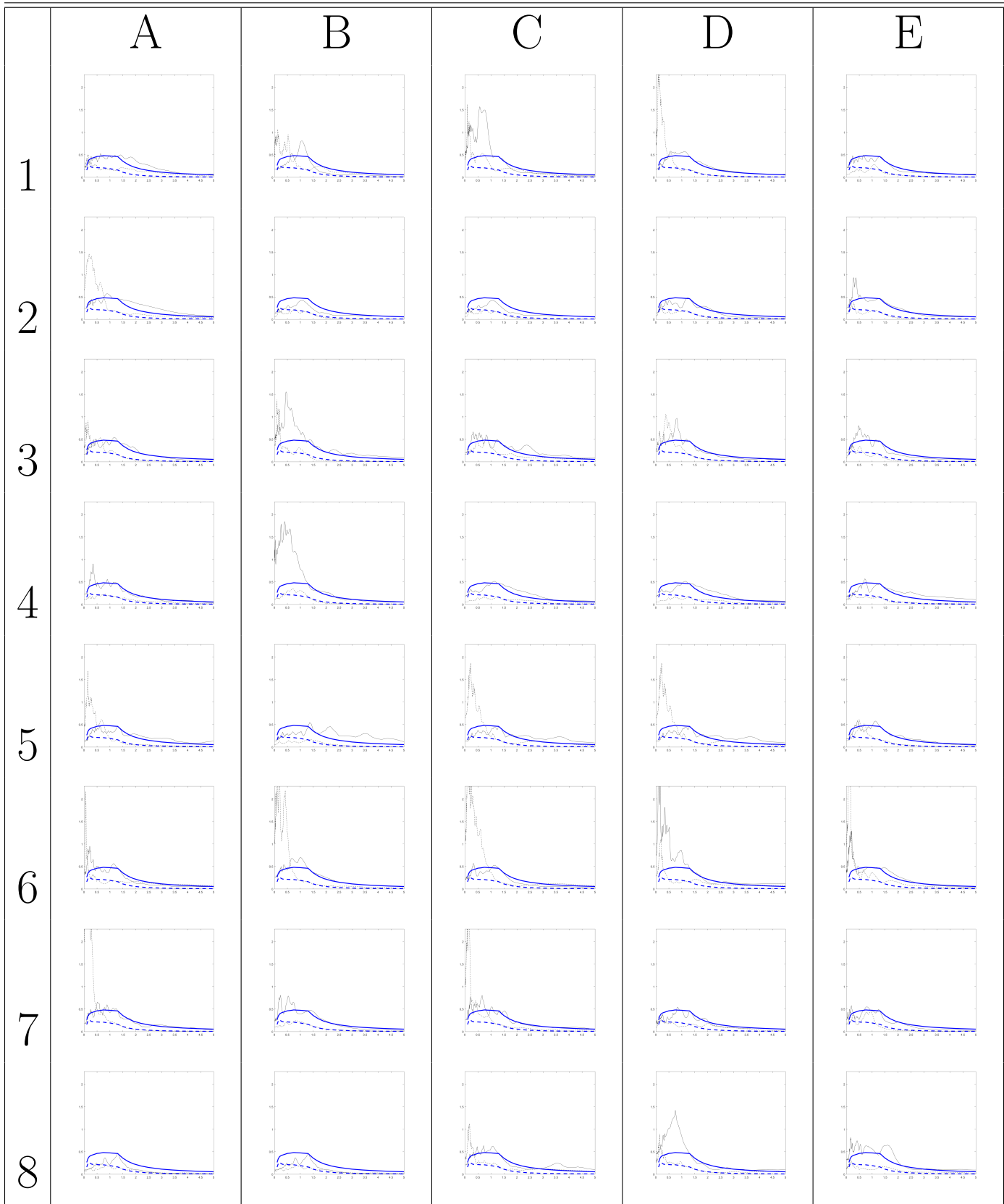


Table B.15: Spectra for Period 1.3, Amp 1.25

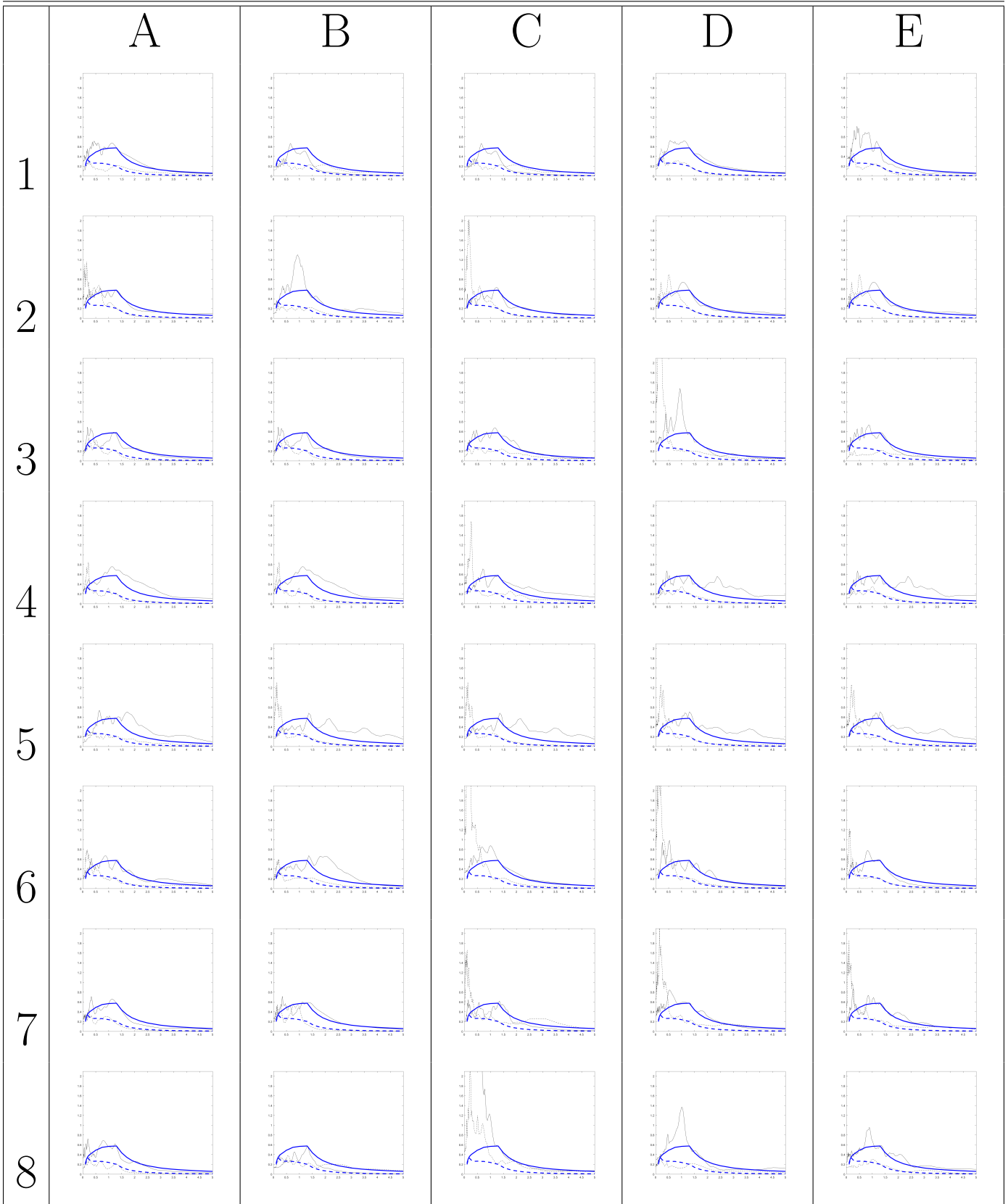


Table B.16: Spectra for Period 1.3, Amp 1.5

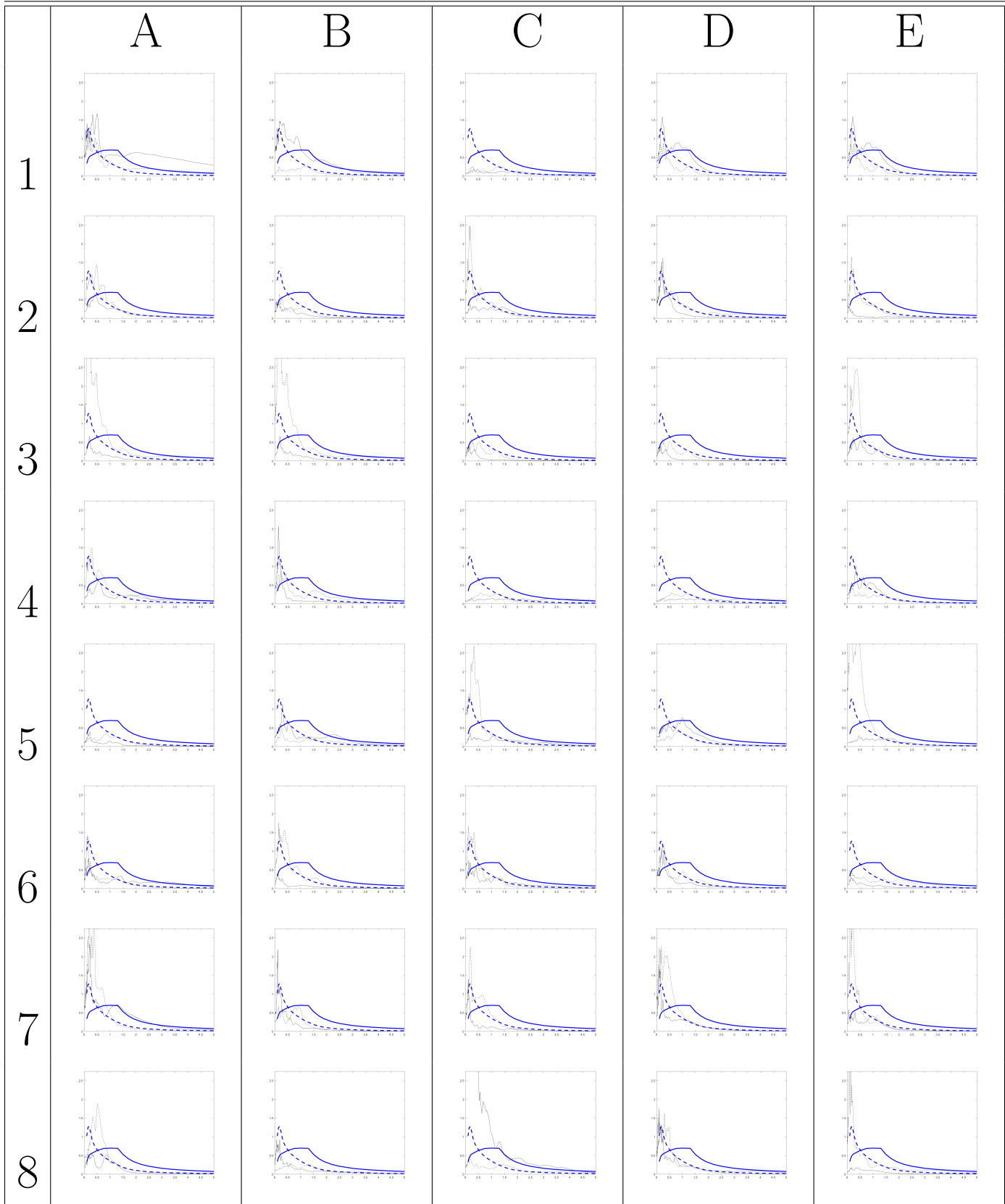


Table B.17: Spectra for Period 1.3, Amp 2.0

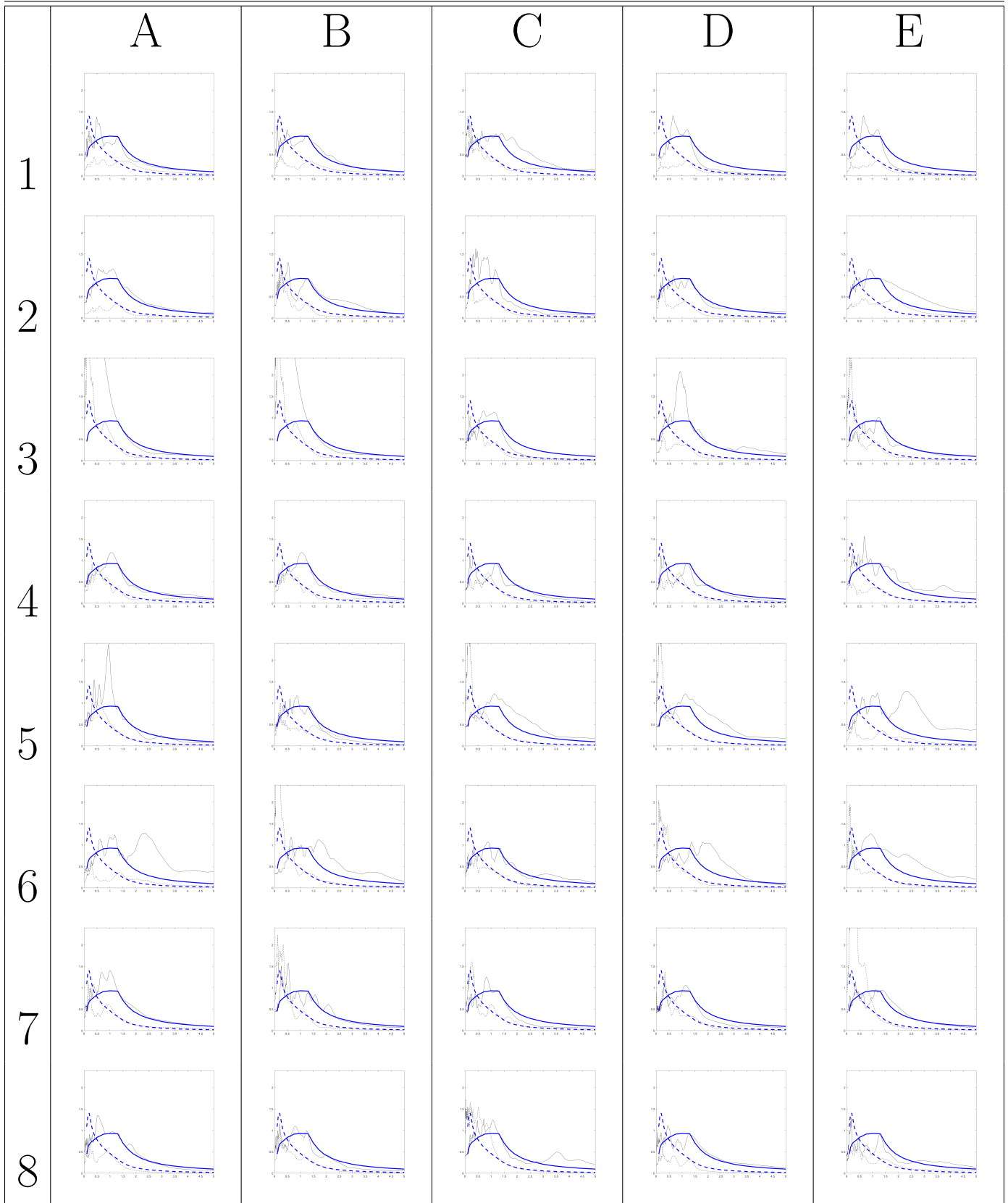


Table B.18: Spectra for Period 1.3, Amp 3.0

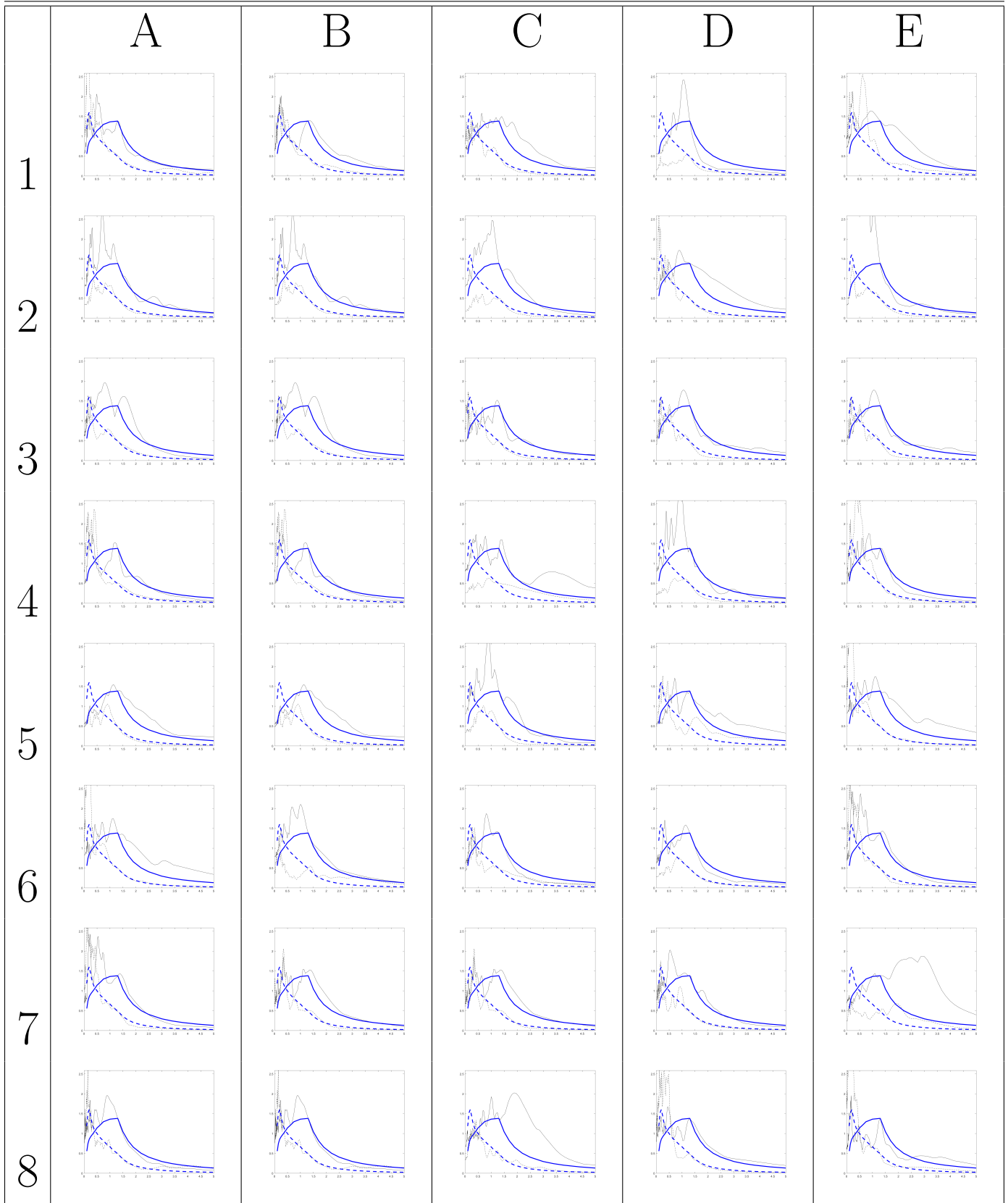


Table B.22: Spectra for Period 2.8, Amp 0.1

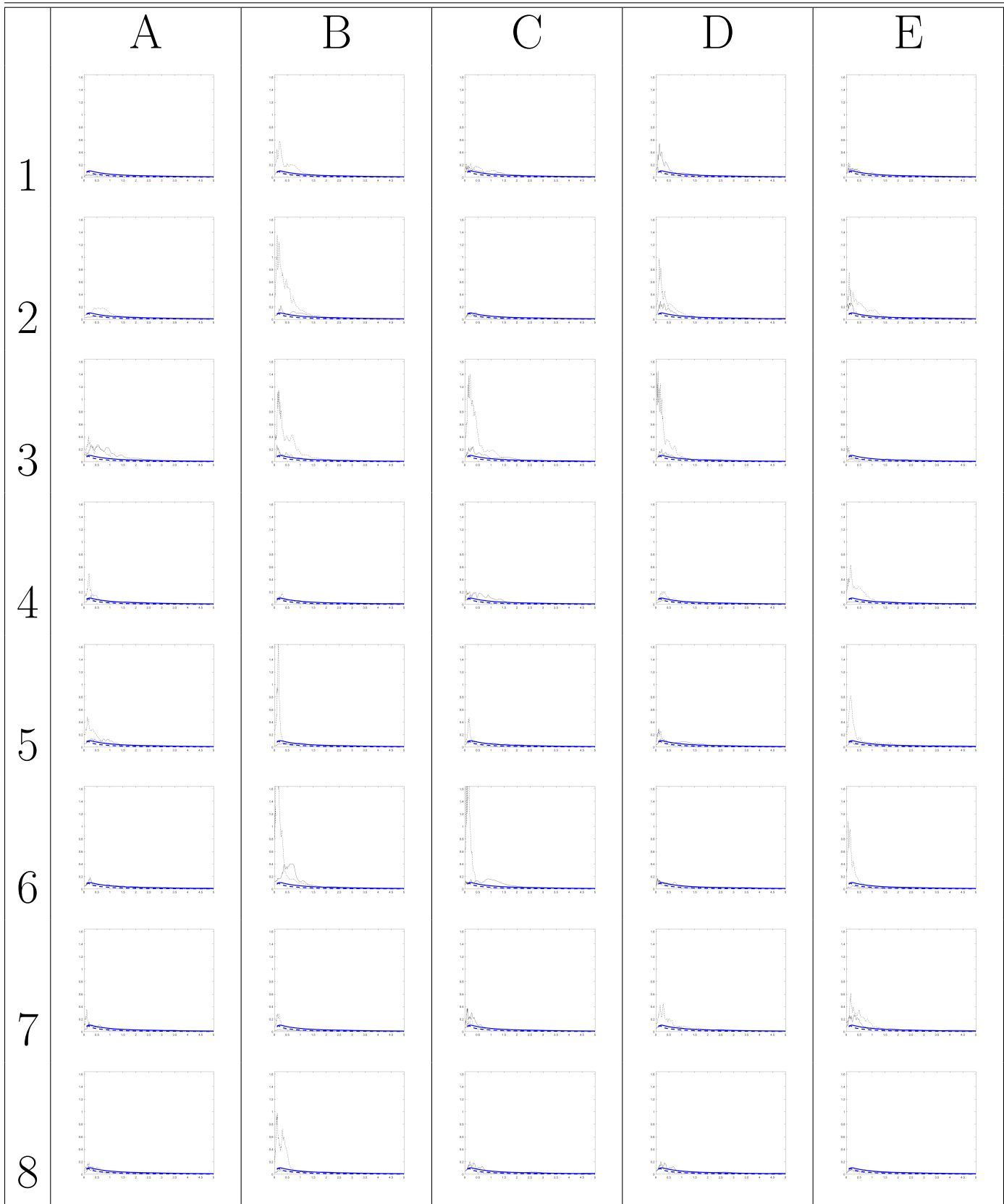


Table B.20: Spectra for Period 2.8, Amp 0.25

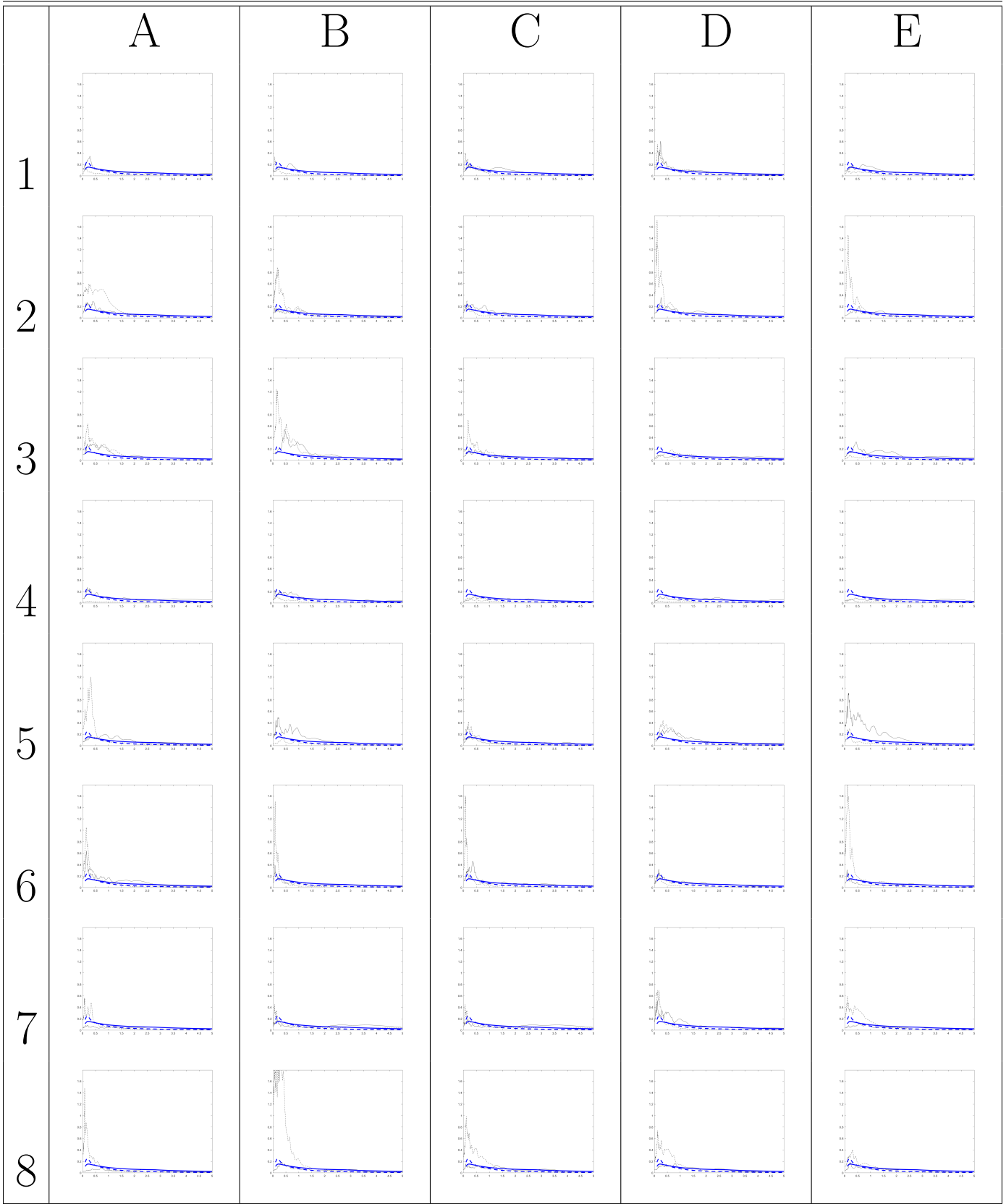


Table B.19: Spectra for Period 2.8, Amp 0.5

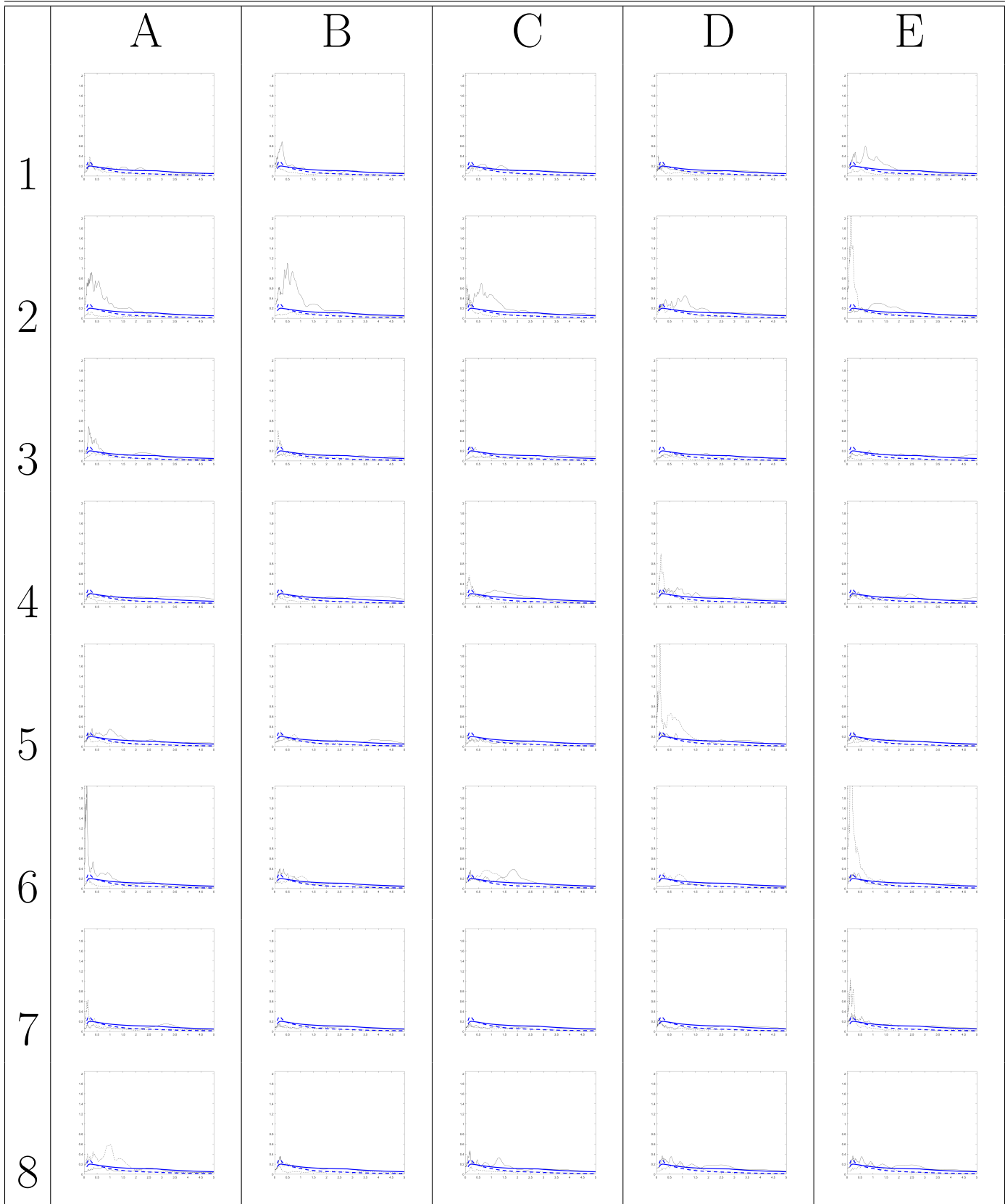


Table B.20: Spectra for Period 2.8, Amp 0.75

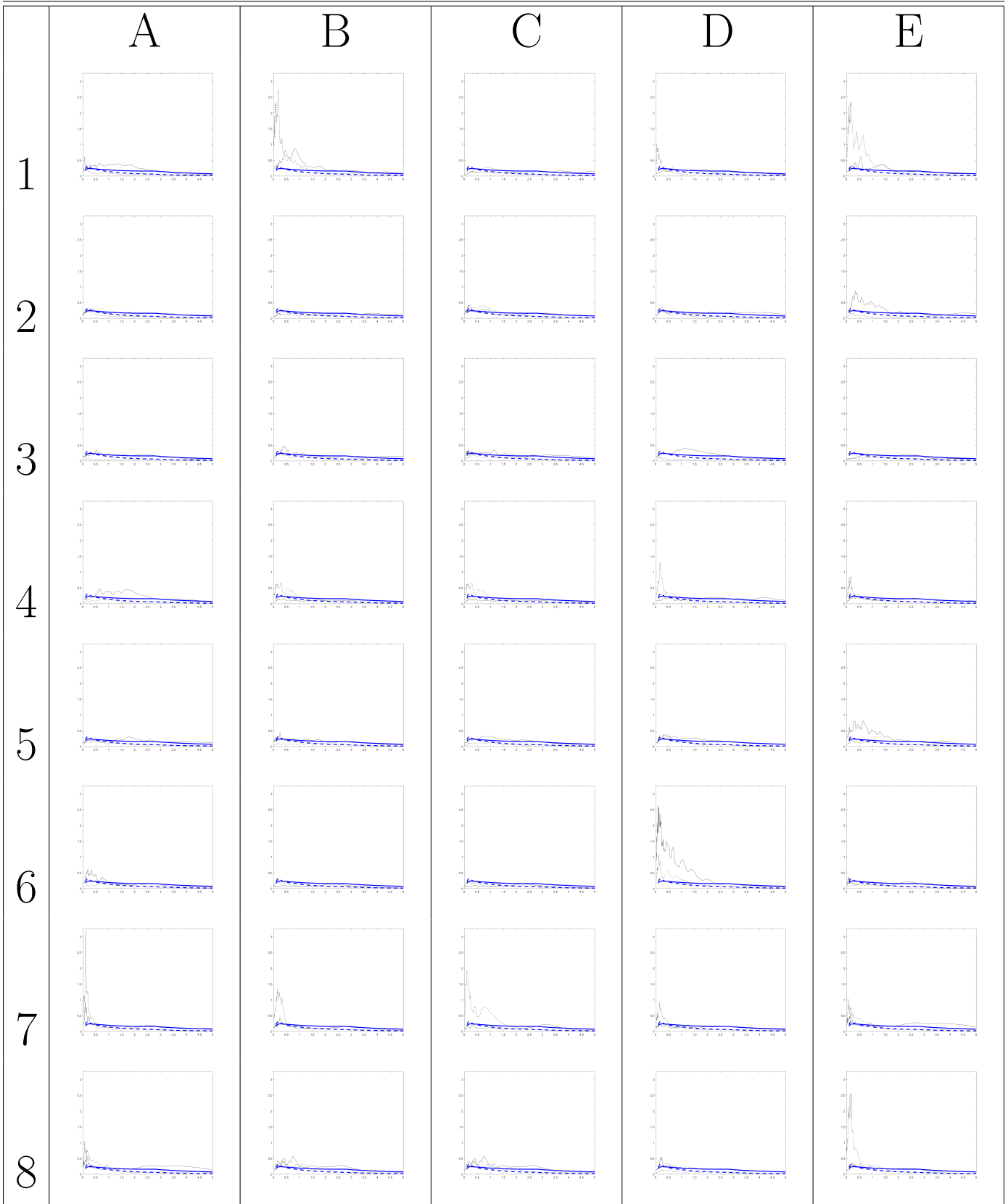


Table B.21: Spectra for Period 2.8, Amp 1.0

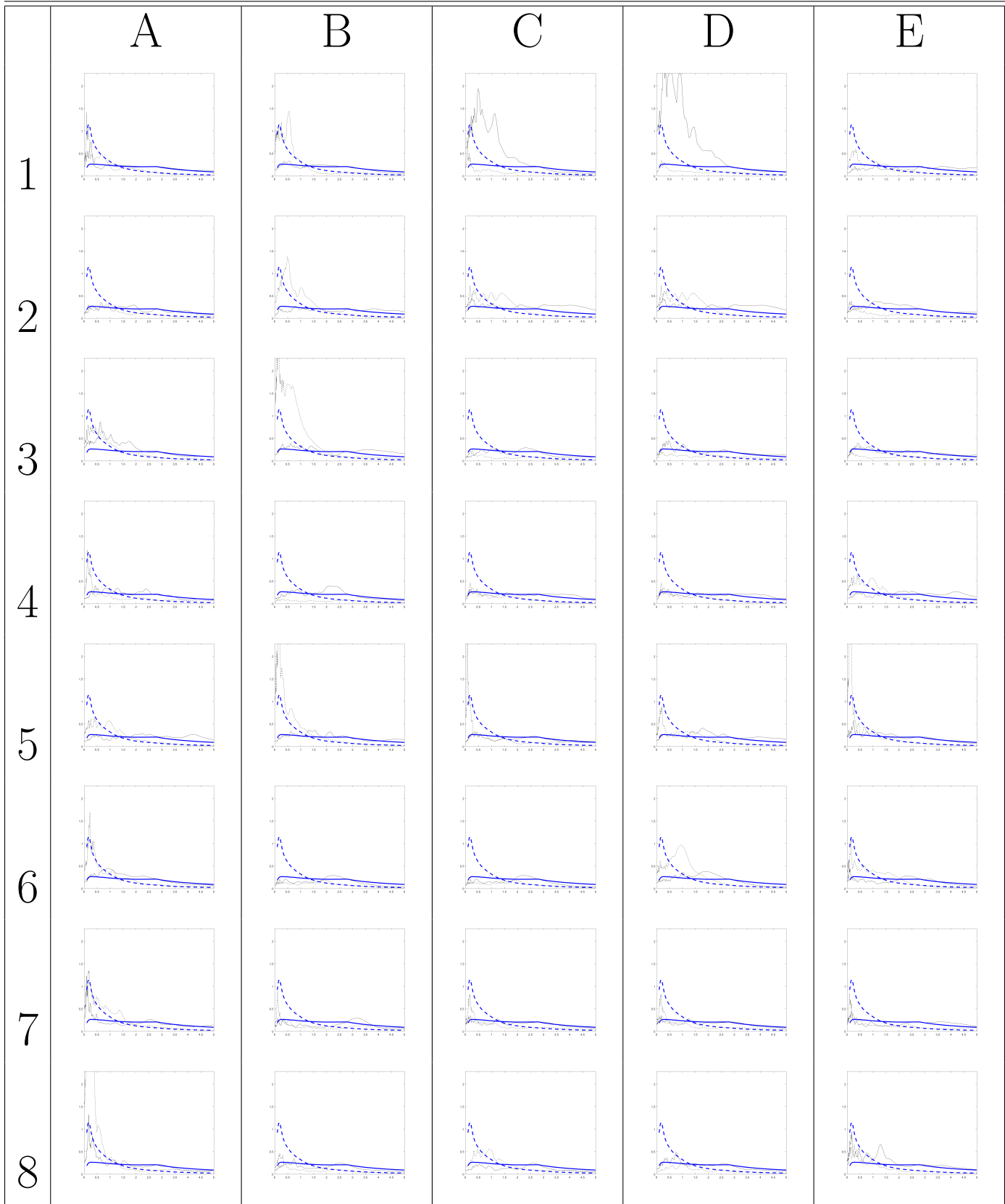


Table B.22: Spectra for Period 2.8, Amp 1.25

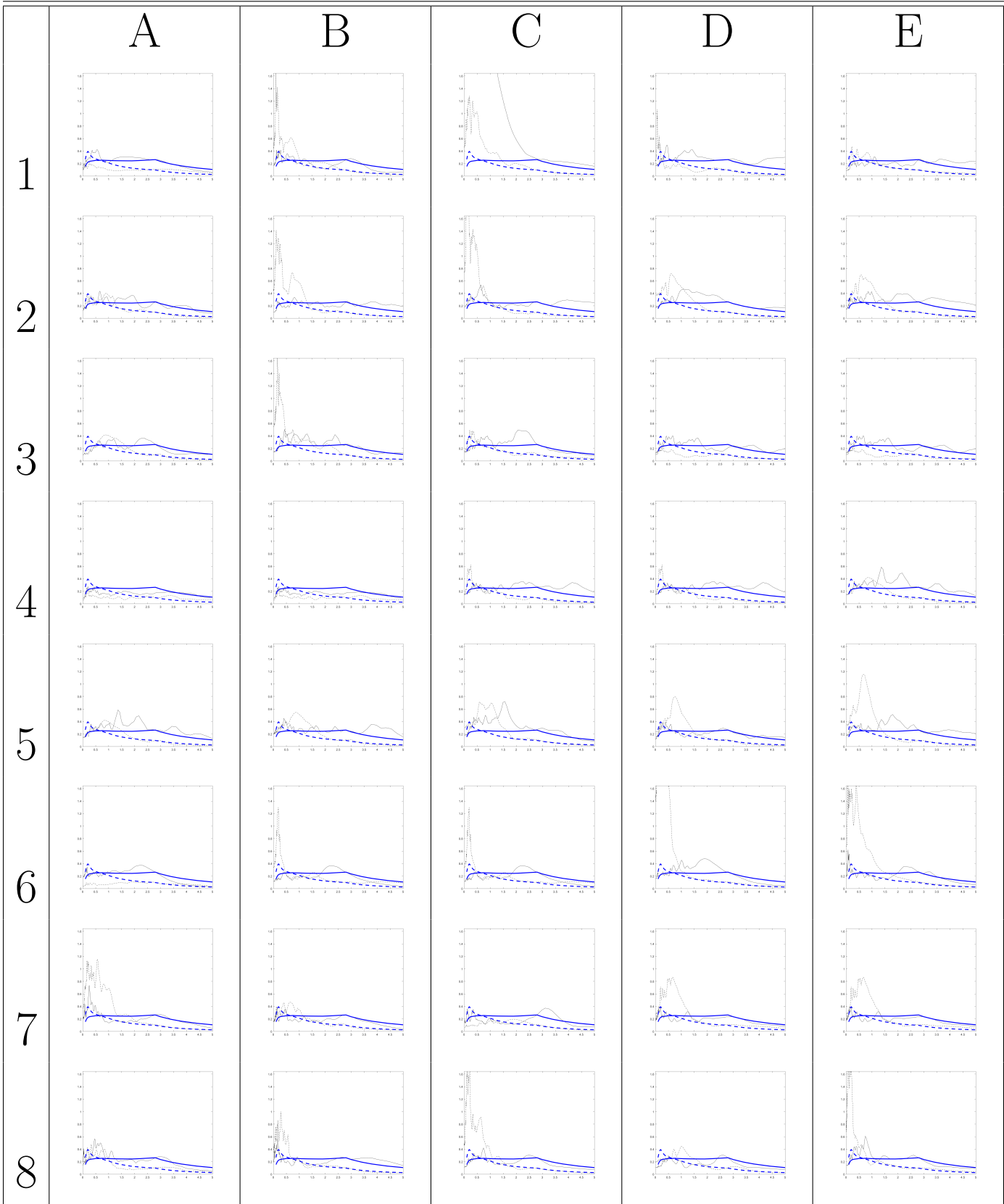


Table B.23: Spectra for Period 2.8, Amp 1.5

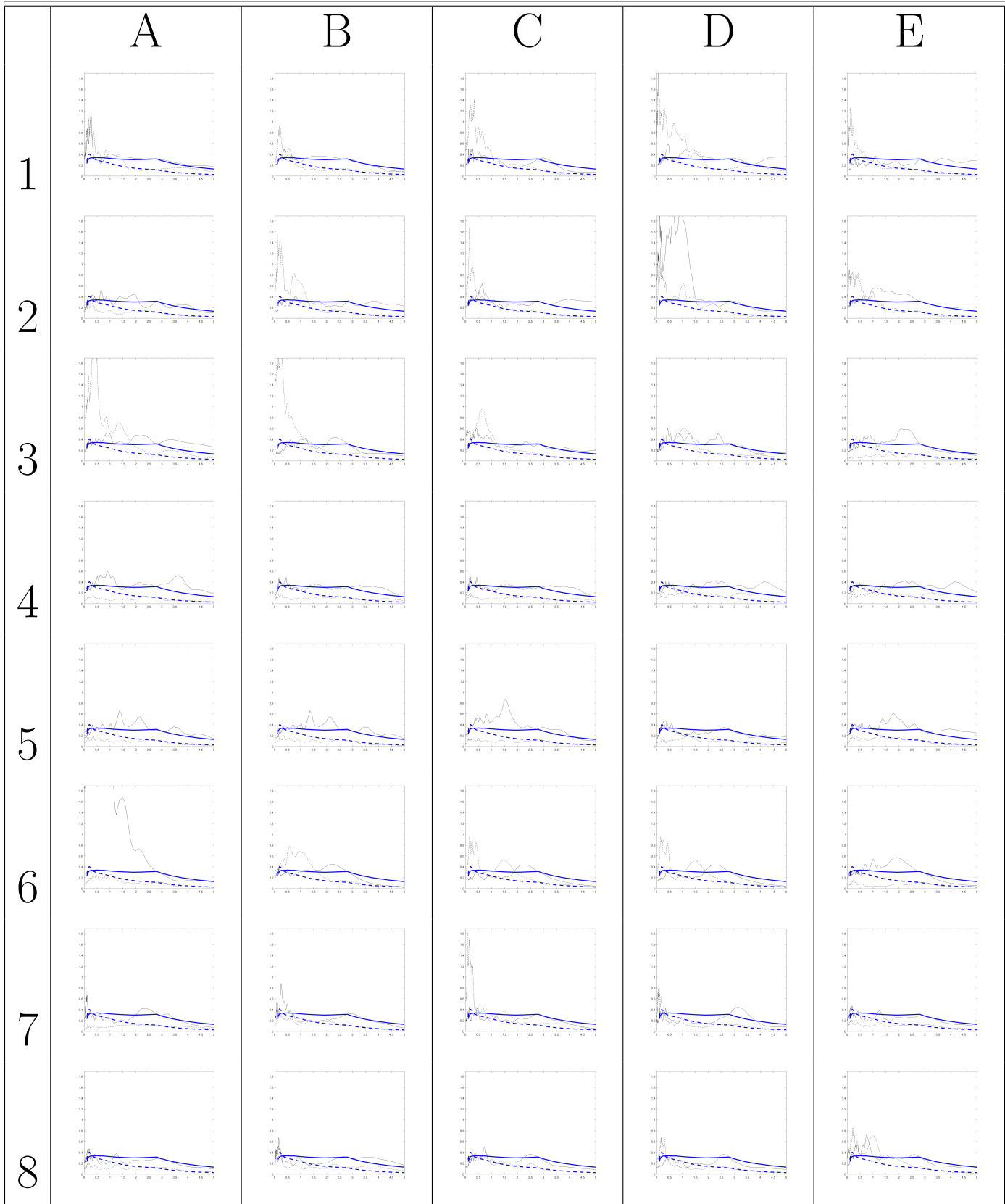


Table B.24: Details for Period 2.8, Amp 1.5

Mainshock Name Aftershock Name	RSN RSN	Direction Direction	Scale Scale	Mainshock Station Aftershock Station	Mag Adj. Mag	Rjb Rjb	Vs30 Vs30	Spec
Imperial Valley-06 10/15/1979 San Fernando 2/9/1971	161 68	NS NS	1.89 1.37	Brawley Airport LA - Hollywood Stor FF	6.53 6.61	10.42 22.77	208.71 316.46	A-1
Imperial Valley-06 10/15/1979 San Fernando 2/9/1971	171 93	EW EW	0.69 2.34	El Centro - Meloland Geot. Array Whittier Narrows Dam	6.53 6.61	0.07 39.45	264.57 298.68	B-1
Loma Prieta 10/18/1989 Managua Nicaragua-01 12/23/1972	806 95	NS NS	0.98 1.24	Sunnyvale - Colton Ave. Managua ESSO	6.93 6.24	24.23 4.06	267.71 288.77	C-1
Chi-Chi Taiwan 9/20/1999 Gazli USSR 5/17/1976	1180 126	EW NS	1.77 0.83	CHY002 Karaky	7.62 6.8	24.96 5.46	235.13 259.59	D-1
Chi-Chi Taiwan 9/20/1999 Westmorland 4/26/1981	1195 314	NS NS	1.37 1.97	CHY026 Brawley Airport	7.62 5.9	29.52 15.41	226.01 208.71	E-1
Chi-Chi Taiwan 9/20/1999 Coalinga-03 6/11/1983	1199 393	NS NS	1.73 2.73	CHY032 Sulphur Baths (temp)	7.62 5.38	35.43 13.32	192.71 617.43	A-2
Chi-Chi Taiwan 9/20/1999 Coalinga-05 7/22/1983	1238 408	EW NS	1.16 2.39	CHY092 Oil Fields Fire Station - FF	7.62 5.77	22.69 11.1	253.72 474.15	B-2
Chi-Chi Taiwan 9/20/1999 Morgan Hill 4/24/1984	1477 457	NS NS	1.91 2.09	TCU031 Gilroy Array 3	7.62 6.19	30.17 13.02	489.22 349.85	C-2
Chi-Chi Taiwan 9/20/1999 N. Palm Springs 7/8/1986	1487 522	NS EW	2.35 2.73	TCU047 Indio	7.62 6.06	35 35.57	520.37 307.54	D-2
Chi-Chi Taiwan 9/20/1999 Superstition Hills-02 11/24/1987	1492 719	NS NS	0.58 2.74	TCU052 Brawley Airport	7.62 6.54	0.66 17.03	579.1 208.71	E-2
Chi-Chi Taiwan 9/20/1999 Loma Prieta 10/18/1989	1501 768	EW NS	1.3 1.91	TCU063 Gilroy Array 4	7.62 6.93	9.78 14.34	476.14 221.78	A-3
Chi-Chi Taiwan 9/20/1999 Cape Mendocino 4/25/1992	1529 825	EW NS	0.7 0.68	TCU102 Cape Mendocino	7.62 7.01	1.49 6.96	714.27 567.78	B-3
Chi-Chi Taiwan 9/20/1999 Cape Mendocino 4/25/1992	1533 828	EW EW	1.24 0.5	TCU106 Petrolia	7.62 7.01	14.97 8.18	451.37 422.17	C-3
Chi-Chi Taiwan 9/20/1999 Kobe Japan 1/16/1995	1534 1114	EW EW	1.17 0.66	TCU107 Port Island (0 m)	7.62 6.9	15.99 3.31	409 198	D-3
Chi-Chi Taiwan 9/20/1999 Chi-Chi Taiwan-03 9/20/1999	1536 2459	NS NS	0.92 1.34	TCU110 CHY026	7.62 6.2	11.58 38.88	212.72 226.01	E-3
Chi-Chi Taiwan 9/20/1999 Chi-Chi Taiwan-03 9/20/1999	1537 2464	NS NS	1.58 1.36	TCU111 CHY033	7.62 6.2	22.12 63.6	237.53 197.63	A-4
Chi-Chi Taiwan 9/20/1999 Chi-Chi Taiwan-03 9/20/1999	1538 2492	NS NS	1.42 2.58	TCU112 CHY076	7.62 6.2	27.48 59.62	190.54 169.84	B-4
Chi-Chi Taiwan 9/20/1999 Chi-Chi Taiwan-03 9/20/1999	1538 2497	EW NS	2.11 2.27	TCU112 CHY082	7.62 6.2	27.48 50.53	190.54 193.69	C-4
Chi-Chi Taiwan 9/20/1999 Chi-Chi Taiwan-03 9/20/1999	1540 2635	EW EW	1.5 2.92	TCU115 TCU089	7.62 6.2	21.76 9.81	215.34 671.52	D-4
Chi-Chi Taiwan 9/20/1999 Chi-Chi Taiwan-03 9/20/1999	1540 2663	NS EW	1.57 1.09	TCU115 TCU141	7.62 6.2	21.76 33.6	215.34 223.04	E-4
Chi-Chi Taiwan 9/20/1999 Chi-Chi Taiwan-04 9/20/1999	1542 2741	NS NS	1.39 2.63	TCU117 CHY082	7.62 6.2	25.42 48.91	198.58 193.69	A-5
Chi-Chi Taiwan 9/20/1999 Chi-Chi Taiwan-04 9/20/1999	1542 2750	NS NS	1.39 2.08	TCU117 CHY099	7.62 6.2	25.42 73.39	198.58 228.84	B-5
Chi-Chi Taiwan 9/20/1999 Chi-Chi Taiwan-04 9/20/1999	1547 2883	NS EW	1.42 1.82	TCU123 TCU109	7.62 6.2	14.91 50.69	270.22 535.13	C-5
Chi-Chi Taiwan 9/20/1999 Chi-Chi Taiwan-04 9/20/1999	1552 2894	NS EW	2.58 1.62	TCU140 TCU123	7.62 6.2	32.95 45.45	223.6 270.22	D-5
Chi-Chi Taiwan 9/20/1999 Chi-Chi Taiwan-06 9/25/1999	1553 3270	NS NS	2.3 0.73	TCU141 CHY030	7.62 6.3	24.19 45.29	223.04 204.71	E-5
Niigata Japan 10/23/2004 Chi-Chi Taiwan-06 9/25/1999	4219 3285	EW EW	2.76 1.28	NIGH01 CHY054	6.63 6.3	9.46 77.63	480.4 172.1	A-6
Chuetsu-oki 7/16/2007 Taiwan SMART1(40) 5/20/1986	4856 3641	NS EW	0.44 2.25	Kashiwazaki City Center SMART1 I11	6.8 6.32	11.09 60	294.38 309.41	B-6
Chuetsu-oki 7/16/2007 Taiwan SMART1(40) 5/20/1986	4875 3648	NS NS	0.25 0.97	Kariwa SMART1 M08	6.8 6.32	12 59.07	282.57 301.05	C-6
Chuetsu-oki 7/16/2007 Cape Mendocino 4/25/1992	4875 3746	EW NS	0.37 0.9	Kariwa Centerville Beach Naval Fac	6.8 7.01	12 18.31	282.57 459.04	D-6
Chuetsu-oki 7/16/2007 Chi-Chi (aftershock 2) Taiwan 9/20/1999	4896 3844	EW EW	0.42 0.94	Kashiwazaki NPP Service Hall Array CHY004	6.8 6.2	10.97 65.57	201 271.3	E-6
Chi-Chi (aftershock 3) Taiwan 9/20/1999 Iwate 6/13/2008	3850 5664	EW NS	1.07 0.48	CHY002 MYG005	6.2 6.9	37.24 13.47	235.13 361.24	A-7
Iwate 6/13/2008 Umbria Marche Italy 9/26/1997	5777 4350	NS NS	1.57 1.17	Shikama Town Gubbio-Piana	6.9 6	31.87 35.91	334.55 492	B-7
Iwate 6/13/2008 Iwate 6/13/2008	5800 5472	NS NS	1.43 2.39	Yokote Masuda Tamati Masu AKT017	6.9 6.9	29.89 33.76	368.34 643.62	C-7
Iwate 6/13/2008 Iwate 6/13/2008	5801 5474	EW NS	1.05 1.45	Hirakamachi Asamai Yokote AKT019	6.9 6.9	36.87 28.79	325.79 640.14	D-7
Iwate 6/13/2008 Iwate 6/13/2008	5803 5781	EW EW	1.74 1.92	Yokote Ju Monjimachi Misato Miyagi Kitaura - A	6.9 6.9	32.56 38.04	343.65 278.35	E-7
Iwate 6/13/2008 Iwate 6/13/2008	5803 5803	NS EW	1.57 0.71	Yokote Ju Monjimachi Yokote Ju Monjimachi	6.9 6.9	32.56 32.56	343.65 343.65	A-8
Iwate 6/13/2008 Iwate 6/13/2008	5810 5810	EW NS	1.37 0.96	Machimukai Town Machimukai Town	6.9 6.9	24.1 24.1	655.45 655.45	B-8
Darfield New Zealand 9/3/2010 Darfield New Zealand 9/3/2010	6888 6952	NS NS	0.69 0.59	Christchurch Cathedral College Papanui High School	7 7	19.89 18.73	198 263.2	C-8
Darfield New Zealand 9/3/2010 Christchurch New Zealand 2/21/2011	6889 8062	NS EW	0.6 0.97	Christchurch Hospital Canterbury Aero Club	7 6.2	18.4 14.41	194 280.26	D-8
Darfield New Zealand 9/3/2010 Christchurch New Zealand 2/21/2011	6952 8067	EW NS	0.92 0.76	Papanui High School Christchurch Cashmere High School	7 6.2	18.73 4.46	263.2 204	E-8

Table B.24: Spectra for Period 2.8, Amp 2.0

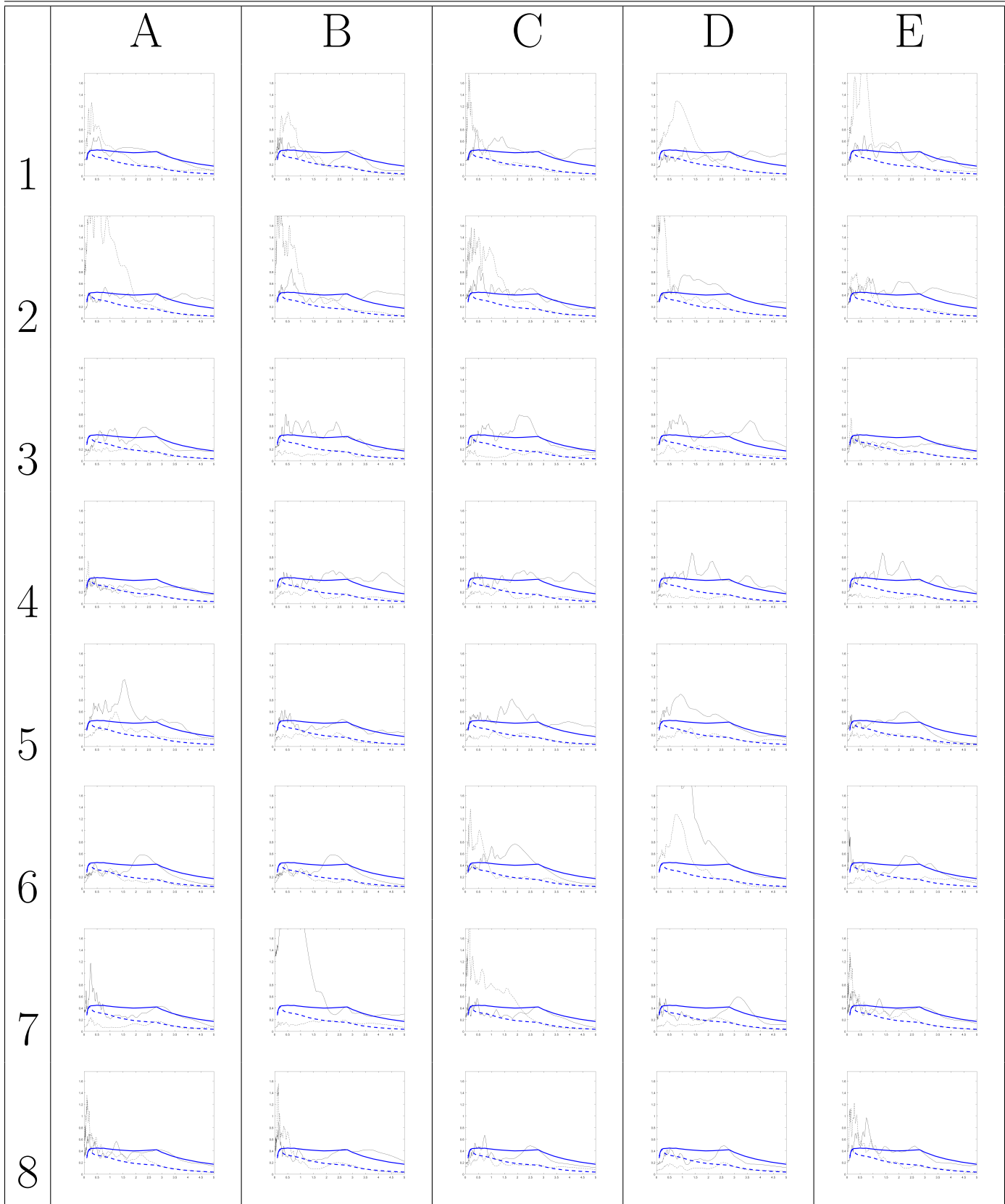


Table B.25: Spectra for Period 2.8, Amp 3.0

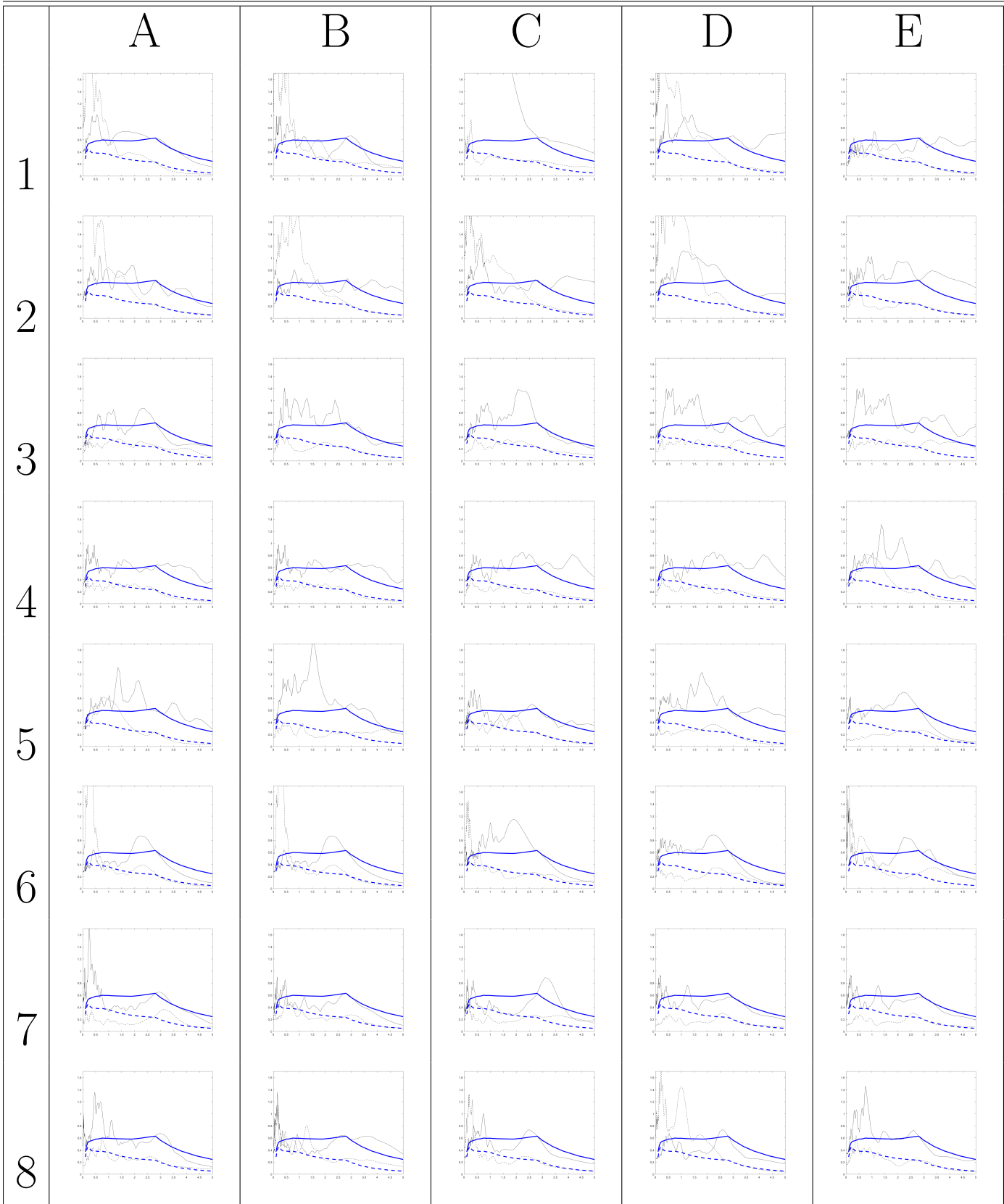


Table B.26: Details for Period 2.8, Amp 3.0

Mainshock Name Aftershock Name	RSN RSN	Direction Direction	Scale Scale	Mainshock Station Aftershock Station	Mag Adj. Mag	Rjb Rjb	Vs30 Vs30	Spec
Imperial Valley-06 10/15/1979 Managua Nicaragua-01 12/23/1972	171 95	EW NS	1.38 2.16	El Centro - Meloland Geot. Array Managua ESSO	6.53 6.24	0.07 4.06	264.57 288.77	A-1
Loma Prieta 10/18/1989 Gazli USSR 5/17/1976	806 126	NS EW	1.96 1.27	Sunnyvale - Colton Ave. Karakyr	6.93 6.8	24.23 5.46	267.71 259.59	B-1
Northridge-01 1/17/1994 Imperial Valley-06 10/15/1979	1051 161	EW NS	5.96 1.54	Pacoima Dam (upper left) Brawley Airport	6.69 6.53	7.01 10.42	2016.13 208.71	C-1
Chi-Chi Taiwan 9/20/1999 Imperial Valley-06 10/15/1979	1180 179	EW NS	3.55 2.03	CHY002 El Centro Array 4	7.62 6.53	24.96 7.05	235.13 208.91	D-1
Chi-Chi Taiwan 9/20/1999 Coalinga-01 5/2/1983	1195 335	NS NS	2.73 2.26	CHY026 Parkfield - Fault Zone 10	7.62 6.36	29.52 31.62	226.01 372.73	E-1
Chi-Chi Taiwan 9/20/1999 Baja California 2/7/1987	1199 585	NS NS	3.45 1.9	CHY032 Cerro Prieto	7.62 5.5	35.43 4.46	192.71 471.53	A-2
Chi-Chi Taiwan 9/20/1999 Loma Prieta 10/18/1989	1238 783	EW NS	2.31 2.29	CHY092 Oakland - Outer Harbor Wharf	7.62 6.93	22.69 74.26	253.72 248.62	B-2
Chi-Chi Taiwan 9/20/1999 Loma Prieta 10/18/1989	1477 802	NS NS	3.83 2.03	TCU031 Saratoga - Aloha Ave	7.62 6.93	30.17 8.5	489.22 380.89	C-2
Chi-Chi Taiwan 9/20/1999 Northridge-01 1/17/1994	1492 953	NS NS	1.16 1.93	TCU052 Beverly Hills - 14145 Mulhol	7.62 6.69	0.66 17.15	579.1 355.81	D-2
Chi-Chi Taiwan 9/20/1999 Chi-Chi Taiwan-03 9/20/1999	1501 2457	EW EW	2.6 0.99	TCU063 CHY024	7.62 6.2	9.78 19.65	476.14 427.73	E-2
Chi-Chi Taiwan 9/20/1999 Chi-Chi Taiwan-03 9/20/1999	1529 2458	EW EW	1.4 1.34	TCU102 CHY025	7.62 6.2	1.49 28.67	714.27 277.5	A-3
Chi-Chi Taiwan 9/20/1999 Chi-Chi Taiwan-03 9/20/1999	1534 2507	EW EW	2.33 0.96	TCU107 CHY101	7.62 6.2	15.99 25.3	409 258.89	B-3
Chi-Chi Taiwan 9/20/1999 Chi-Chi Taiwan-03 9/20/1999	1536 2509	NS EW	1.83 1.28	TCU110 CHY104	7.62 6.2	11.58 35.05	212.72 223.24	C-3
Chi-Chi Taiwan 9/20/1999 Chi-Chi Taiwan-03 9/20/1999	1537 2650	NS EW	3.15 1.58	TCU111 TCU116	7.62 6.2	22.12 22.13	237.53 493.09	D-3
Chi-Chi Taiwan 9/20/1999 Chi-Chi Taiwan-03 9/20/1999	1537 2663	EW EW	3.94 1.9	TCU111 TCU141	7.62 6.2	22.12 33.6	237.53 223.04	E-3
Chi-Chi Taiwan 9/20/1999 Chi-Chi Taiwan-04 9/20/1999	1538 2744	NS NS	2.84 1.71	TCU112 CHY088	7.62 6.2	27.48 48.41	190.54 318.52	A-4
Chi-Chi Taiwan 9/20/1999 Chi-Chi Taiwan-06 9/25/1999	1538 3270	EW NS	4.23 1.46	TCU112 CHY030	7.62 6.3	27.48 45.29	190.54 204.71	B-4
Chi-Chi Taiwan 9/20/1999 Chi-Chi Taiwan-06 9/25/1999	1540 3285	EW EW	3 2.53	TCU115 CHY054	7.62 6.3	21.76 77.63	215.34 172.1	C-4
Chi-Chi Taiwan 9/20/1999 Chi-Chi Taiwan-06 9/25/1999	1540 3311	NS EW	3.13 1.54	TCU115 CHY092	7.62 6.3	21.76 43.93	215.34 253.72	D-4
Chi-Chi Taiwan 9/20/1999 Chi-Chi Taiwan-06 9/25/1999	1542 3320	EW EW	2.97 2.95	TCU117 CHY111	7.62 6.3	25.42 68.97	198.58 276.34	E-4
Chi-Chi Taiwan 9/20/1999 Taiwan SMART1(40) 5/20/1986	1542 3648	NS NS	2.77 1.98	TCU117 SMART1 M08	7.62 6.32	25.42 59.07	198.58 301.05	A-5
Chi-Chi Taiwan 9/20/1999 Chi-Chi (aftershock 3) Taiwan 9/20/1999	1547 3850	NS NS	2.83 2.92	TCU123 CHY002	7.62 6.2	14.91 37.24	270.22 235.13	B-5
Chi-Chi Taiwan 9/20/1999 Umbria Marche Italy 9/26/1997	1552 4350	NS EW	5.16 1.96	TCU140 Gubbio-Piana	7.62 6	32.95 35.91	223.6 492	C-5
Chi-Chi Taiwan 9/20/1999 Chuetsu-oki 7/16/2007	1553 4856	NS NS	4.6 0.36	TCU141 Kashiwazaki City Center	7.62 6.8	24.19 11.09	223.04 294.38	D-5
Chuetsu-oki 7/16/2007 Chuetsu-oki 7/16/2007	4856 4875	NS NS	0.88 0.2	Kashiwazaki City Center Kariwa	6.8 6.8	11.09 12	294.38 282.57	E-5
Chuetsu-oki 7/16/2007 Chuetsu-oki 7/16/2007	4875 4896	NS EW	0.5 0.35	Kariwa Kashiwazaki NPP Service Hall Array	6.8 6.8	12 10.97	282.57 201	A-6
Chuetsu-oki 7/16/2007 Iwate 6/13/2008	4875 5495	EW NS	0.75 2.23	Kariwa AKTH19	6.8 6.9	12 34.54	282.57 287.96	B-6
Chuetsu-oki 7/16/2007 Iwate 6/13/2008	4896 5656	EW NS	0.85 0.86	Kashiwazaki NPP Service Hall Array IWTH24	6.8 6.9	10.97 5.18	201 486.41	C-6
Chuetsu-oki 7/16/2007 Iwate 6/13/2008	5264 5664	NS NS	0.7 0.4	NIG018 MYG005	6.8 6.9	10.78 13.47	198.26 361.24	D-6
Iwate 6/13/2008 Iwate 6/13/2008	5664 5775	NS EW	0.97 2.55	MYG005 Tamati Ono	6.9 6.9	13.47 28.91	361.24 561.59	E-6
Iwate 6/13/2008 Iwate 6/13/2008	5777 5801	NS EW	3.14 0.86	Shikama Town Hirakamachi Asamai Yokote	6.9 6.9	31.87 36.87	334.55 325.79	A-7
Iwate 6/13/2008 Iwate 6/13/2008	5800 5805	NS NS	2.85 1.54	Yokote Masuda Tamati Masu Yokote City - Nobita	6.9 6.9	29.89 41.51	368.34 253.07	B-7
Iwate 6/13/2008 Iwate 6/13/2008	5801 5810	EW EW	2.1 1.12	Hirakamachi Asamai Yokote Machimukai Town	6.9 6.9	36.87 24.1	325.79 655.45	C-7
Iwate 6/13/2008 Darfield New Zealand 9/3/2010	5803 6888	EW NS	3.48 0.57	Yokote Ju Monjimachi Christchurch Cathedral College	6.9 7	32.56 19.89	343.65 198	D-7
Iwate 6/13/2008 Darfield New Zealand 9/3/2010	5803 6889	NS NS	3.13 0.49	Yokote Ju Monjimachi Christchurch Hospital	6.9 7	32.56 18.4	343.65 194	E-7
Iwate 6/13/2008 Darfield New Zealand 9/3/2010	5805 6952	NS EW	3.78 0.75	Yokote City - Nobita Papanui High School	6.9 7	41.51 18.73	253.07 263.2	A-8
Iwate 6/13/2008 Darfield New Zealand 9/3/2010	5810 6962	EW EW	2.75 1.08	Machimukai Town ROLC	6.9 7	24.1 1.54	655.45 295.74	B-8
Darfield New Zealand 9/3/2010 Christchurch New Zealand 2/21/2011	6888 8062	NS EW	1.38 1.88	Christchurch Cathedral College Canterbury Aero Club	7 6.2	19.89 14.41	198 280.26	C-8
Darfield New Zealand 9/3/2010 Christchurch New Zealand 2/21/2011	6889 8067	NS NS	1.21 1.55	Christchurch Hospital Christchurch Cashmere High School	7 6.2	18.4 4.46	194 204	D-8
Darfield New Zealand 9/3/2010 Christchurch New Zealand 2/21/2011	6952 8118	EW EW	1.83 0.78	Papanui High School Papanui High School	7 6.2	18.73 9.06	263.2 263.2	E-8

Appendix C

MEDIAN SHIFT PROBABILITY EXCEL IMPLEMENTATION

C.1 User Interface

This excel tool has been constructed as an implementation of the Median Shift Probability (MSP) method introduced in Chapter 5. The version included with this Thesis is considered Version 1.0. It is anticipated that future versions will address both expected updates and required bug fixes, but the structure of the program will likely remain unchanged.

Upon successful opening of the excel file, the user is shown only a single excel sheet named "Inputs". This sheet is the only interface required to complete the MSP method. Figure C.1 shows a screen capture of the initial portion of the "Inputs" sheet, where some bibliographical information is available to the user. Below this information, a legend is provided which indicates the type of cells shown in the "Inputs" sheet. These are categorized as:

Input These are required user inputs. While example values of these cells are provided in this appendix, the values are expected to vary significantly between buildings and variations in these values can lead to important changes in the obtained results. A user should therefore input each value manually.

Optional Input These are inputs which is available for modification by the user, but default values are provided which will likely satisfy a majority of buildings being considered. These default values are provided as an estimation and will likely lead to similar conclusions as those obtained from those inputted by a user.

Calculation Result These are results obtained from internal calculations completed by the tool. A user should not modify these cells as they are included in the "Inputs" sheet for informative purposes only. It is important to note that protected mode is not enforced on these cells to allow future development.

Output These are final results which are of interest to the user when obtaining conclusions relevant to the objective of the MSP method.

Instructions These are small reminder instructions provided throughout the sheet. Once a user becomes familiar with this tool, this appendix can be replaced with only the information provided by these cells.

The input cells for the first step are located to the right of the bibliographical information and the cell legend, as shown in Figure C.1. The required inputs consist of building and owner specific parameters, and include the desired rate of return, the occupancy time, building value, floor area, and a drop-down menu to select from various occupancy types. The restriction on the occupancy type selection is required to obtain non-structural component quantity information. Beyond these inputs, several optional inputs are provided which focus on the casualty estimation portion of the building. The various default values provided are obtained from several sources

previously mentioned in Chapter 4 and Chapter 5 (DHS/FEMA 2007, FEMA 2012, DOT 2016).

Median Shift Probability (MSP) Method for Upgrade Viability

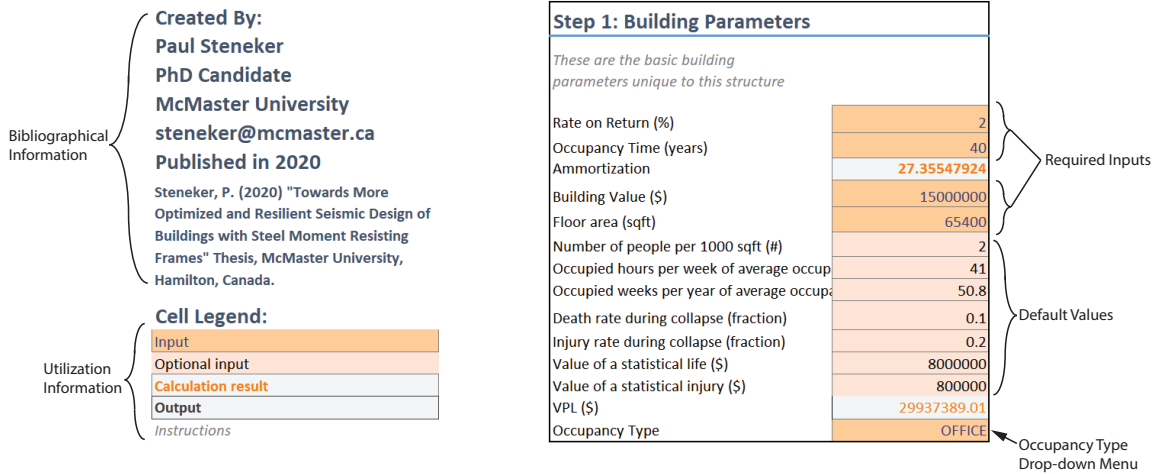


Figure C.1: Screen Shot of Owner Parameter Step

Once the building and owner parameters have been selected, the second step should be undertaken. This consists of specifying the original structural configuration of the building. Currently, there are 5 various structural materials available for selection: steel, reinforced concrete, masonry, cold formed steel, and wood, where the preceding 2 materials are currently limited to light-weight construction. Once a material is selected, a user can specify up to 12 various elements to be included in the loss analysis. Quantities of each elements also need to be specified. A screen shot of this interface in the "Inputs" sheet is shown in Figure C.2.

Step 2: Structural Component Population		
Element	Steel	Quantity
B1031.001	Bolted shear tab gravity connections	276
B1031.021a	Welded column splices, Column W < 150 plf	35
B1035.041	Pre-Northridge WUF-B beam-column joint, beam one s	16
B1035.051	Pre-Northridge WUF-B beam-column joint, beam both	16
B1035.052	Pre-Northridge WUF-B beam-column joint, beam both	8
B1035.042	Pre-Northridge WUF-B beam-column joint, beam one s	8
B1031.011b	Steel Column Base Plates, Column 150 plf < W < 300 t	35

Figure C.2: Screen Shot of Structural Component Population Step

Following the input of the structural components, a user should specify the site hazard properties of the building. This is completed by provided the site hazard curve information, typically obtained from a national geological survey service (e.g. USGS 2014). A user must determine the intensity measure to be used in the analysis. It is recommended that the intensity measure used be multiples of the maximum considered earthquake spectral acceleration as this value is often used as a reference or a design spectral acceleration in building codes. A user should then provide a series of intensity measures and corresponding return periods for their site. A minimum of 3 stripes is required, but a user should target at least 5 intensities for inclusion, with a focus on including a majority of intensities at levels lower than the design level intensity. As shown in Figure C.3, a graphical display is included which shows the calculated annual frequency of exceedance obtained from the site hazard curve information provided.

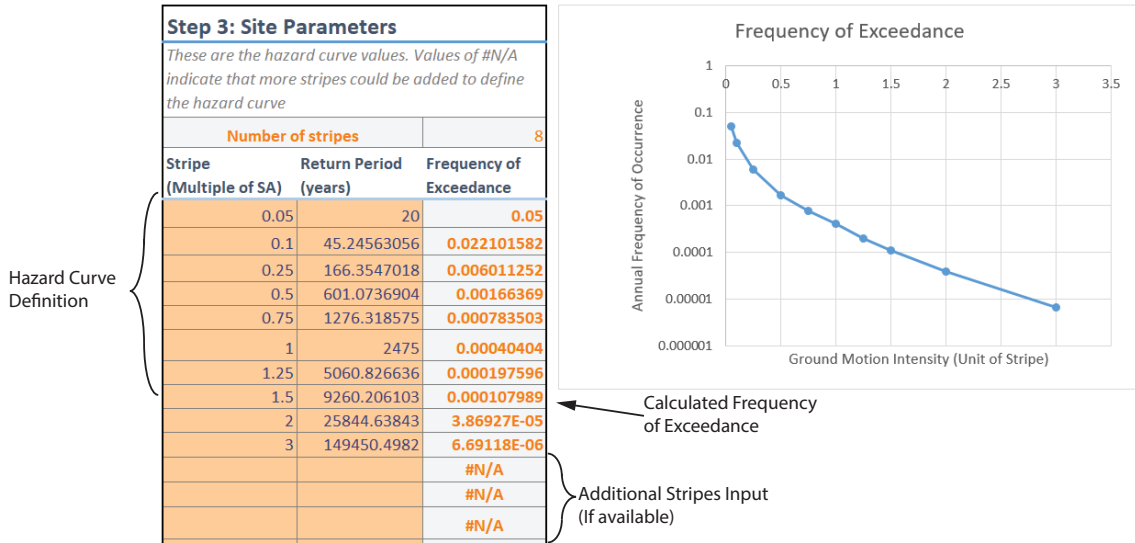


Figure C.3: Screen Shot of Site Parameters Step

Once the site parameters are included, the user should move down the sheet to Step 4 where information regarding the non-structural component population is specified. The population of non-structural components is divided among several different element categories in order to utilize the normative quantity estimation information provided by ATC in FEMA P-58 (FEMA 2012). The default components initially assumed by the program consist of components which are expected to have the lowest overall seismic performance, as determined by their damage state fragility curve parameters. If a user specifies a component in the drop-down menu, their selection will automatically override the default assumption, as specified in the define damage state column. Some components require a user input to determine their capacity, such as anchorage detailing for machinery. This will be indicated in the damage state column as a "User" value, and will require modifications to the "NS Perf" sheet of the program, addressed in the next Section. Once a component is either selected, or the default component is used, the user is

able to modify the quantity percentile of the component occupying the building. The population quantity was tabulated by ATC as a statistical sample of the number of components in a typical building for each occupancy type. However, the user is able to select the statistical quartile of their component population, either specifying the bottom 10%, the mean (50%) or the upper 90% of the sample distribution. Finally, the user is able to estimate the upgrade cost associated with each component as a percentage of the repair cost of the component. This method of estimation provides an easy understanding and comparison of the expected tasks and scope of work required for upgrade versus for repair. Default values are provided as those obtained from Chapter 5, determined using RSMMeans. The remaining 2 columns identify which components have been selected for upgrade in both the strategy consisting of only non-structural components, and the combined structural and non-structural upgrades options. These values indicate a non-structural component’s upgrade cost as a percentage of the building value, and will be updated following completion of Step 5.

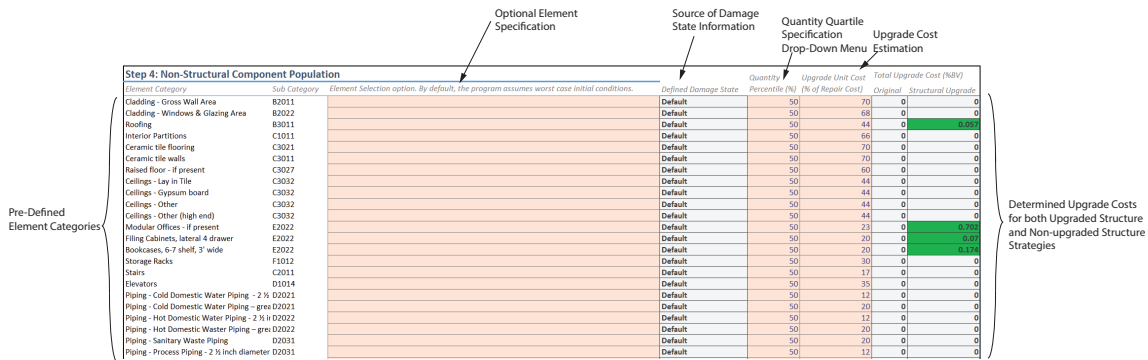


Figure C.4: Screen Shot of Non-Structural Component Population Step

Finally, the last step in the process consists of summarizing the building analysis results. The user must input the median and beta value for all four curves

obtained from the analysis conducted on the original building. Once inserted, the user is immediately notified of the overall viability of non-structural upgrades as the program tabulates the BCR values for each component in the original structure. The overall performance of the upgrade strategy limited to only non-structural components is summarized in the first set of large BCR and NPV values, which will change from a light red to light green if a viable strategy is determined. To determine the viability of a structural upgrade in a Level 1 framework analysis, the user must first enter the estimated structural upgrade cost. The Q values must then be modified as appropriate for the upgrade under consideration, and modifications should be made to all 4 Q values before a user verifies the viability of the strategy. Once the modifications are complete, the viability of the combined structural and non-structural component upgrade strategy is indicated in either dark red or dark green at the bottom of the section. Four graphical windows are available, as shown in Figure C.5, which present the lognormal curves of both the original and upgraded structure for all four loss categories.

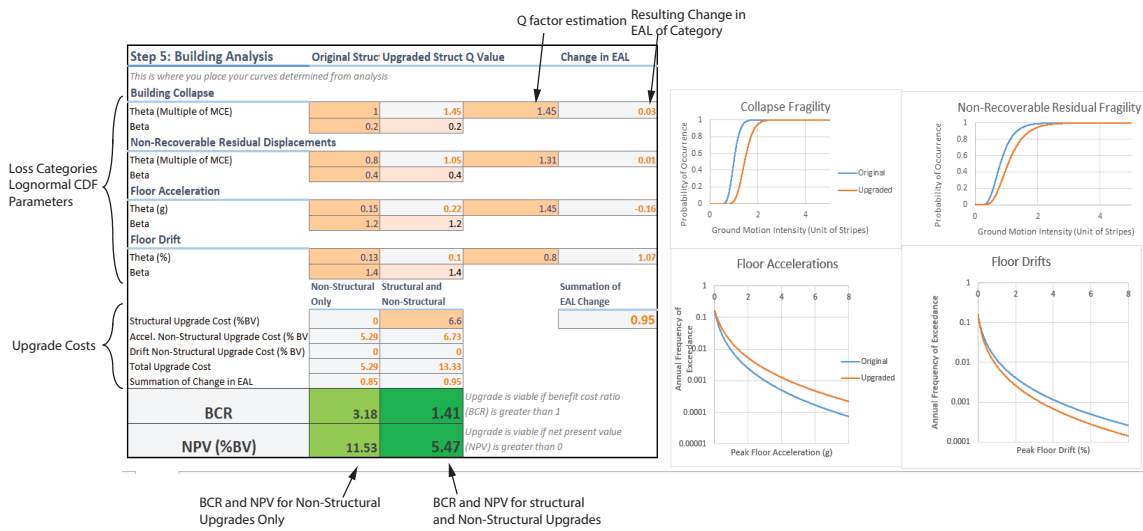


Figure C.5: Screen Shot of Building Analysis Step

C.2 Hidden Calculation Sheets

The majority of the sheets included in this program have been hidden using the built in Excel "hide" feature. These sheets include all of the calculations required for the MSP method. Typically, a user does not require access to these sheets, but some modifications may be desired. Should a user require access, they can simply right click on the "Inputs" sheet tab, shown in Figure C.6, and select "Unhide...". A menu will appear which shows all of the hidden calculation sheets. A brief description of each sheet is provided in this appendix, and contact with the author is always possible for further details.

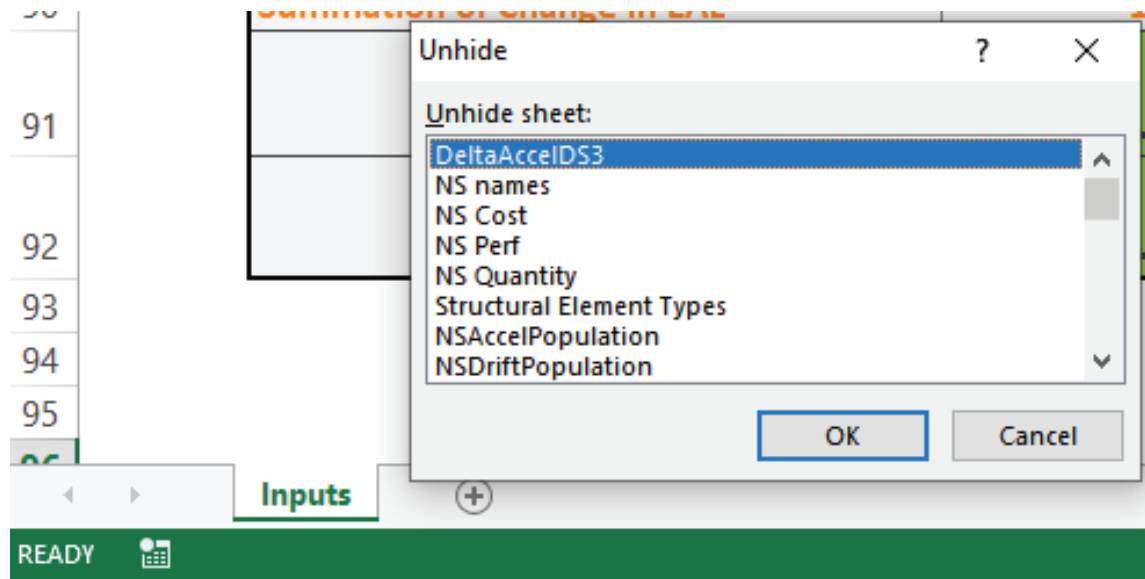


Figure C.6: Screen Shot of Location of Calculation Sheets

NS names This sheet simply organizes the non-structural component names into categories which allow for their selection using the drop-down menus.

NS Cost This sheet contains all of the repair costing data for all of the damage states of all the components included in FEMA P-58 (FEMA 2012). The data includes mean values for the 3 different quantity percentages, as well as the data for the reduction in repair due to economies of scale. However, for the MSP method, only the median value of the repair cost is used for each damage state.

NS Perf This sheet contains all of the fragility curve specification for all of the damage states of all the components included in FEMA P-58 (FEMA 2012). The data is used to determine the median and lognormal standard deviation parameters needed to determine the expected damage of each component at each damage state. If a component is selected which requires User inputs, the

user will need to open this sheet and modify the relevant cells.

NS Quantity This sheet contains both the quantity estimations for all the non-structural component categories, as well as provides the default component values. This sheet determines the lowest and highest performing version of each component category as these are the components initially assumed to be the original and upgraded components in the building.

Structural Element Types This sheet includes the lists needed to select from the various structural components in Step 2. No other information is included in this sheet.

NSAccelPopulation / NSDriftPopulation These sheets calculated the BCR of either the acceleration or drift sensitive components, respectively. Both sheets contain summaries of the information needed for each component, such as repair and upgrade cost, and the lognormal parameters for both the original and upgraded components. The sheets also calculate the BCR for both the original building and the building with the structural upgrade. A user should begin here when attempting to understand the functions of the tool.

AccelIDS, UPAccelIDS, DriftDS, etc... These sheets simply calculate the integral of the product of the floor hazard curve and component fragility curve for unique damage states. The UP version of these sheets uses the hazard curve of the upgraded structure, while the original structures hazard curve is used in the Accel or Drift versions. Currently, the tool only considers the first 3 damage states, but does differentiate between mutual, sequential or simultaneous. Future versions will include more damage states if needed but current quantities appear sufficient for the components considered.

Delta... These sheets simply calculate the difference in expected annual damage of each component obtained by upgrading the component. This is done by calculating the difference in the fragility curve, before calculating the integral of the product of the hazard curve and resulting change in fragility curve. These sheets are included for backward compatibility and will be replaced in future versions of the tool

DeltaUP... These sheets are similar as their original (non-”UP”) counterparts, but use the hazard curve obtained from the upgraded structure. Similarly to their contemporaries, these sheets will be rendered obsolete in future versions of this tool, to be replaced with a simplified approach using the results from the AccelDS, UpAccelDS, DriftDS, etc... sheets.

C.3 References

DOT (Department of Transportation) (2016) “Guidance on Treatment of the Economic Value of a Statistical Life (VSL) in U.S. Department of Transportation Analyses – 2016 Adjustment.” *U.S. Department of Transportation Office of the Secretary of Transportation, Memorandum to Secretarial Officers*, August 8th, 2016, Washington, D.C.

DHS/FEMA (2007), ”Multi-hazard Loss Estimation Methodology: Earthquake Model, HAZUS-MH MR3 Technical Manual”, *National Institute of Building Sciences (NIBS) for the Department of Homeland Security, Emergency Preparedness and Response Directorate*, Federal Emergency Management Agency, Mitigation Division.

FEMA (2012). “Seismic Performance Assessment of Buildings - Methodology.”
Report P-58 Federal Emergency Management Agency, Washington, D.C.

USGS (United States Geological Survey) (2014). “Unified Hazard Tool” Version
4.1.9 (Lat: 47.6, Long: -122.3, T: 1.0 Sec)